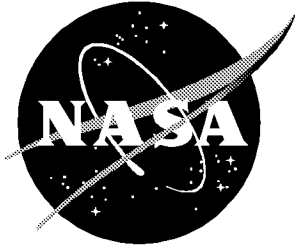


NASA/TP-2001-211260
AMCOM/AFDD/TR-00-A-003
ARL-TR-2154



Wind Tunnel Evaluation of a Model Helicopter Main-Rotor Blade With Slotted Airfoils at the Tip

*Kevin W. Noonan
Joint Research Program Office
Aeroflightdynamics Directorate
U.S. Army Aviation and Missile Command
Langley Research Center, Hampton, Virginia*

*William T. Yeager, Jr., Jeffrey D. Singleton,
Matthew L. Wilbur, and Paul H. Mirick
Vehicle Technology Center
U.S. Army Research Laboratory
Langley Research Center, Hampton, Virginia*

The NASA STI Program Office . . . in Profile

Since its founding, NASA has been dedicated to the advancement of aeronautics and space science. The NASA Scientific and Technical Information (STI) Program Office plays a key part in helping NASA maintain this important role.

The NASA STI Program Office is operated by Langley Research Center, the lead center for NASA's scientific and technical information. The NASA STI Program Office provides access to the NASA STI Database, the largest collection of aeronautical and space science STI in the world. The Program Office is also NASA's institutional mechanism for disseminating the results of its research and development activities. These results are published by NASA in the NASA STI Report Series, which includes the following report types:

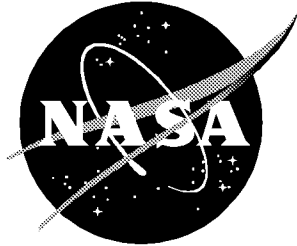
- **TECHNICAL PUBLICATION.** Reports of completed research or a major significant phase of research that present the results of NASA programs and include extensive data or theoretical analysis. Includes compilations of significant scientific and technical data and information deemed to be of continuing reference value. NASA counterpart of peer-reviewed formal professional papers, but having less stringent limitations on manuscript length and extent of graphic presentations.
- **TECHNICAL MEMORANDUM.** Scientific and technical findings that are preliminary or of specialized interest, e.g., quick release reports, working papers, and bibliographies that contain minimal annotation. Does not contain extensive analysis.
- **CONTRACTOR REPORT.** Scientific and technical findings by NASA-sponsored contractors and grantees.
- **CONFERENCE PUBLICATION.** Collected papers from scientific and technical conferences, symposia, seminars, or other meetings sponsored or co-sponsored by NASA.
- **SPECIAL PUBLICATION.** Scientific, technical, or historical information from NASA programs, projects, and missions, often concerned with subjects having substantial public interest.
- **TECHNICAL TRANSLATION.** English-language translations of foreign scientific and technical material pertinent to NASA's mission.

Specialized services that complement the STI Program Office's diverse offerings include creating custom thesauri, building customized databases, organizing and publishing research results . . . even providing videos.

For more information about the NASA STI Program Office, see the following:

- Access the NASA STI Program Home Page at <http://www.sti.nasa.gov>
- Email your question via the Internet to help@sti.nasa.gov
- Fax your question to the NASA STI Help Desk at (301) 621-0134
- Telephone the NASA STI Help Desk at (301) 621-0390
- Write to:
NASA STI Help Desk
NASA Center for AeroSpace Information
7121 Standard Drive
Hanover, MD 21076-1320

NASA/TP-2001-211260
AMCOM/AFDD/TR-00-A-003
ARL-TR-2154



Wind Tunnel Evaluation of a Model Helicopter Main-Rotor Blade With Slotted Airfoils at the Tip

*Kevin W. Noonan
Joint Research Program Office
Aeroflightdynamics Directorate
U.S. Army Aviation and Missile Command
Langley Research Center, Hampton, Virginia*

*William T. Yeager, Jr., Jeffrey D. Singleton,
Matthew L. Wilbur, and Paul H. Mirick
Vehicle Technology Center
U.S. Army Research Laboratory
Langley Research Center, Hampton, Virginia*

National Aeronautics and
Space Administration

Langley Research Center
Hampton, Virginia 23681-2199

December 2001

The use of trademarks or names of manufacturers in this report is for accurate reporting and does not constitute an official endorsement, either expressed or implied, of such products or manufacturers by the National Aeronautics and Space Administration or the U.S. Army.

Available from:

NASA Center for AeroSpace Information (CASI)
7121 Standard Drive
Hanover, MD 21076-1320
(301) 621-0390

National Technical Information Service (NTIS)
5285 Port Royal Road
Springfield, VA 22161-2171
(703) 605-6000

Summary

Data for rotors using unconventional airfoils are of interest to permit an evaluation of this technology's capability to meet the U.S. Army's need for increased helicopter mission effectiveness and improved safety and survivability. Thus, an experimental investigation was conducted in the Langley Transonic Dynamics Tunnel (TDT) to evaluate the effect of using slotted airfoils in the rotor blade tip region (85 to 100 percent radius) on rotor aerodynamic performance and loads. Four rotor configurations were tested in forward flight at advance ratios from 0.15 to 0.45 and in hover in-ground effect. The hover tip Mach number was 0.627, which is representative of a design point of 4000-ft geometric altitude and a temperature of 95°F. The baseline rotor configuration had a conventional single-element airfoil in the tip region. A second rotor configuration had a forward-slotted airfoil with a -6° slat, a third configuration had a forward-slotted airfoil with a -10° slat, and a fourth configuration had an aft-slotted airfoil with a 3° flap (trailing edge down).

The results of this investigation indicate that the -6° slat configuration offers some performance and loads benefits over the other three configurations. At the higher rotor lift coefficients at each advance ratio, the -6° slat configuration had the lowest rotor torque coefficient, whereas the baseline rotor had the lowest torque coefficient for the lower lift coefficients. For hover in-ground effect, the -6° slat configuration had the lowest torque coefficient for rotor lift coefficients greater than about 0.007, and the baseline rotor had the lowest torque coefficient for lift coefficients less than this value. The -6° slat configuration had the lowest pitch-link loads (normalized, half peak to peak) at the higher rotor lift coefficients at each advance ratio. However, the maximum 4-per-revolution (4P) fixed-system vertical loads (normalized) of both forward-slotted rotor configurations were generally higher than those of the other two configurations for advance ratios up through 0.25.

Introduction

The U.S. Army has determined a need for increased mission effectiveness and improved safety and survivability from its future helicopter fleet by analyzing the capabilities of the current fleet (ref. 1).

This need can be addressed, in part, by the development of main rotors that will allow larger payload capability, higher forward flight speeds, increased range and endurance, and greater maneuverability and agility. For fiscal year 2005, the Army's stated aeromechanics technical objectives include a 16-percent increase in maximum blade loading and a 6-percent increase in rotor aerodynamic efficiency (ref. 1). Both advanced single-element airfoils and new rotor blade planforms can contribute to increased main rotor performance. However, current rotor airfoils are finely tuned shapes that produce high lift while maintaining acceptable pitching moments and drag levels. Further dramatic improvements in the lift and drag characteristics of advanced, single-element rotor airfoils are unlikely. Thus, the application of conventional technology alone cannot meet the Army's future aeromechanics needs, so unconventional technology must be evaluated.

Slotted airfoils have recently been considered by the Army for main rotor application because of their high lift potential. Experimental two-dimensional aerodynamic characteristics for two of these slotted airfoils confirmed the expected high lift capability (ref. 2). During the design of the slotted airfoils, it was questioned whether favorable two-dimensional performance, if obtained, would be preserved in the three-dimensional, unsteady, rotating environment of a main rotor blade. To evaluate the potential benefits in rotor performance associated with using unconventional (slotted) airfoils, the development of a model rotor that incorporated slotted airfoils was undertaken concurrently with the development of the two-dimensional slotted airfoil sections (ref. 2).

An experimental investigation was conducted in the Langley Transonic Dynamics Tunnel (TDT) to determine the effect of using slotted airfoils in the rotor blade tip region (85 to 100 percent radius) on rotor aerodynamic performance and loads. To make this determination, an aeroelastically scaled model rotor that could be configured in the rotor tip region for a baseline, single-element airfoil and for two types of slotted airfoils was tested over a range of shaft angles at advance ratios from 0.15 to 0.45 and in hover in-ground effect. This rotor was designated the HIMARCS I (High Maneuverability and Agility Rotor and Control System) rotor.

Symbols

The positive directions of forces, angles, and velocities are shown in figure 1.

A	balance axial force, lb	PL HPP	normalized half peak-to-peak pitch-link load
a	speed of sound, ft/sec	PM FSO _{4p}	normalized oscillatory 4-per-revolution fixed-system pitching moment (pitching moment at balance centroid)
C_D	rotor drag coefficient, $\frac{D}{\rho \pi R^2 (\Omega R)^2}$	PM HPP	normalized half peak-to-peak fixed-system pitching moment
C_L	rotor lift coefficient, $\frac{L}{\rho \pi R^2 (\Omega R)^2}$	Q	rotor shaft torque, measured from balance yawing moment, ft-lb
C_Q	rotor torque coefficient, $\frac{Q}{\rho \pi R^3 (\Omega R)^2}$	R	rotor radius, ft
D	rotor drag, $N \sin \alpha_s + A \cos \alpha_s$, lb	r	spanwise distance along blade radius measured from center of rotation, ft
d	rotor diameter, ft	RM FSO _{4p}	normalized oscillatory 4-per-revolution fixed-system rolling moment (rolling moment at balance centroid)
EI	rotor blade bending stiffness, lb-ft ²	RM HPP	normalized half peak-to-peak fixed-system rolling moment
FM	rotor figure of merit, $0.707 \frac{C_L^{3/2}}{C_Q}$	V	free-stream velocity, ft/sec
f_D	vehicle equivalent parasite area, ft ²	z	distance from wind tunnel floor to rotor hub, ft
GJ	rotor blade torsional stiffness, lb-ft ²	α_s	rotor-shaft angle of attack, deg
L	rotor lift, $N \cos \alpha_s - A \sin \alpha_s$, lb	$\Delta ()$	change in specified quantity
M_T	rotor hover tip Mach number, $\frac{\Omega R}{a} = 0.627$	θ	rotor blade collective pitch angle at $\frac{r}{R} = 0.75$, positive nose up, deg
m	rotor blade section mass per unit length, slugs/ft	θ_1	twist angle built into rotor blade, positive nose up, relative to blade root end (station 6.87 in.), deg
N	balance normal force, lb	μ	rotor advance ratio, $\frac{V}{\Omega R}$
N FSO _{4p}	normalized oscillatory 4-per-revolution fixed-system normal (balance normal force) load	ρ	mass density of test medium, slugs/ft ³
		ψ	rotor blade azimuth angle, deg
		Ω	rotor rotational velocity, rad/sec

Abbreviations:

ARES	aeroelastic rotor experimental system
bsl	baseline
FFT	fast Fourier transform
4P	4 per revolution
HIMARCS	High Maneuverability and Agility Rotor and Control System
LE	leading edge
TDT	Transonic Dynamics Tunnel
TE	trailing edge

Apparatus

Wind Tunnel

The testing was conducted in the Langley Transonic Dynamics Tunnel (TDT); a schematic of the tunnel is shown in figure 2. The TDT, a continuous flow tunnel with a slotted test section, is capable of operation up to Mach 1.2 at stagnation pressures from near vacuum to atmospheric. The tunnel test section is 16 ft square with cropped corners and has a cross-sectional area of 248 ft². Presently, air or R-134a may be used as a test medium, although Freon 12 was previously available. Freon 12, at a nominal density of 0.006 slugs/ft³, was used as the test medium during this investigation. Because of its high molecular weight and low speed of sound, the use of Freon 12 aids the matching of model-rotor-scale Reynolds number and Mach number to full-scale values. Because the primary purpose of these tests involved rotor aerodynamic performance, matching full-scale Mach number at Reynolds numbers higher than those obtainable by testing in air was of particular interest (ref. 3). The use of Freon 12 as a test medium also allows the easing of some restrictions on model structural design while still maintaining dynamic similarity. For example, the heavier test medium permits a heavier, less efficient structural design to obtain the required stiffness characteristics, thus easing design and fabrication requirements of the model (ref. 4).

Model Description

A set of model rotor blades with aeroelastic scaling representative of a typical full-scale blade was used during this investigation. A sketch of a High Maneuverability and Agility Rotor and Control System (HIMARCS I) rotor blade is shown in figure 3. Current-generation, single-element airfoils and advanced slotted airfoils were selected for this rotor. The 10-percent-thick RC(4)-10 airfoil was selected for the inboard region ($r/R \leq 0.80$) based on its proven performance (ref. 5) as an inboard airfoil section. The RC(4)-10 airfoil has high maximum lift coefficients at Mach numbers up to 0.5, very low pitching-moment coefficients over a broad range of Mach numbers and low angles of attack, and moderately high drag divergence Mach numbers at low angles of attack. The 8-percent-thick, slotted RC(6)-08 and the single-element RC(6)-08 airfoils were selected for the tip region ($r/R \geq 0.85$) because both were specifically developed for that part of a rotor blade (refs. 2 and 6). The single-element RC(6)-08 airfoil has a proven performance as a rotor tip region airfoil section (ref. 6) and thus served as the baseline tip airfoil section. The single-element RC(6)-08 airfoil has moderately high maximum lift coefficients at Mach numbers up to 0.5, very low pitching-moment coefficients over a broad range of Mach numbers and angles of attack, and very high drag divergence Mach numbers at low angles of attack (ref. 6). A smooth transition was made between these different inboard and outboard airfoil shapes ($0.80 \leq r/R \leq 0.85$). The blade tip region was selected for the application of the slotted airfoil based on the following rationale. Retreating blade stall can limit both high-speed forward flight and maneuverability across the speed range. Retreating blade stall is likely to occur first in the tip region because a thin airfoil with little camber must be used there to minimize compressibility effects on the advancing side of the rotor disc at high forward flight speeds. A thin, slotted airfoil might provide a much higher stall boundary while maintaining good drag divergence characteristics (ref. 2). The tip region of the model blades can be configured as the baseline airfoil or a slotted airfoil (fig. 3). Section A-A in figure 3(a) illustrates the baseline airfoil, two of the forward-slotted airfoil configurations that were tested, and one of the aft-slotted airfoil configurations that was tested. One forward-slotted configuration had a -6° slat, and the second one had a -10° slat. The

details of the shapes for both forward-slotted airfoil sections are given in reference 2. The aft-slotted configuration that was tested had a 3° flap angle (trailing edge down). Details of the flap attachment to the rotor tip are shown in figure 3(b). The details of the aft-slotted airfoil shape (flap gap, overlap, flap pivot point) and the aerodynamic data for this airfoil are not yet published. However, the coordinates for all airfoil sections used on the HIMARCS I rotor are given in tables I to V. The tip region airfoil section was changed from the baseline airfoil by interchanging the nose or tail fairing piece with a slat or a flap, respectively.

Based on the following considerations, a linear twist distribution of -8° was selected for this rotor blade. The slotted airfoils were expected to delay the airfoil section stall to higher angles of attack, compared to a conventional tip airfoil section. Thus, reducing the blade twist from the typical range of -12° to -16° would not degrade the retreating blade stall boundary and would be beneficial in reducing compressibility effects in high-speed forward flight. On the advancing side of the rotor disc at high forward speeds, the tip region of a rotor blade with high twist can be operating at negative angles of attack, causing shocks to develop near the nose of the airfoil on the lower surface. Reducing the blade twist can thus reduce the potential for shock formation on the lower surface. A linear, low-twist rate (deg/in.) would also make it easier to fabricate the small size fairings, flaps, and slats. The -8° linear twist distribution selected may not be the optimum twist for this kind of rotor because no attempt was made to identify the optimum twist distribution. The thrust-weighted solidity of the HIMARCS I rotor was chosen to be 0.101 so that comparisons, with the same basis, could be made with other rotors that were previously tested in the Langley TDT (refs. 7 and 8).

Naturally, there are some small blade-to-blade differences in the structural properties within any set of rotor blades. Typical mass, flapwise stiffness, and torsional stiffness distributions (measured) are shown in figures 4 to 6. The edgewise stiffness distribution was not measured. The actual mass distribution was not determined for an entire blade because of additional costs. The outer part of the blade is configured by assembling small, interchangeable pieces that require close dimensional tolerances. A large part of the root

end of a blade was required for a pull test to demonstrate that the blade design could safely accommodate the design loads. Thus, one entire blade would be needed to measure the full-blade mass distribution, and the inner third of a second blade would be needed for a pull-test specimen. Instead, one sample blade without the interchangeable tip pieces was partially cut into 20 segments (from $r/R = 0.44$ to 0.83) to check the actual mass distribution against the target mass distribution (fig. 4). The actual mass distribution is close to the target values except for the outermost blade segment. The inner portion of the sample blade was used as a pull-test specimen. The measured non-rotating blade natural frequencies for a cantilevered boundary condition are given in table VI. The natural frequencies were measured for the baseline configuration for each blade in the set (four blades plus one spare blade). Additionally, the natural frequencies were measured for the 0° flap and the -10° slat configurations for blade 4. Each leading-edge slat was made of stainless steel and was fabricated as a single piece with an integral bracket. The addition of a slat likely resulted in local stiffening of the blade, and thus the highest frequencies were measured for the -10° slat configuration.

Each blade set was tested by using the aeroelastic rotor experimental system (ARES) test bed shown in figures 7 and 8 (ref. 7). The ARES test bed has a streamlined fuselage shape which encloses the rotor controls and drive system and is powered by a variable-frequency synchronous motor rated at 47-hp output at 12 000 rpm. The motor is connected to the rotor shaft through a belt-driven, two-stage speed reduction system. The ARES test bed rotor blade pitch control system and rotor shaft angle of attack are remotely controlled from the wind tunnel control room. The model rotor shaft angle of attack is varied by an electrically controlled hydraulic actuator. Blade collective pitch and lateral and longitudinal cyclic pitch are input to the rotor through the swash plate, which is positioned by three hydraulic actuators. The model rotor hub used in this investigation was a four-bladed articulated hub with coincident lead-lag and flapping hinges. The hub operated with a measured pitch-flap coupling ratio of 0.5 (flap up, pitch down).

Instrumentation mounted on the ARES test bed allows continuous displays of model control settings, rotor forces and moments, blade loads, and pitch-link

loads. For these tests, one pitch link was instrumented with a strain gauge to measure pitch-link tension and compression loads. Rotor blade flap and lag motions are measured by rotary potentiometers mounted on the rotor hub. Rotor shaft speed is determined by a magnetic sensor. The rotating blade data are transferred to the fixed system through a 30-channel slip-ring assembly. Rotor forces and moments are measured by a six-component strain gauge balance mounted below the pylon and drive system. Rotor lift and drag are determined from the measured balance normal and axial forces (fig. 1). Rotor torque is measured by the balance yawing moment component. The balance is fixed with respect to the rotor shaft and pitches with the fuselage. By design, fuselage forces and moments are not transmitted to the balance.

Data Acquisition

Test Conditions

The purpose of the test was to obtain data to evaluate the effect of slotted airfoils on rotor performance and loads. Therefore, data for the baseline and slotted rotor configurations were obtained at the same nominal test conditions defined by μ , M_T , α_s , and θ . Data were obtained in hover and in forward flight from $\mu = 0.15$ to 0.45 . The hover tip Mach number was 0.627 , which is representative of a design point of 4000 -ft geometric altitude and a temperature of 95°F . In hover ($\mu = 0$), data were obtained at $z/d = 0.83$. At each test point in forward flight, the rotor rotational speed and tunnel conditions were adjusted to give the desired values of M_T and μ . The ARES test bed was then pitched to the desired α_s , and the tunnel conditions were readjusted, if required. Blade collective pitch was changed to obtain variations in rotor lift. To facilitate data acquisition and reduce blade loads, rotor cyclic pitch was used to remove rotor first-harmonic flapping with respect to the rotor shaft at each test point. The maximum obtainable value of θ (and thus C_L) at each combination of μ and α_s was determined by either blade or pitch-link loads, or by ARES test bed drive-system limits.

Methods and Processing

Model deadweight tares were determined throughout the range of α_s for each blade set, that is, with each

rotor tip airfoil configuration. Aerodynamic rotor hub tares were determined throughout the test ranges of α_s and μ at 640 rpm (nominal rpm for $M_T = 0.627$) with the blades removed and the blade cuffs set at a pitch angle of 8° . Both deadweight and aerodynamic hub tares have been removed from the data presented herein. The sum of the deadweight and aerodynamic hub tares in coefficient form for $\mu = 0.35$ and $\alpha_s = -8^\circ$ is $C_L = -0.000045$, $C_D = -0.000822$, and $C_Q = 0.000036$. These values represent the magnitude of the total tares removed from the data for test conditions near the middle of the test envelope. No corrections for tunnel wall effects have been applied to the data, but as cited in reference 9, these effects are considered small for the flight conditions presented herein.

The values of C_L , C_D , and C_Q were obtained from the average of 5000 data samples taken at a rate of 1000 data samples/sec with a filter cutoff of 200 Hz. A harmonic analysis was used to reduce ARES rotor and fixed-system loads to magnitude and phase components for harmonics through 8 per revolution. For a typical harmonic analysis, 12 rotor revolutions of data are processed by using a fast Fourier transform (FFT) with checks provided on the signal periodicity and rotor speed. These checks ensure data integrity and allow processing to occur without signal windowing and the associated loss of signal power. Experience with ARES has shown that using more than 12 revolutions of data produces no increase in the accuracy of results for harmonics up through 8 per revolution; therefore, all data presented herein have been processed by using 12 rotor revolutions of data.

All pitch-link oscillatory loads were normalized to the largest pitch-link oscillatory load measured on any rotor configuration throughout the speed range tested. All 4-per-revolution (4P) fixed-system forces and moments were normalized to the largest corresponding 4P fixed-system force or moment generated by any rotor configuration throughout the speed range tested. Similarly, all half peak-to-peak moments were normalized to the largest corresponding half peak-to-peak moment generated by any rotor configuration throughout the speed range tested. This normalizing procedure was chosen because neither the fixed system nor the rotating system of the ARES test bed is a dynamically scaled representation of any existing helicopter. Therefore, scaling measured model data up to

full-scale values would not be meaningful. Ground vibration tests of the ARES test bed have shown no dynamic amplification of any strain gauge balance channels at the rotor 4P frequency.

Measurement Quality

The quality of the performance data obtained during this investigation was addressed. Based on a static calibration of the strain gauge balance used to measure rotor lift, drag, and shaft torque, the accuracy of the measurement of these variables is within the following ranges:

$$C_L: \pm 0.000138$$

$$C_D: \pm 0.000040$$

$$C_Q: \pm 0.000016$$

During the test, 1080 data points were obtained. From this data set, 259 points were repeat points taken at random. The repeated points included data within any particular run (increasing then decreasing θ for constant α_s and μ) as well as run-to-run repeat points (resetting of all test parameters, i.e., θ , α_s , and μ). The average deviation in C_L , C_D , and C_Q (ΔC_L , ΔC_D , ΔC_Q) was determined between the originally obtained data points and the repeat data points. The average positive deviations and average negative deviations for constant values of μ , M_T , α_s , θ , and zero 1-per-revolution flapping, with respect to the shaft, were determined to be as follows:

Within any particular run (259 points):

$$\Delta C_L: +0.000032 \text{ to } -0.000018$$

$$\Delta C_D: +0.000005 \text{ to } -0.000008$$

$$\Delta C_Q: +0.000001 \text{ to } -0.000001$$

Run to run (34 points):

$$\Delta C_L: +0.000015 \text{ to } -0.000050$$

$$\Delta C_D: +0.000008 \text{ to } -0.000028$$

$$\Delta C_Q: +0.000003 \text{ to } -0.000006$$

As shown, these average deviations were all within the accuracy of the static calibration of the strain gauge balance.

Presentation of Results

The hover and forward flight rotor performance data obtained during this investigation are presented in figures 9 to 15 as combinations of C_L , C_D , and C_Q . The loads data presented in figures 16 to 21 are outlined in detail on page 7. The value of C_Q for each forward flight rotor task, defined by specific values of μ , C_L , C_D , and M_T , was obtained by plotting C_L versus C_D and C_L versus C_Q at each μ for a range of shaft angles (appendix figs. A1 to A32) and then by interpolating from C_D versus C_Q cross plots (figs. A33 to A40) for the value of C_Q at the desired C_L and C_D . The desired value of C_D (table A3) was obtained by using a full-scale value of f_D , obtained from aircraft manufacturer's information, to first determine D and consequently C_D as follows:

$$D = f_D(1/2 \rho V^2)$$

$$C_D = \frac{-D}{\rho \pi R^2 (\Omega R)^2} = \frac{-f_D \mu^2}{2\pi R^2}$$

The chosen values of f_D represented both a utility-type helicopter and a scout-type helicopter. The C_Q versus μ results are presented for representative values of C_L and full-scale f_D at one value of M_T . In general, the range of the data in the C_Q versus μ plots was limited by the maximum C_L that could be attained by the rotor configurations at the higher test advance ratios. For example, the highest value of μ shown for $C_L \geq 0.0081$ is 0.35 because none of the rotor configurations were able to reach these C_L values at $\mu = 0.40$. All C_Q values presented fell within the range of the interpolated data in the C_D versus C_Q plots; that is, no extrapolations were made to obtain any of the C_Q values.

Loads data are presented in figures 16 to 21 and consist of pitch-link and fixed-system oscillatory loads. Pitch-link loads data are presented as normalized oscillatory (half peak-to-peak) load versus C_L . The fixed-system loads data, also presented as a function of C_L , are normalized 4P normal force, both normalized 4P and normalized oscillatory pitching

moment, and both normalized 4P and normalized oscillatory rolling moment. The pitch-link and fixed-system loads data are presented for five values of μ at values of α_s as being representative of what would be required to bracket the propulsive force needed to represent the same full-scale equivalent parasite areas

used in the performance data figures (figs. 10 to 15). Thus, the rotor configurations may not be at the same C_D when compared at the same μ , α_s , and C_L . This method of presentation was chosen because it was believed that the loads data were too nonlinear to allow interpolation, as with the performance data.

The data are presented in the following figures:

	Figure
Rotor hover performance	9
Rotor forward-flight performance	10–15
Pitch-link oscillatory loads	16
Fixed-system oscillatory vertical force	17
Fixed-system oscillatory moments	18–21

Discussion of Results

The primary purpose of this investigation was to obtain data for evaluating the performance of rotors using slotted airfoils in the blade tip region. The forward-flight performance of all rotor configurations was defined by the C_Q required at a given rotor task specified by the parameters C_L , C_D , μ , and M_T .

Rotor Performance

The hover performance of all rotor configurations tested for a tip Mach number of 0.627 and a value of $z/d = 0.83$ is presented in figure 9. This performance is expressed in terms of C_L versus C_Q in figure 9(a) and in terms of figure of merit (FM) versus C_L in figure 9(b). Two values of C_L are of interest in this figure. A C_L of 0.0081 is representative of a UH-60A helicopter at a gross weight of 18500 lb at a density representative of 4000 ft/95°F, and a C_L of 0.0086 is representative of a scout-type helicopter at a gross weight of 10500 lb at the same altitude-temperature condition. The data indicate that at C_L 's of 0.0081 and 0.0086, the -6° LE slat configuration had the lowest C_Q . For lift coefficients greater than about 0.007, the -6° LE slat configuration also had the lowest C_Q , whereas for lift coefficients less than 0.007, the baseline rotor had the lowest C_Q . Similarly, the highest FM for $C_L > 0.007$ was attained by the -6° LE slat configuration. Below this C_L , the baseline rotor had the highest FM. The hover performance of the 3° TE flap configuration was slightly below that of the baseline

rotor, while that of the -10° LE slat configuration was the lowest of all four configurations. The highest FM, 0.65, was reached at the highest lift coefficient attained, 0.01. This relatively low maximum value of FM may be caused by recirculation effects that occurred because the tunnel floor was in the normal position for forward-flight test conditions. From previous investigations in the Langley TDT (ref. 7), hover data for different rotors at the same $z/d = 0.83$ indicated significantly higher FM values than those shown in figure 9(b). However, in the reference 7 investigation, the tunnel floor was in a lowered position, which opens up a gap between the floor and each tunnel side-wall that would tend to reduce any potential recirculation effects. During this investigation, it was not possible to put the tunnel floor in the lowered position because of operational restrictions in place at the time.

Figures 10 and 12 show the forward-flight performance of the four rotor configurations, in terms of C_Q versus μ , for a range of rotor lift coefficients and three values of f_D at $M_T = 0.627$. The value of f_D used in figure 10 is representative of a UH-60A Blackhawk helicopter, and the values of f_D used in figure 12 are representative of both low-drag and high-drag configurations for a scout-type helicopter. For $C_L = 0.007$ (fig. 10(a)), the baseline rotor configuration had the lowest C_Q for advance ratios up to 0.3, but it had about the same C_Q as the -6° LE slat configuration at $\mu = 0.35$. The 3° TE flap configuration had about the same performance as that of the -6° LE slat configuration for $C_L = 0.007$. For $C_L = 0.0081$ (fig. 10(b)), the baseline rotor again had the lowest C_Q for μ up to

about 0.30, but at $\mu = 0.35$, the -6° LE slat configuration had a significantly lower C_Q than the other configurations. The 3° TE flap configuration had about the same performance as that of the -6° LE slat configuration for μ up to 0.30 at $C_L = 0.0081$. The -6° LE slat configuration had the minimum C_Q for μ greater than about 0.23 for $C_L = 0.009$ (fig. 10(c)); at lower advance ratios, the baseline rotor again had the minimum C_Q . The 3° TE flap configuration had a higher C_Q than both the baseline and the -6° LE slat configuration for μ less than about 0.30 at $C_L = 0.009$. The -10° LE slat configuration had the highest C_Q at all advance ratios for the three lift coefficients shown in figure 10. Figure 11 illustrates the differences in rotor torque coefficient between the configurations with slotted airfoils and the baseline rotor for the conditions representing a utility helicopter. For the -6° LE slat configuration, increased rotor lift coefficient resulted in greater reductions in C_Q from that of the baseline rotor at advance ratios of 0.30 and 0.35.

Figure 12 shows that for $C_L = 0.0086$ and $f_D = 12.0 \text{ ft}^2$, the -6° LE slat configuration had the lowest C_Q for $\mu = 0.30$, and the baseline rotor had the lowest C_Q for advance ratios less than 0.25 (fig. 12(a)). For the same C_L and $f_D = 18.5 \text{ ft}^2$, the -6° LE slat configuration had the lowest C_Q for μ greater than about 0.25, and the baseline rotor had the lowest C_Q for μ less than about 0.25 (fig. 12(c)). The 3° TE flap configuration had a $C_Q \geq$ that of both the baseline, and -6° LE slat configuration for $C_L = 0.0086$ (figs. 12(a) and 12(c)). For $C_L = 0.0095$ and both values of f_D , the -6° LE slat configuration had the lowest C_Q for $\mu = 0.25$ or greater, and a C_Q about the same as that of the baseline rotor, which was below that of the other two configurations, for $\mu \leq 0.20$ (figs. 12(b) and 12(d)). The 3° TE flap configuration had a $C_Q >$ both the baseline and -6° LE slat configuration for $\mu \leq 0.25$ and $C_L = 0.0095$. Except for $\mu = 0.30$ and $C_L = 0.0095$, the -10° LE slat configuration had the highest C_Q at all conditions presented. For the -6° LE slat configuration and $\mu = 0.30$, increased C_L resulted in larger reductions in C_Q relative to the baseline rotor (fig. 13). At an advance ratio of 0.25, increased C_L also changed a disadvantage of the -6° LE slat configuration, relative to the baseline rotor, to an improvement over the baseline rotor (fig. 13).

The lifting capability in forward flight is presented in terms of C_Q versus C_L for a representative f_D

(18.5 ft^2) at four advance ratios in figure 14. At each advance ratio, the -6° LE slat configuration had the lowest C_Q at the higher lift coefficients, and the baseline rotor had the minimum C_Q at the lower lift coefficients. The crossover point of the -6° LE slat configuration curve and the baseline rotor curve occurred at lower values of C_L , with increasing advance ratio. For example, the -6° LE slat configuration had the lowest C_Q for $C_L > 0.0098$ at $\mu = 0.15$ and for $C_L \geq 0.0081$ at $\mu = 0.30$. At each advance ratio, the -10° LE slat configuration had the highest C_Q at the lower lift coefficients. Figure 15 highlights the differences in C_Q between the slotted airfoil configurations and the baseline rotor for increasing C_L at fixed advance ratios. The advantage of the -6° LE slat configuration over the baseline rotor occurred at lower lift coefficients with increasing advance ratio (figs. 15(a) to 15(d)). For a fixed C_L (e.g., 0.0095), the advantage of the -6° LE slat configuration over the baseline rotor increased with increasing advance ratio (figs. 15(b) to 15(d)). Both LE slat configurations generally attained higher lift coefficients than the other two configurations at each advance ratio. This result may be caused by blade stall that caused the abrupt increase in pitch-link loads (fig. 16) for the 3° TE flap configuration and for the baseline rotor to occur at lower lift coefficients than the corresponding C_L 's for the LE slat configurations. At high rotor lift coefficients, the tip region of the rotor blade would be expected to reach high angles of attack. The LE slat airfoils would reach higher angles of attack before stalling than would the single-element baseline airfoil (refs. 2 and 6) or the 3° TE flap airfoil. This stall delay is caused by the favorable effect of the slot flow on the airfoil upper surface boundary layer development.

For the same tasks (figs. 10 to 15), the -6° LE slat configuration had a lower C_Q than the -10° LE slat configuration. It is believed that this lower C_Q is due to the generally lower drag levels of the -6° LE slat airfoil section, as compared to the -10° LE slat airfoil section shown in reference 2.

Pitch-Link and Fixed-System Loads

The loads data are presented in figures 16 to 21 as a function of the rotor lift coefficient for fixed rotor shaft angles of attack at advance ratios from 0.15 to 0.35. The range of rotor shaft angles of attack presented for each μ brackets the value of propulsive

force required to offset the values of f_D used in the aerodynamic performance figures (figs. 10 to 15).

The variation of the half peak-to-peak pitch-link loads with rotor lift coefficient is shown in figure 16. All configurations exhibit the same general trend of increasing pitch-link loads with increasing rotor lift coefficient. At the higher rotor C_L 's at each advance ratio, the two rotors with LE slats had lower pitch-link loads than the other two configurations, and the -6° LE slat configuration had loads that were equal to or lower than those of the -10° LE slat configuration. The rotor lift coefficient, at which the oscillatory loads for the configurations with a LE slat diverged from those of the other two rotor configurations, was lowered with increasing advance ratio. For example, the oscillatory pitch-link loads for the LE slat configurations diverged from those for the baseline rotor, and the 3° TE flap configuration at a C_L of about 0.008 for $\mu = 0.15$ (fig. 16(a)) and at a C_L of about 0.007 for $\mu = 0.25$ (fig. 16(e)). For $\mu \leq 0.30$ and lift coefficients higher than about 0.007, the oscillatory pitch-link loads for the baseline rotor and the 3° TE flap configuration were nearly identical. At $\mu = 0.35$, the oscillatory pitch-link loads for the baseline rotor were the highest of any configuration for C_L 's greater than about 0.006.

The 4P fixed-system normal loads, as a function of the rotor lift coefficient, are shown in figure 17. For $\mu \leq 0.25$, the general trend of the data was the same for all rotor configurations; that is, the loads increased up to a peak value with increasing C_L and then decreased with further increases in C_L . For this same range of μ , the maximum 4P normal loads of both LE slat configurations were higher than those of the other two configurations except at $\alpha_s = -4^\circ$ at $\mu = 0.25$ (fig. 17(f)), where the maximum load of the baseline rotor was about the same as that of the LE slat configurations. The maximum normal loads of the -6° LE slat configuration were about the same as those of the -10° LE slat configuration, except at $\alpha_s = 0^\circ$ at $\mu = 0.25$ (fig. 17(e)), where the maximum load of the -6° LE slat configuration was higher. In general, the loads of the 3° TE flap configuration were the lowest for all conditions at advance ratios up through 0.25. For $\mu = 0.30$ ($\alpha_s = -8^\circ$) and $\mu = 0.35$, the 4P loads of the baseline and 3° TE flap configurations tended to increase with increasing C_L , whereas the loads of the LE slat configurations tended to peak at a C_L value less than the highest C_L shown.

The half peak-to-peak fixed-system pitching moments are shown in figure 18. For advance ratios up through 0.25, the data for all configurations exhibited the same trend; the pitching moments first increased with increasing C_L and then decreased with further increases in C_L . For this same range of μ , the maximum half peak-to-peak pitching moments of both LE slat configurations were generally higher than those of the other two configurations. The maximum half peak-to-peak pitching moments of the baseline and the 3° TE flap configurations were about the same for advance ratios up through 0.25. For $\mu \geq 0.30$, the half peak-to-peak pitching moments of all configurations, except the -6° LE slat configuration, increased with increasing rotor lift coefficient ($C_L \geq 0.004$). At the higher lift coefficients for $\mu \geq 0.30$, the pitching moments of the -6° LE slat configuration typically reached a maximum and then a plateau ($\mu = 0.35$, $\alpha_s = -4^\circ$) or decline ($\mu = 0.30$, $\alpha_s = -8^\circ$ and $\mu = 0.35$, $\alpha_s = -8^\circ$). In general, the -10° LE slat configuration had the highest half peak-to-peak pitching moments for all μ and $0.006 \leq C_L \leq 0.01$. The trends of the 4P fixed-system pitching moments (fig. 19) were very similar to the trends of the half peak-to-peak fixed-system pitching moments just described.

The half peak-to-peak fixed system rolling moments are shown in figure 20. For advance ratios up through 0.25, the half peak-to-peak rolling moments of all rotor configurations increased with increasing rotor lift coefficient. However, for $\mu \geq 0.30$, the half peak-to-peak rolling moments of some configurations increased, leveled out, and then increased again with continuous increases in C_L . For $\mu = 0.15$ ($\alpha_s = -2^\circ$) and $\mu = 0.20$, the half peak-to-peak rolling moments of all configurations fell within a narrow band for the range of lift coefficients shown. At the higher lift coefficients for $\mu \geq 0.25$, the half peak-to-peak rolling moments of the -10° LE slat configuration were the highest; the moments of the other three configurations generally fell within a narrow band. The 4P fixed-system rolling moments are presented in figure 21. With the notable exception at $\mu = 0.30$, the 4P rolling moments of all rotor configurations generally increased with increasing rotor lift coefficient. For $\mu = 0.30$, the 4P rolling moments of some configurations remained nearly constant for a range of rotor C_L . At the higher lift coefficients for $\mu \geq 0.25$, the -10° LE slat configuration had the highest 4P rolling moments.

Conclusions

An experimental investigation was conducted in the Langley Transonic Dynamics Tunnel (TDT) to evaluate the effect of using slotted airfoils in the rotor blade tip region (85 to 100 percent radius) on rotor aerodynamic performance and loads. Four rotor configurations were tested in forward flight at advance ratios from 0.15 to 0.45 and in hover in-ground effect. The hover tip Mach number was 0.627. The baseline rotor configuration had a conventional single-element airfoil in the tip region. A second rotor configuration had a forward-slotted airfoil with a -6° slat, a third configuration had a forward-slotted airfoil with a -10° slat, and a fourth configuration had an aft-slotted airfoil with a 3° flap. In general, the results of this investigation indicated that the -6° slat configuration had some performance and loads benefits over the other three configurations at the higher rotor lift coefficients at each advance ratio. The specific conclusions which support these results follow:

1. In hover for lift coefficients $C_L >$ about 0.007, the -6° slat configuration had the lowest rotor torque coefficient C_Q , whereas for lower lift coefficients, the baseline rotor had the lowest C_Q . Similarly, the highest figure of merit (FM) for $C_L > 0.007$ was attained by the -6° slat configuration, and below this C_L , the baseline rotor had the highest figure of merit.

2. In forward flight at a lift coefficient of 0.0081 and a vehicle equivalent parasite area ($f_D = 29.94 \text{ ft}^2$) representative of a utility helicopter, the -6° slat configuration had the lowest C_Q for advance ratios $\mu >$ about 0.30, and the baseline rotor had the lowest C_Q for advance ratios < 0.30 . For a lift coefficient of 0.0095 and a vehicle equivalent parasite area ($f_D = 18.5 \text{ ft}^2$) representative of a scout helicopter, the -6° slat configuration had the lowest C_Q for $\mu = 0.25$ or greater. For advance ratios of 0.20 and less, the baseline rotor and the -6° slat configuration had about the same C_Q , which was lower than that of the other two configurations.

3. In forward flight for $f_D = 18.5 \text{ ft}^2$, the -6° slat configuration had the lowest C_Q at the higher range of lift coefficients attained at each advance ratio. The baseline rotor had the lowest C_Q for the lower range of lift coefficients attained at each advance ratio. The crossover point of the -6° slat configuration curve and

the baseline rotor curve occurred at lower values of C_L with increasing advance ratio.

4. At the higher rotor C_L 's at each advance ratio, the two configurations with a slat had lower pitch-link loads (half peak to peak) than the other two configurations, and the -6° slat configuration had loads that were equal to or lower than those of the -10° slat configuration. The rotor lift coefficient, at which the oscillatory loads for the configurations with a slat diverged from those of the other two rotor configurations, was lowered with increasing advance ratio.

5. The maximum 4-per-revolution (4P) fixed-system vertical loads of both forward-slotted configurations were generally higher than those of the other two configurations for advance ratios up through 0.25.

6. For advance ratios up through 0.25, the maximum fixed-system pitching moments (half peak to peak) of both forward-slotted configurations were generally higher than those of the other two configurations. At the higher lift coefficients for $\mu \geq 0.25$, the fixed-system rolling moments (half peak to peak) of the -10° slat configuration were the highest, while those of the other three configurations generally lay within a narrow band.

References

1. Aeromechanics Steering Committee: *DoD Rotary Wing Vehicles Subarea Aeromechanics Technology Effort—STI Program Plan*. ATCOM, ARL, Dec. 1996.
2. Noonan, Kevin W.; Allison, Dennis O.; and Stanaway, Sharon: Investigation of a Slotted Rotorcraft Airfoil at Mach Numbers From 0.20 to 0.88 at Full-Scale Reynolds Numbers. *Aeromechanics Specialists Conference—A Conference on Aerodynamics, Acoustics and Dynamics*, AHS, Jan. 1994, pp. 4.5-1-4.5-20.
3. Singleton, Jeffrey D.; and Yeager, William T., Jr.: Important Scaling Parameters for Testing Model-Scale Helicopter Rotors. AIAA-98-2881, June 1998.
4. Lee, Charles: *Weight Considerations in Dynamically Similar Model Rotor Design*. SAWE Paper No. 659, May 1998.
5. Noonan, Kevin W.: *Aerodynamic Characteristics of Two Rotorcraft Airfoils Designed for Application to the Inboard Region of a Main Rotor Blade*. NASA TP-3009, 1990.

6. Noonan, Kevin W.: *Aerodynamic Characteristics of a Rotorcraft Airfoil Designed for the Tip Region of a Main Rotor Blade*. NASA TM-4264, 1991.
7. Yeager, William T., Jr.; Mantay, Wayne R.; Wilbur, Matthew L.; Cramer, Robert G., Jr.; and Singleton, Jeffrey D.: *Wind-Tunnel Evaluation of an Advanced Main-Rotor Blade Design for a Utility-Class Helicopter*. NASA TM-89129, 1987.
8. Yeager, William T., Jr.; Noonan, Kevin W.; Singleton, Jeffrey D.; Wilbur, Matthew L.; and Mirick, Paul H.: *Performance and Vibratory Loads Data From a Wind-Tunnel Test of a Model Helicopter Main-Rotor Blade With a Paddle-Type Tip*. NASA TM-4754, 1997.
9. Mantay, Wayne R.; Yeager, William T., Jr.; Hamouda, M-Nabil; Cramer, Maj. Robert G.; and Langston, Chester W.: *Aeroelastic Model Helicopter Rotor Testing in the Langley TDT*. NASA TM-86440, 1985.

Table I. Design Coordinates for RC(4)-10 Airfoil

Upper surface		Lower surface	
Station	Ordinate	Station	Ordinate
0.00000	-0.00573	0.00000	-0.00573
0.00286	0.00431	0.00469	-0.01591
0.00907	0.01318	0.01435	-0.02182
0.02354	0.02598	0.01646	-0.02270
0.04704	0.03888	0.02518	-0.02566
0.07369	0.04795	0.03560	-0.02820
0.10019	0.05367	0.06187	-0.03158
0.12614	0.05732	0.08498	-0.03234
0.15184	0.05979	0.10824	-0.03201
0.17723	0.06158	0.13205	-0.03127
0.20256	0.06300	0.15612	-0.03061
0.22776	0.06416	0.18050	-0.03028
0.25296	0.06514	0.20493	-0.03026
0.30315	0.06661	0.22949	-0.03043
0.35314	0.06738	0.25406	-0.03070
0.37814	0.06742	0.30340	-0.03139
0.40330	0.06716	0.35293	-0.03209
0.42839	0.06654	0.37770	-0.03237
0.45368	0.06550	0.40230	-0.03255
0.47889	0.06401	0.42697	-0.03260
0.50376	0.06213	0.45145	-0.03247
0.52871	0.05988	0.47600	-0.03216
0.55362	0.05732	0.50089	-0.03166
0.57851	0.05451	0.52571	-0.03097
0.60342	0.05145	0.55057	-0.03009
0.62834	0.04814	0.57544	-0.02906
0.65324	0.04462	0.60030	-0.02793
0.67816	0.04091	0.62514	-0.02675
0.70298	0.03709	0.65000	-0.02554
0.72769	0.03325	0.67485	-0.02433
0.75250	0.02945	0.69979	-0.02311
0.77720	0.02581	0.72484	-0.02187
0.80171	0.02238	0.74980	-0.02061
0.82631	0.01914	0.77487	-0.01927
0.85097	0.01609	0.80011	-0.01782
0.87570	0.01321	0.82528	-0.01622
0.90051	0.01051	0.85039	-0.01442
0.92535	0.00801	0.87542	-0.01244
0.95019	0.00572	0.90037	-0.01031
0.97503	0.00365	0.92530	-0.00808
1.00000	0.00179	0.95023	-0.00573
		0.97515	-0.00316
		1.00000	0.00020

Table II. Design Coordinates for RC(6)-08 Airfoil

Upper surface		Lower surface	
Station	Ordinate	Station	Ordinate
0.00000	-0.00398	0.00000	-0.00398
0.00101	0.00050	0.00399	-0.01100
0.00298	0.00402	0.00702	-0.01277
0.00985	0.01112	0.01515	-0.01562
0.02214	0.01866	0.02786	-0.01825
0.04764	0.02759	0.05236	-0.02137
0.07476	0.03290	0.07524	-0.02340
0.09881	0.03587	0.10119	-0.02519
0.12450	0.03813	0.12550	-0.02652
0.14934	0.03984	0.15066	-0.02764
0.17465	0.04132	0.17535	-0.02858
0.19999	0.04257	0.20001	-0.02943
0.22480	0.04356	0.22519	-0.03022
0.24990	0.04439	0.25009	-0.03094
0.30006	0.04568	0.29994	-0.03213
0.34986	0.04655	0.35014	-0.03287
0.37491	0.04677	0.37509	-0.03302
0.40002	0.04680	0.39997	-0.03300
0.42499	0.04660	0.42500	-0.03276
0.45000	0.04613	0.45000	-0.03229
0.47501	0.04541	0.47499	-0.03157
0.49996	0.04444	0.50003	-0.03062
0.52513	0.04321	0.52459	-0.02958
0.55034	0.04174	0.54965	-0.02848
0.57516	0.04006	0.57483	-0.02733
0.60021	0.03816	0.59978	-0.02615
0.62547	0.03604	0.62452	-0.02493
0.65038	0.03379	0.64961	-0.02365
0.67564	0.03135	0.67435	-0.02233
0.70032	0.02882	0.69967	-0.02095
0.72563	0.02612	0.72435	-0.01955
0.75085	0.02338	0.74913	-0.01812
0.77543	0.02074	0.77456	-0.01658
0.80043	0.01811	0.79956	-0.01505
0.82535	0.01555	0.82464	-0.01345
0.85028	0.01302	0.84971	-0.01183
0.87517	0.01055	0.87482	-0.01017
0.90009	0.00822	0.89990	-0.00848
0.92502	0.00612	0.92496	-0.00672
0.94996	0.00433	0.95002	-0.00481
0.97495	0.00277	0.97503	-0.00270
1.00000	0.00104	1.00000	-0.00024

Table III. Design Coordinates for -6° LE Slat Airfoil

Slat				Main element			
Upper surface		Lower surface		Upper surface		Lower surface	
Station	Ordinate	Station	Ordinate	Station	Ordinate	Station	Ordinate
-0.05958	-0.00605	-0.05958	-0.00605	0.00000	-0.01000	0.00000	-0.01000
-0.05963	-0.00424	-0.05853	-0.00903	0.00019	-0.00775	0.00460	-0.01908
-0.05924	-0.00212	-0.05625	-0.01163	0.00294	-0.00220	0.00932	-0.02147
-0.05749	0.00219	-0.05402	-0.01307	0.00746	0.00344	0.01877	-0.02349
-0.05597	0.00463	-0.05151	-0.01414	0.01685	0.01183	0.02755	-0.02428
-0.05367	0.00757	-0.04876	-0.01505	0.02625	0.01808	0.03762	-0.02498
-0.05170	0.00967	-0.04354	-0.01600	0.03561	0.02330	0.04670	-0.02553
-0.04705	0.01380	-0.03856	-0.01539	0.04506	0.02739	0.07053	-0.02675
-0.04237	0.01721	-0.03425	-0.01308	0.06868	0.03374	0.09406	-0.02776
-0.03756	0.02020	-0.02979	-0.00925	0.09210	0.03777	0.14101	-0.02941
-0.03279	0.02281	-0.02494	-0.00417	0.13910	0.04246	0.18893	-0.03084
-0.02812	0.02510	-0.02037	0.00070	0.18615	0.04431	0.23579	-0.03197
-0.02333	0.02724	-0.01588	0.00549	0.23389	0.04560	0.28202	-0.03270
-0.01857	0.02918	-0.01147	0.01027	0.28015	0.04643	0.32905	-0.03292
-0.01395	0.03088	-0.00695	0.01500	0.32717	0.04684	0.37607	-0.03249
-0.00914	0.03255	-0.00259	0.01943	0.37413	0.04650	0.41507	-0.03145
-0.00432	0.03411	0.00203	0.02368	0.42111	0.04523	0.47007	-0.02926
0.00054	0.03558	0.00660	0.02738	0.46814	0.04307	0.51705	-0.02715
0.00524	0.03692	0.01173	0.03094	0.51513	0.04008	0.56435	-0.02489
0.01014	0.03824	0.01592	0.03361	0.56221	0.03633	0.61108	-0.02248
0.01500	0.03949	0.02094	0.03651	0.60927	0.03201	0.65812	-0.01987
0.01998	0.04072	0.03461	0.04292	0.65617	0.02712	0.70512	-0.01711
0.02472	0.04182			0.70317	0.02205	0.75206	-0.01423
0.03451	0.04392			0.75022	0.01710	0.79899	-0.01120
				0.79717	0.01232	0.84602	-0.00801
				0.84421	0.00790	0.89298	-0.00456
				0.89122	0.00427	0.91657	-0.00259
				0.91475	0.00282	0.93999	-0.00023
				0.93999	0.00103		

Table IV. Design Coordinates for -10° LE Slat Airfoil

Slat				Main element			
Upper surface		Lower surface		Upper surface		Lower surface	
Station	Ordinate	Station	Ordinate	Station	Ordinate	Station	Ordinate
-0.07931	-0.01781	-0.07931	-0.01781	0.00000	-0.01000	0.00000	-0.01000
-0.07949	-0.01601	-0.07805	-0.02070	0.00019	-0.00775	0.00460	-0.01908
-0.07925	-0.01386	-0.07559	-0.02314	0.00294	-0.00220	0.00932	-0.02147
-0.07780	-0.00945	-0.07327	-0.02443	0.00746	0.00344	0.01877	-0.02349
-0.07645	-0.00691	-0.07069	-0.02531	0.01685	0.01183	0.02755	-0.02428
-0.07436	-0.00381	-0.06788	-0.02603	0.02625	0.01808	0.03762	-0.02498
-0.07255	-0.00157	-0.06261	-0.02661	0.03561	0.02330	0.04670	-0.02553
-0.06820	0.00287	-0.05769	-0.02566	0.04506	0.02739	0.07053	-0.02675
-0.06376	0.00660	-0.05355	-0.02306	0.06868	0.03374	0.09406	-0.02776
-0.05917	0.00991	-0.04937	-0.01893	0.09210	0.03777	0.14101	-0.02941
-0.05460	0.01284	-0.04489	-0.01352	0.13910	0.04246	0.18893	-0.03084
-0.05010	0.01546	-0.04067	-0.00834	0.18615	0.04431	0.23579	-0.03197
-0.04547	0.01793	-0.03652	-0.00324	0.23389	0.04560	0.28202	-0.03270
-0.04086	0.02019	-0.03245	0.00183	0.28015	0.04643	0.32905	-0.03292
-0.03637	0.02222	-0.02828	0.00686	0.32717	0.04684	0.37607	-0.03249
-0.03168	0.02421	-0.02423	0.01158	0.37413	0.04650	0.41507	-0.03145
-0.02698	0.02611	-0.01993	0.01614	0.42111	0.04523	0.47007	-0.02926
-0.02224	0.02791	-0.01562	0.02015	0.46814	0.04307	0.51705	-0.02715
-0.01764	0.02958	-0.01075	0.02406	0.51513	0.04008	0.56435	-0.02489
-0.01285	0.03124	-0.00676	0.02702	0.56221	0.03633	0.61108	-0.02248
-0.00809	0.03282	-0.00196	0.03026	0.60927	0.03201	0.65812	-0.01987
-0.00320	0.03440	0.01124	0.03761	0.65617	0.02712	0.70512	-0.01711
0.00145	0.03582			0.70317	0.02205	0.75206	-0.01423
0.01106	0.03860			0.75022	0.01710	0.79899	-0.01120
				0.79717	0.01232	0.84602	-0.00801
				0.84421	0.00790	0.89298	-0.00456
				0.89122	0.00427	0.91657	-0.00259
				0.91475	0.00282	0.93999	-0.00023
				0.93999	0.00103		

Table V. Design Coordinates for 3° TE Flap Airfoil

Main element				Flap			
Upper surface		Lower surface		Upper surface		Lower surface	
Station	Ordinate	Station	Ordinate	Station	Ordinate	Station	Ordinate
0.00000	0.00000	0.00000	0.00000	0.68000	-0.00600	0.68000	-0.00600
0.00406	0.00947	0.00397	-0.00658	0.68125	-0.00278	0.68267	-0.01324
0.00739	0.01304	0.00765	-0.00873	0.68332	0.00068	0.68619	-0.01555
0.01482	0.01868	0.01456	-0.01120	0.68662	0.00339	0.68932	-0.01702
0.02242	0.02284	0.02264	-0.01308	0.69334	0.00700	0.69243	-0.01808
0.03751	0.02874	0.03765	-0.01547	0.69996	0.00946	0.69877	-0.01940
0.04977	0.03215	0.04982	-0.01691	0.70682	0.01126	0.70486	-0.02010
0.05613	0.03356	0.05625	-0.01756	0.71300	0.01222	0.71140	-0.02059
0.07498	0.03692	0.07515	-0.01925	0.71939	0.01268	0.74347	-0.02162
0.11253	0.04112	0.11257	-0.02168	0.72600	0.01262	0.77530	-0.02266
0.15010	0.04380	0.15018	-0.02351	0.73243	0.01224	0.80729	-0.02376
0.18769	0.04587	0.18766	-0.02493	0.73877	0.01167	0.83944	-0.02482
0.22519	0.04744	0.22521	-0.02616	0.74510	0.01090	0.87127	-0.02578
0.26276	0.04861	0.26272	-0.02724	0.75154	0.01000	0.90327	-0.02659
0.30030	0.04948	0.30023	-0.02812	0.76104	0.00858	0.93544	-0.02727
0.33786	0.05014	0.33789	-0.02875	0.77677	0.00619	0.96743	-0.02753
0.37540	0.05048	0.37541	-0.02905	0.80872	0.00127	0.98331	-0.02716
0.41295	0.05039	0.41295	-0.02897	0.84038	-0.00371	0.99940	-0.02595
0.45048	0.04977	0.45049	-0.02840	0.87212	-0.00874		
0.48803	0.04854	0.48804	-0.02728	0.90428	-0.01351		
0.52560	0.04674	0.52558	-0.02573	0.93574	-0.01764		
0.56315	0.04443	0.56312	-0.02394	0.96777	-0.02108		
0.60072	0.04166	0.60057	-0.01886	0.98355	-0.02259		
0.63827	0.03846	0.61566	-0.01346	0.99948	-0.02433		
0.67586	0.03482	0.63066	-0.00676				
0.71347	0.03095	0.64570	0.00085				
0.75096	0.02684	0.66076	0.00903				
		0.67568	0.01708				
		0.68319	0.02067				
		0.69073	0.02356				
		0.69827	0.02564				
		0.70569	0.02697				
		0.71311	0.02765				
		0.75096	0.02600				

Table VI. HIMARCS I Rotor Blade Measured Natural Frequencies, Hz

Configuration	Blade number	1st flapwise bending	2nd flapwise bending	3rd flapwise bending	1st torsion	1st chordwise bending
Baseline	1	3.75	22.75	61.00	87.50	17.50
Baseline	2	3.85	23.75	62.50	87.25	17.35
Baseline	3	3.75	23.50	62.25	88.00	17.75
Baseline	4	3.75	23.50	62.50	87.25	17.50
Baseline	5	3.75	23.50	62.75	86.50	17.25
0° TE flap	4	3.85	23.38	62.50	86.75	17.50
−10° LE slat	4	4.00	23.88	62.75	88.50	18.10

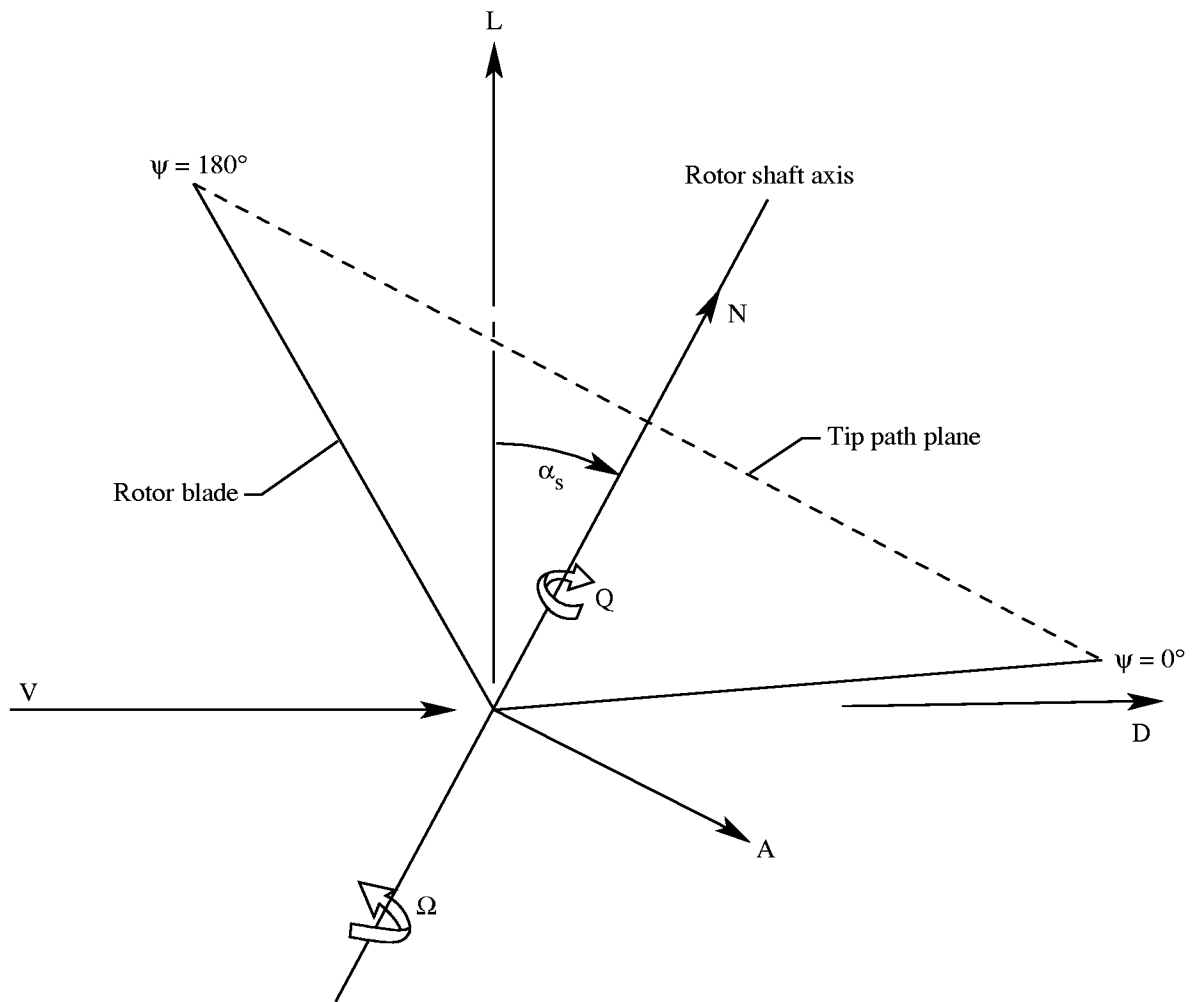
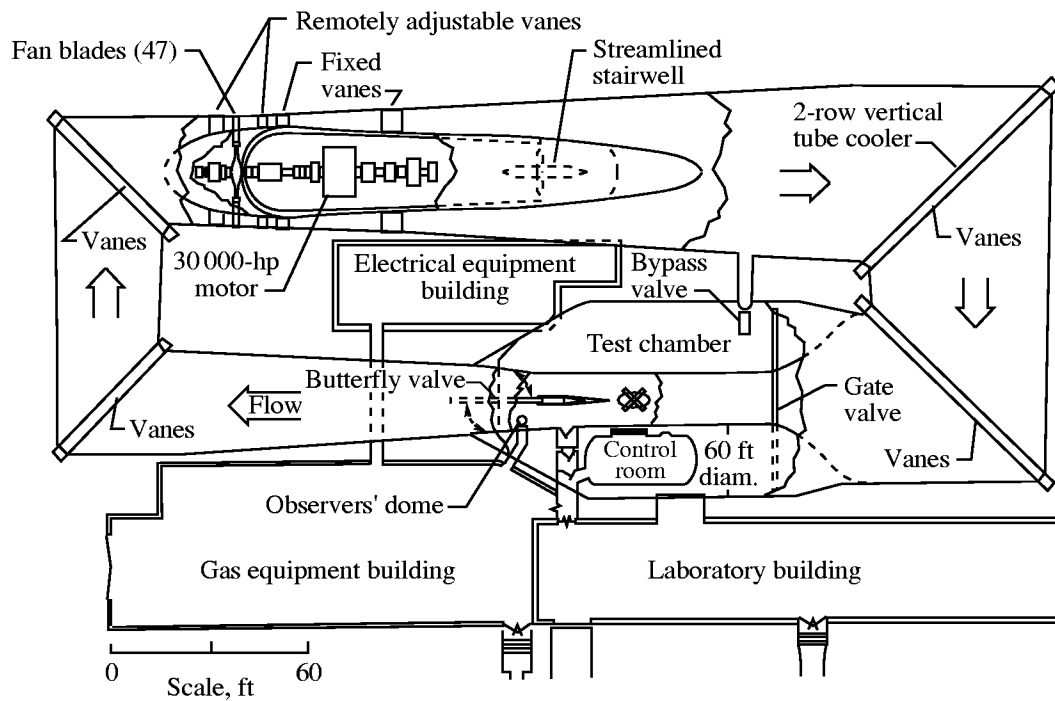
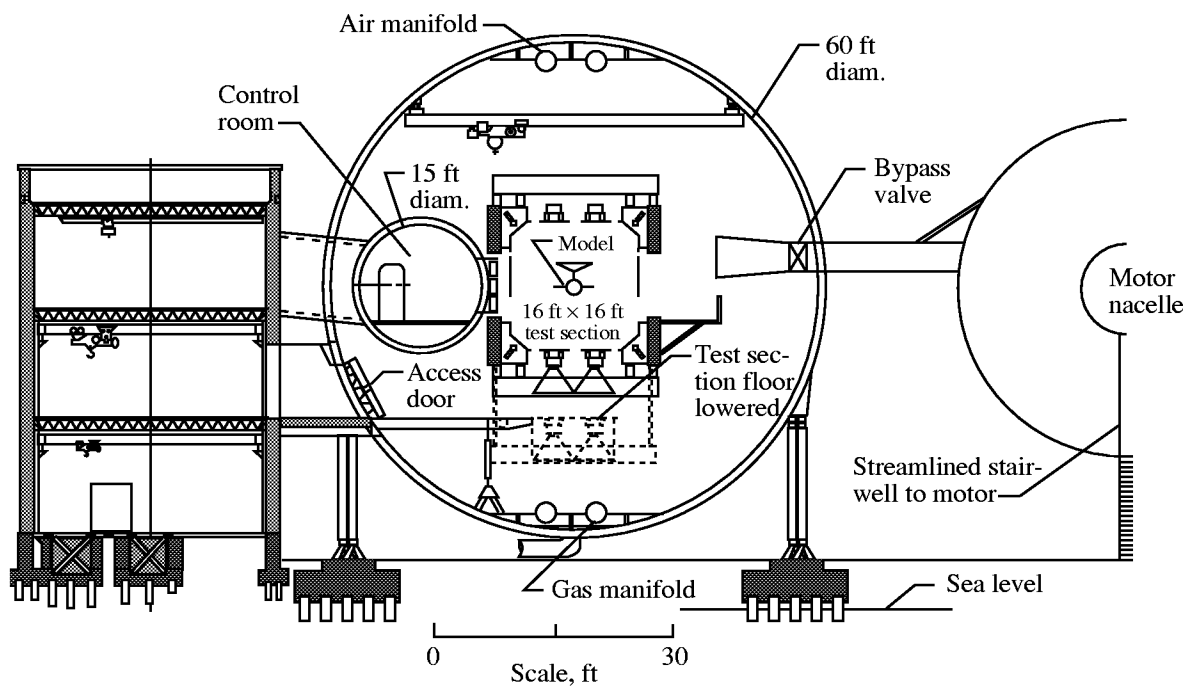


Figure 1. Notation showing positive directions of forces, angles, and velocities.

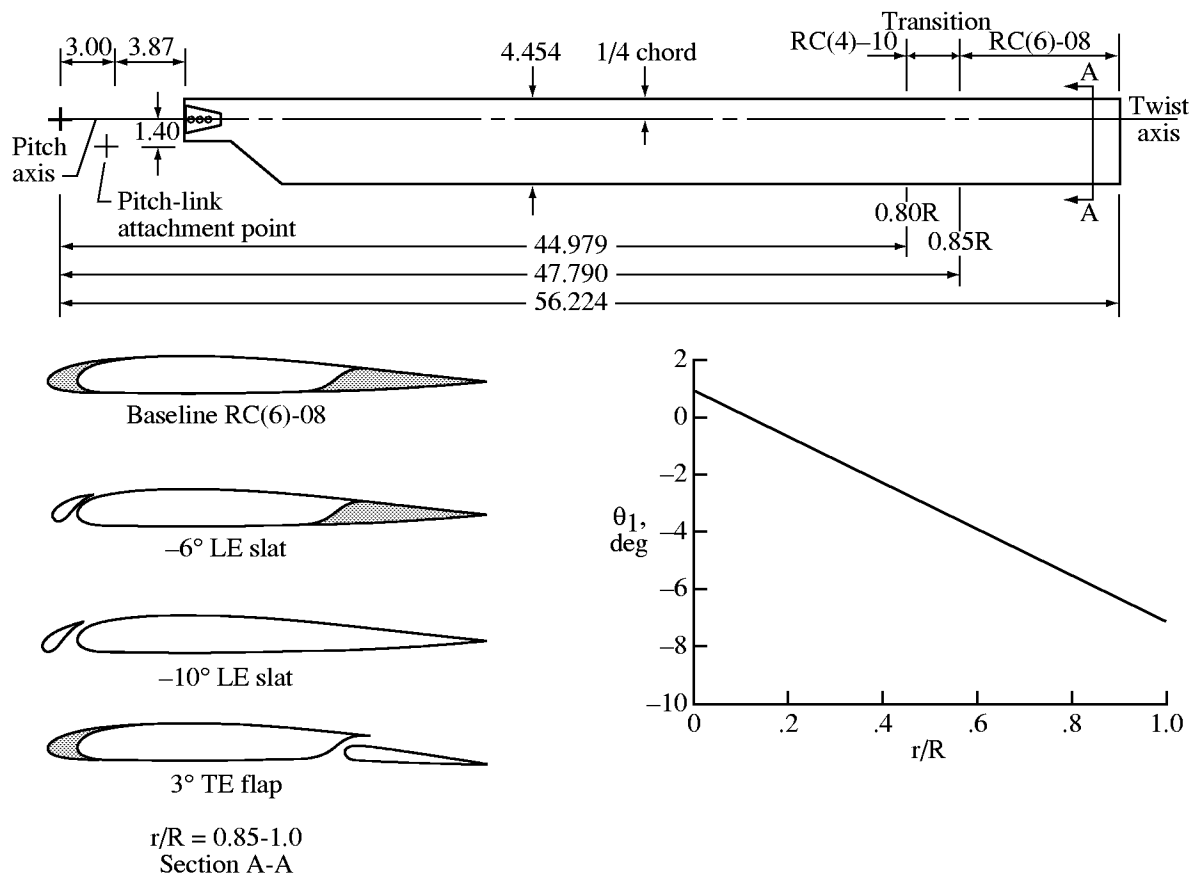


(a) Top view.



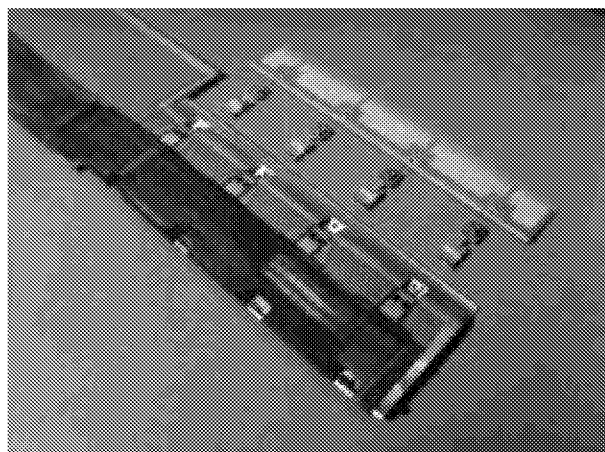
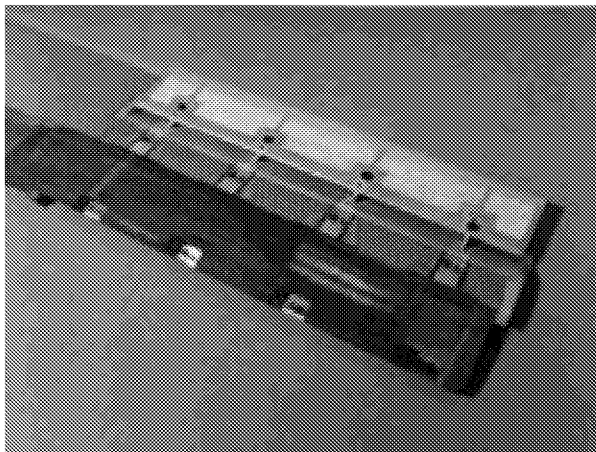
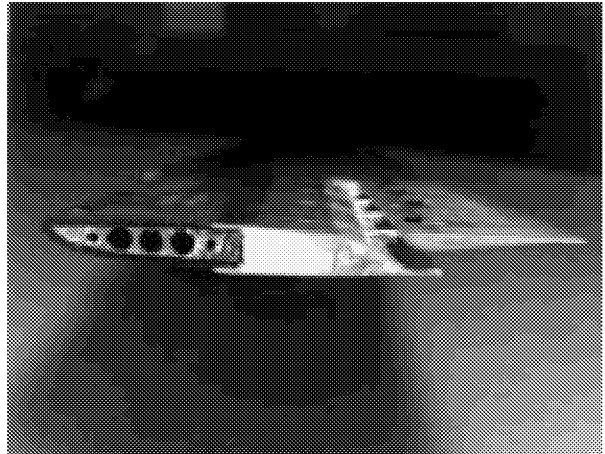
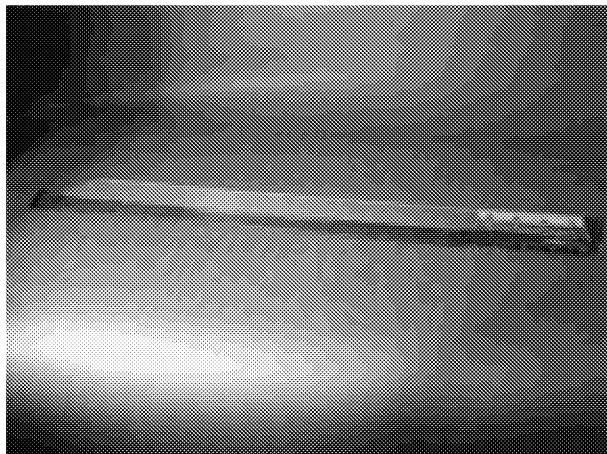
(b) Cross-sectional view.

Figure 2. The Langley Transonic Dynamics Tunnel (TDT).



(a) Geometry and twist distribution.

Figure 3. HIMARCS I rotor blade. Linear dimensions are in inches.



(b) HIMARCS I rotor blade with 0° TE flap and no LE slat or LE fairing piece.

Figure 3. Concluded.

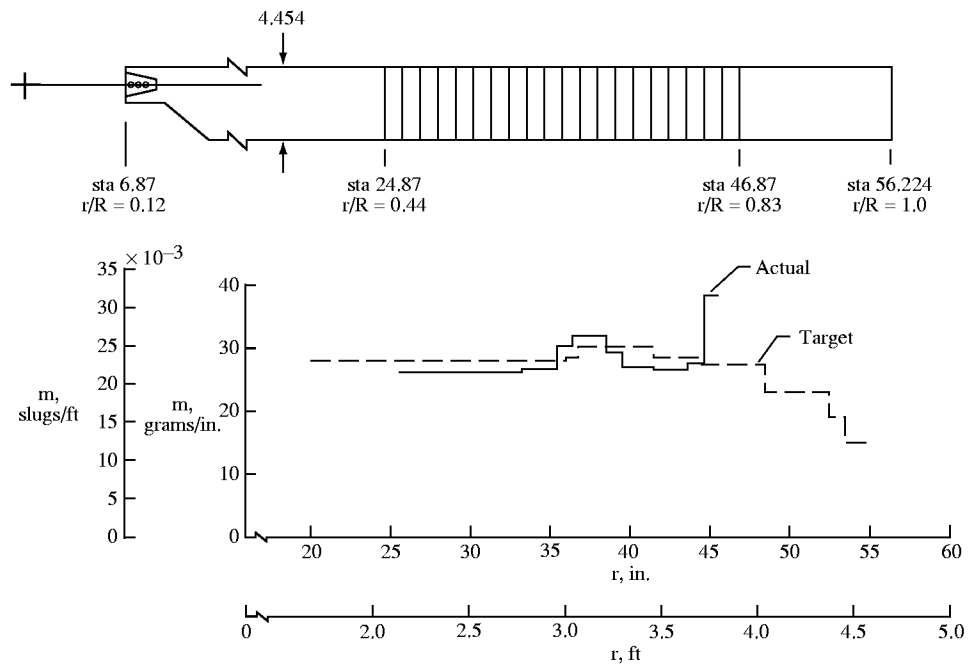


Figure 4. HIMARCS I rotor blade mass distribution (typical). Blade stations are in inches.

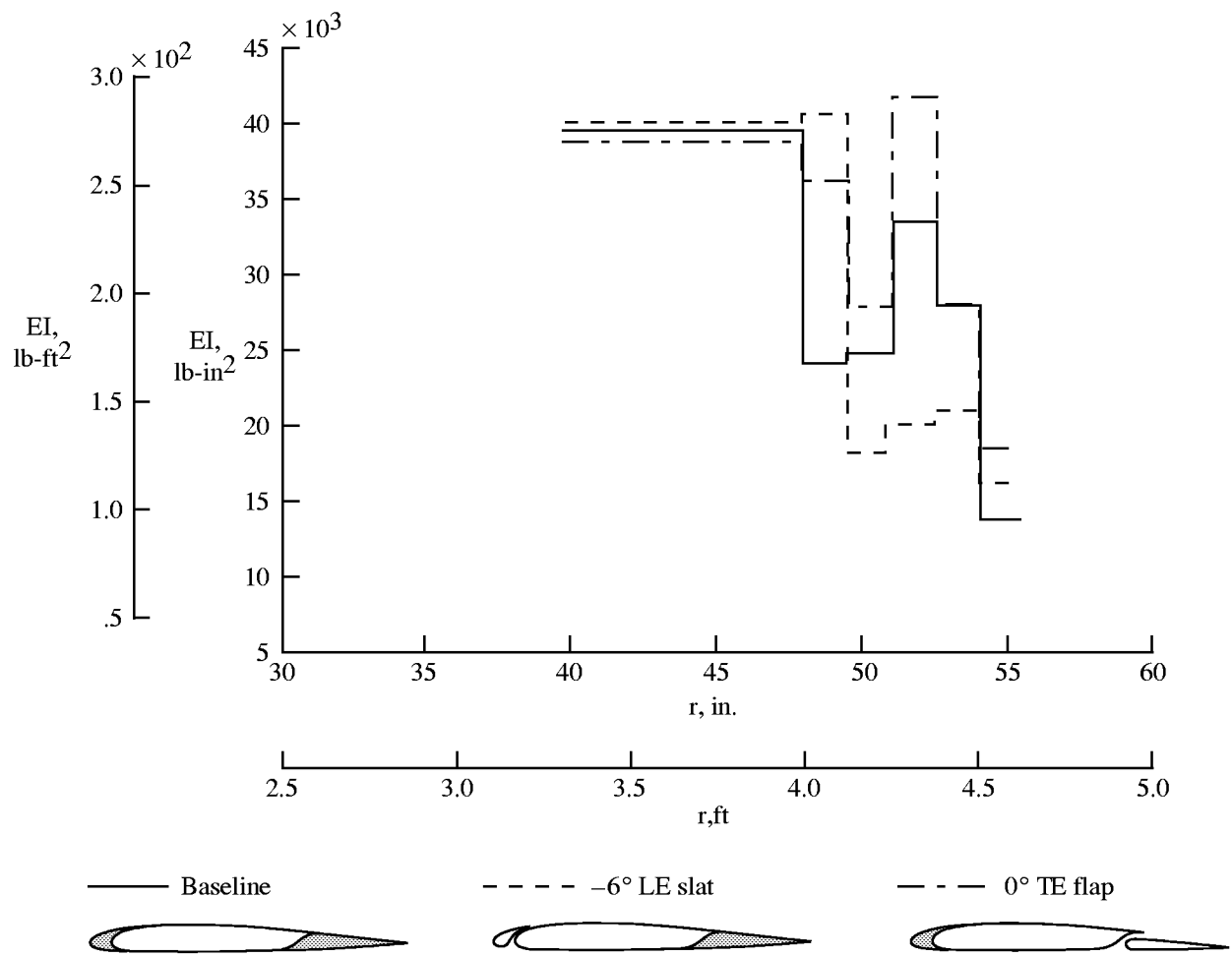


Figure 5. HIMARCS I rotor blade flapwise stiffness distributions (typical).

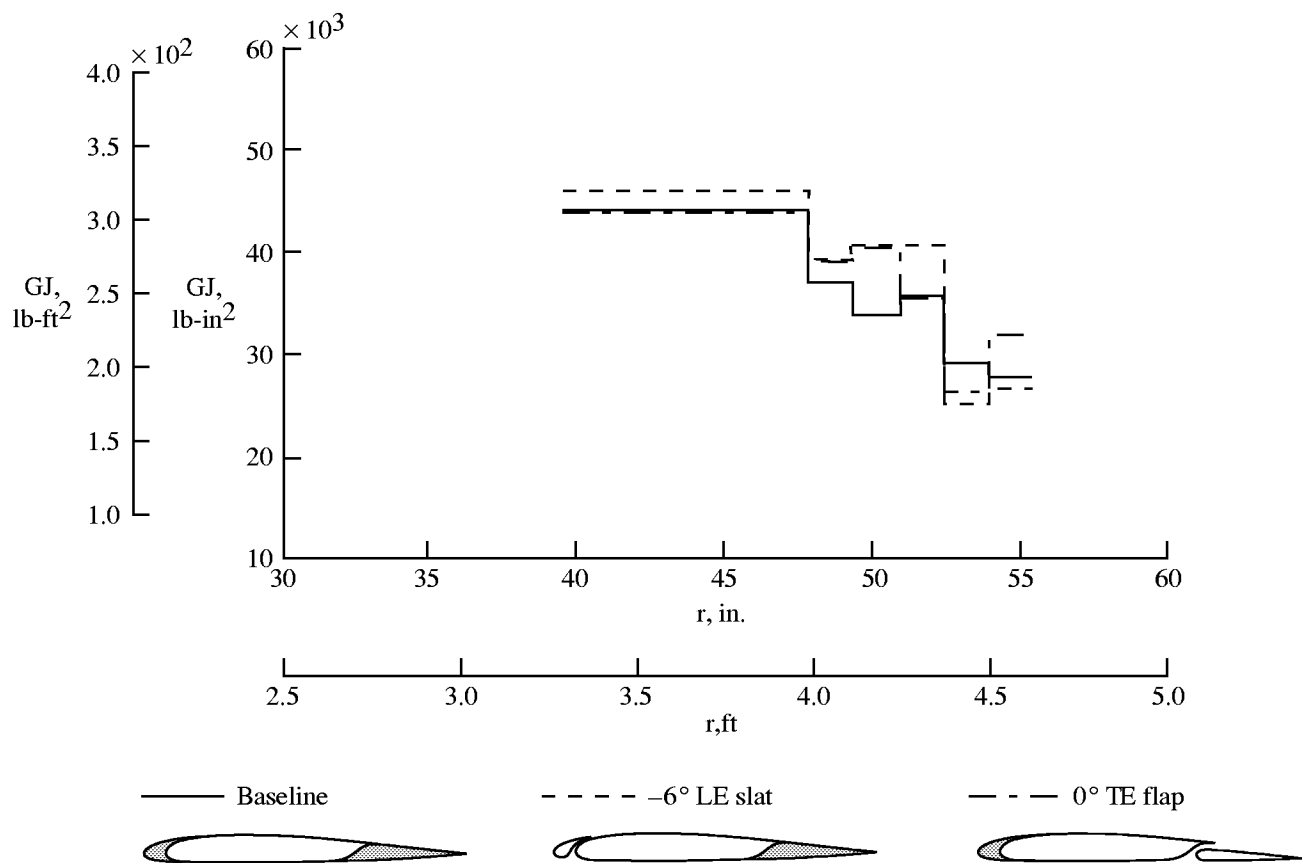


Figure 6. HIMARCS I rotor blade torsional stiffness distributions (typical).

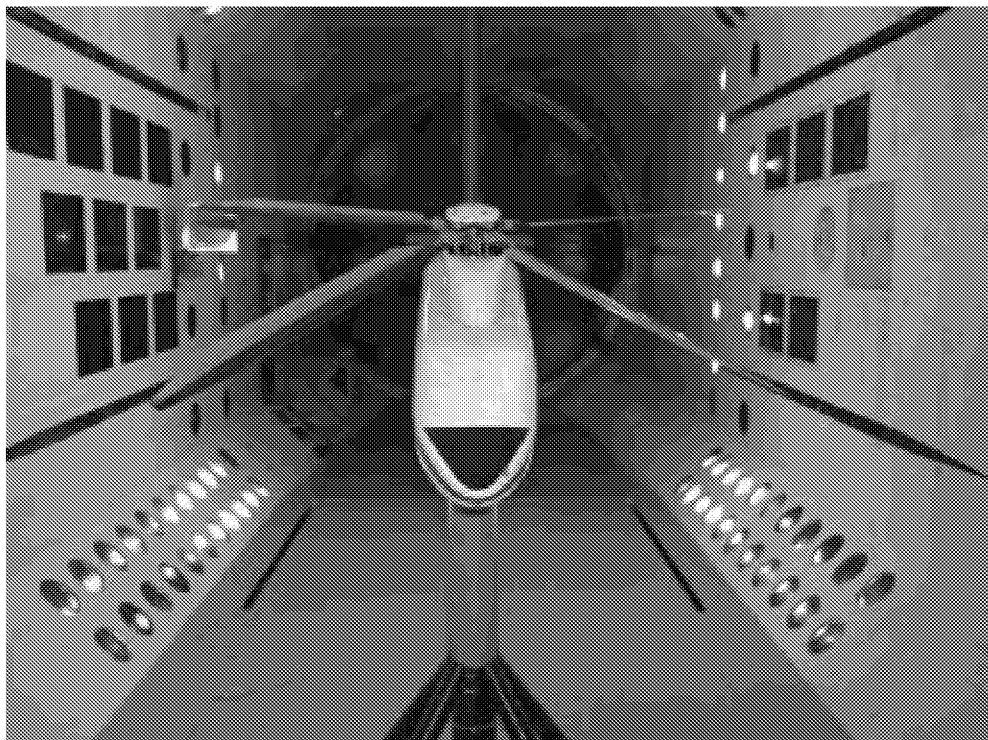


Figure 7. Aeroelastic rotor experimental system (ARES) test bed in Langley Transonic Dynamics Tunnel.

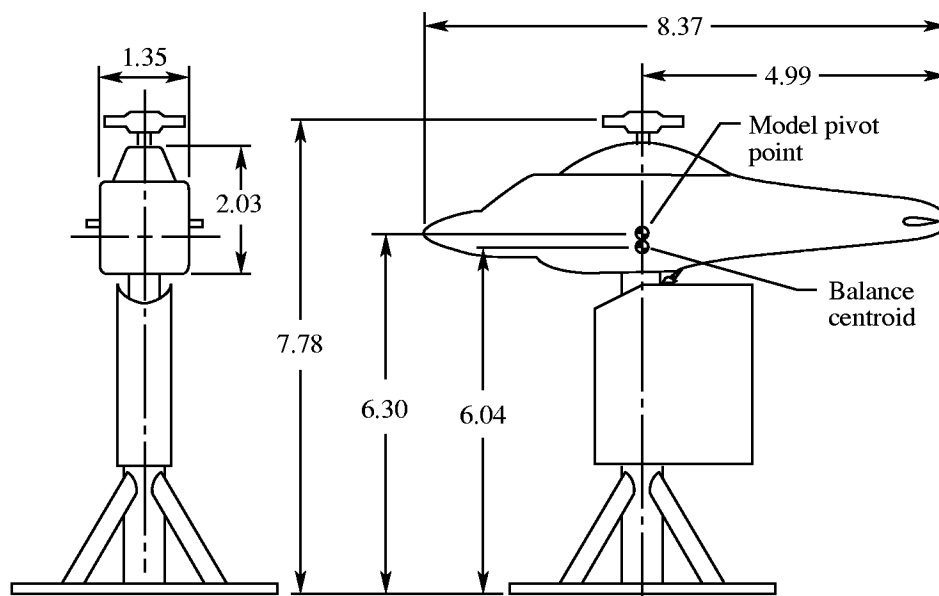
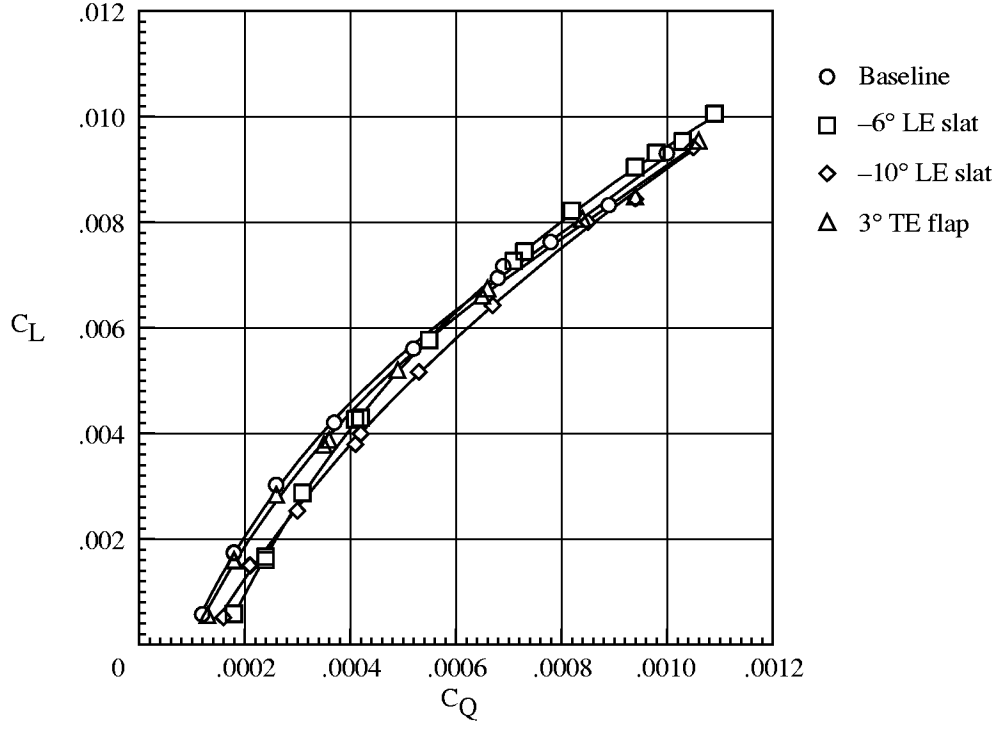
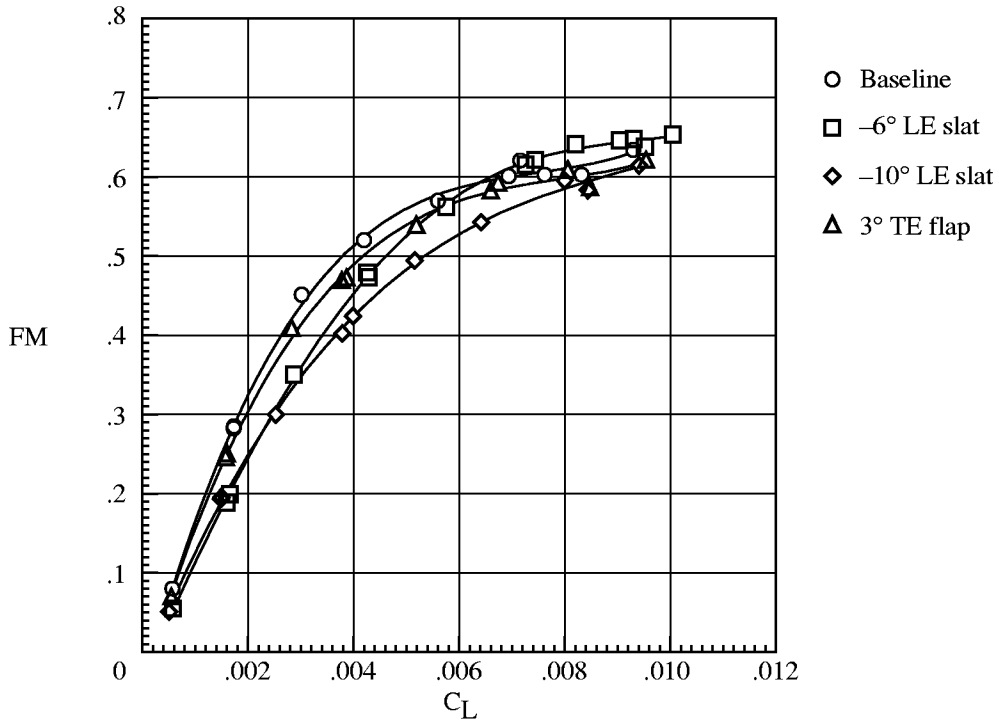


Figure 8. Schematic of aeroelastic rotor experimental system (ARES) test bed. All dimensions are in feet.

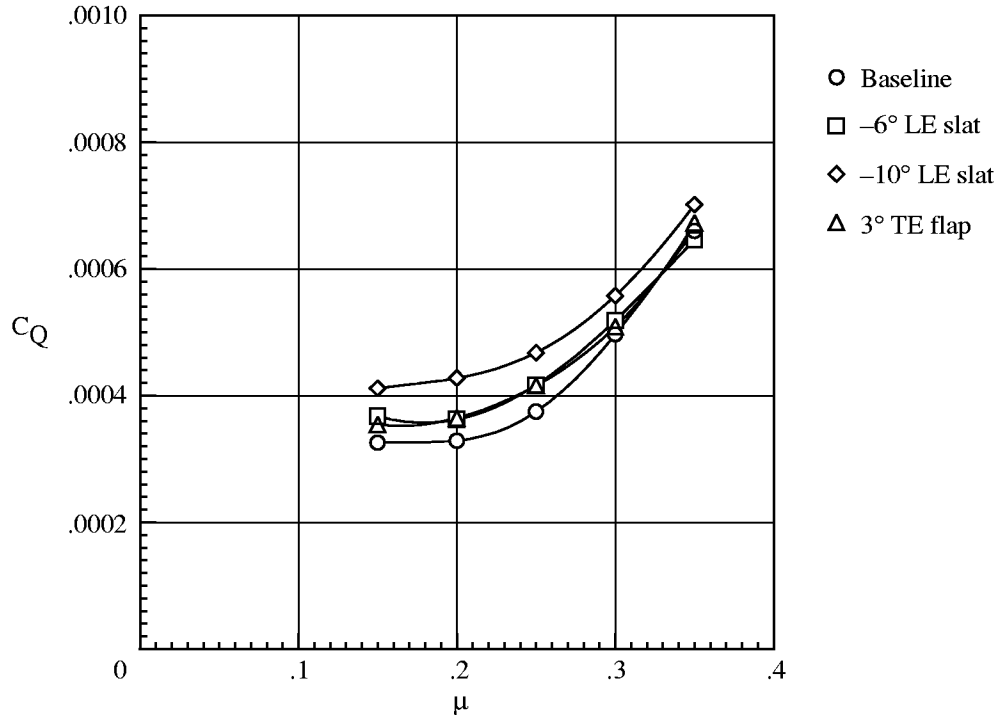


(a) C_L versus C_Q .

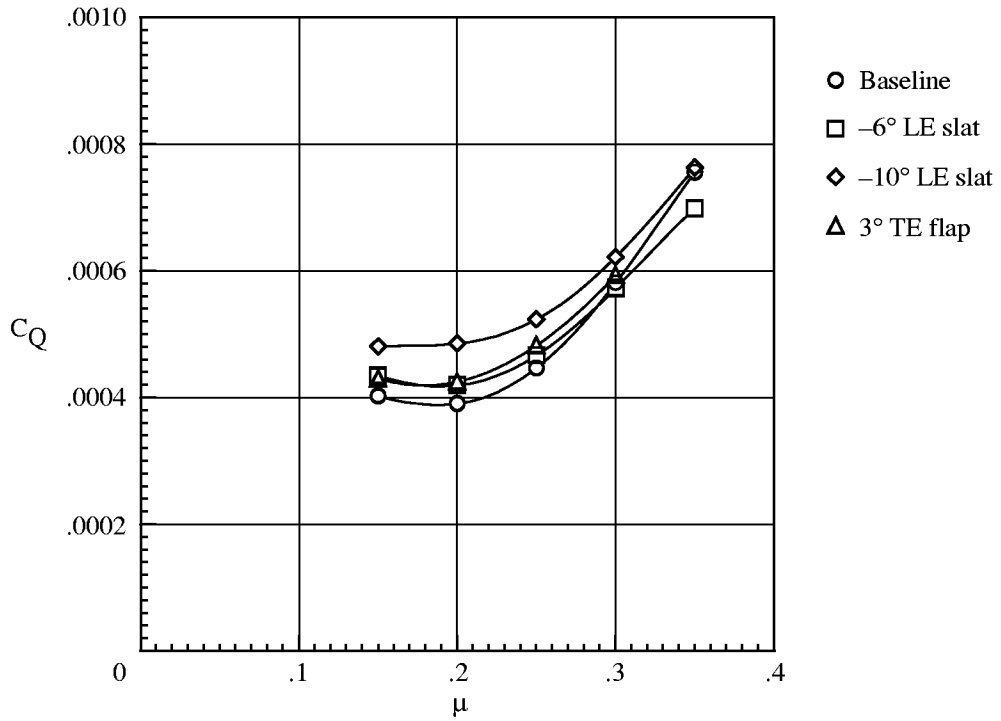


(b) Figure of merit.

Figure 9. Rotor hover performance at $M_T = 0.627$ and $z/d = 0.83$.

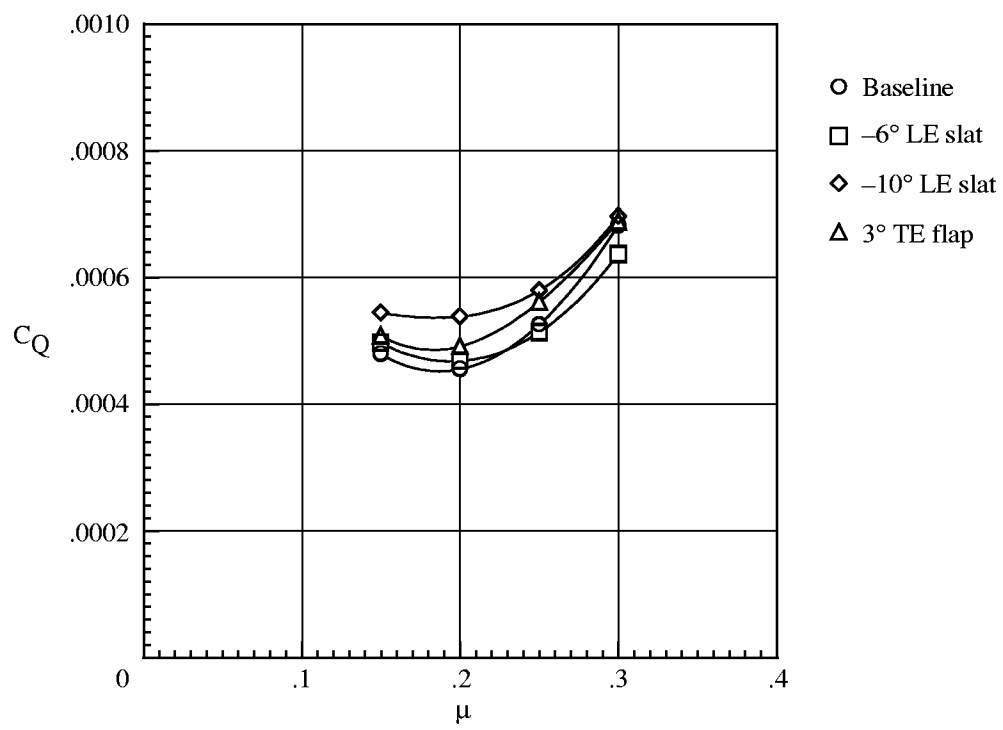


(a) $C_L = 0.007$.



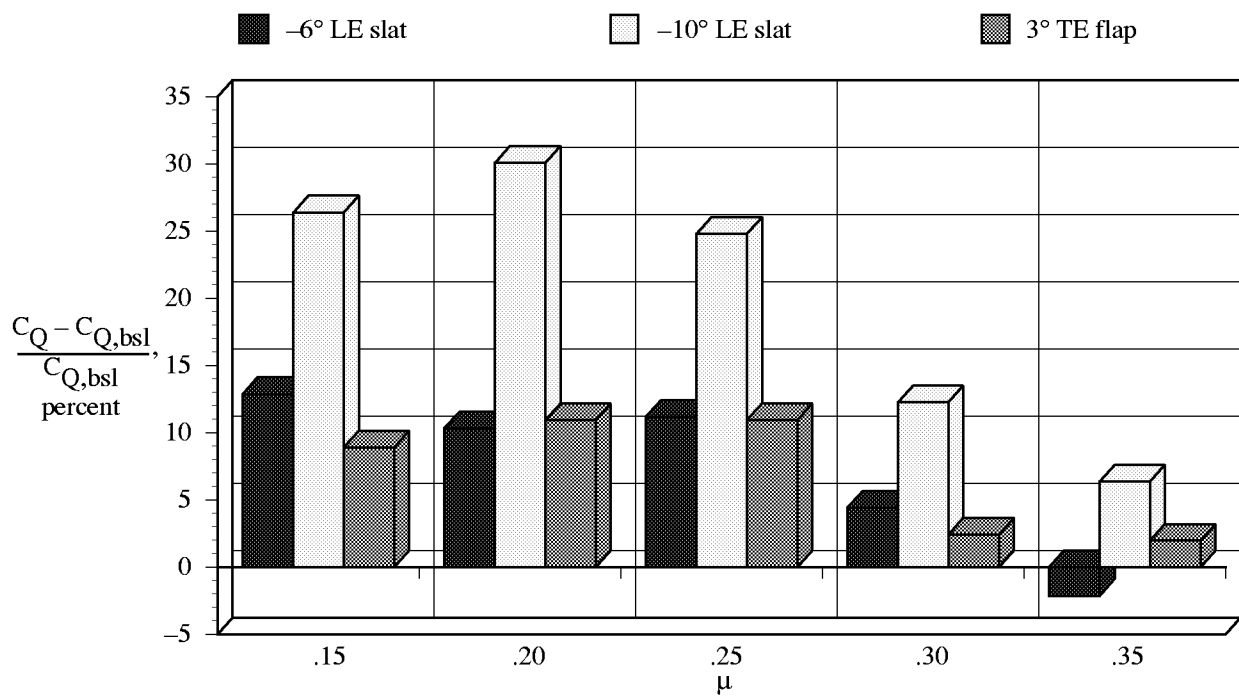
(b) $C_L = 0.0081$.

Figure 10. Variation of rotor torque coefficient with advance ratio for $f_D = 29.94 \text{ ft}^2$ and $M_T = 0.627$.

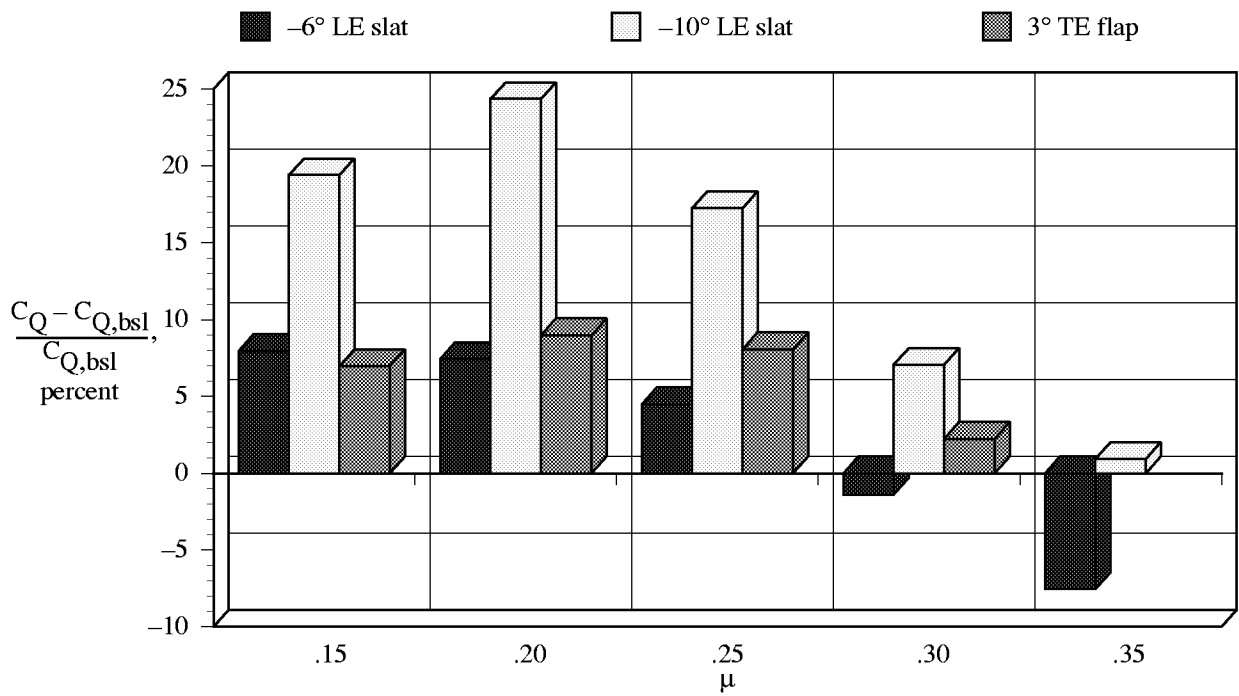


(c) $C_L = 0.009$.

Figure 10. Concluded.

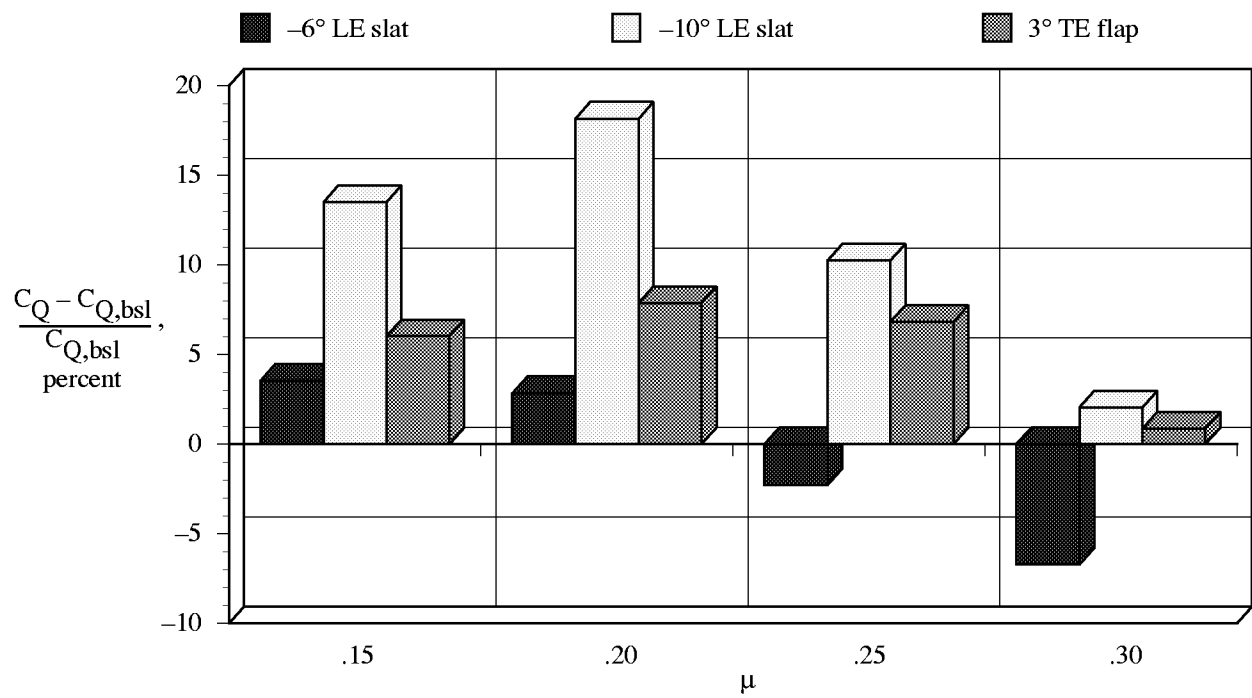


(a) $C_L = 0.007$.



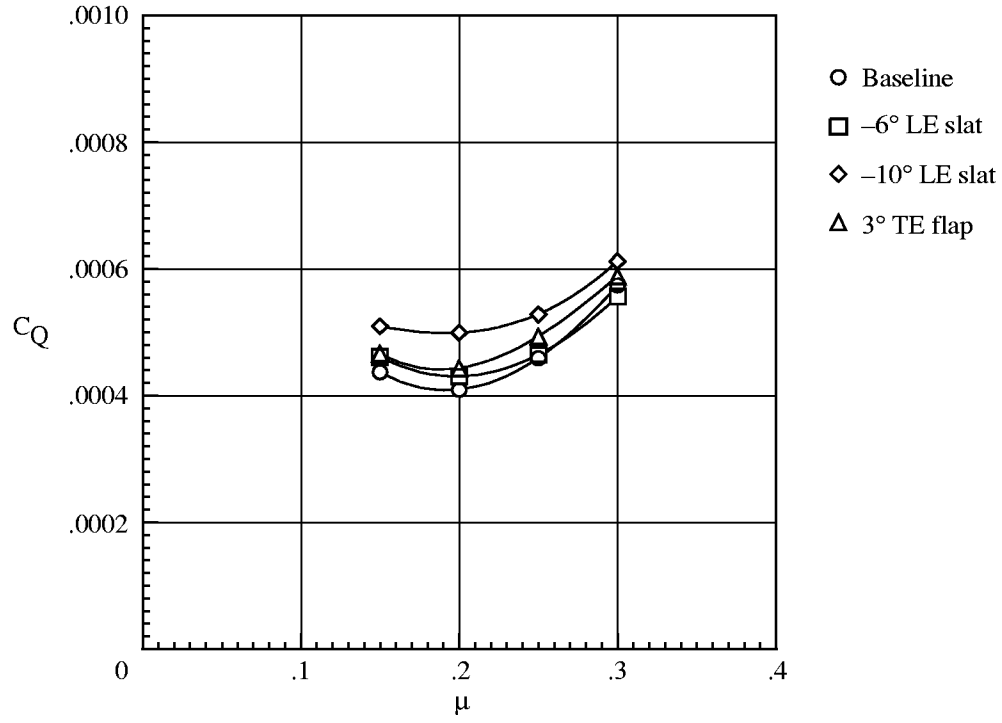
(b) $C_L = 0.0081$.

Figure 11. Performance of slotted rotor configurations relative to baseline rotor for $f_D = 29.94 \text{ ft}^2$.

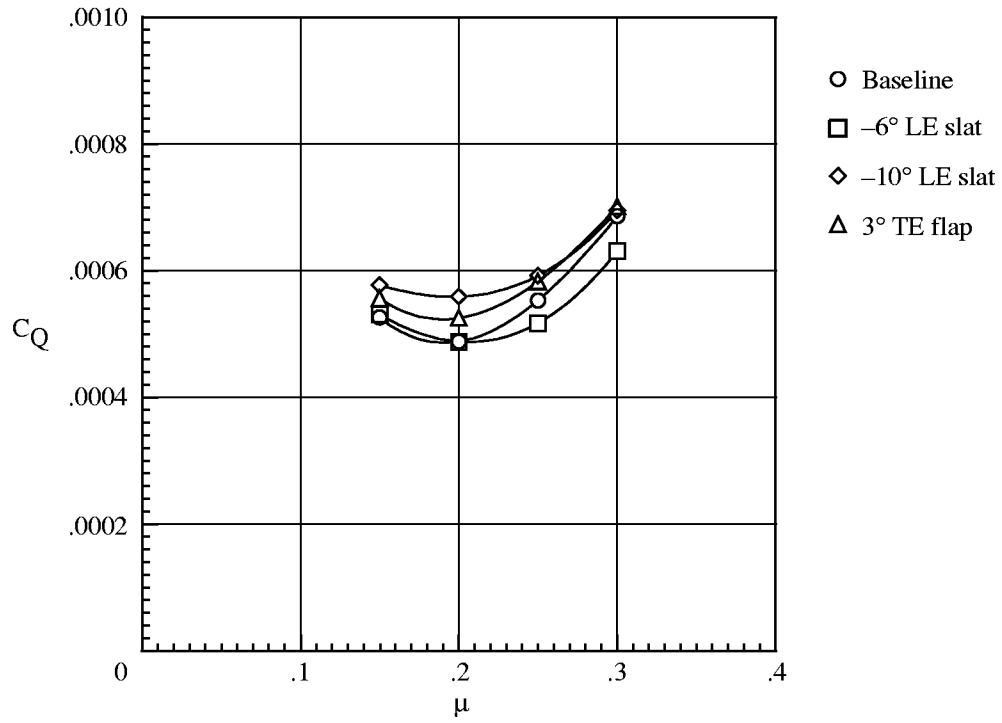


(c) $C_L = 0.009$.

Figure 11. Concluded.

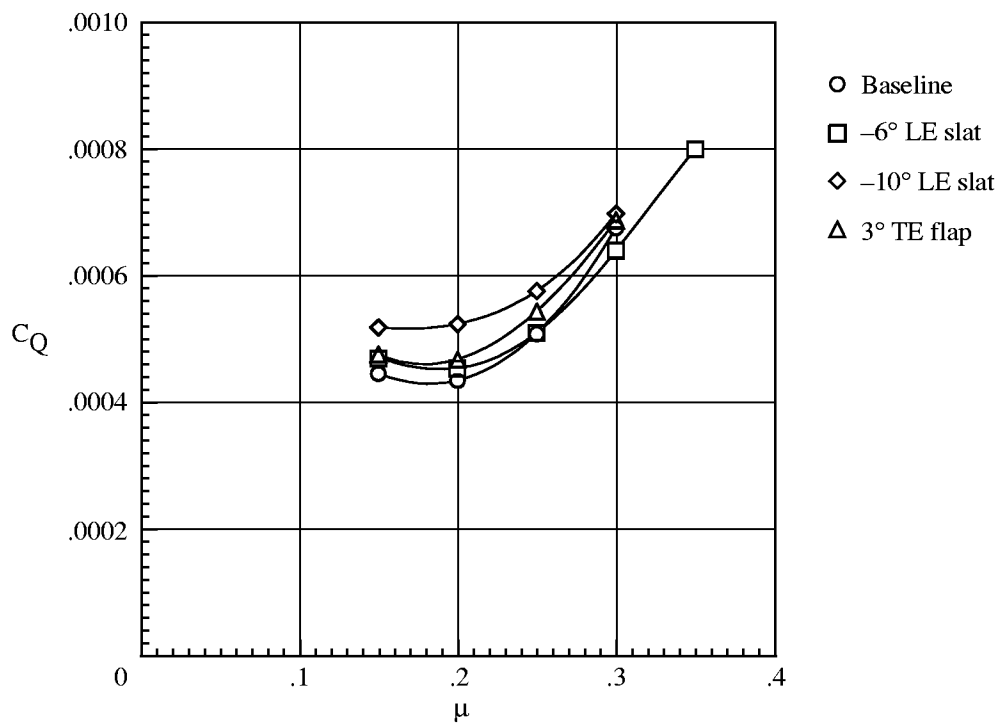


(a) $C_L = 0.0086$; $f_D = 12.0 \text{ ft}^2$.

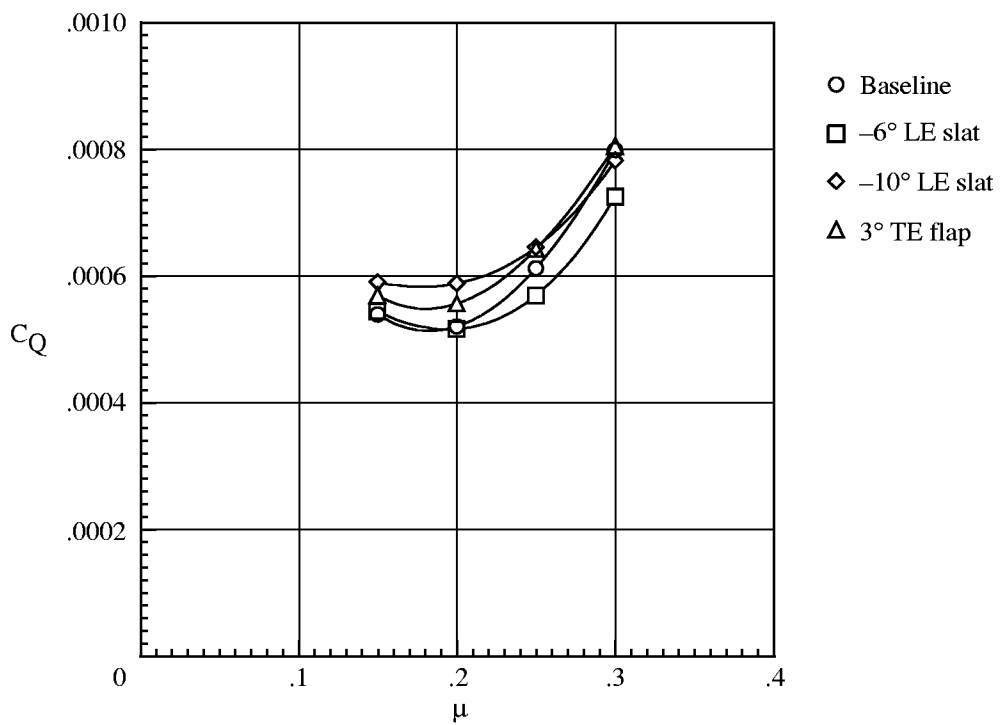


(b) $C_L = 0.0095$; $f_D = 12.0 \text{ ft}^2$.

Figure 12. Variation of rotor torque coefficient with advance ratio for $M_T = 0.627$.

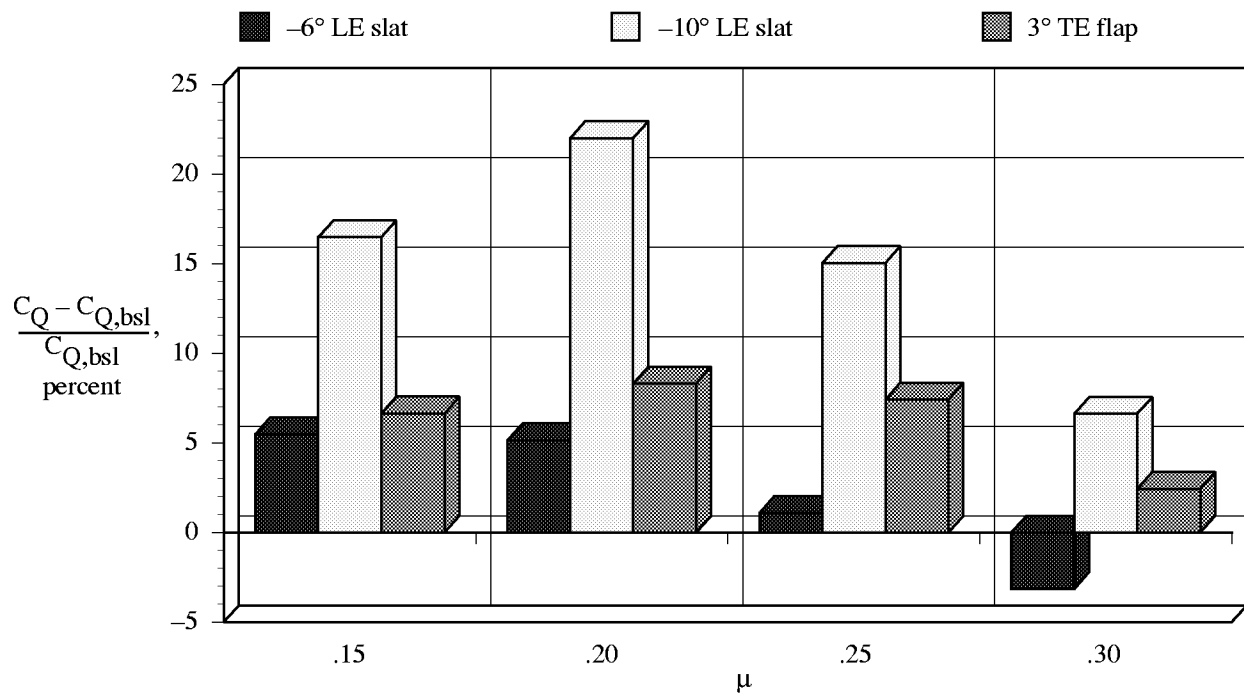


(c) $C_L = 0.0086$; $f_D = 18.5 \text{ ft}^2$.

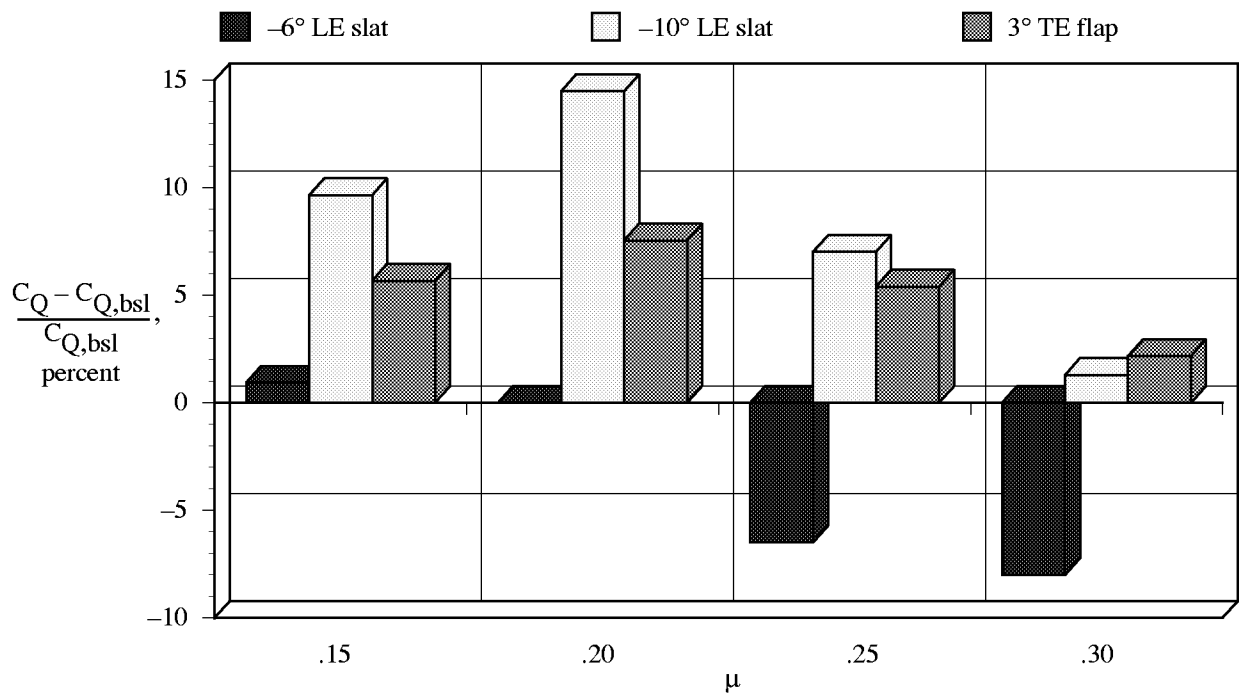


(d) $C_L = 0.0095$; $f_D = 18.5 \text{ ft}^2$.

Figure 12. Concluded.

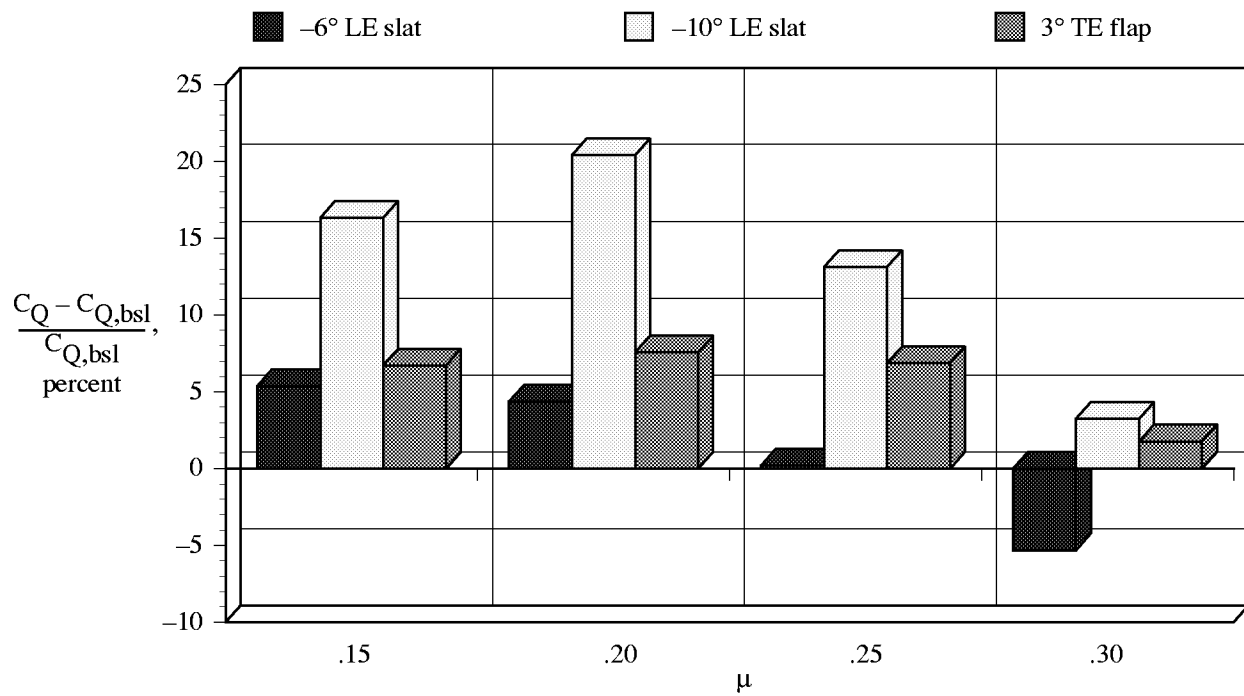


(a) $C_L = 0.0086; f_D = 12.0 \text{ ft}^2$.

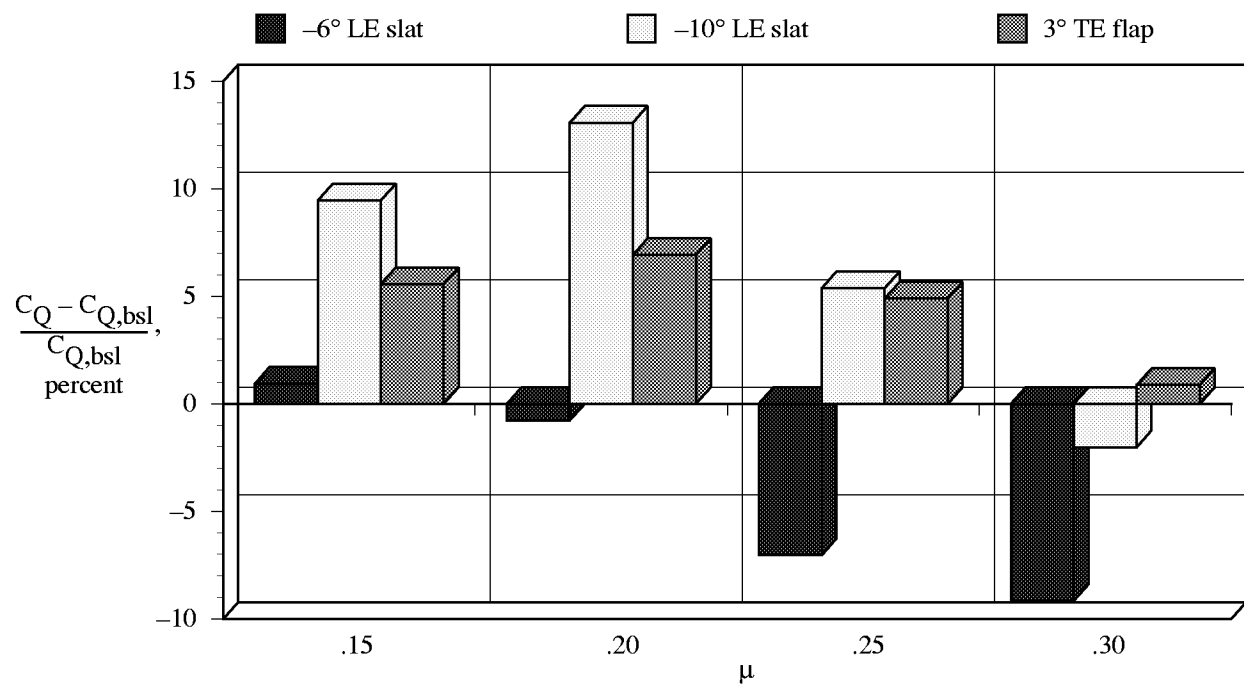


(b) $C_L = 0.0095; f_D = 12.0 \text{ ft}^2$.

Figure 13. Performance of slotted rotor configurations relative to baseline rotor for $M_T = 0.627$.

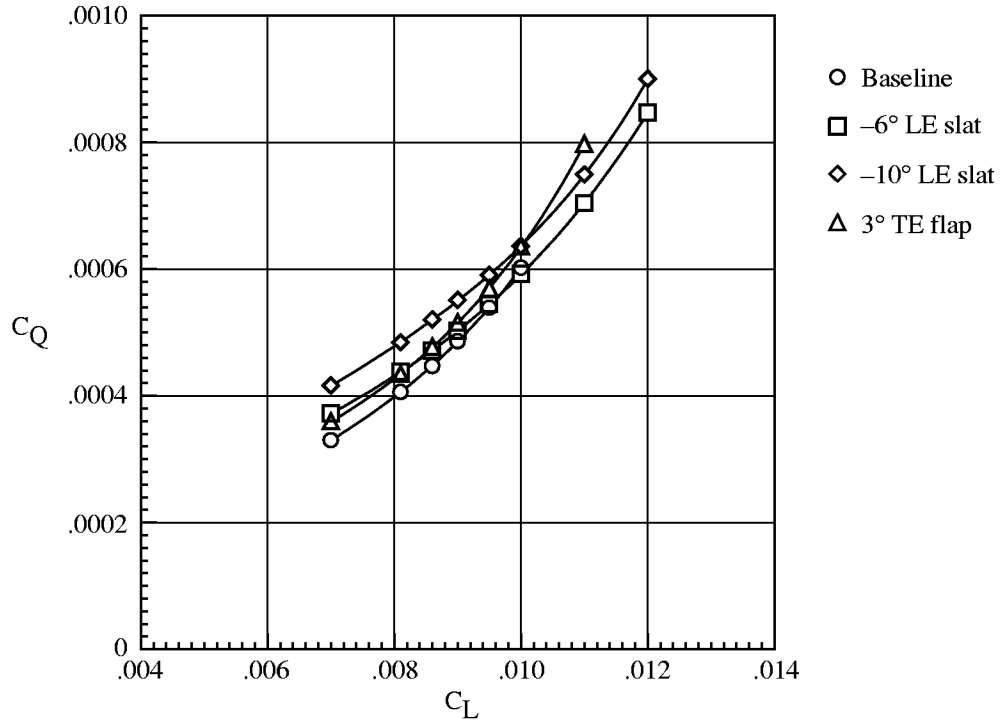


(c) $C_L = 0.0086; f_D = 18.5 \text{ ft}^2$.

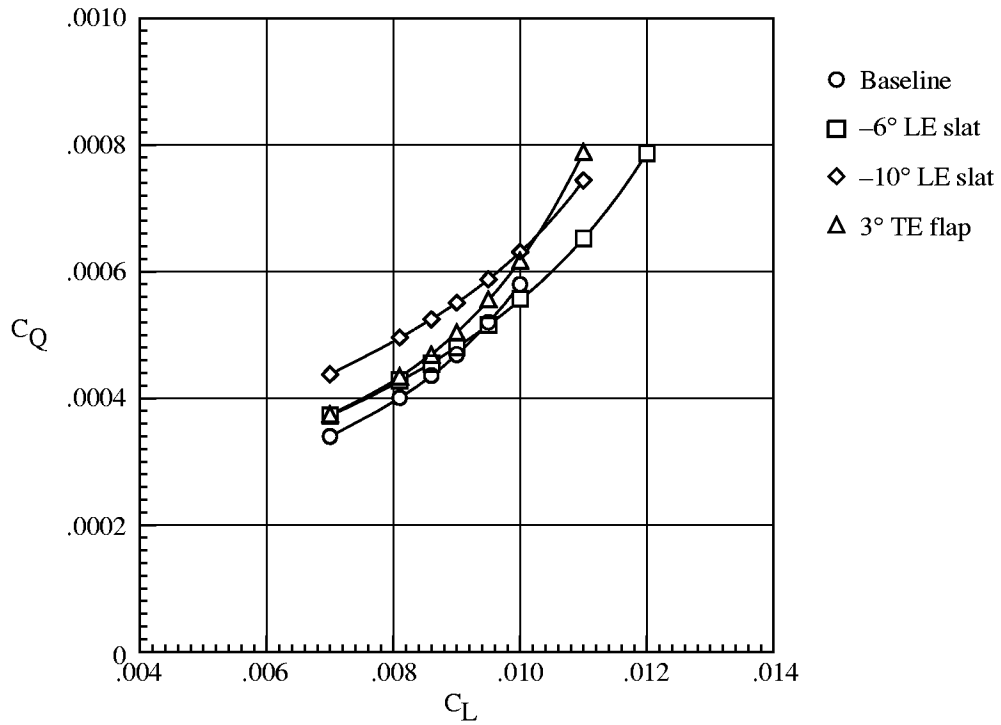


(d) $C_L = 0.0095; f_D = 18.5 \text{ ft}^2$.

Figure 13. Concluded.

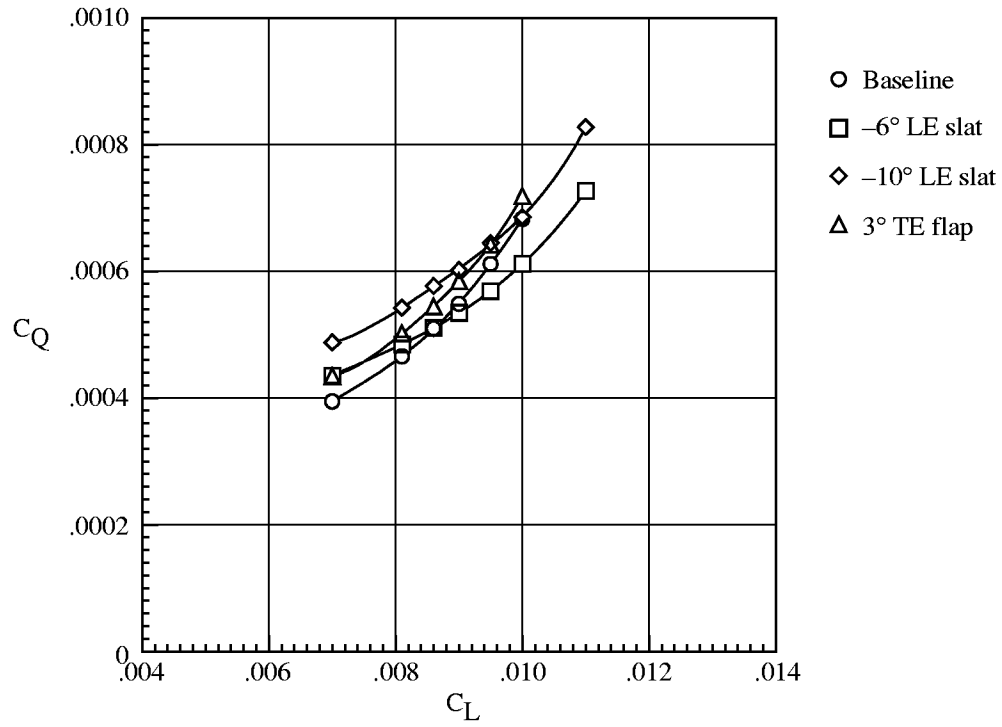


(a) $\mu = 0.15$.

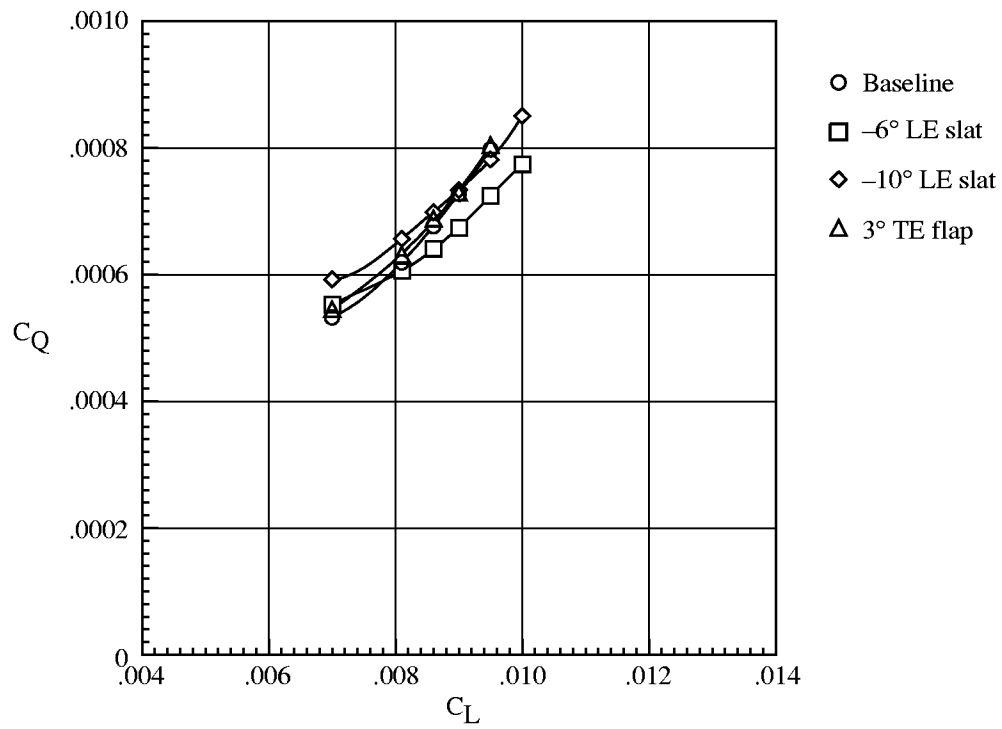


(b) $\mu = 0.20$.

Figure 14. Variation of rotor torque coefficient with lift coefficient for $f_D = 18.5 \text{ ft}^2$ and $M_T = 0.627$.

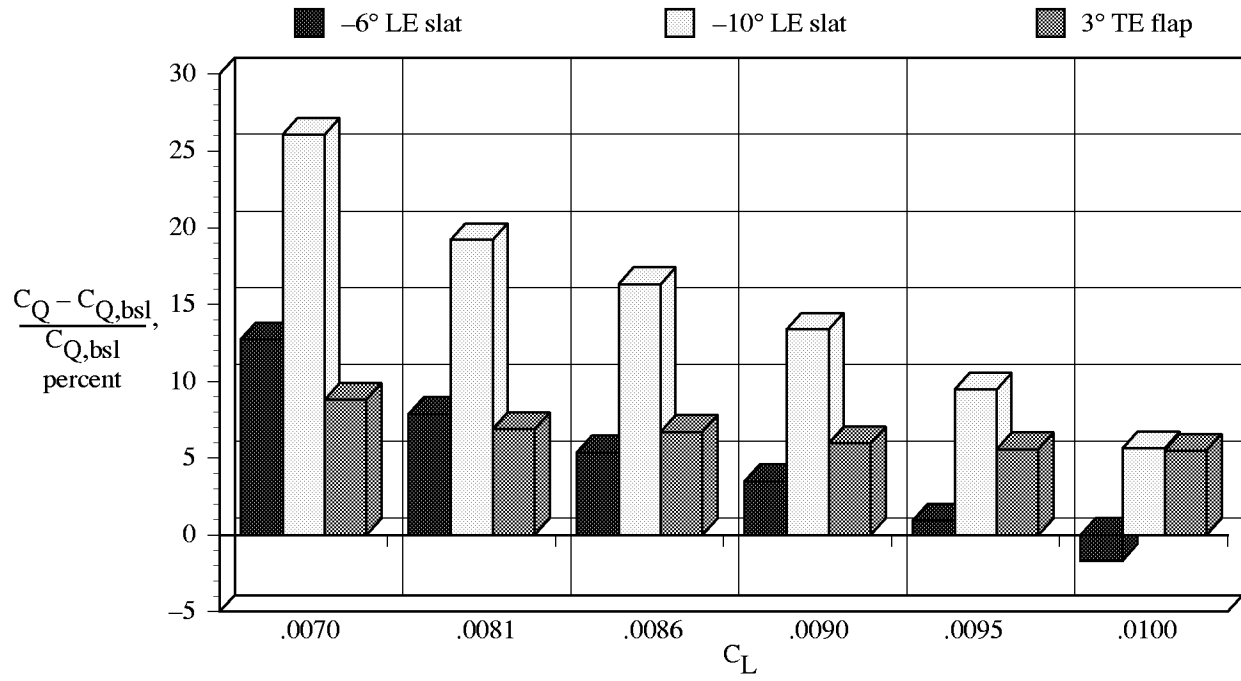


(c) $\mu = 0.25$.

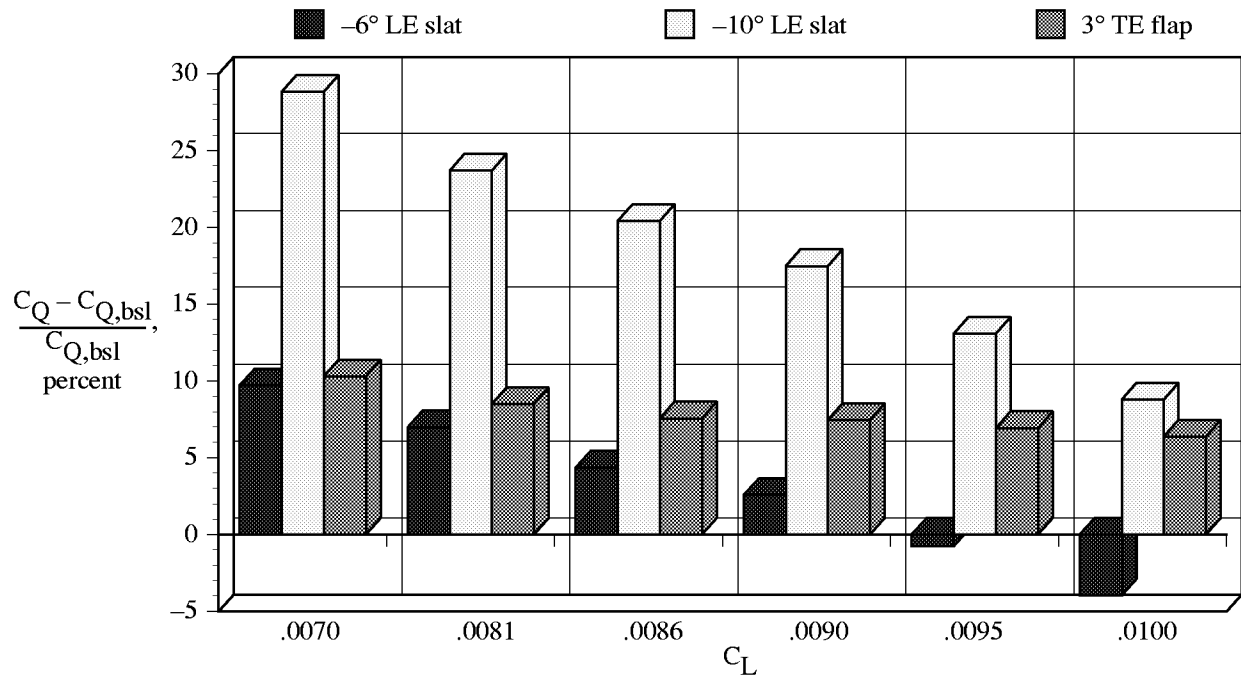


(d) $\mu = 0.30$.

Figure 14. Concluded.

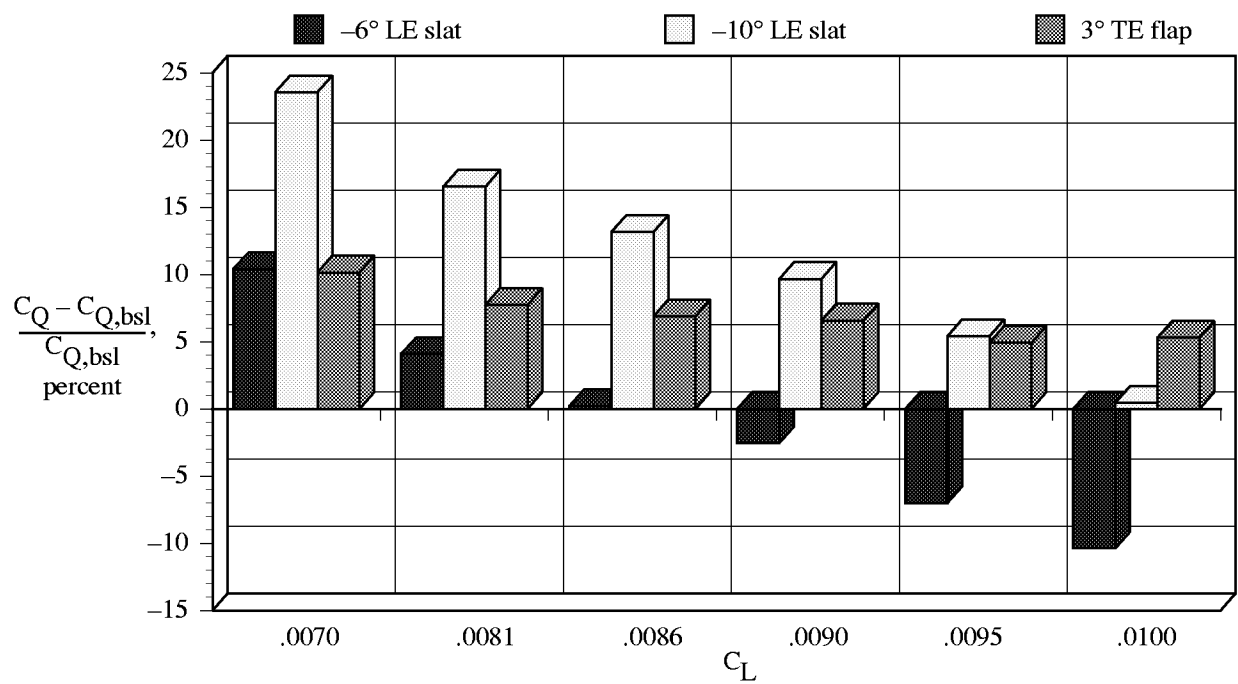


(a) $\mu = 0.15$.

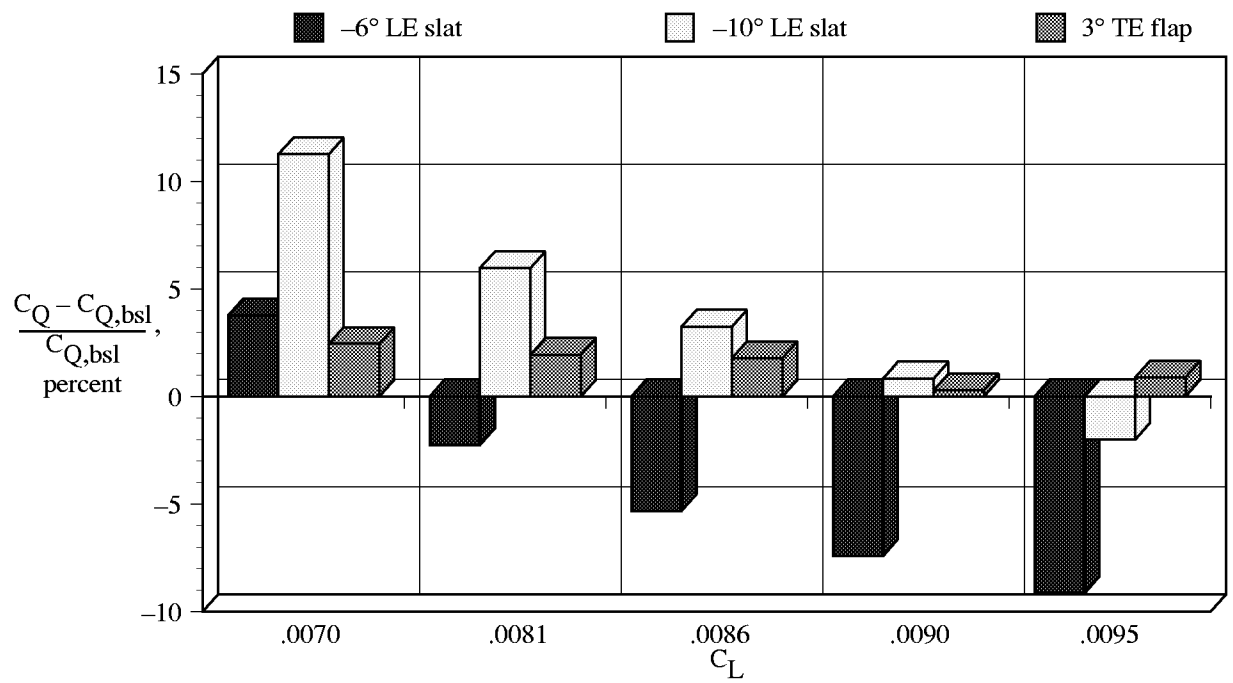


(b) $\mu = 0.20$.

Figure 15. Performance of slotted rotor configurations relative to baseline rotor for $f_D = 18.5 \text{ ft}^2$.

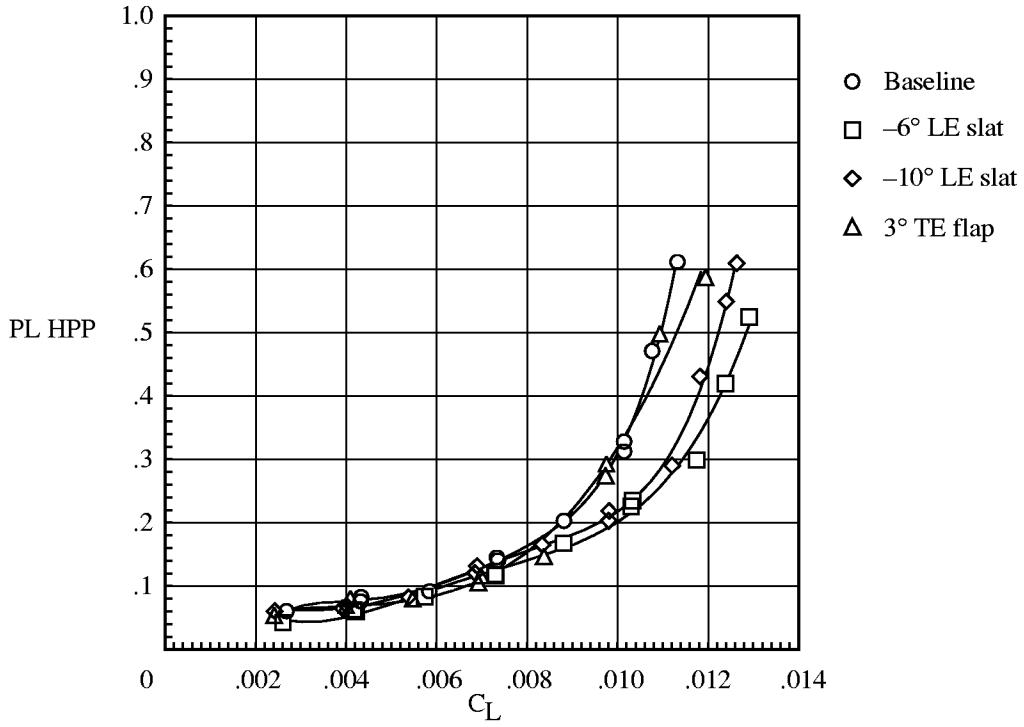


(c) $\mu = 0.25$.

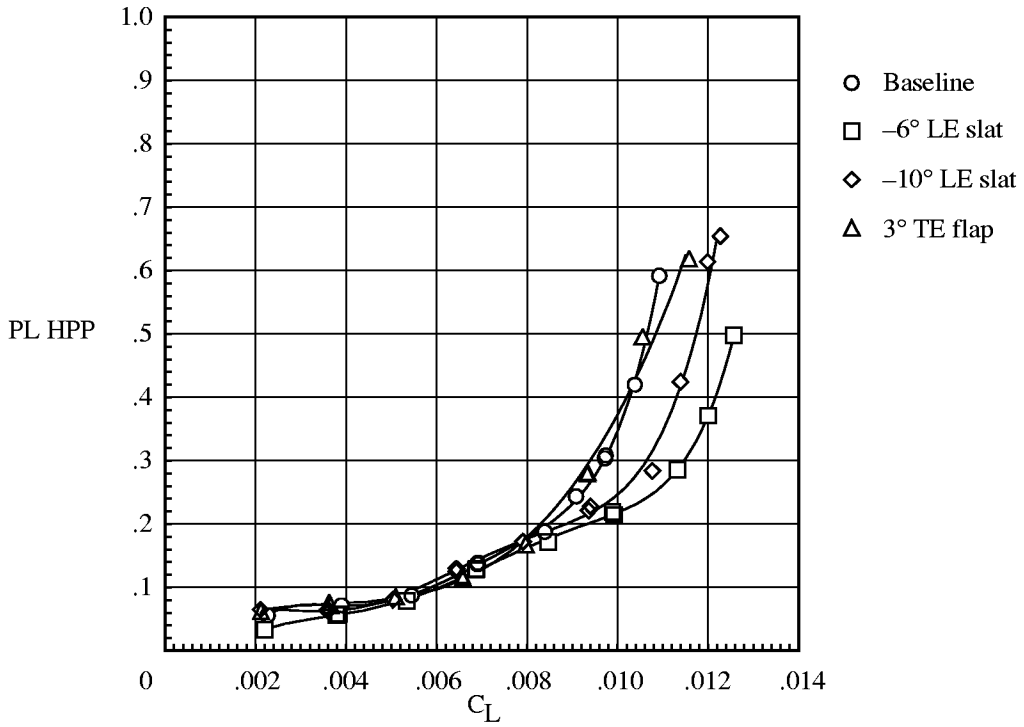


(d) $\mu = 0.30$.

Figure 15. Concluded.

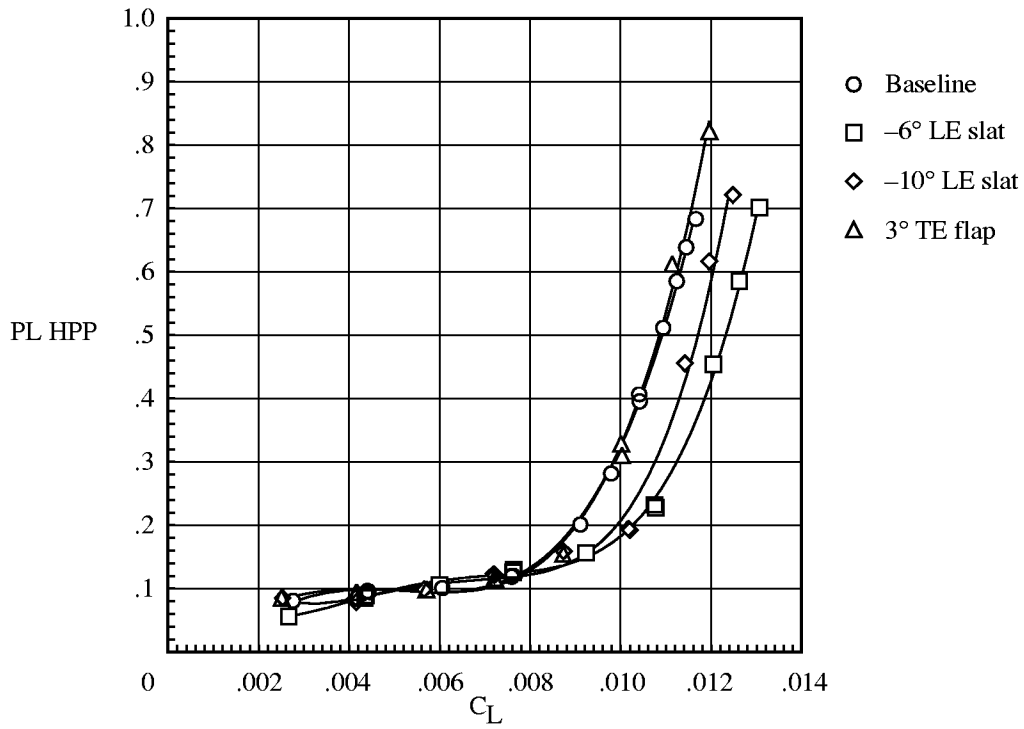


(a) $\mu = 0.15$; $\alpha_s = 0^\circ$.

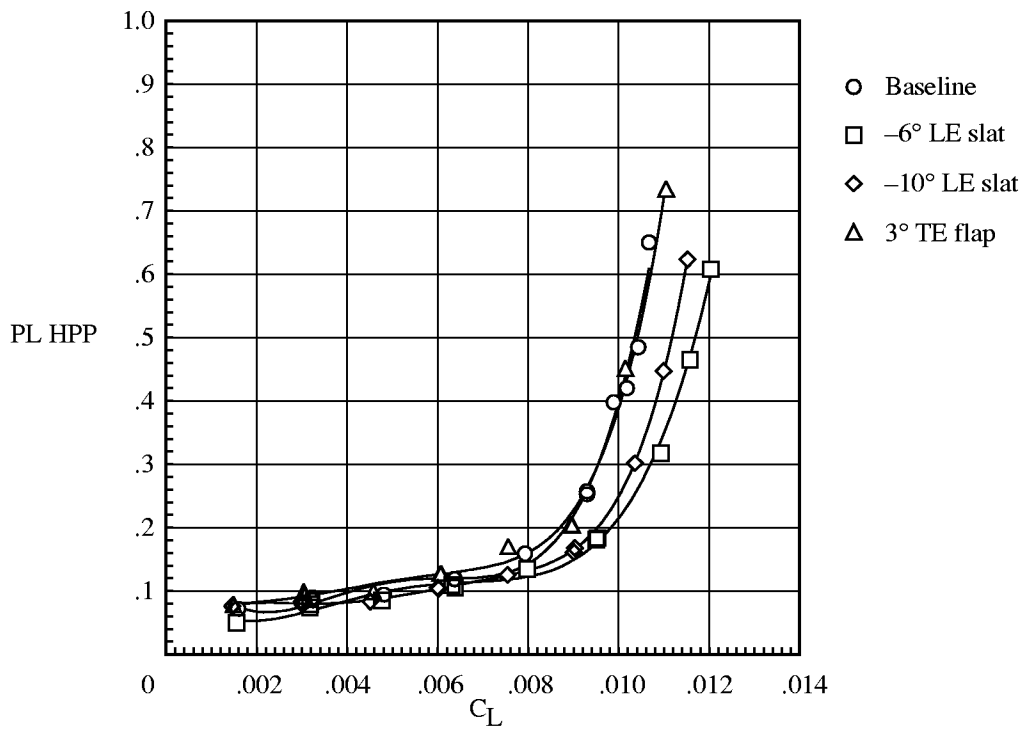


(b) $\mu = 0.15$; $\alpha_s = -2^\circ$.

Figure 16. Variation of pitch-link oscillatory loads with rotor lift coefficient for $M_T = 0.627$.

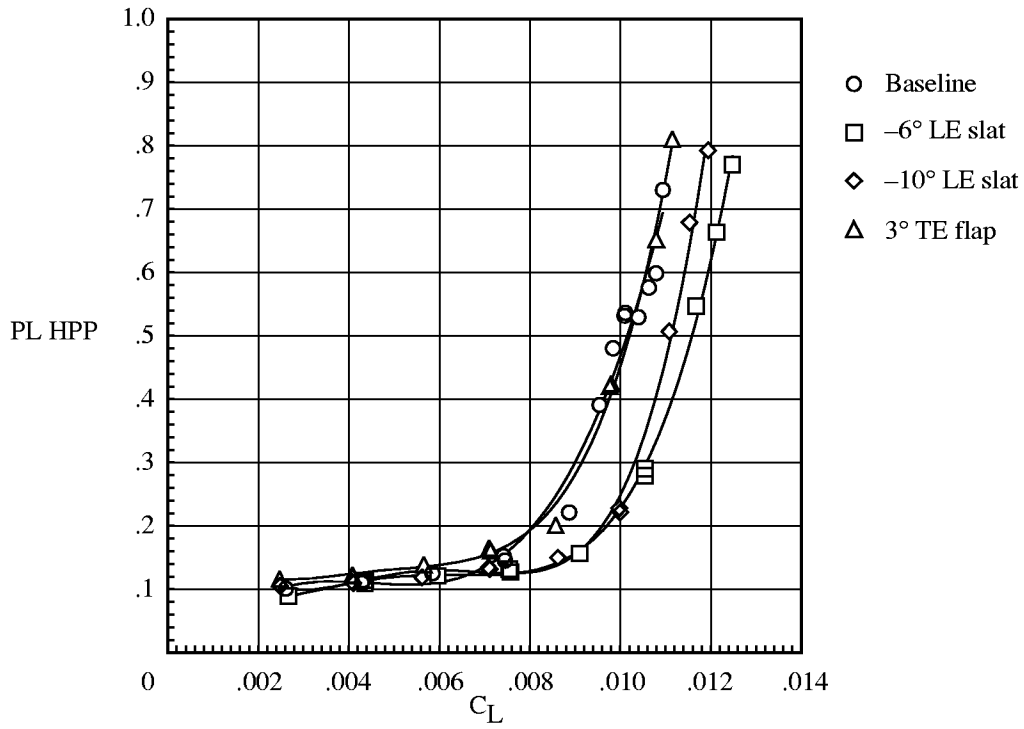


(c) $\mu = 0.20$; $\alpha_s = 0^\circ$.

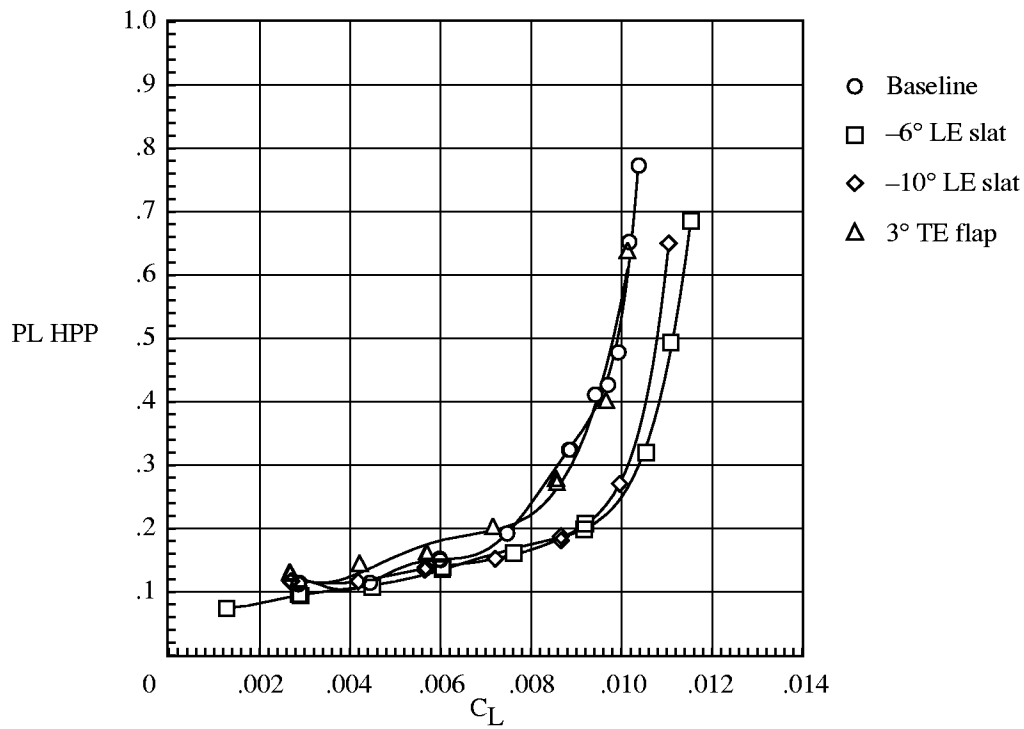


(d) $\mu = 0.20$; $\alpha_s = -4^\circ$.

Figure 16. Continued.

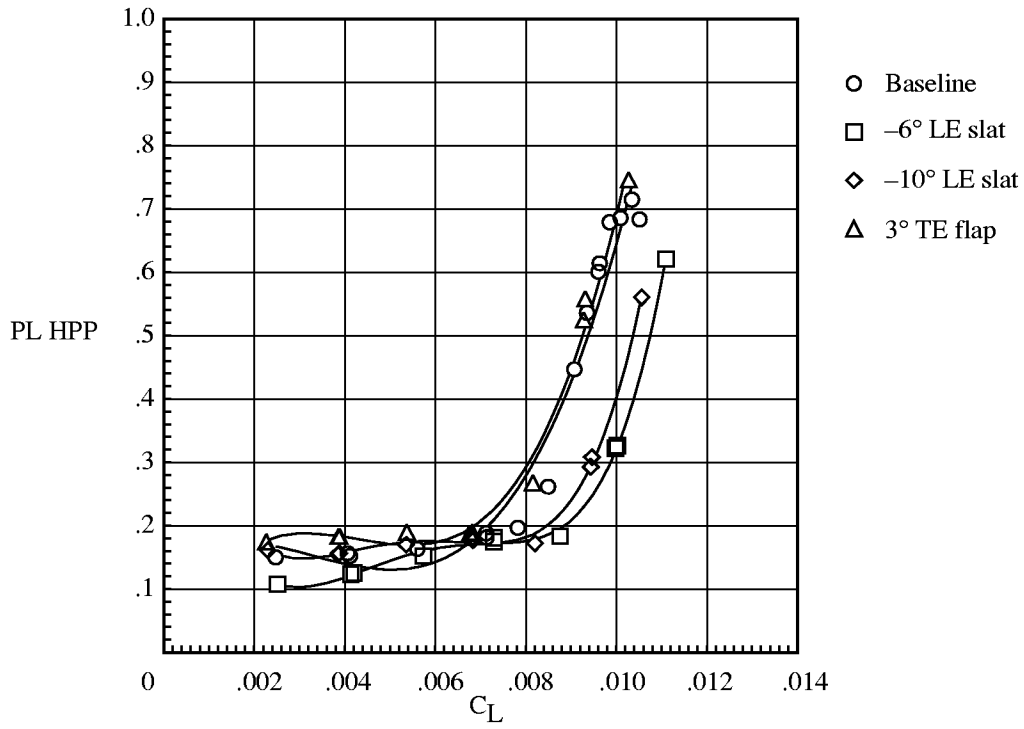


(e) $\mu = 0.25$; $\alpha_s = 0^\circ$.

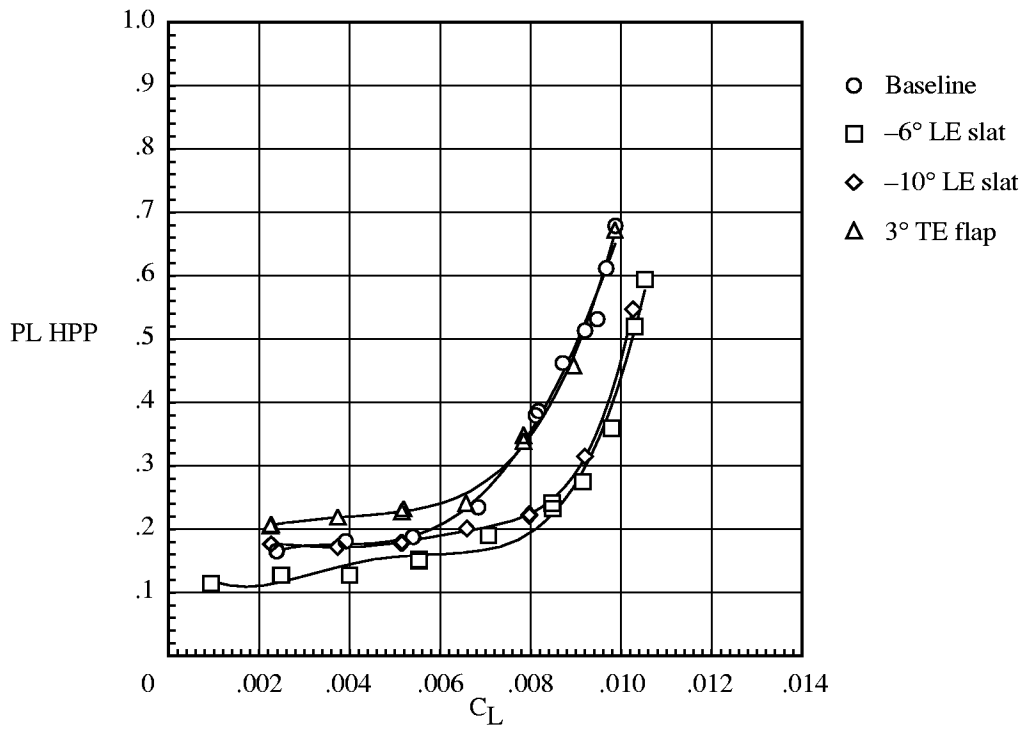


(f) $\mu = 0.25$; $\alpha_s = -4^\circ$.

Figure 16. Continued.

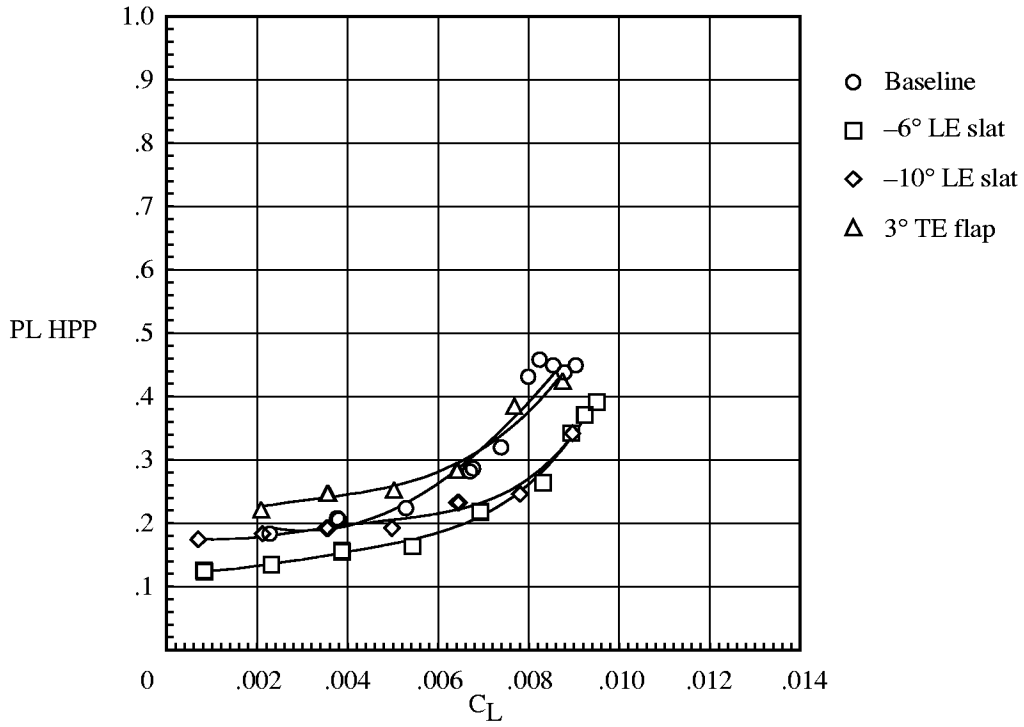


(g) $\mu = 0.30$; $\alpha_s = 0^\circ$.

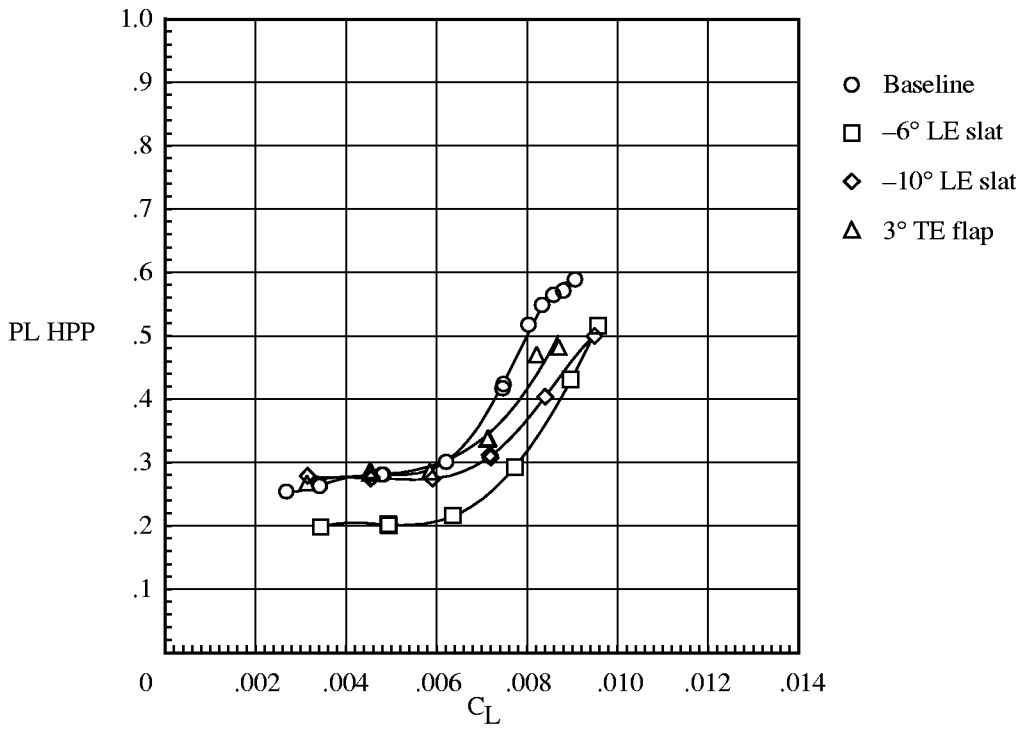


(h) $\mu = 0.30$; $\alpha_s = -4^\circ$.

Figure 16. Continued.

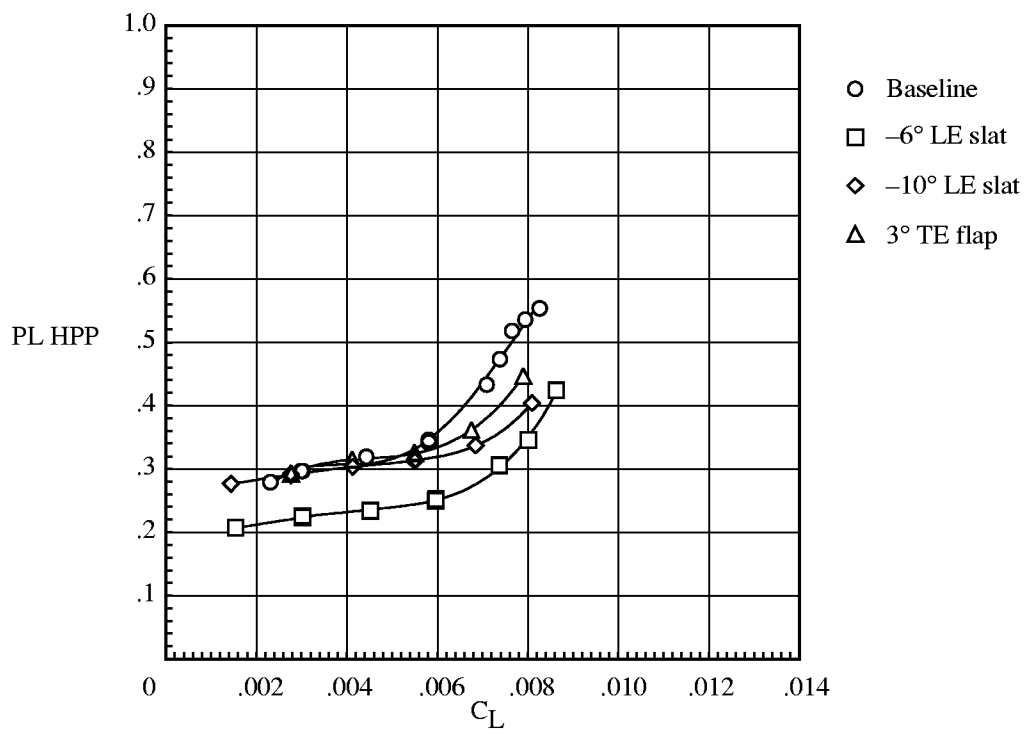


(i) $\mu = 0.30$; $\alpha_s = -8^\circ$.



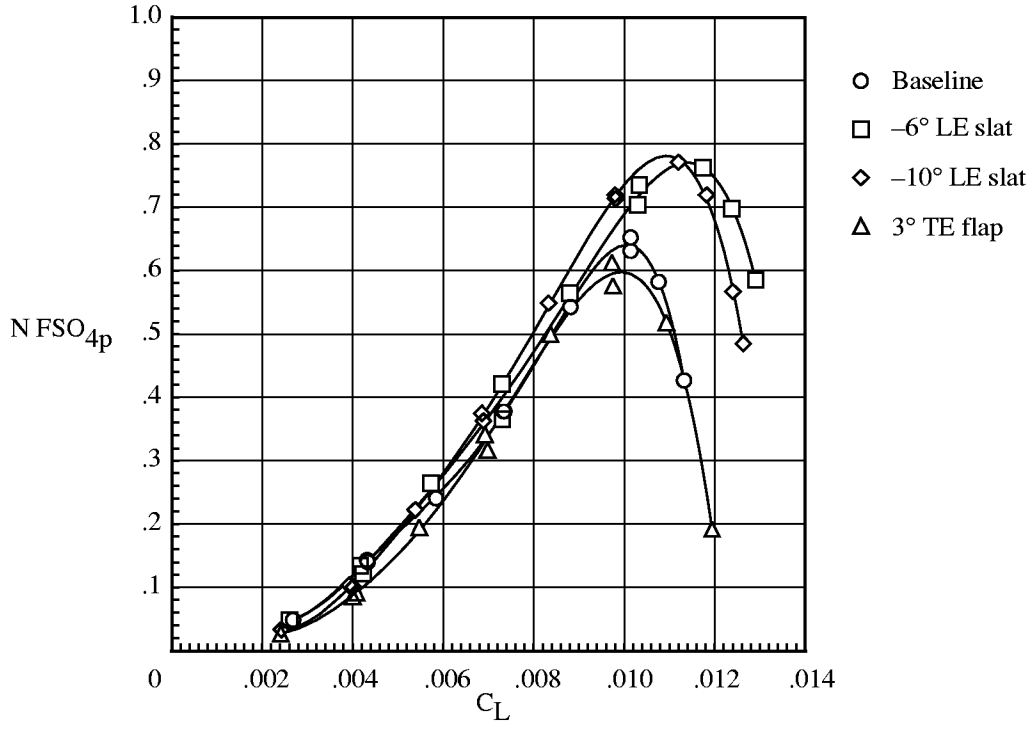
(j) $\mu = 0.35$; $\alpha_s = -4^\circ$.

Figure 16. Continued.

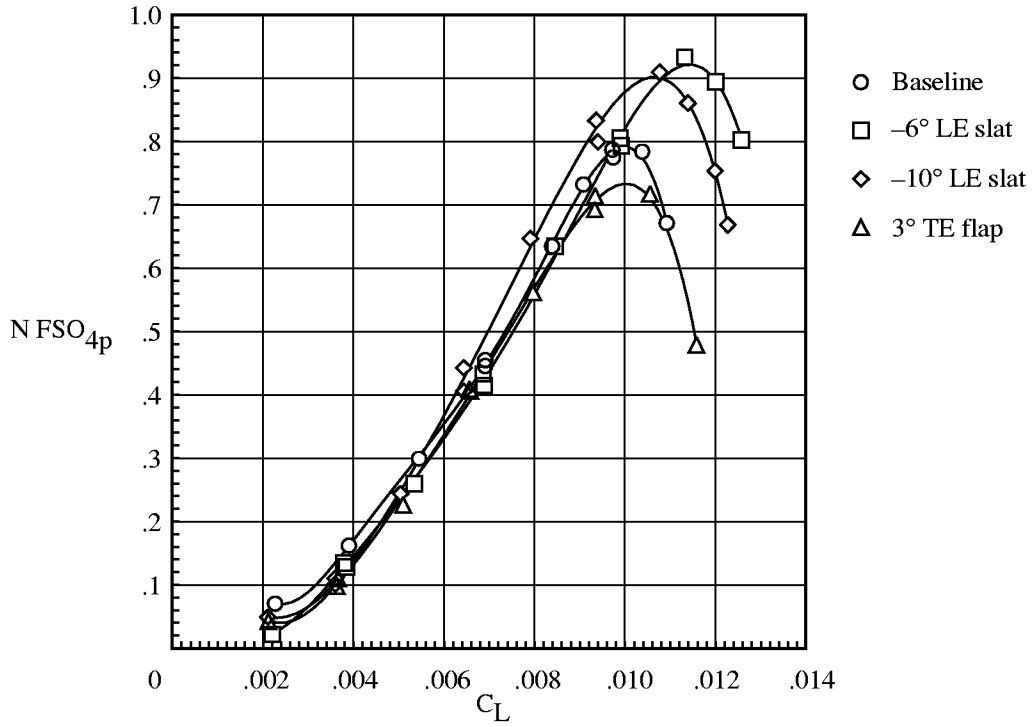


(k) $\mu = 0.35$; $\alpha_s = -8^\circ$.

Figure 16. Concluded.

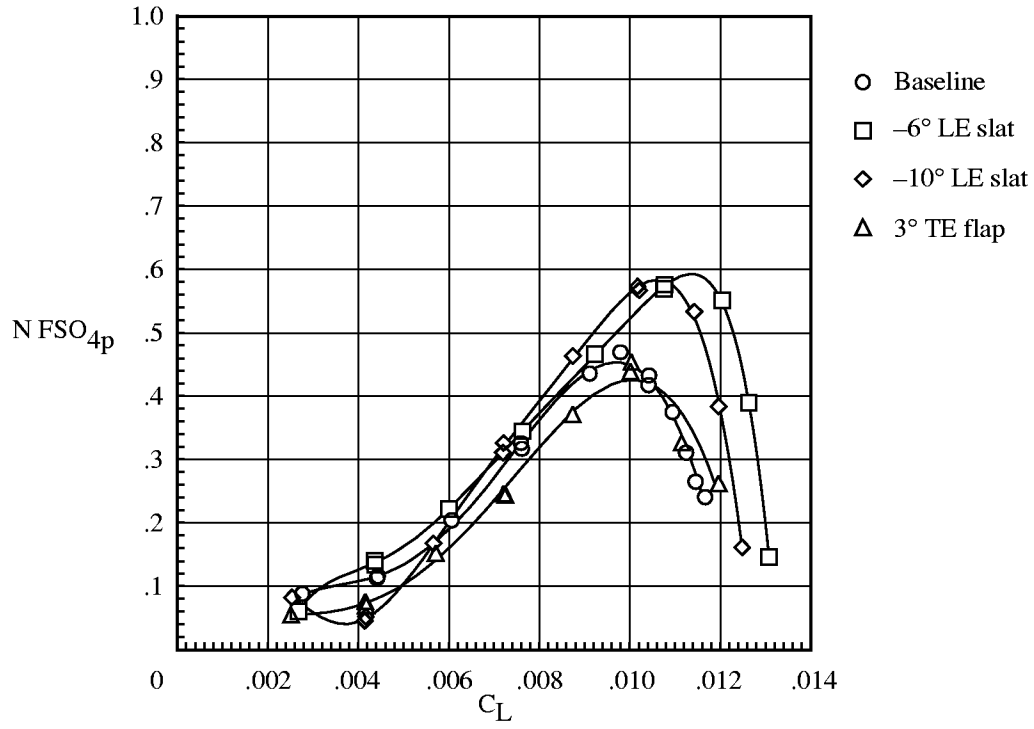


(a) $\mu = 0.15$; $\alpha_s = 0^\circ$.

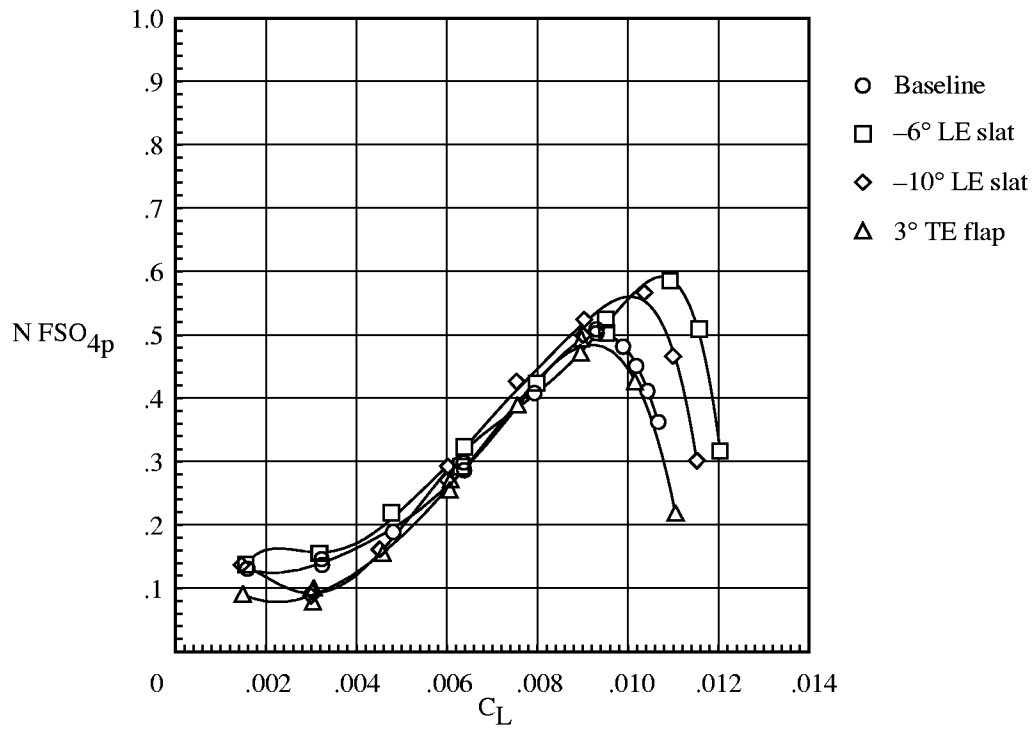


(b) $\mu = 0.15$; $\alpha_s = -2^\circ$.

Figure 17. Variation of 4P fixed-system normal loads with rotor lift coefficient; $M_T = 0.627$.

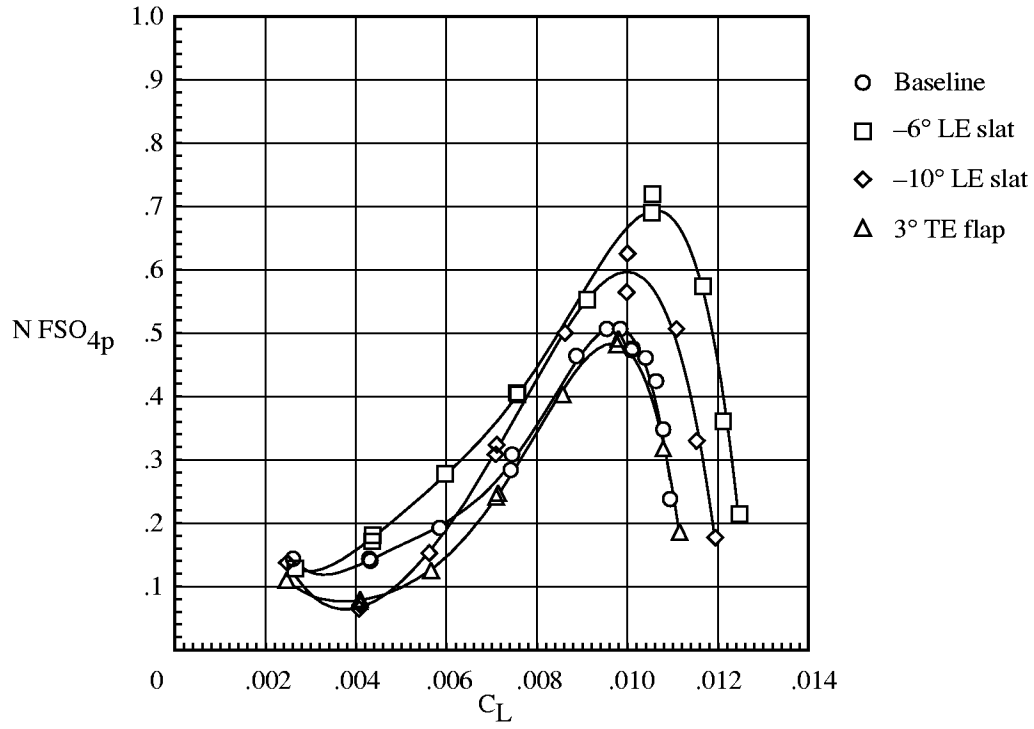


(c) $\mu = 0.20$; $\alpha_s = 0^\circ$.

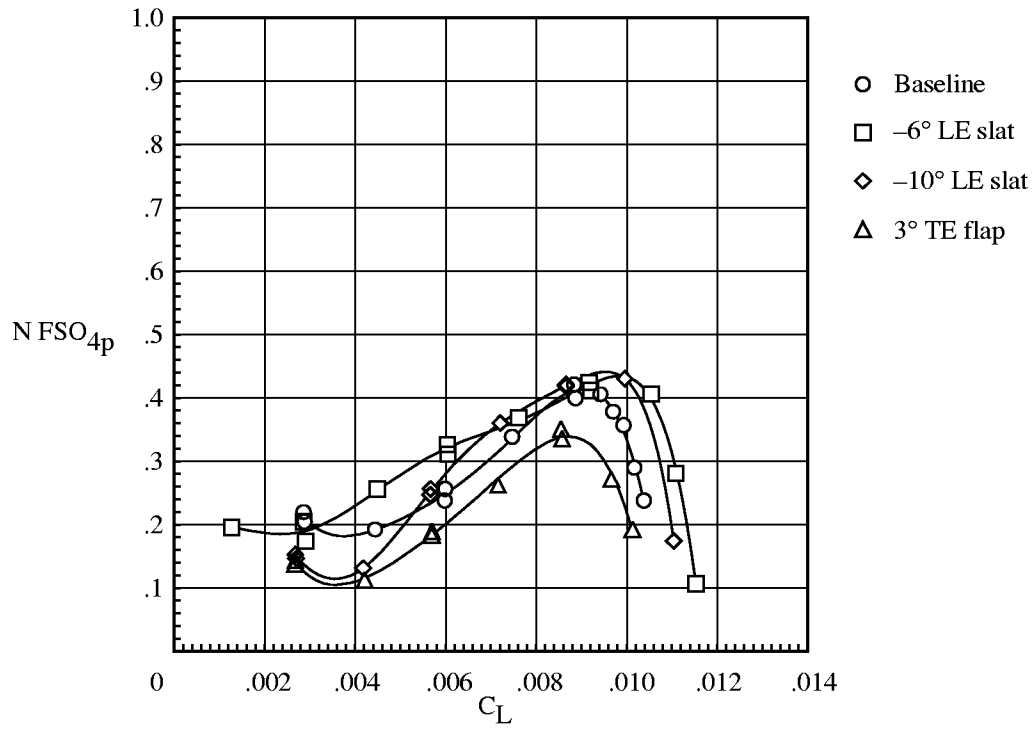


(d) $\mu = 0.20$; $\alpha_s = -4^\circ$.

Figure 17. Continued.

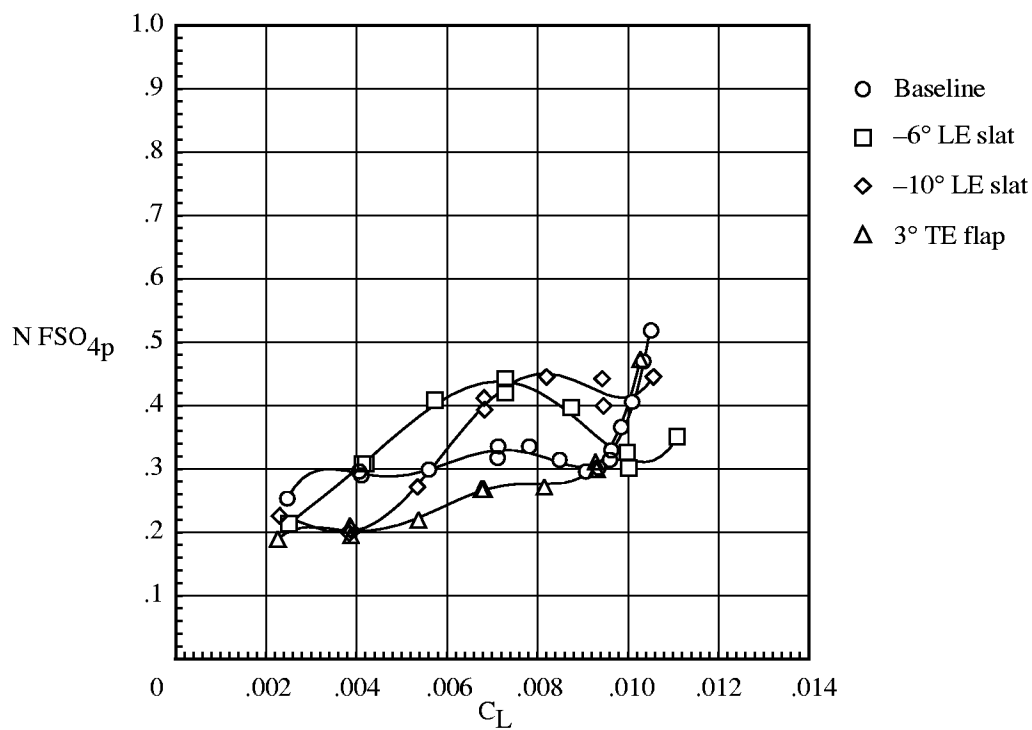


(e) $\mu = 0.25$; $\alpha_s = 0^\circ$.

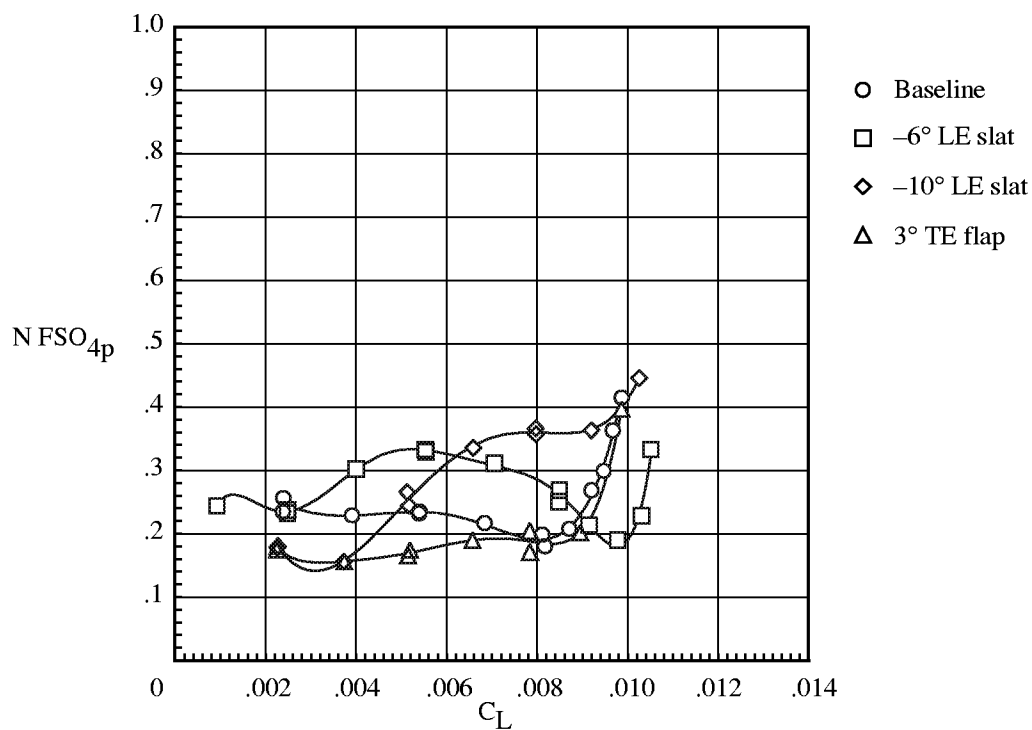


(f) $\mu = 0.25$; $\alpha_s = -4^\circ$.

Figure 17. Continued.

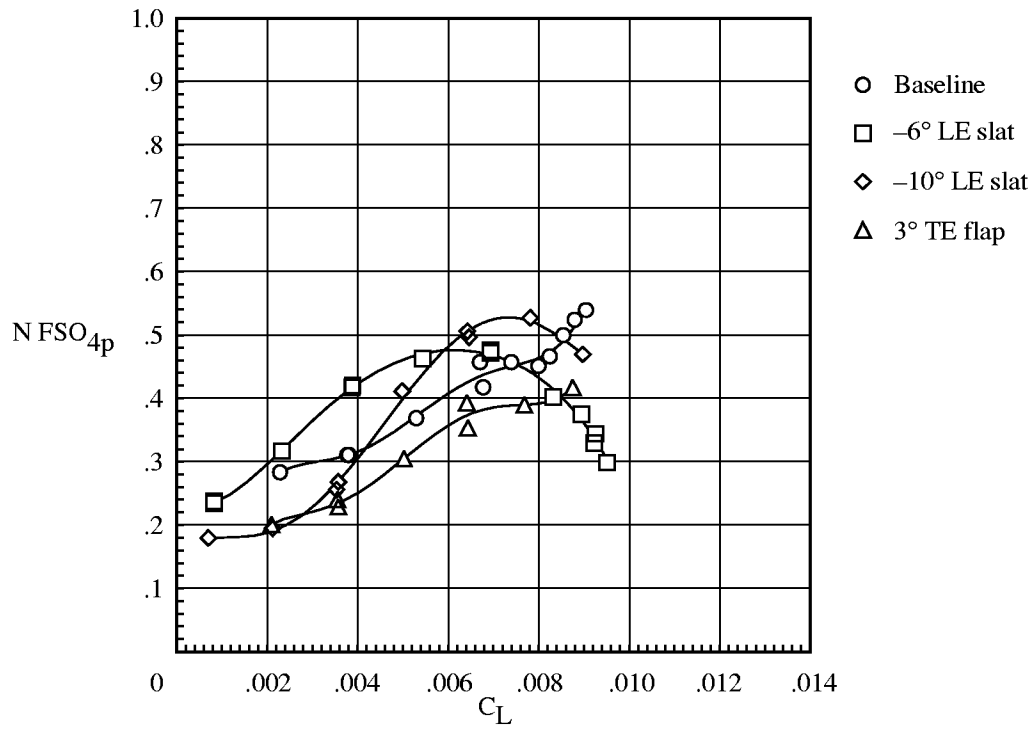


(g) $\mu = 0.30$; $\alpha_s = 0^\circ$.

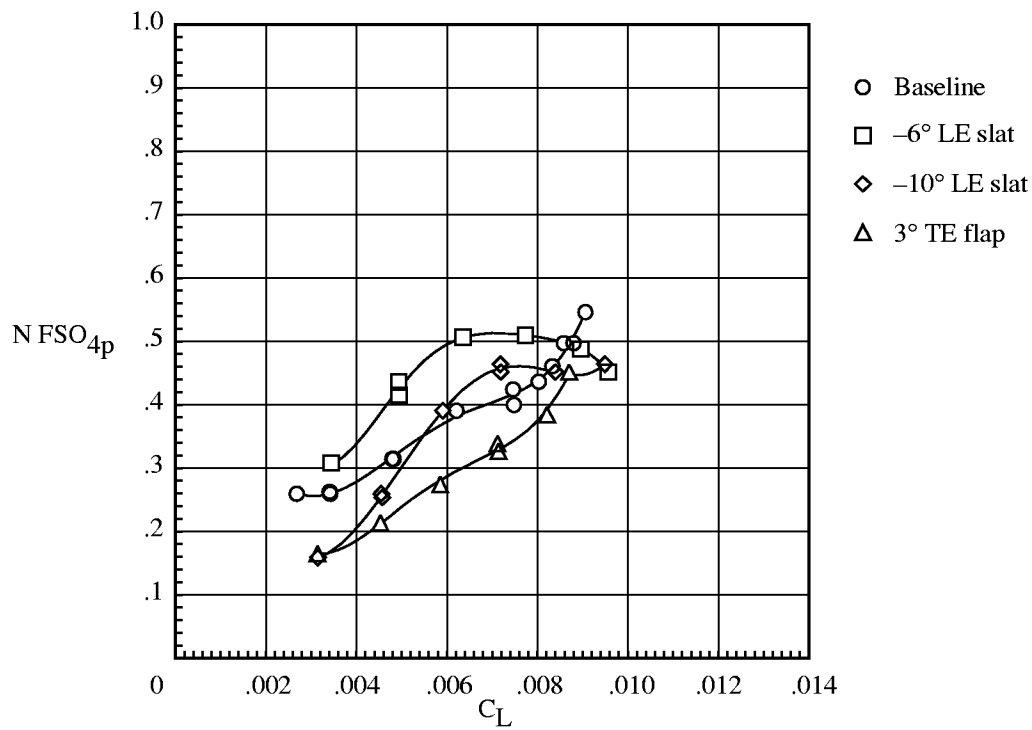


(h) $\mu = 0.30$; $\alpha_s = -4^\circ$.

Figure 17. Continued.

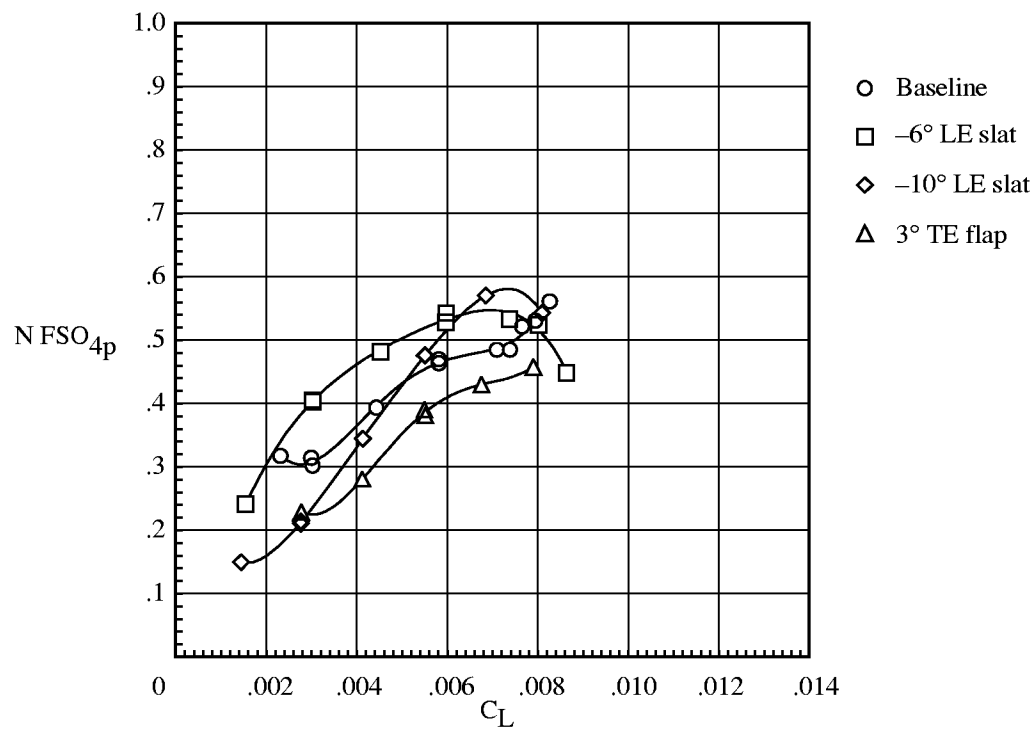


(i) $\mu = 0.30$; $\alpha_s = -8^\circ$.



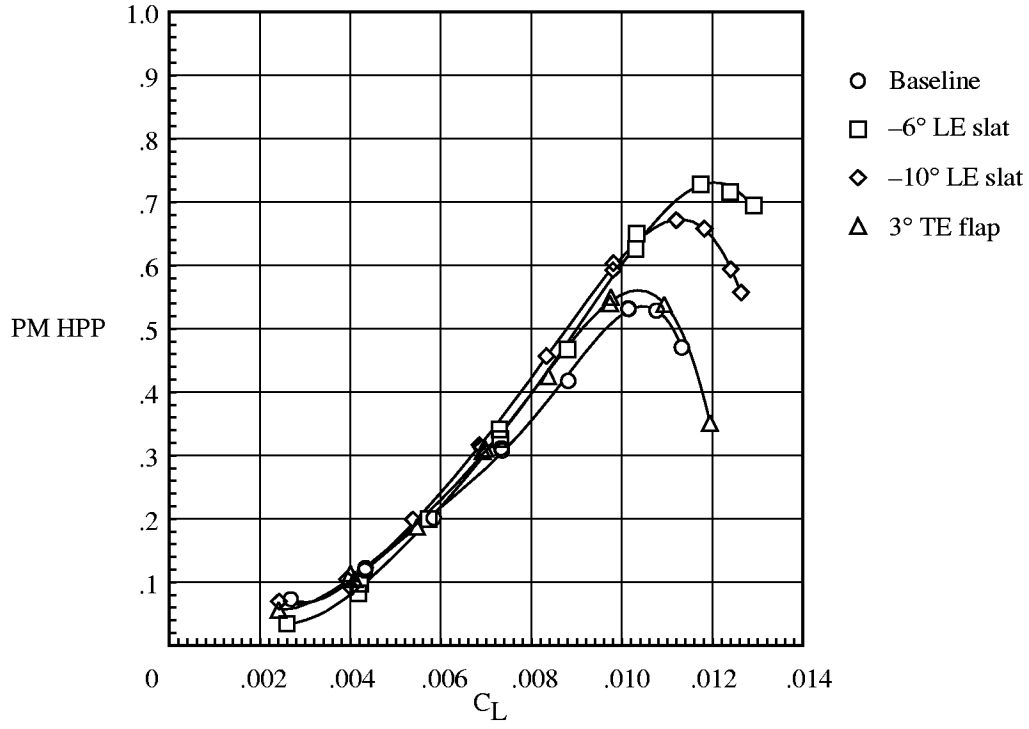
(j) $\mu = 0.35$; $\alpha_s = -4^\circ$.

Figure 17. Continued.

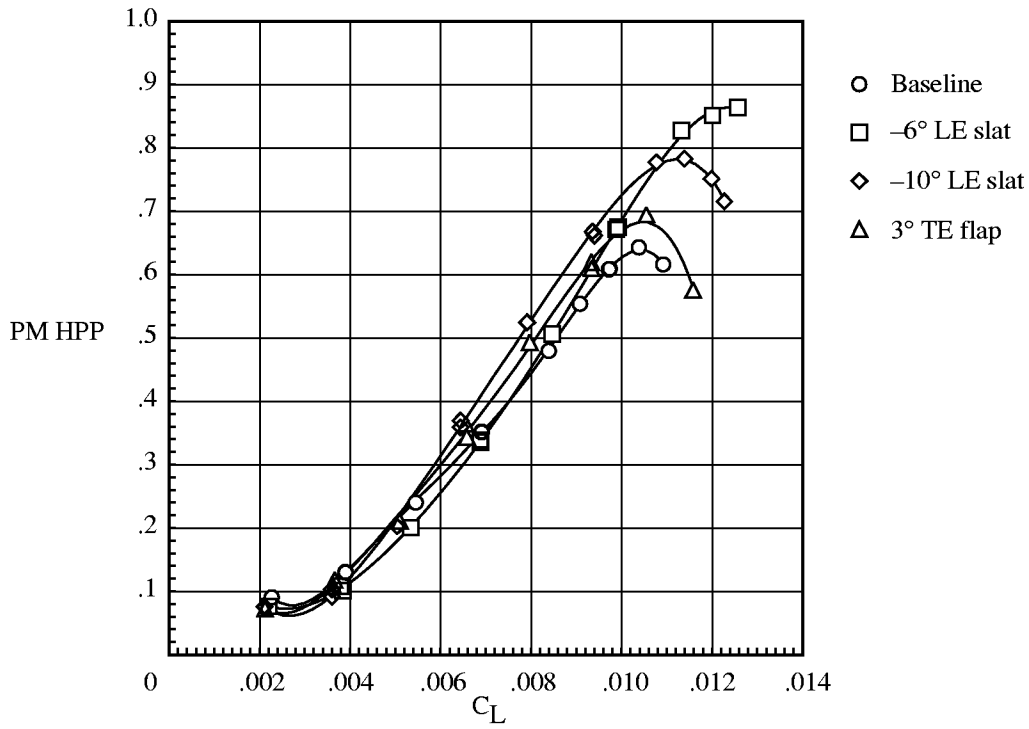


(k) $\mu = 0.35$; $\alpha_s = -8^\circ$.

Figure 17. Concluded.

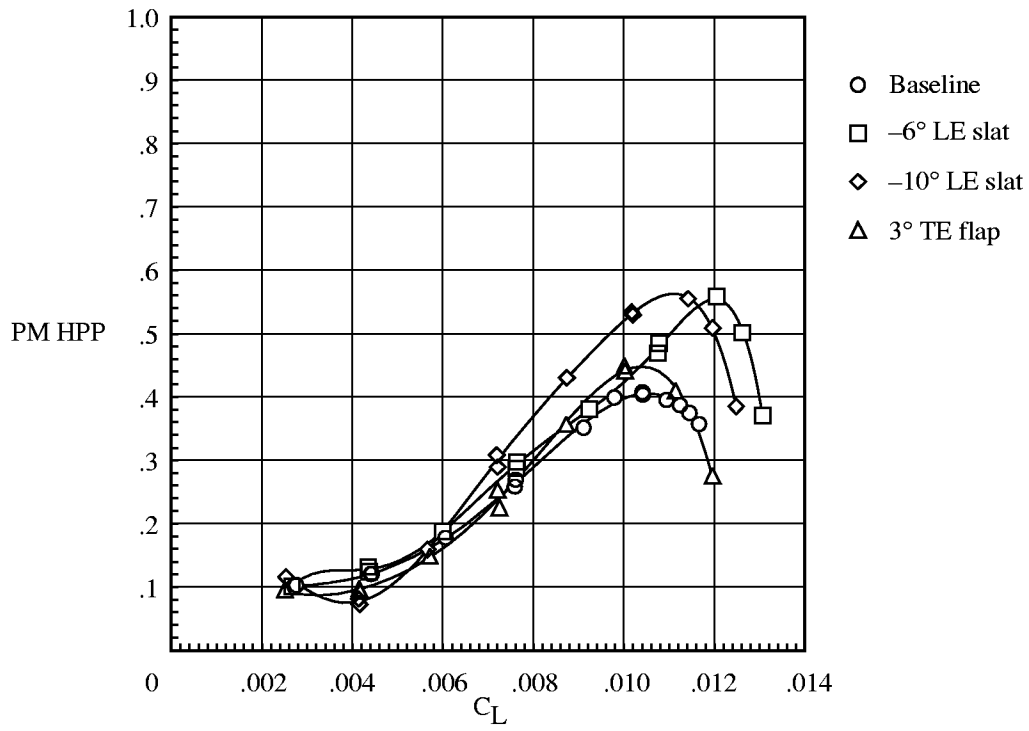


(a) $\mu = 0.15$; $\alpha_s = 0^\circ$.

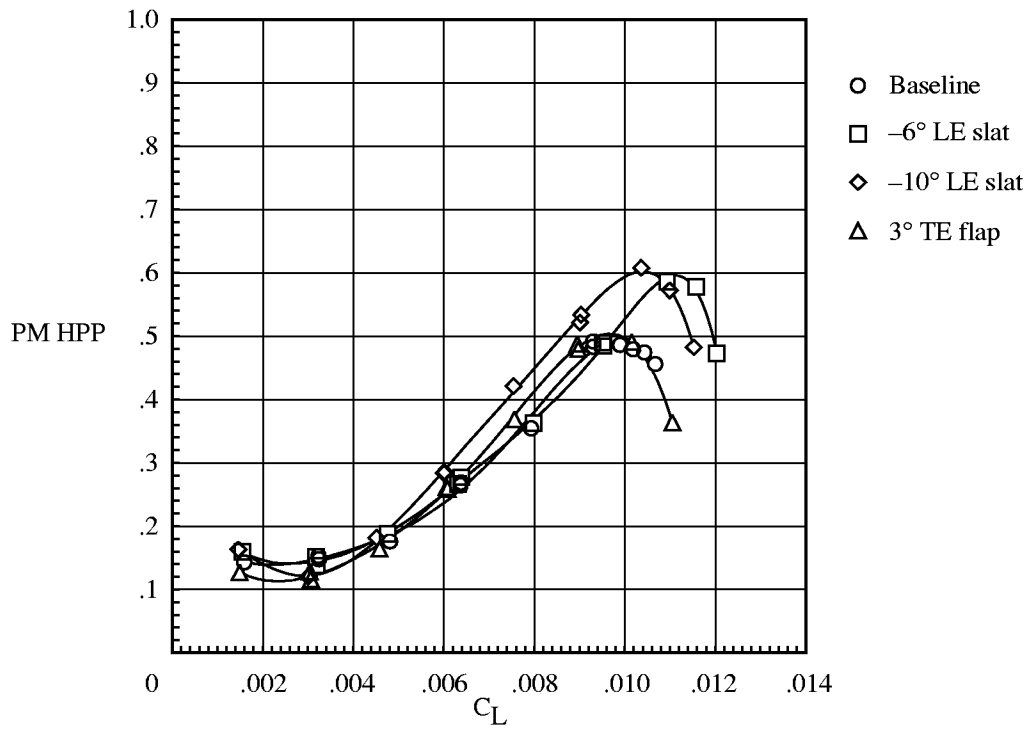


(b) $\mu = 0.15$; $\alpha_s = -2^\circ$.

Figure 18. Variation of fixed-system pitching-moment oscillatory loads with rotor lift coefficient; $M_T = 0.627$.

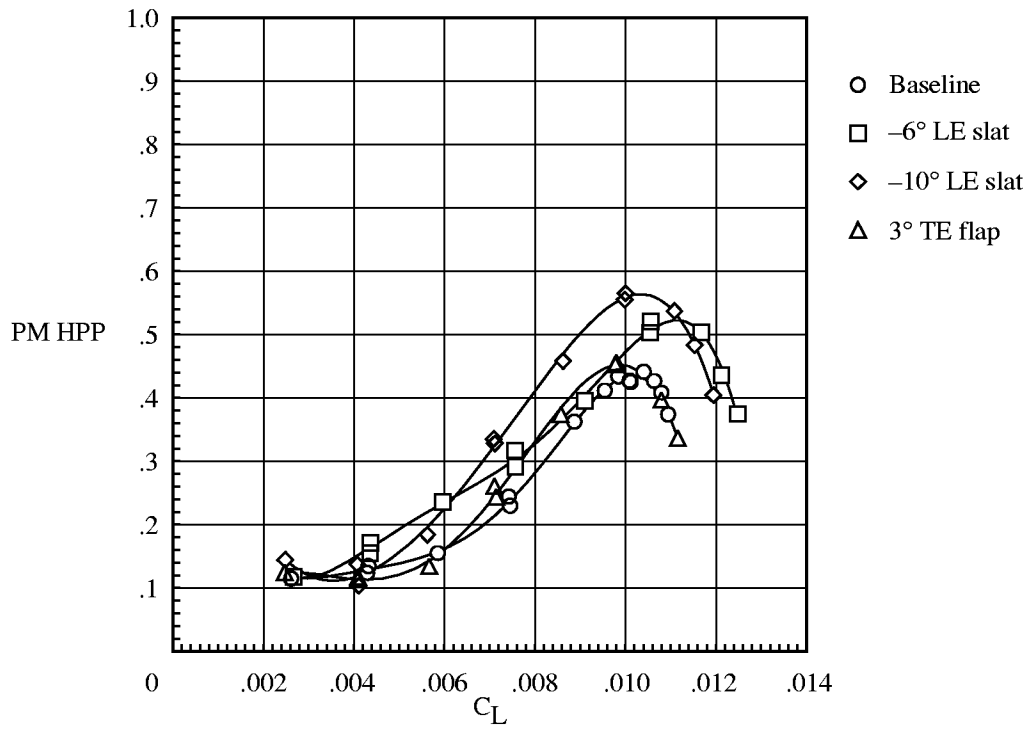


(c) $\mu = 0.20$; $\alpha_s = 0^\circ$.

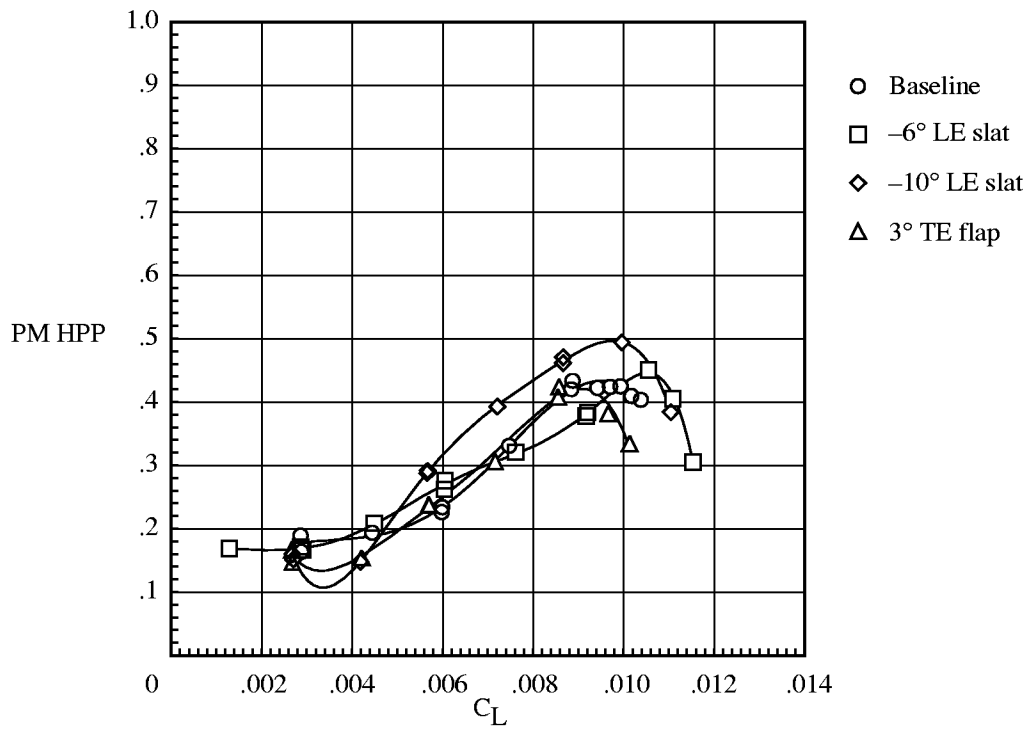


(d) $\mu = 0.20$; $\alpha_s = -4^\circ$.

Figure 18. Continued.

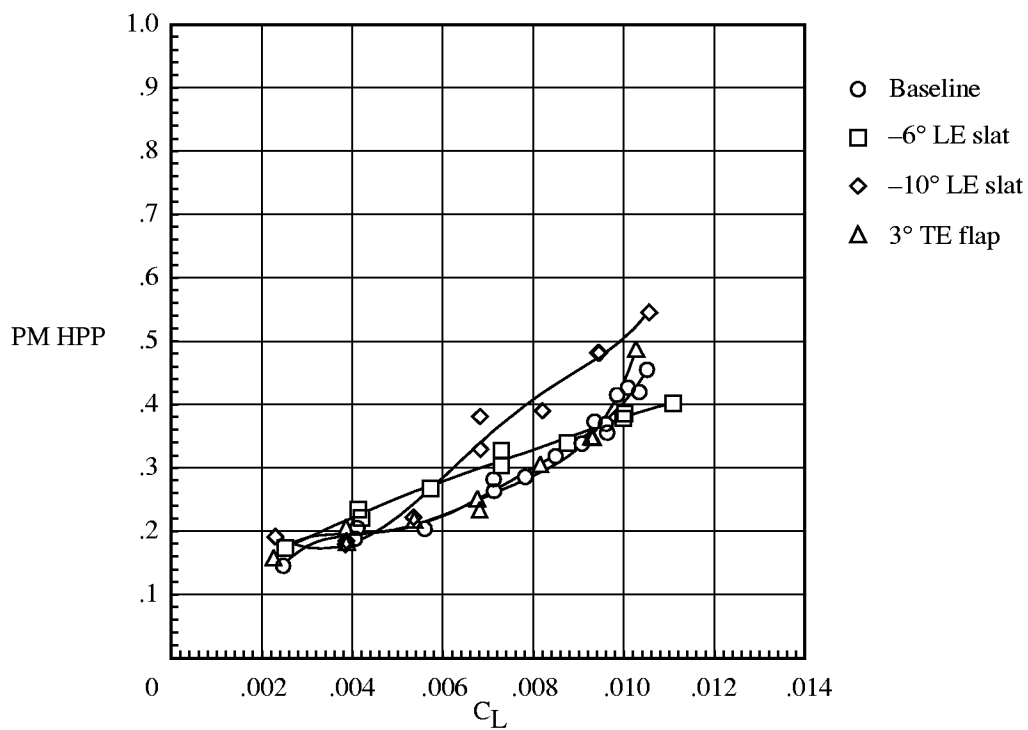


(e) $\mu = 0.25$; $\alpha_s = 0^\circ$.

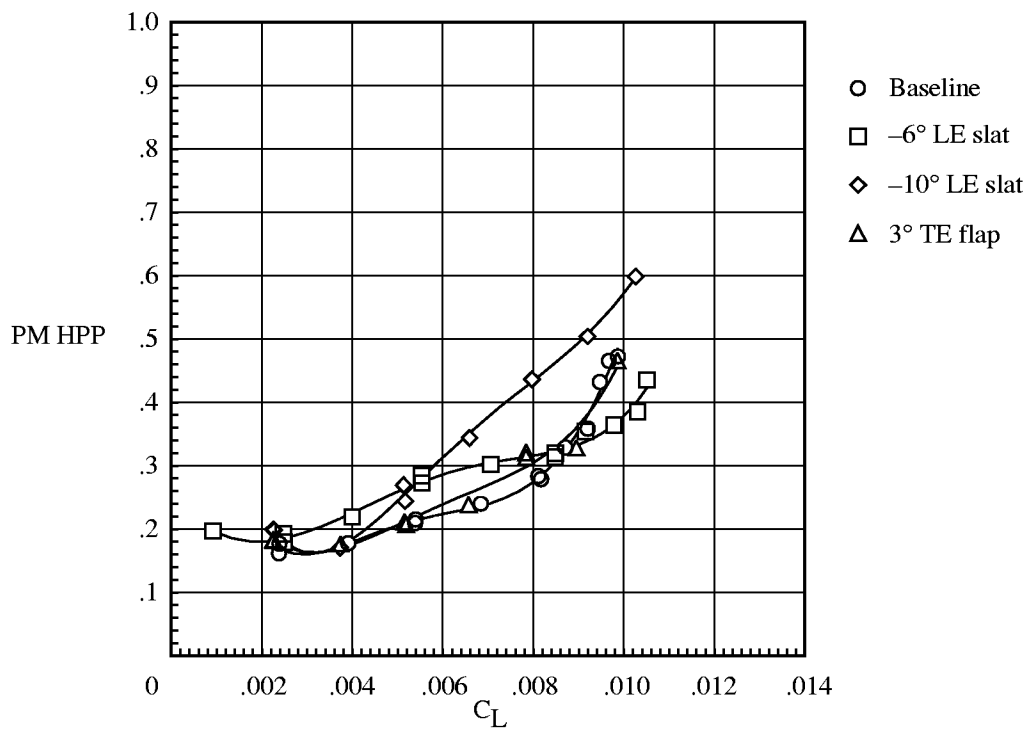


(f) $\mu = 0.25$; $\alpha_s = -4^\circ$.

Figure 18. Continued.

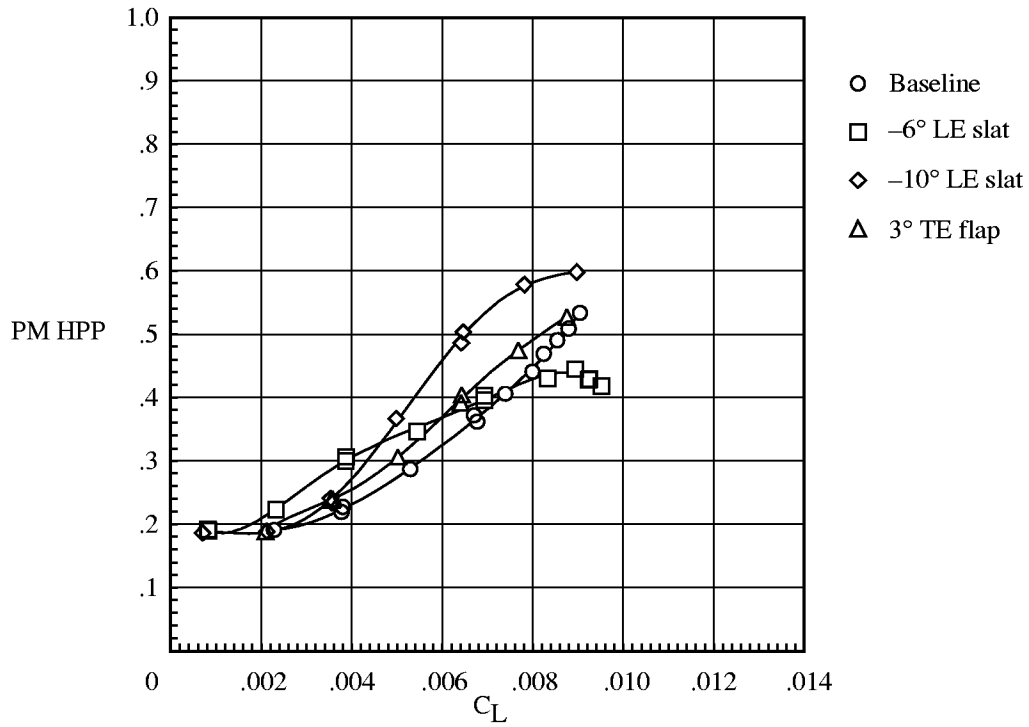


(g) $\mu = 0.30$; $\alpha_s = 0^\circ$.

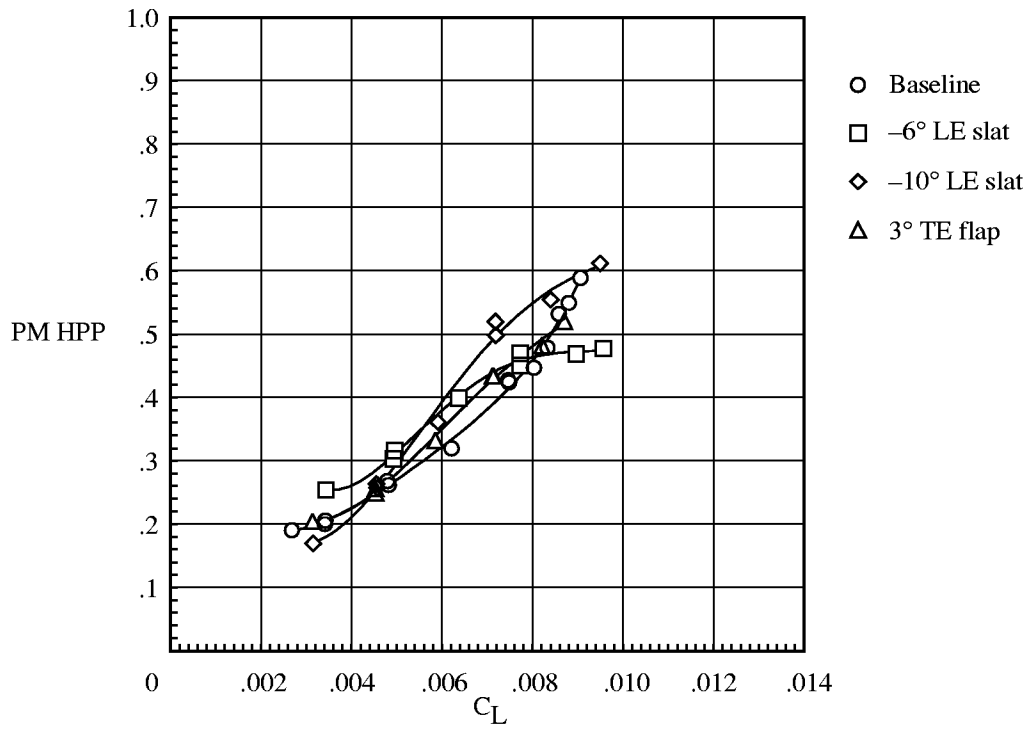


(h) $\mu = 0.30$; $\alpha_s = -4^\circ$.

Figure 18. Continued.

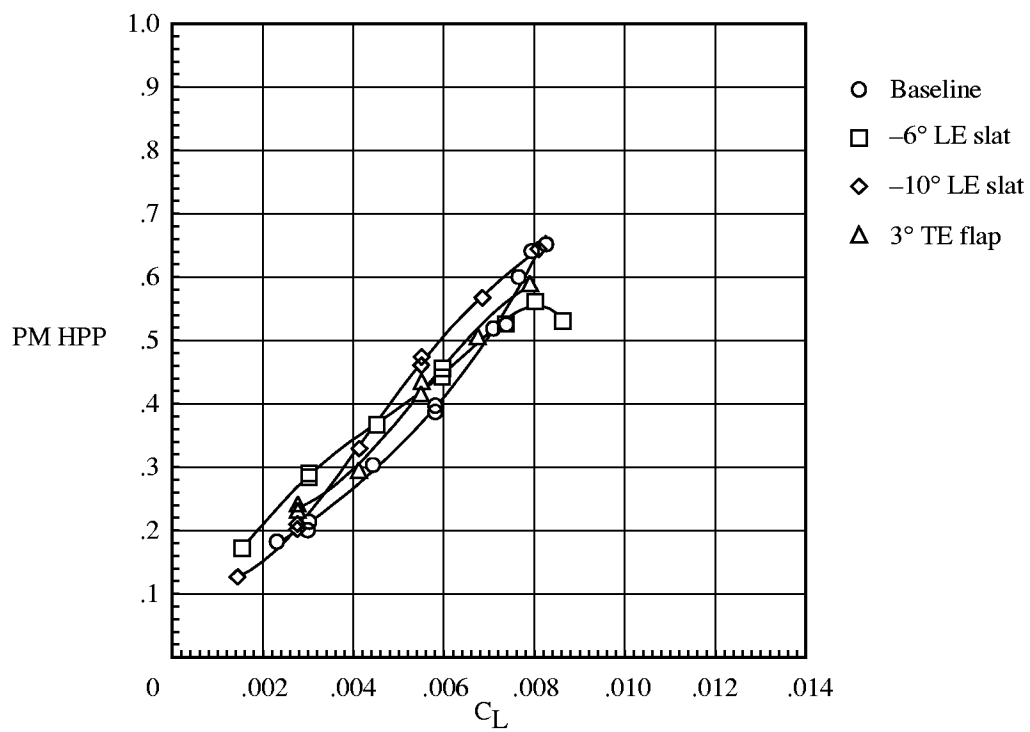


(i) $\mu = 0.30$; $\alpha_s = -8^\circ$.



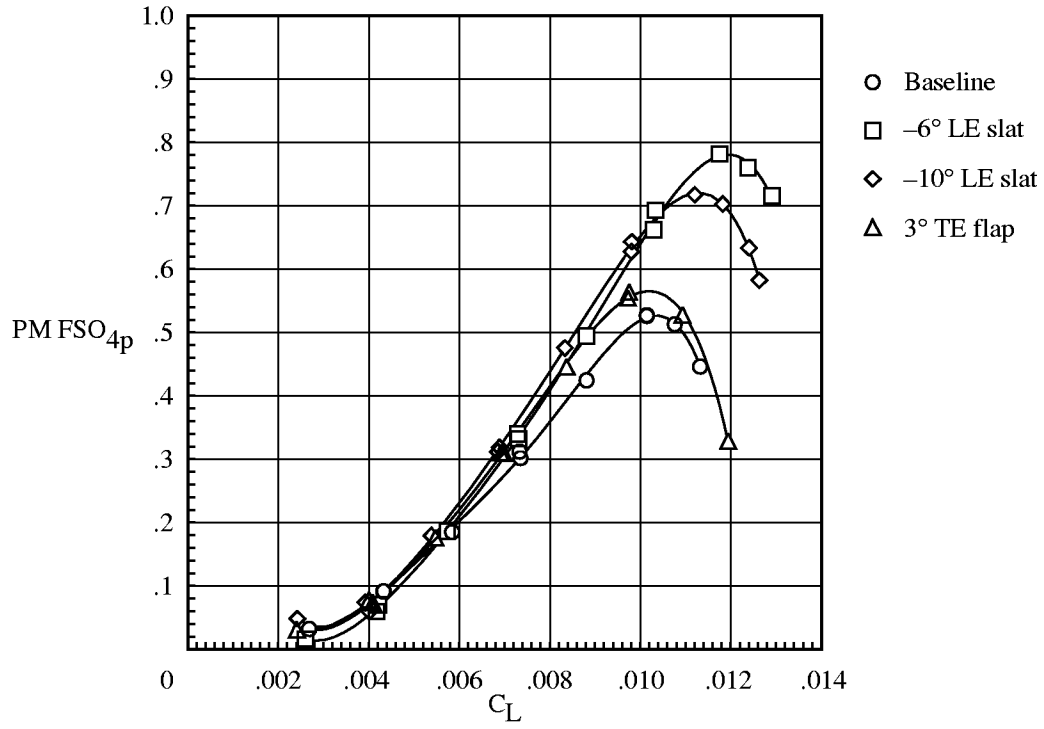
(j) $\mu = 0.35$; $\alpha_s = -4^\circ$.

Figure 18. Continued.

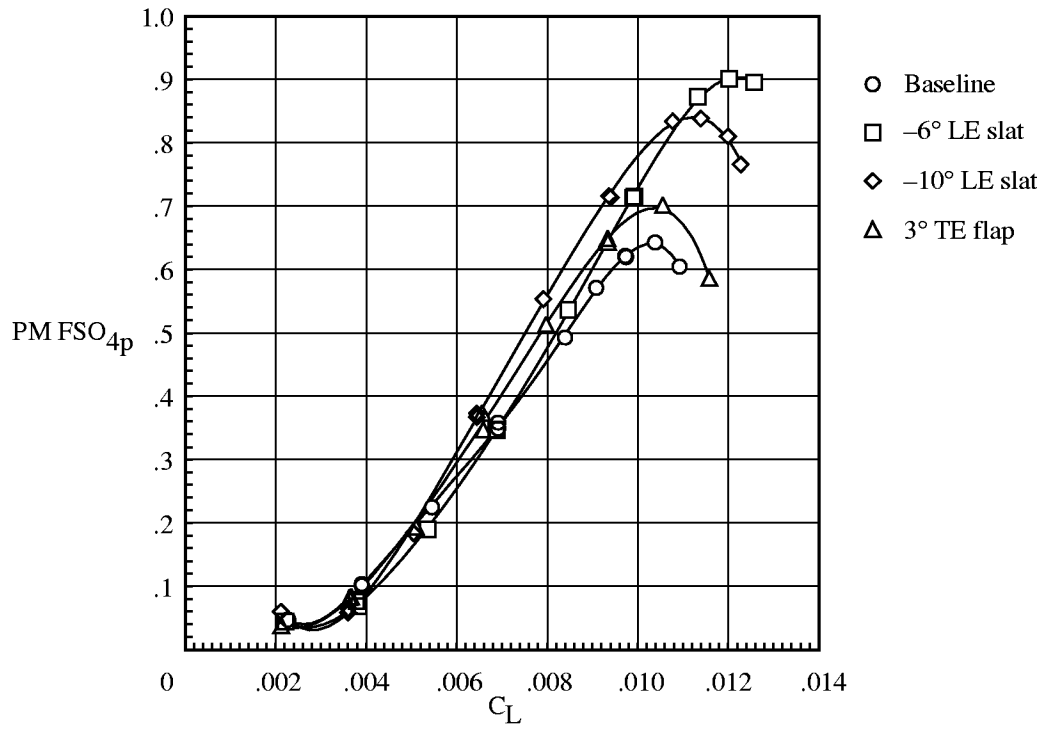


(k) $\mu = 0.35$; $\alpha_s = -8^\circ$.

Figure 18. Concluded.

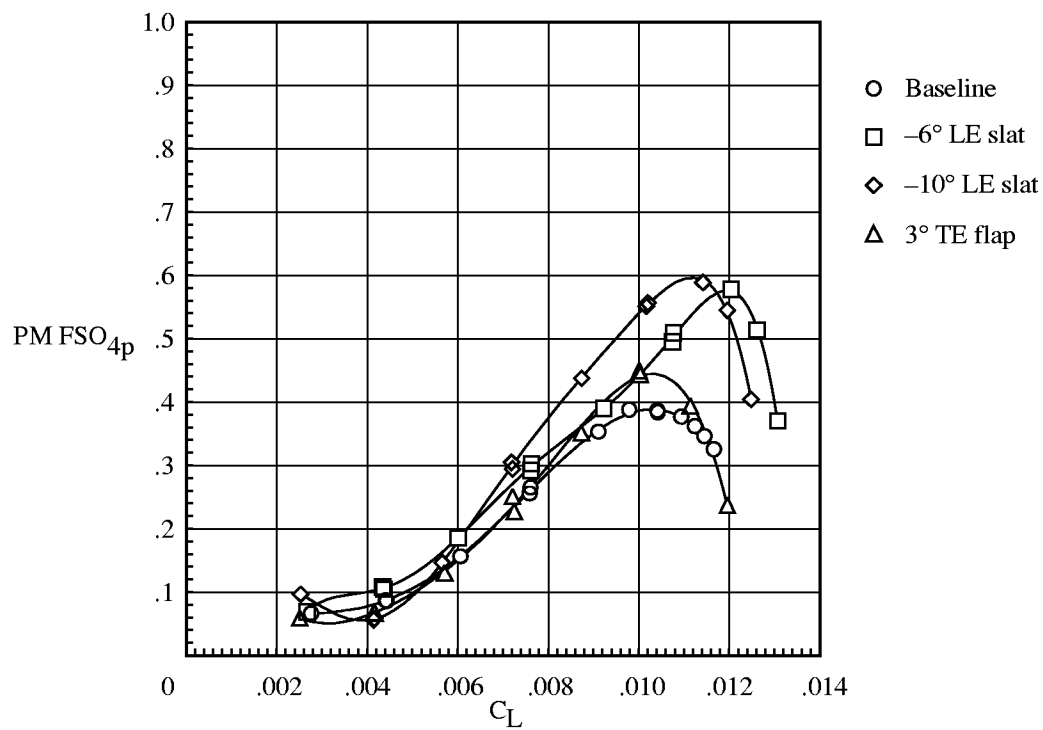


(a) $\mu = 0.15$; $\alpha_s = 0^\circ$.

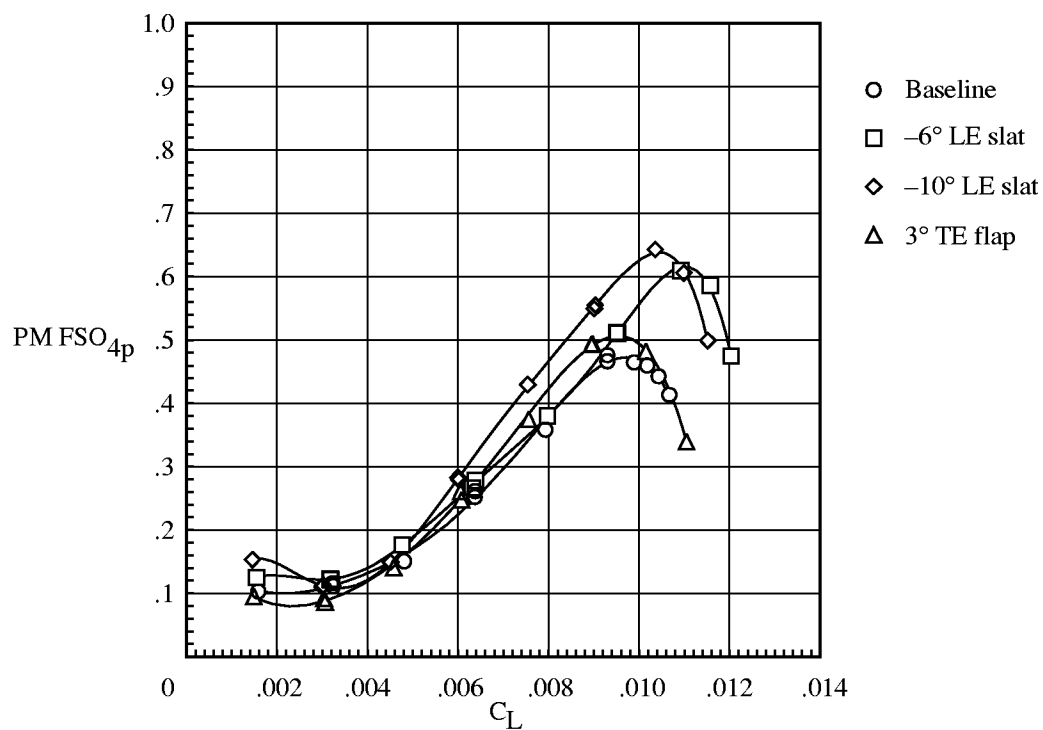


(b) $\mu = 0.15$; $\alpha_s = -2^\circ$.

Figure 19. Variation of 4P fixed-system pitching moments with rotor lift coefficient; $M_T = 0.627$.

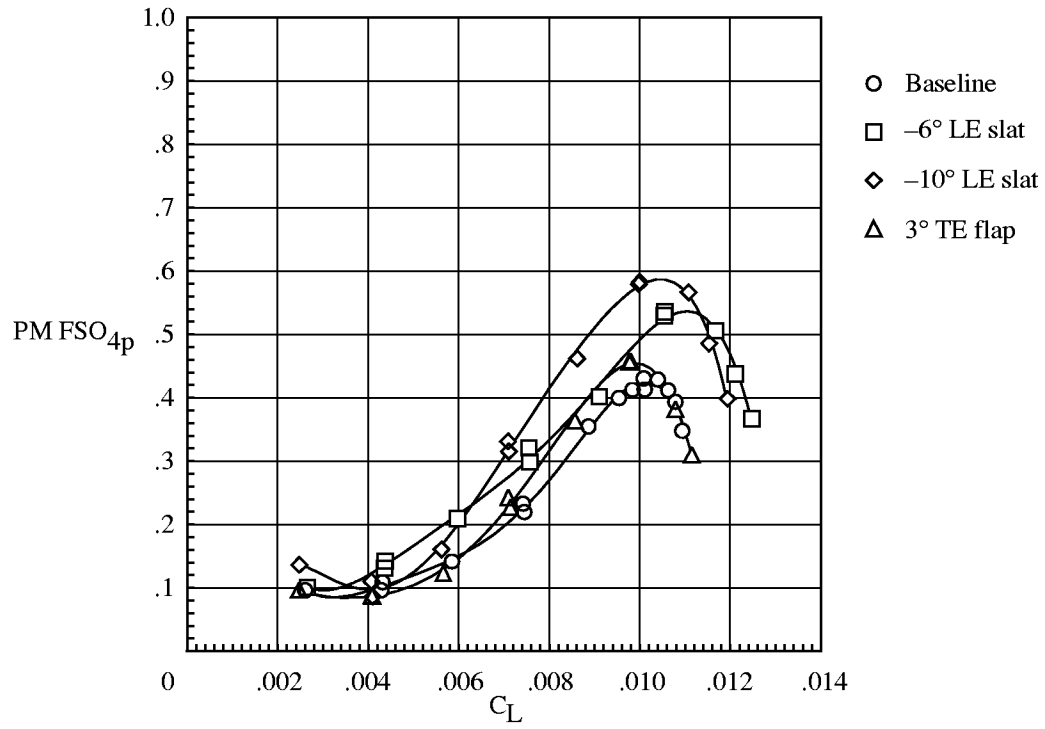


(c) $\mu = 0.20$; $\alpha_s = 0^\circ$.

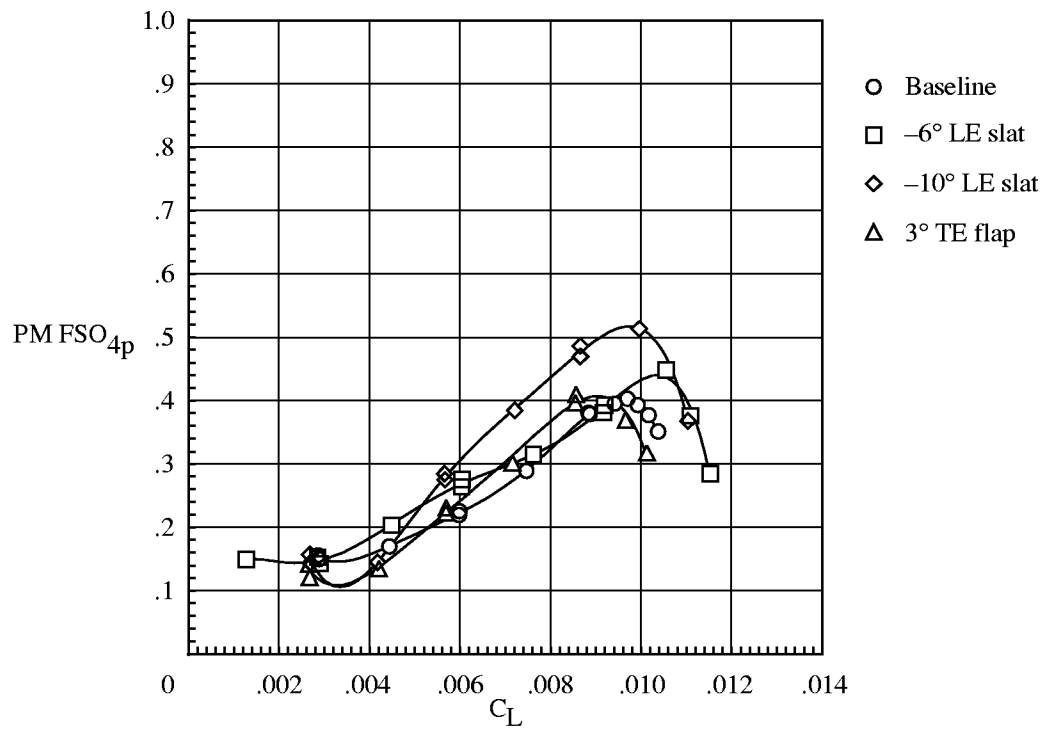


(d) $\mu = 0.20$; $\alpha_s = -4^\circ$.

Figure 19. Continued.



(e) $\mu = 0.25$; $\alpha_s = 0^\circ$.



(f) $\mu = 0.25$; $\alpha_s = -4^\circ$.

Figure 19. Continued.

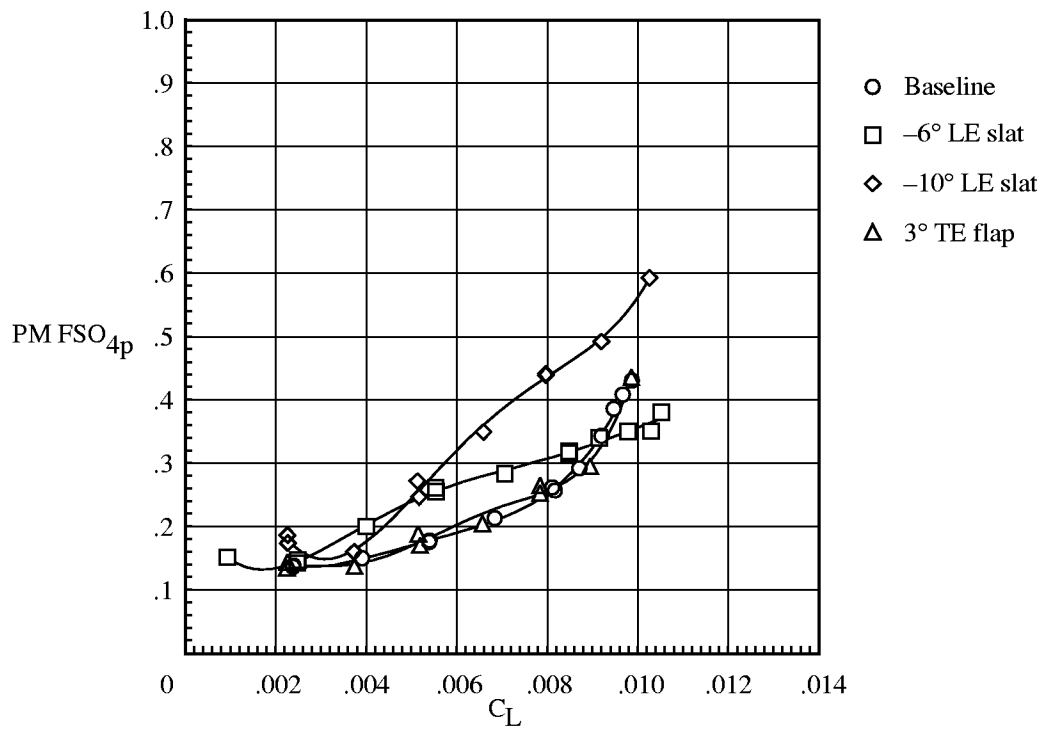
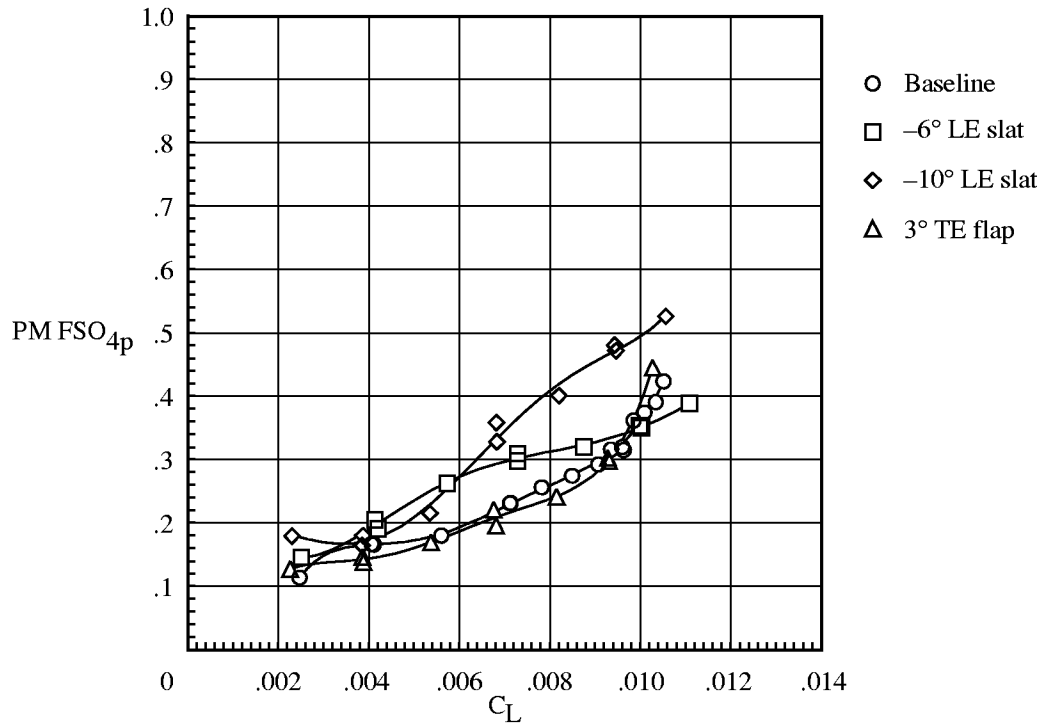
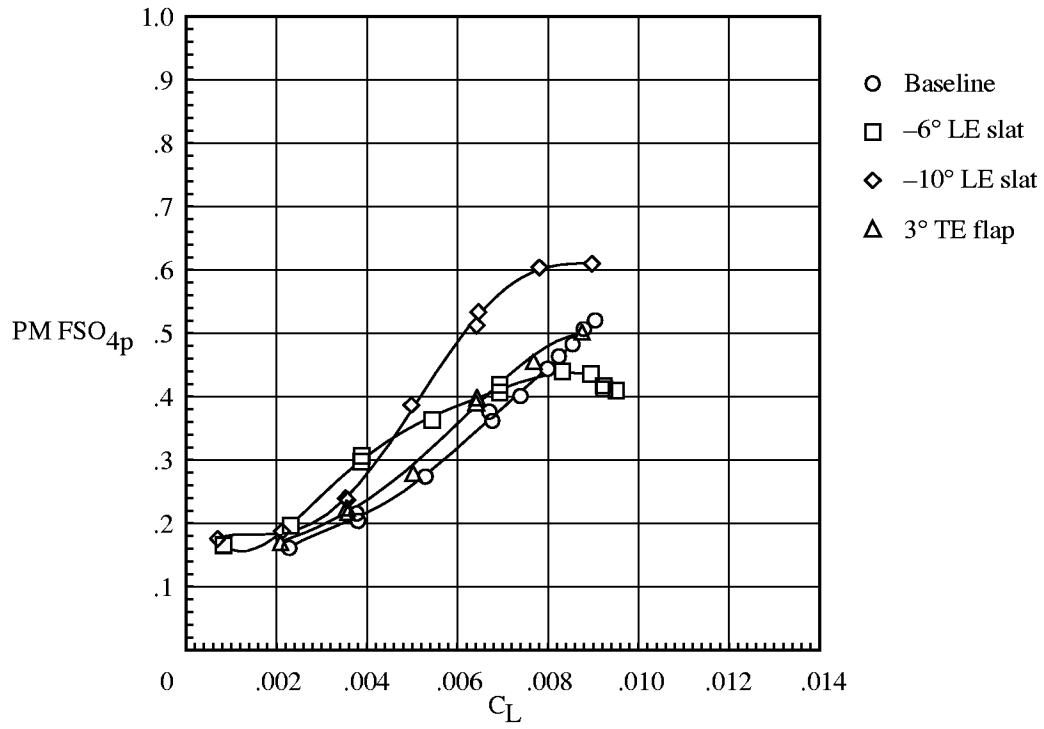
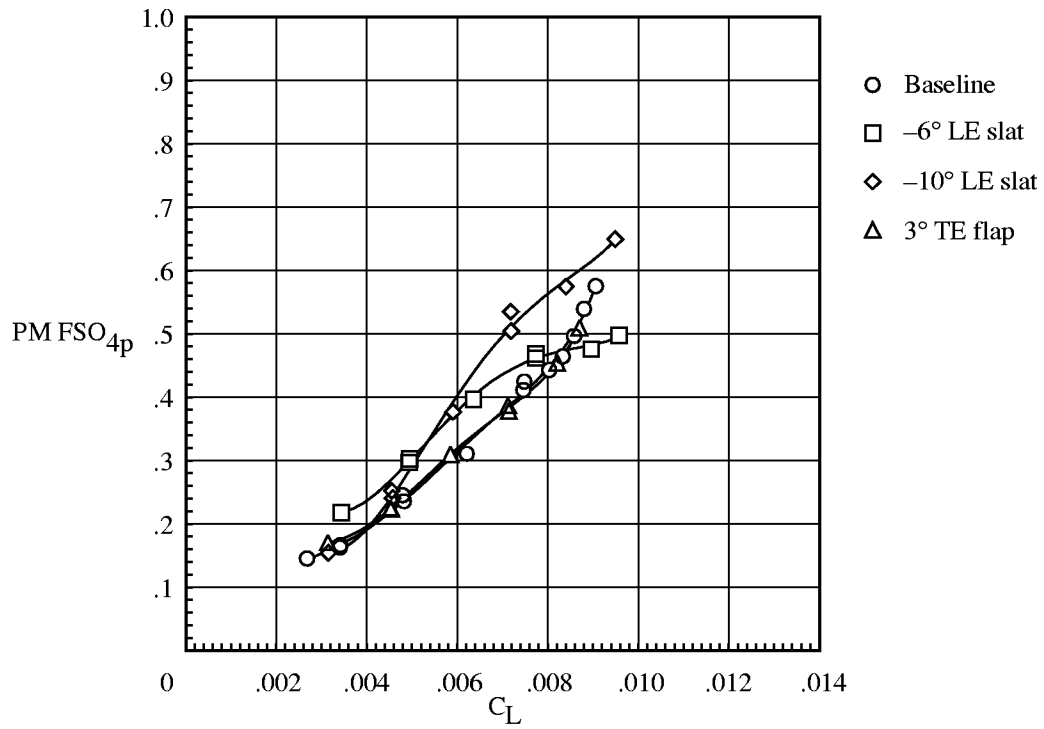


Figure 19. Continued.

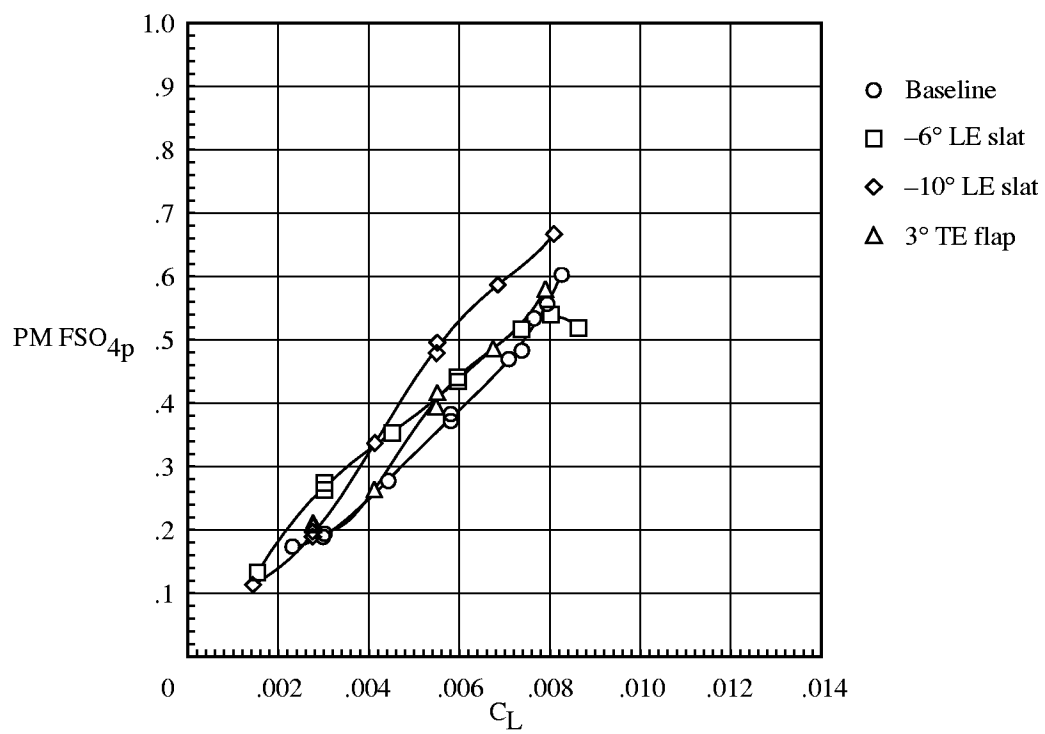


(i) $\mu = 0.30$; $\alpha_s = -8^\circ$.



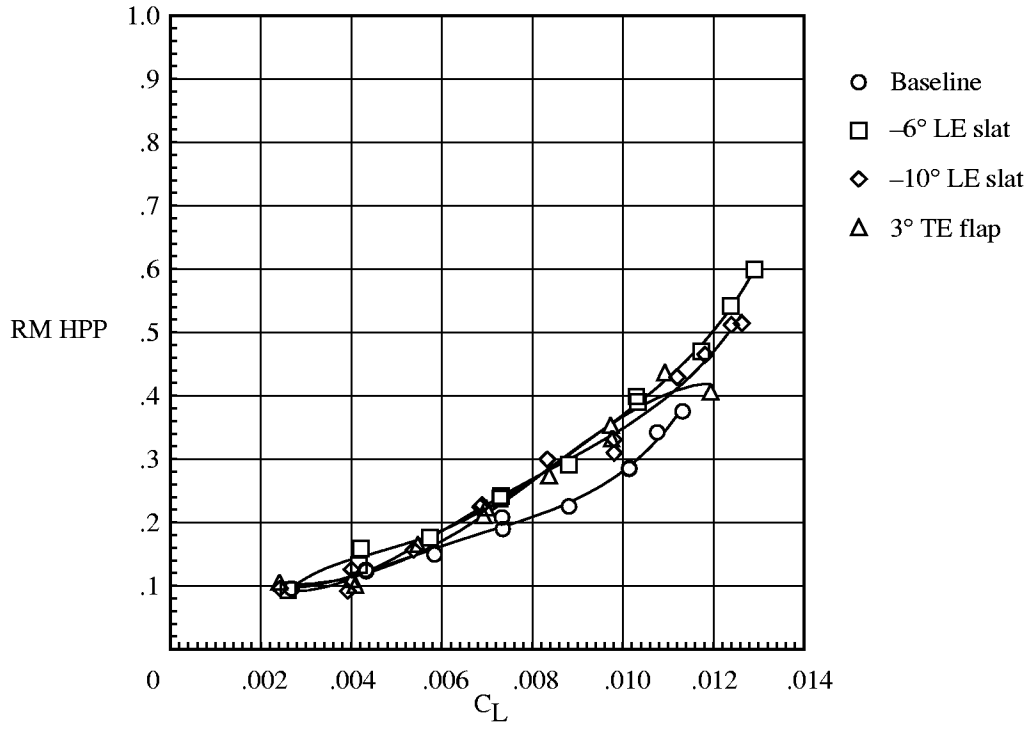
(j) $\mu = 0.35$; $\alpha_s = -4^\circ$.

Figure 19. Continued.

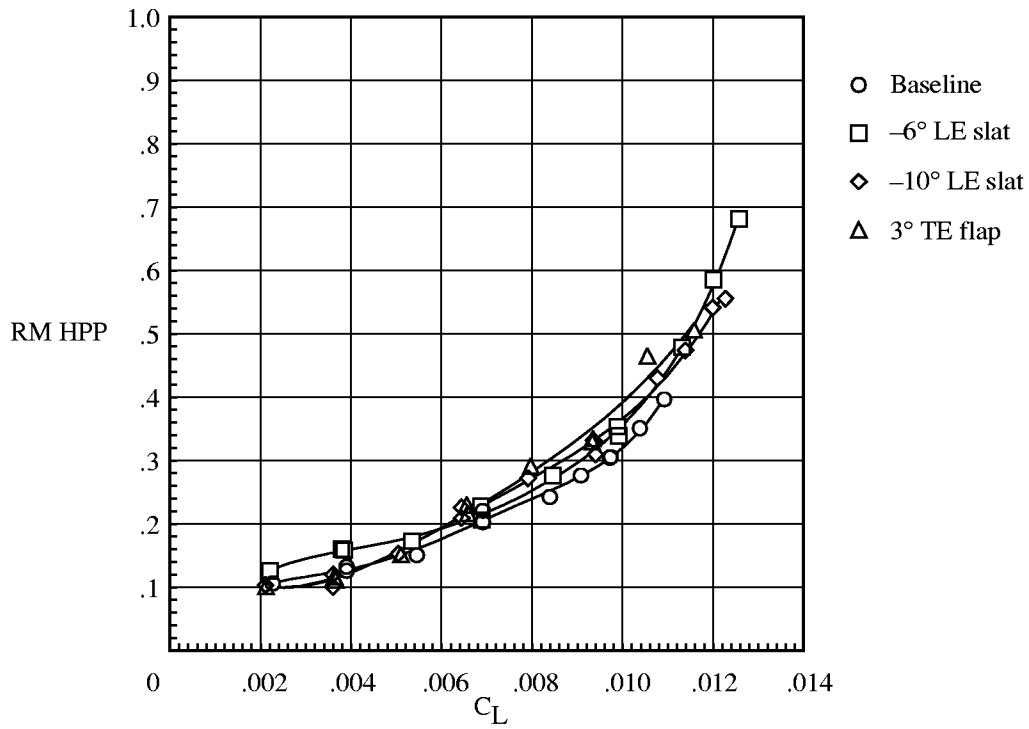


(k) $\mu = 0.35$; $\alpha_s = -8^\circ$.

Figure 19. Concluded.

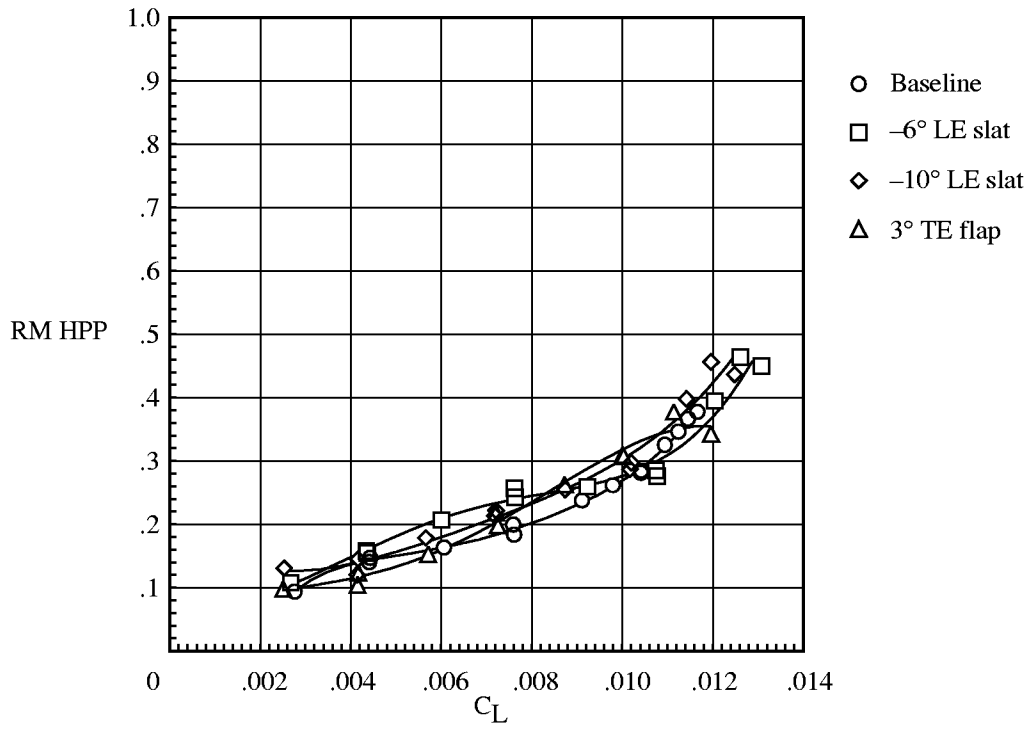


(a) $\mu = 0.15$; $\alpha_s = 0^\circ$.

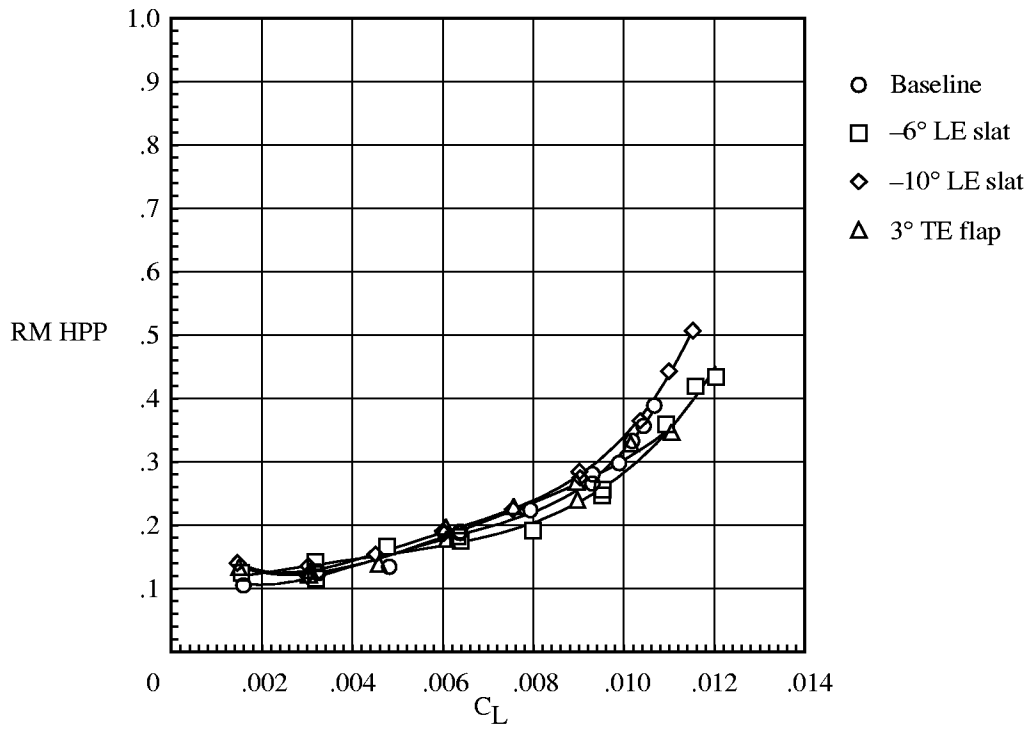


(b) $\mu = 0.15$; $\alpha_s = -2^\circ$.

Figure 20. Variation of fixed-system rolling-moment oscillatory loads with rotor lift coefficient; $M_T = 0.627$.

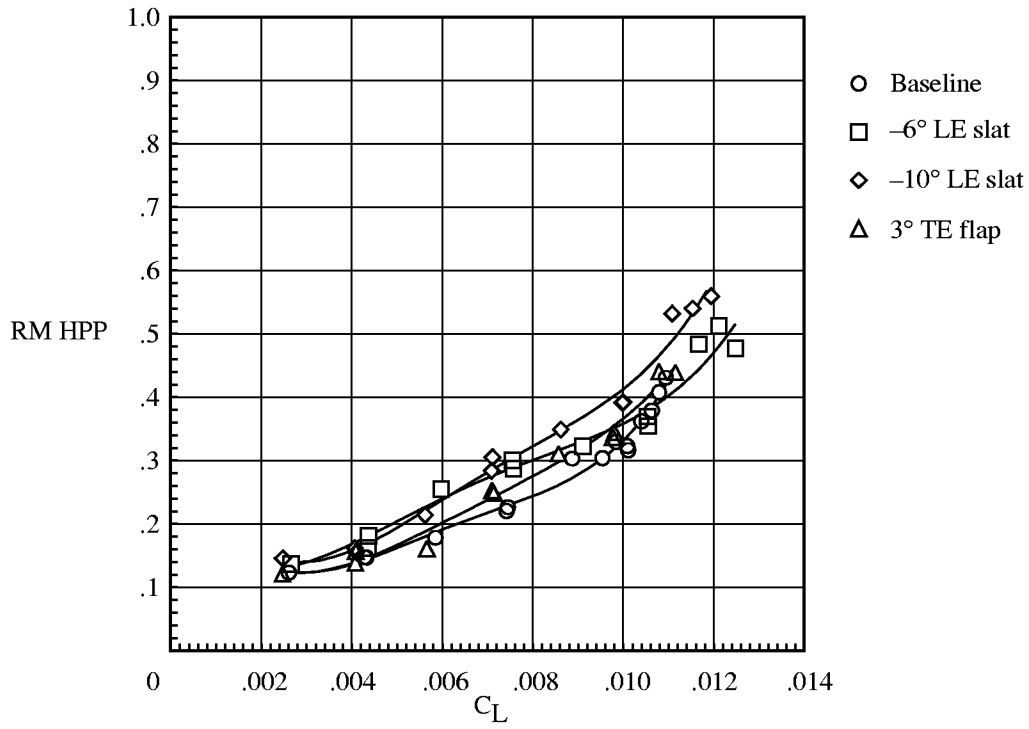


(c) $\mu = 0.20$; $\alpha_s = 0^\circ$.

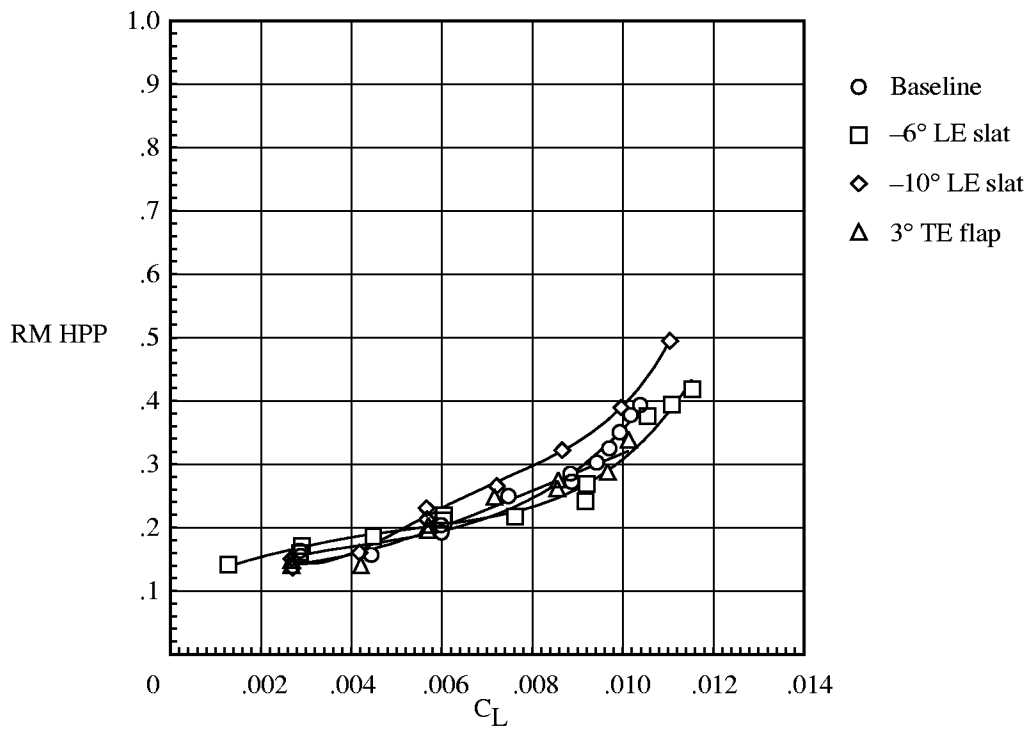


(d) $\mu = 0.20$; $\alpha_s = -4^\circ$.

Figure 20. Continued.

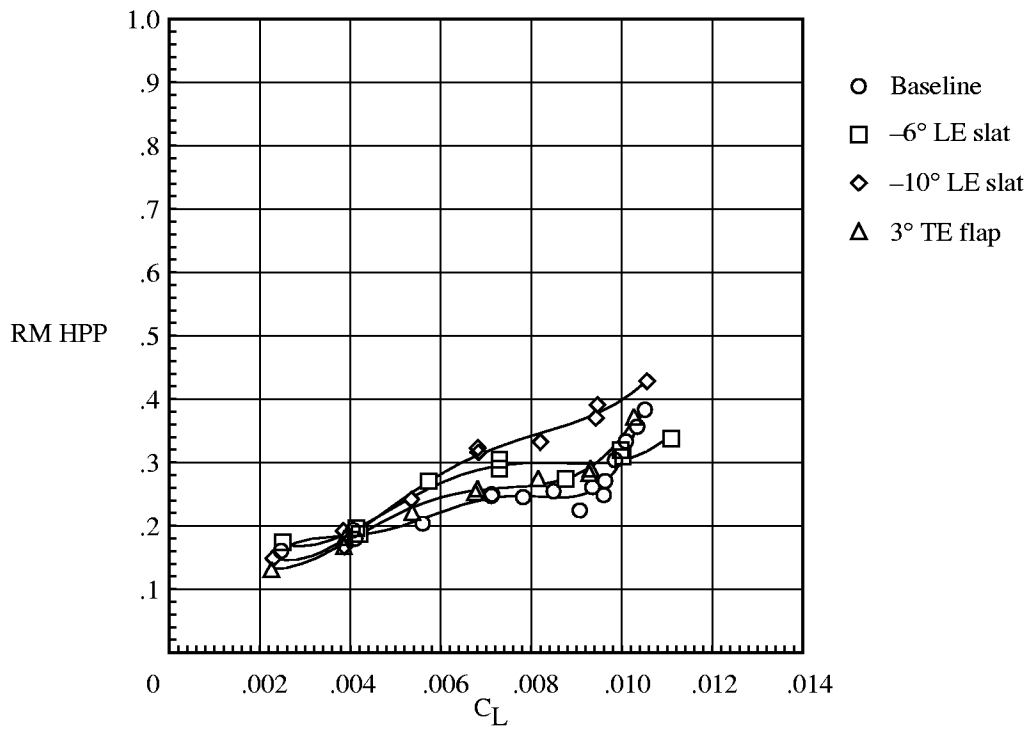


(e) $\mu = 0.25$; $\alpha_s = 0^\circ$.

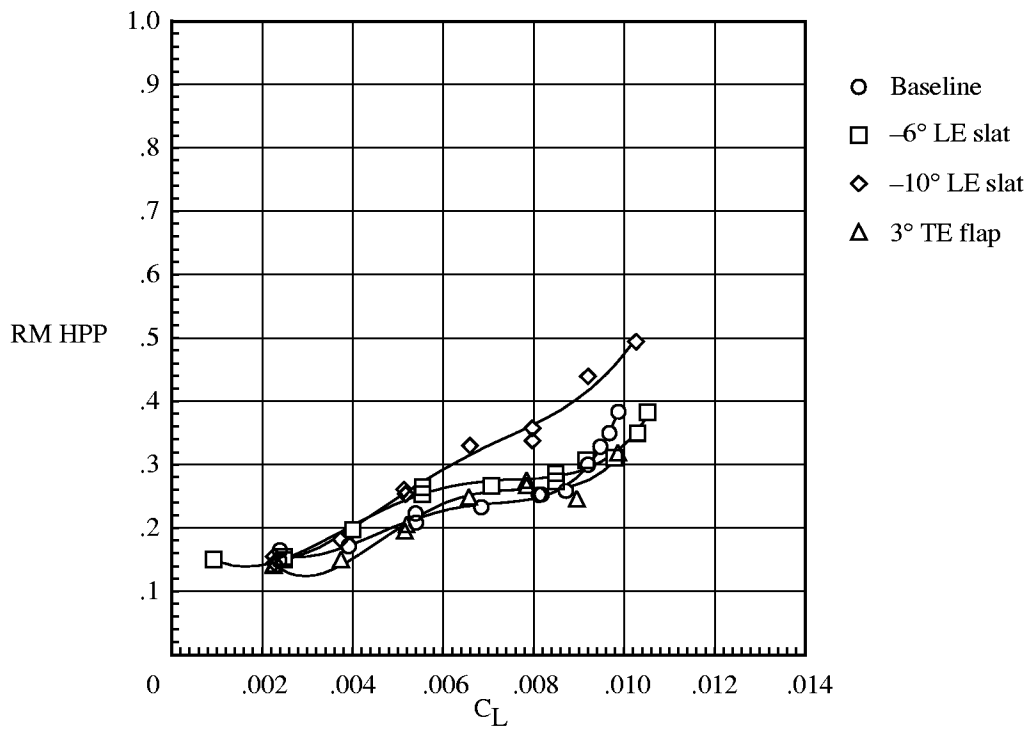


(f) $\mu = 0.25$; $\alpha_s = -4^\circ$.

Figure 20. Continued.

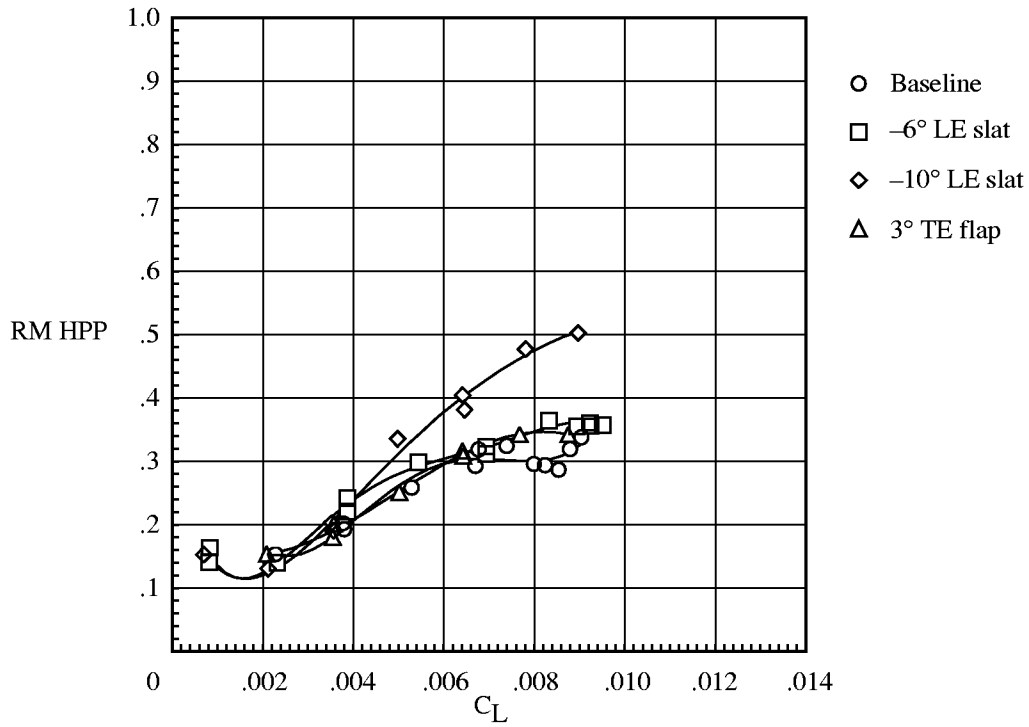


(g) $\mu = 0.30$; $\alpha_s = 0^\circ$.

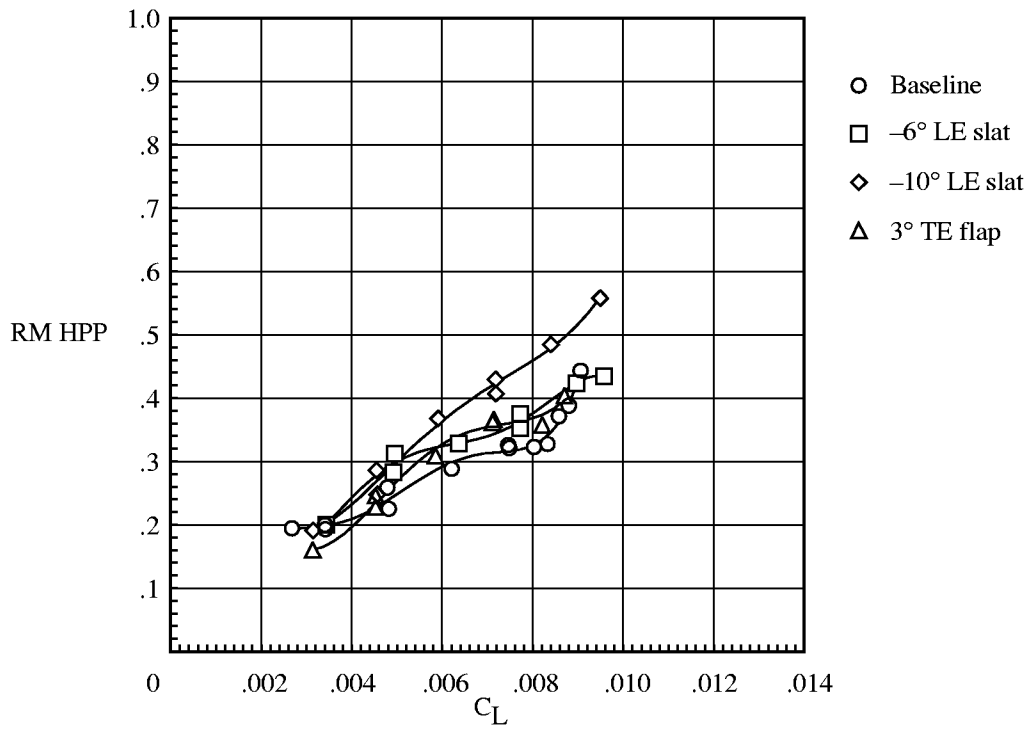


(h) $\mu = 0.30$; $\alpha_s = -4^\circ$.

Figure 20. Continued.

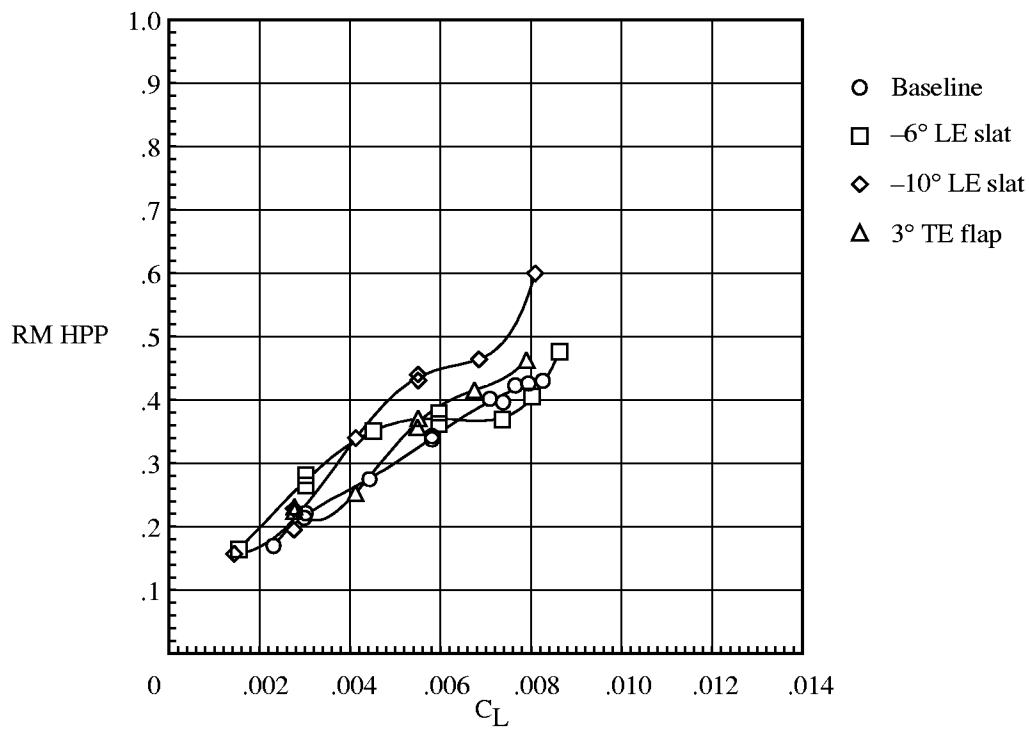


(i) $\mu = 0.30$; $\alpha_s = -8^\circ$.



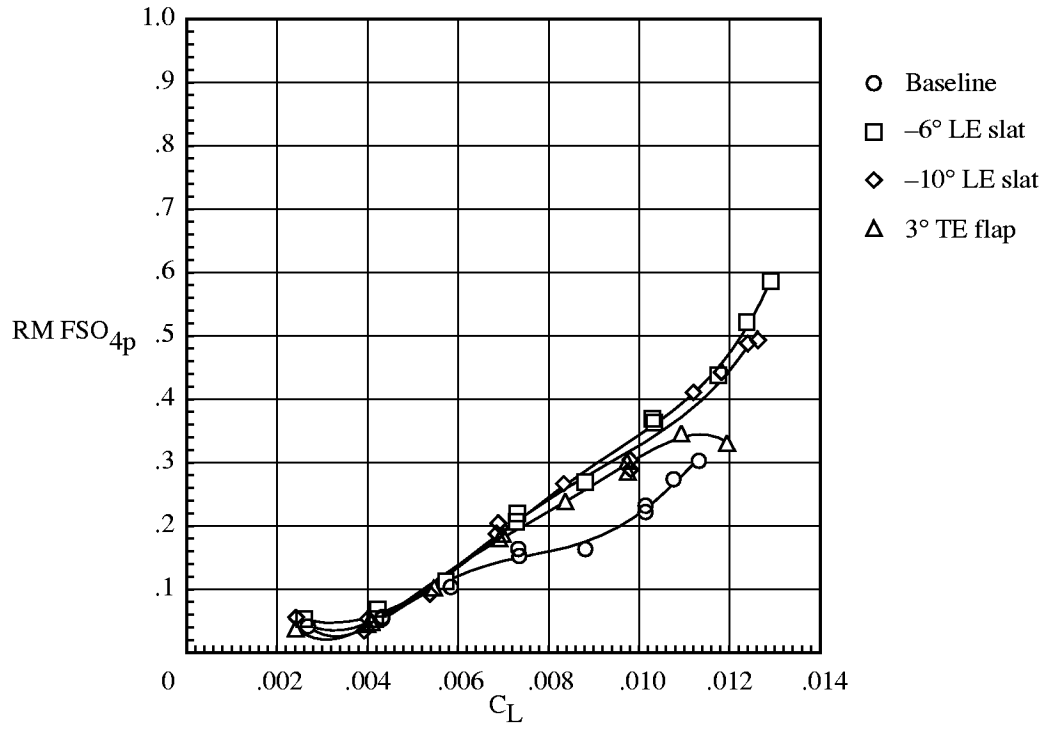
(j) $\mu = 0.35$; $\alpha_s = -4^\circ$.

Figure 20. Continued.

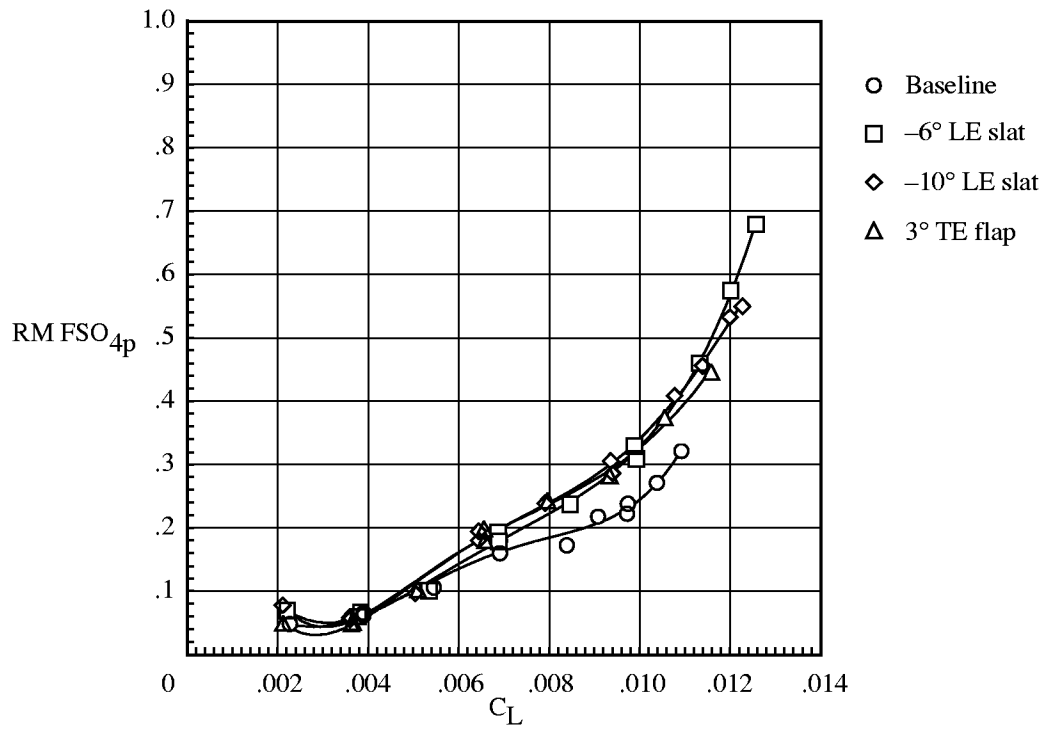


(k) $\mu = 0.35$; $\alpha_s = -8^\circ$.

Figure 20. Concluded.

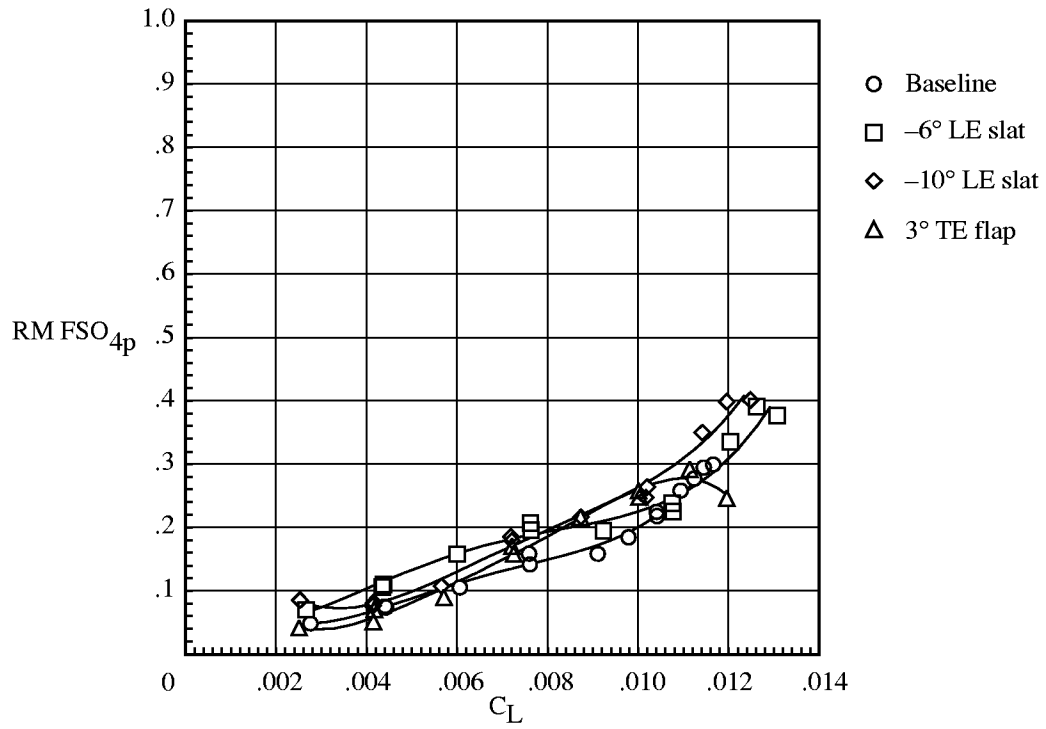


(a) $\mu = 0.15$; $\alpha_s = 0^\circ$.

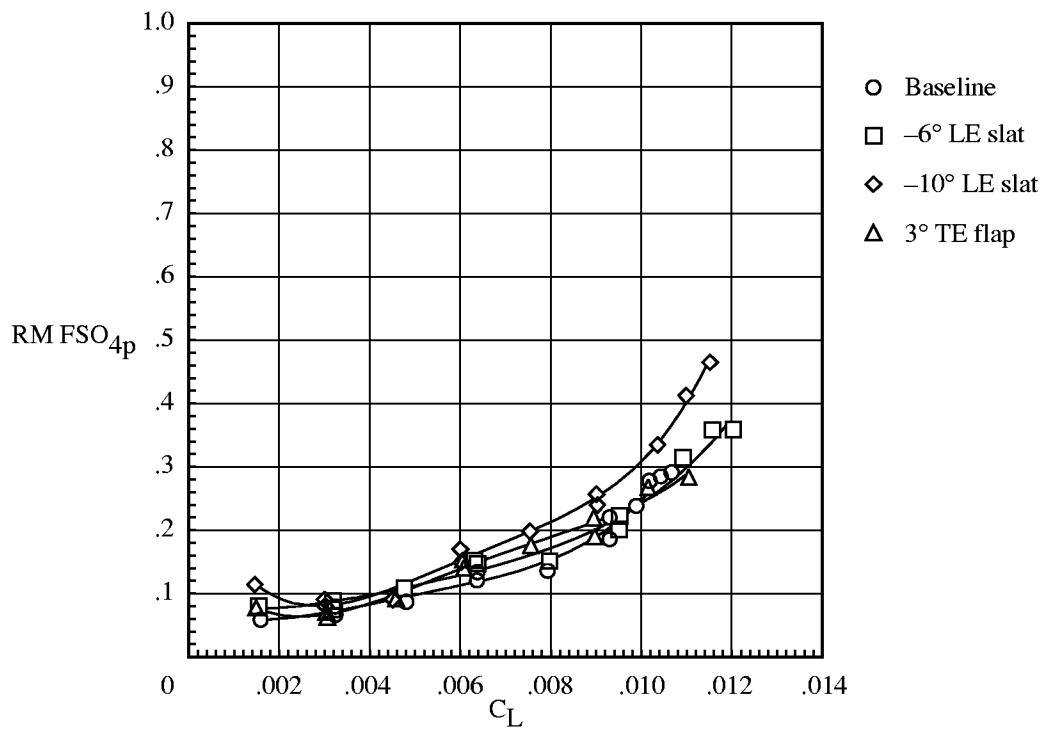


(b) $\mu = 0.15$; $\alpha_s = -2^\circ$.

Figure 21. Variation of 4P fixed-system rolling moments with rotor lift coefficient; $M_T = 0.627$.

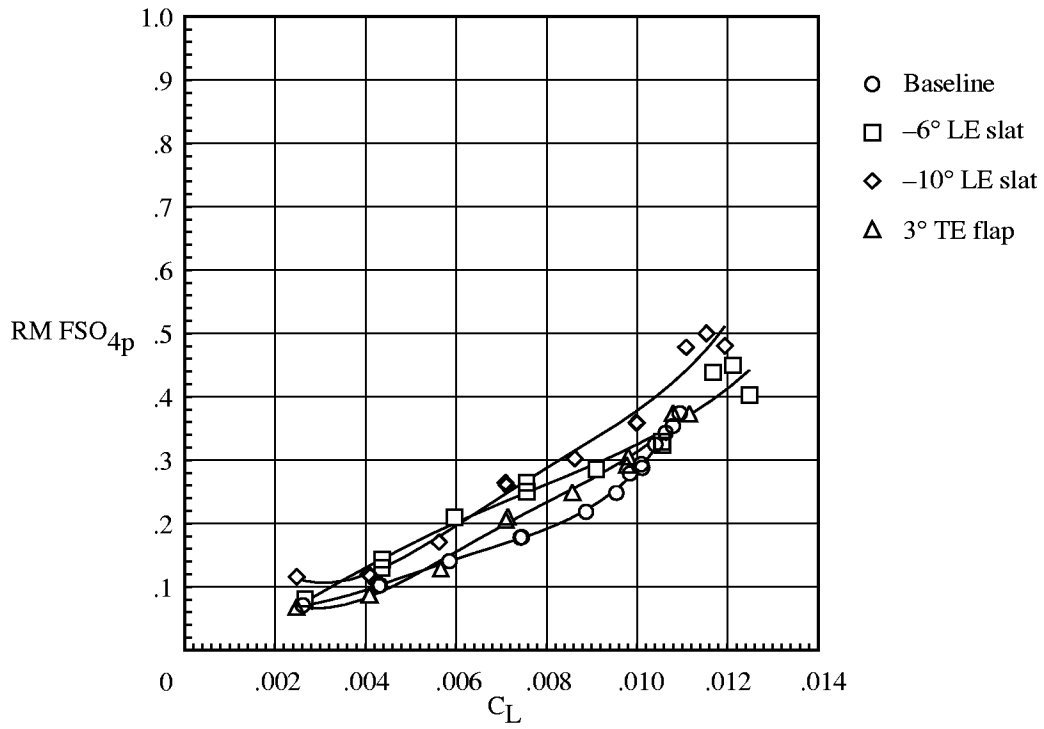


(c) $\mu = 0.20$; $\alpha_s = 0^\circ$.

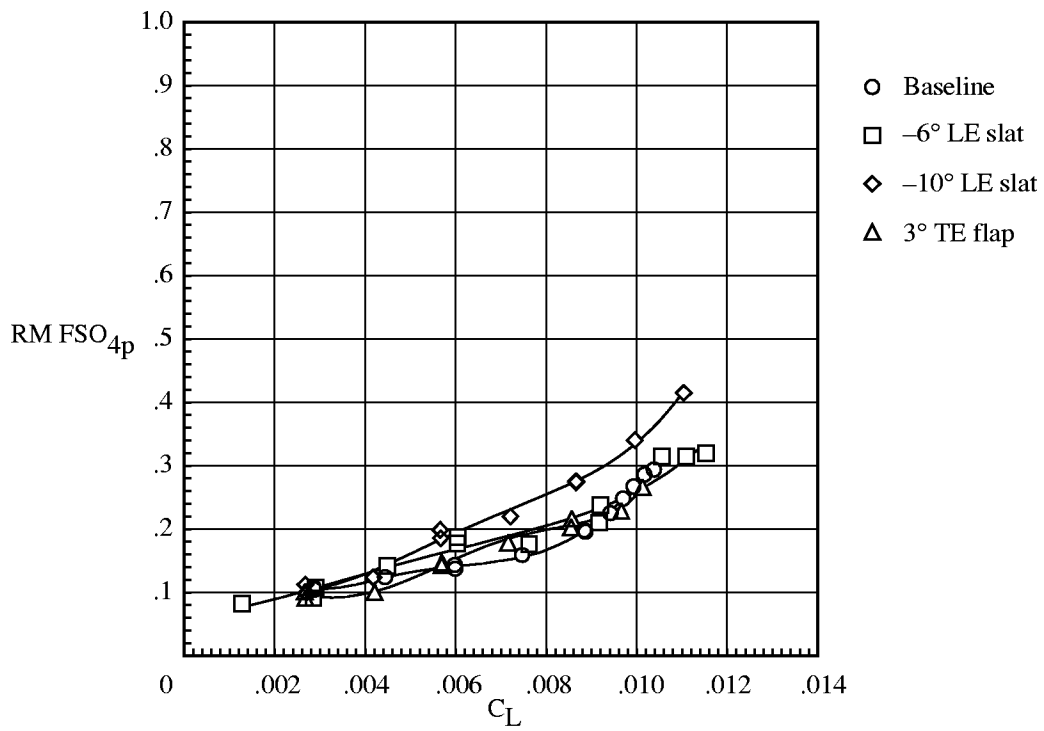


(d) $\mu = 0.20$; $\alpha_s = -4^\circ$.

Figure 21. Continued.

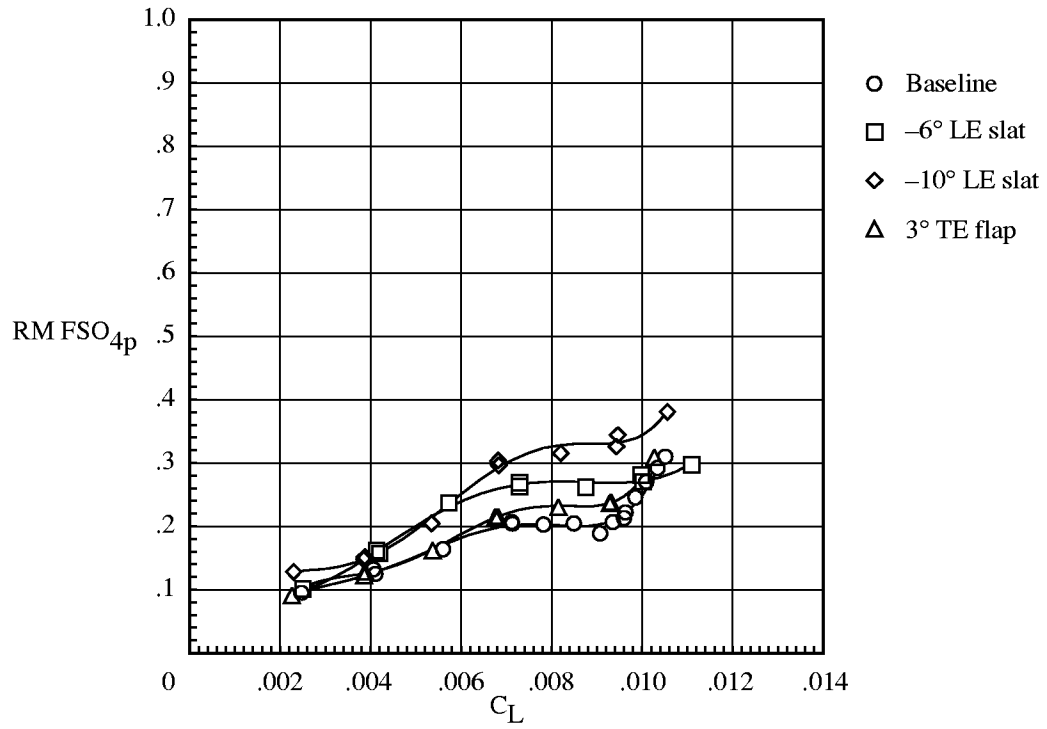


(e) $\mu = 0.25$; $\alpha_s = 0^\circ$.

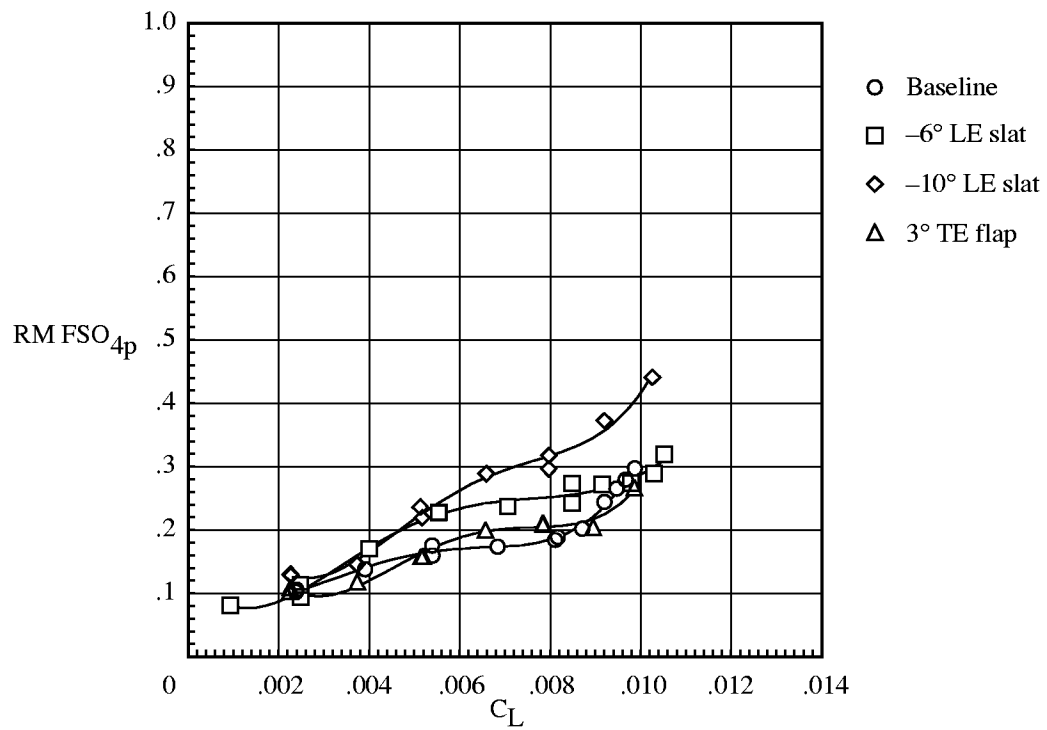


(f) $\mu = 0.25$; $\alpha_s = -4^\circ$.

Figure 21. Continued.

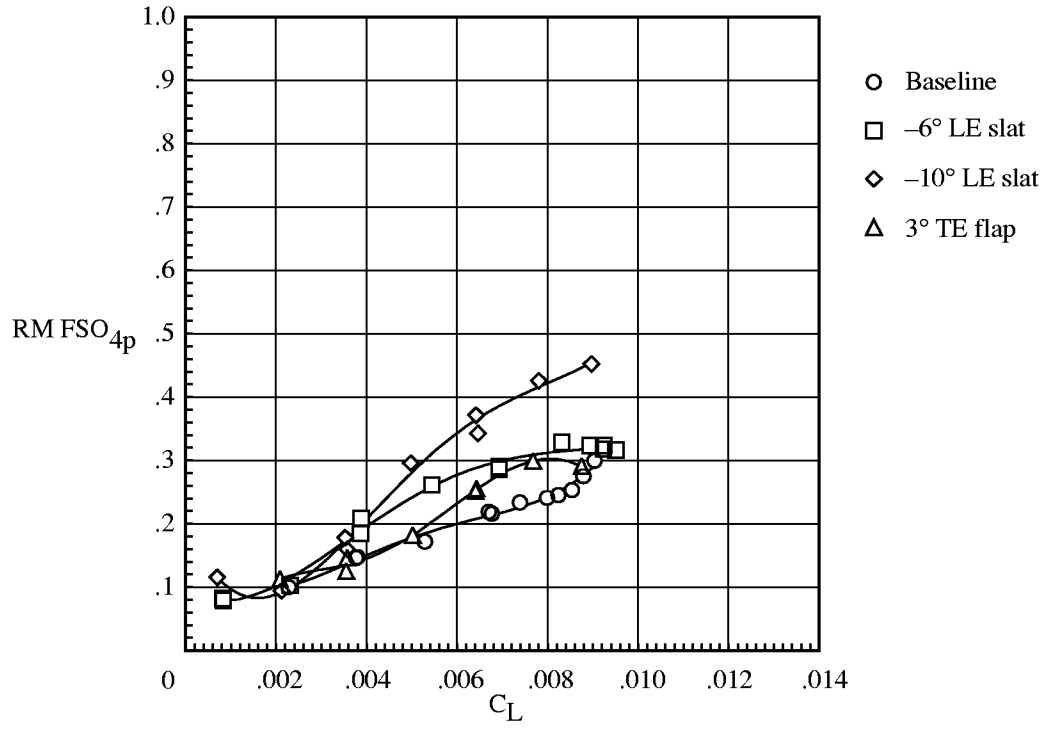


(g) $\mu = 0.30$; $\alpha_s = 0^\circ$.

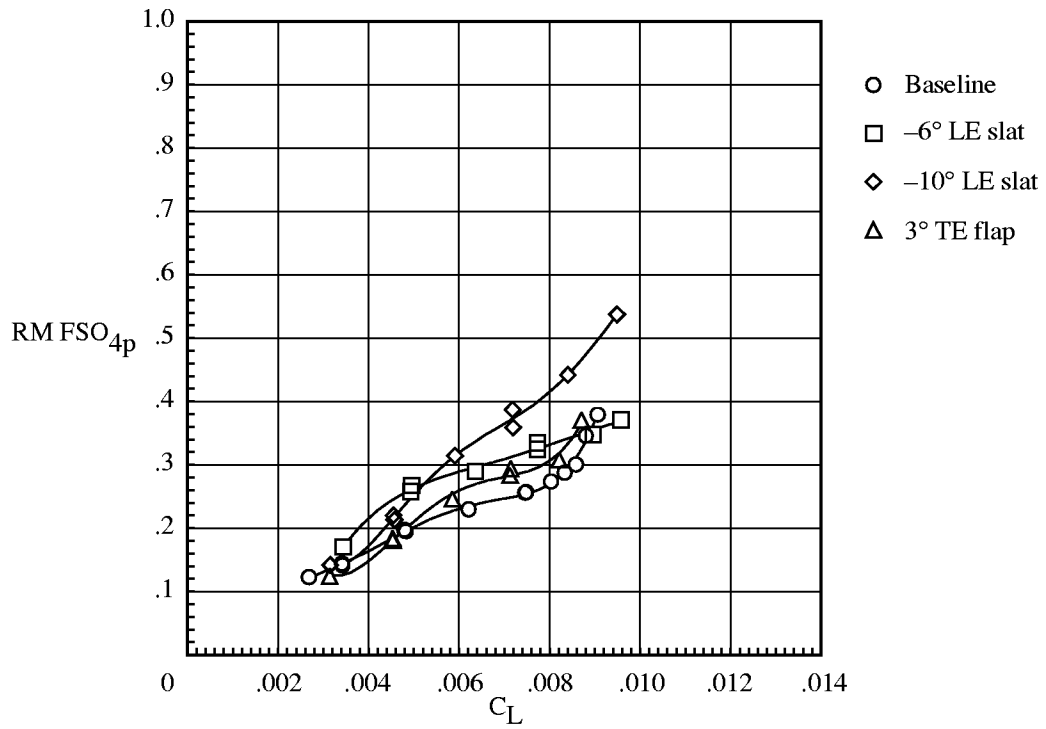


(h) $\mu = 0.30$; $\alpha_s = -4^\circ$.

Figure 21. Continued.

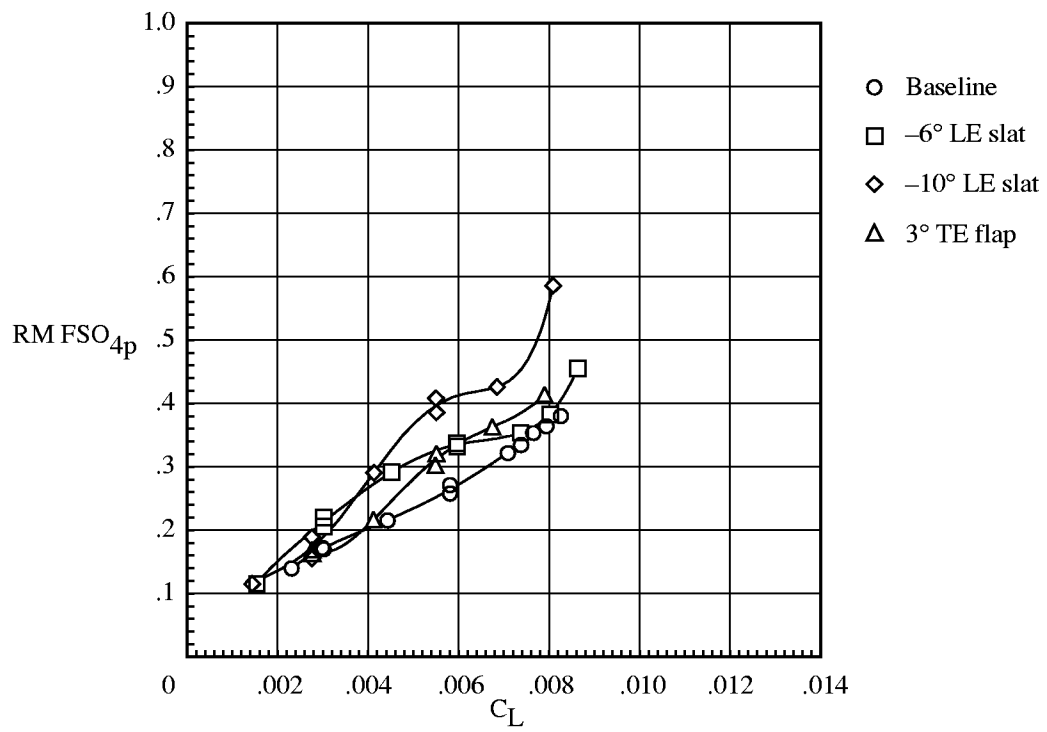


(i) $\mu = 0.30$; $\alpha_s = -8^\circ$.



(j) $\mu = 0.35$; $\alpha_s = -4^\circ$.

Figure 21. Continued.



(k) $\mu = 0.35$; $\alpha_s = -8^\circ$.

Figure 21. Concluded.

Appendix

The basic forward flight performance data of the four rotor configurations are presented in figures A1 to A32, and the C_D versus C_Q cross plots made from those basic data are presented in figures A33 to A40, as shown in tables A1 and A2, respectively. Table A3 contains the drag coefficients that correspond to full-scale values of f_D .

Table A1. Basic Performance Data for Blade Configurations

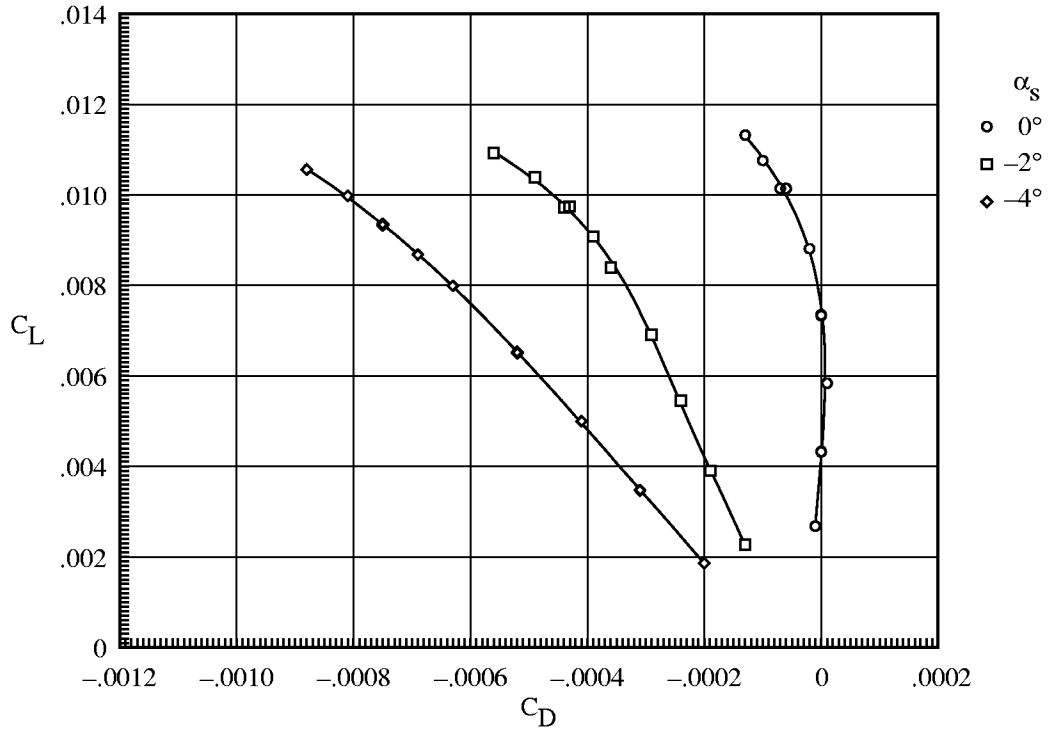
Parameter	μ	α_s , deg (typical)	Figures for rotor configuration—			
			Baseline	−6° LE slat	−10° LE slat	3° TE flap
C_L vs C_D and C_L vs C_Q	0.15	0.0	A1	A9	A17	A25
		−2.0				
		−4.0				
	0.20	0.0	A2	A10	A18	A26
		−4.0				
		−8.0				
	0.25	0.0	A3	A11	A19	A27
		−4.0				
		−8.0				
	0.30	0.0	A4	A12	A20	A28
		−4.0				
		−8.0				
	0.35	−4.0	A5	A13	A21	A29
		−8.0				
		−12.0				
		−15.0				
	0.40	−4.0	A6	A14	A22	A30
		−8.0				
		−12.0				
		−15.0				
	0.42 or 0.43	−4.0	A7	A15	A23	A31
		−8.0				
		−12.0				
	0.45	−15.0	A8	A16	A24	A32
		−4.0				
		−8.0				
		−12.0				
		−15.0				

Table A2. Comparison of Configurations, C_D Versus C_Q Cross Plots

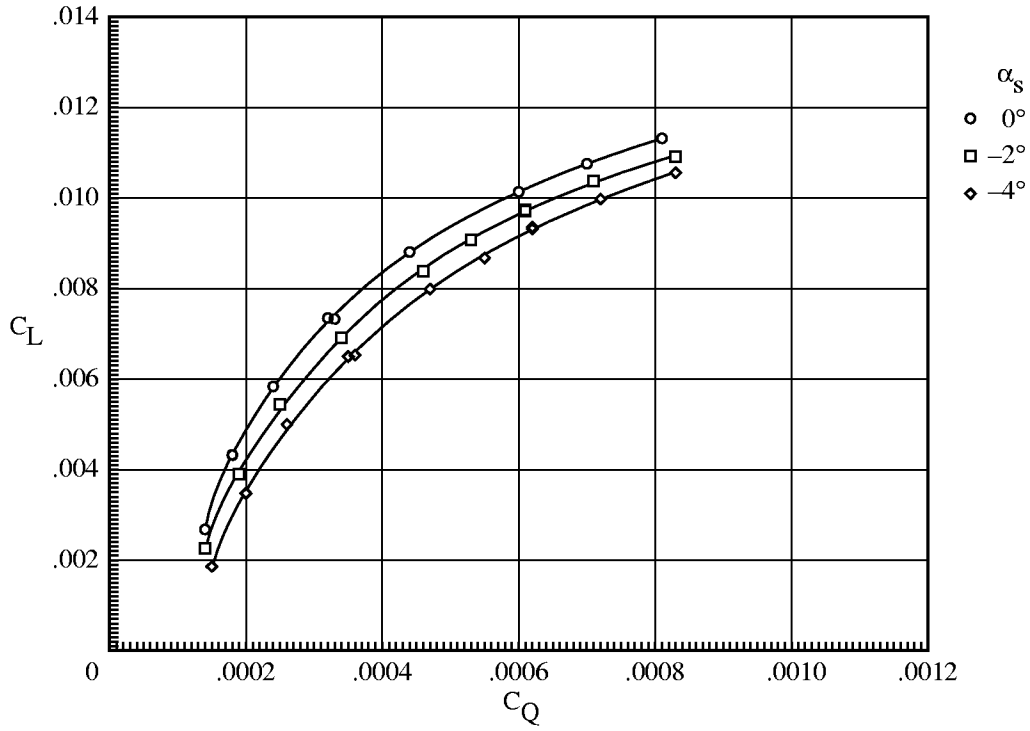
μ	Figures for C_L —							
	0.007	0.0081	0.0086	0.009	0.0095	0.010	0.011	0.012
0.15	A33(a)	A34(a)	A35(a)	A36(a)	A37(a)	A38(a)	A39(a)	A40(a)
0.20	A33(b)	A34(b)	A35(b)	A36(b)	A37(b)	A38(b)	A39(b)	A40(b)
0.25	A33(c)	A34(c)	A35(c)	A36(c)	A37(c)	A38(c)	A39(c)	
0.30	A33(d)	A34(d)	A35(d)	A36(d)	A37(d)	A38(d)		
0.35	A33(e)	A34(e)	A35(e)					
0.40	A33(f)							
0.43	A33(g)							

Table A3. Drag Coefficients Corresponding to Full-Scale Values of f_D

Utility helicopter (full-scale) $R = 26.835$ ft		Scout helicopter (full-scale) $R = 19.5$ ft		
μ	C_D for—	μ	C_D for—	C_D for—
	$f_D = 29.94$ ft ²		$f_D = 12.0$ ft ²	$f_D = 18.5$ ft ²
0.15	−0.000149	0.15	−0.000113	−0.000174
0.20	−0.000265	0.20	−0.000201	−0.000310
0.25	−0.000414	0.25	−0.000314	−0.000484
0.30	−0.000596	0.30	−0.000452	−0.000697
0.35	−0.000811	0.35	−0.000615	−0.000949
0.40	−0.001059	0.40	−0.000804	−0.001239
0.43	−0.001224	0.43	−0.000929	−0.001432

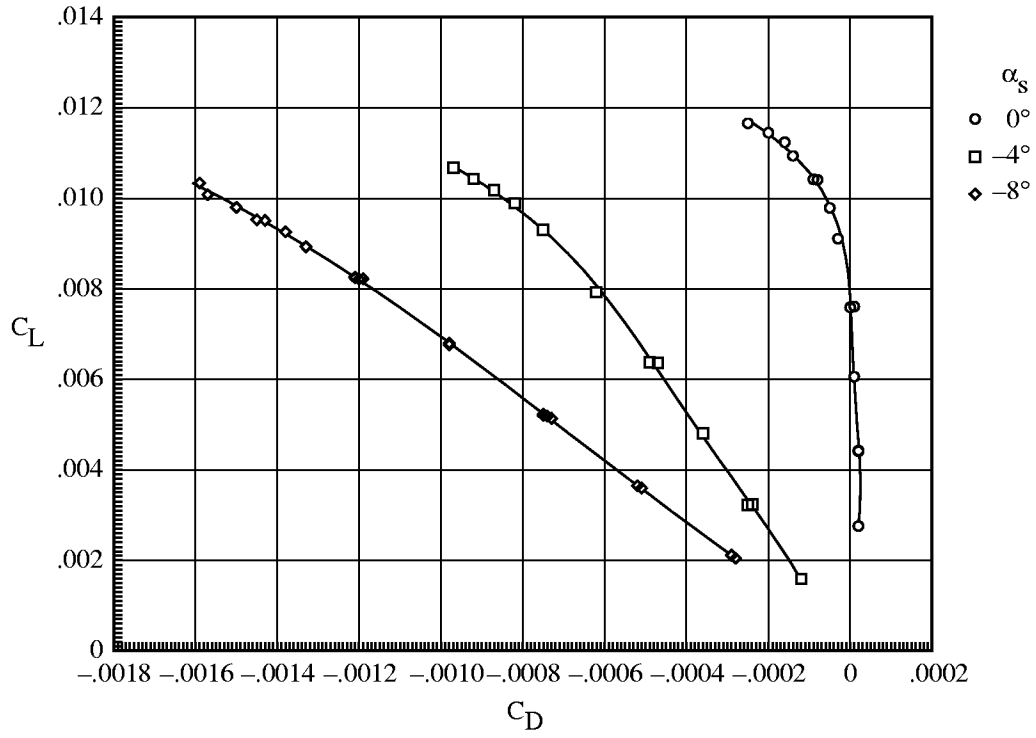


(a) C_L versus C_D .

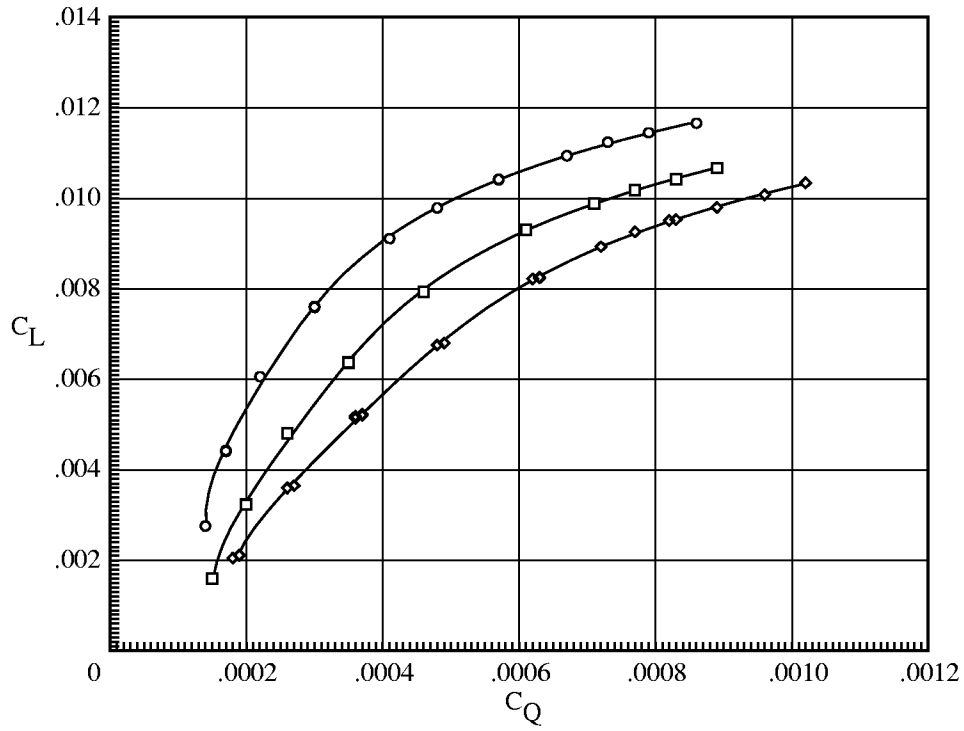


(b) C_L versus C_Q .

Figure A1. Basic forward-flight characteristics of baseline rotor for $\mu = 0.15$.

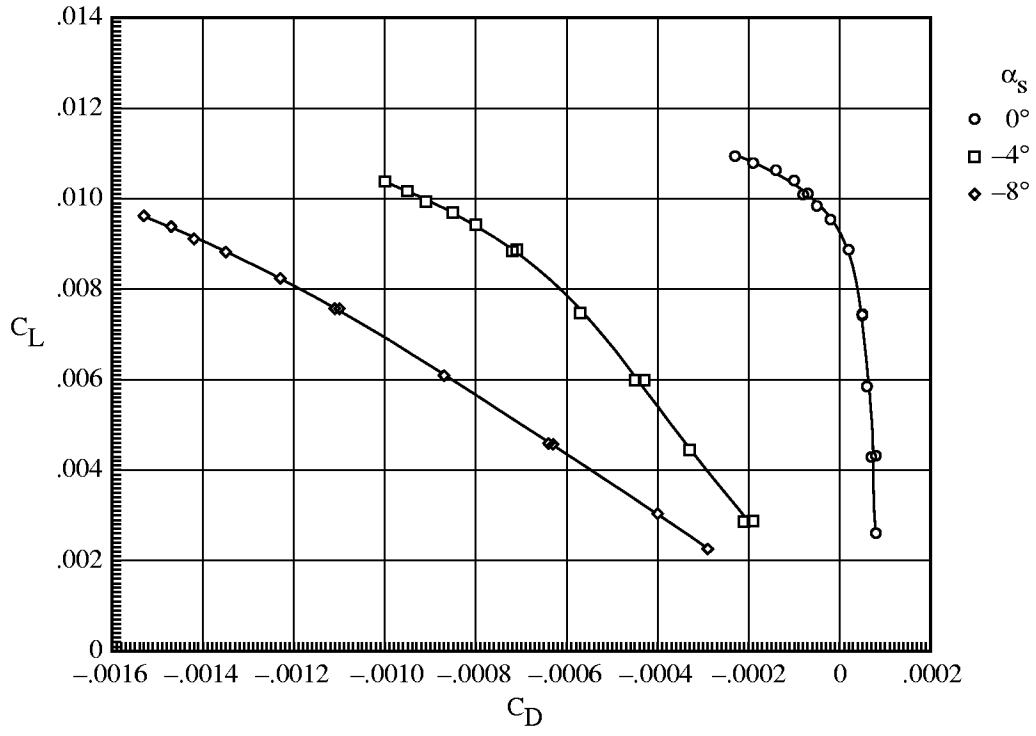


(a) C_L versus C_D .

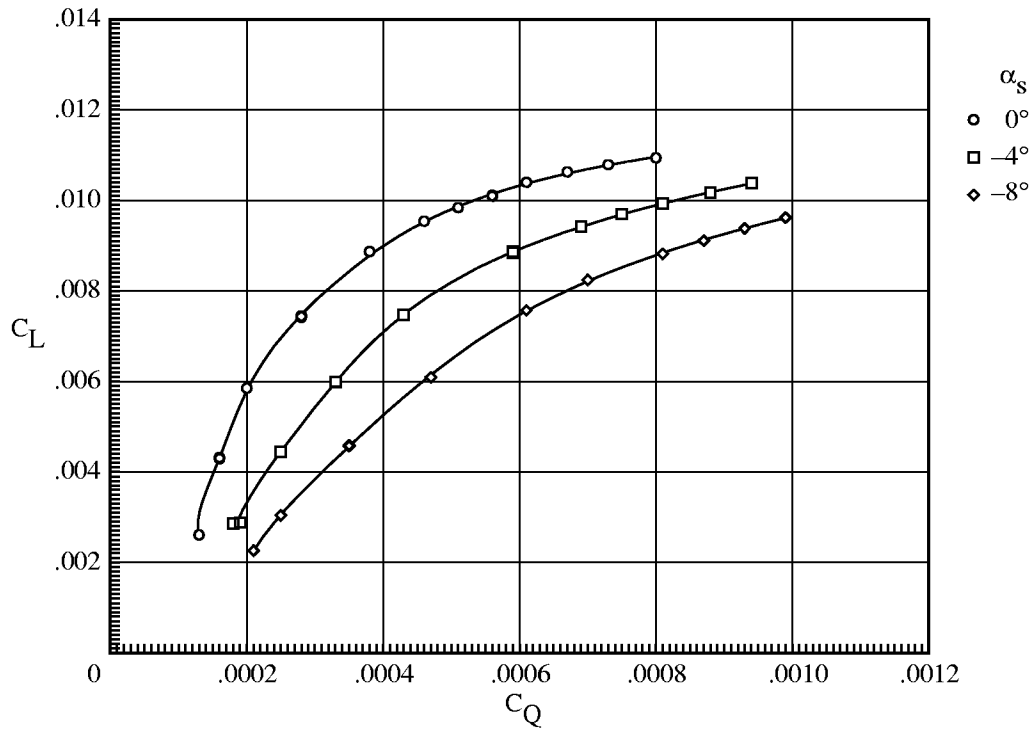


(b) C_L versus C_Q .

Figure A2. Basic forward-flight characteristics of baseline rotor for $\mu = 0.20$.

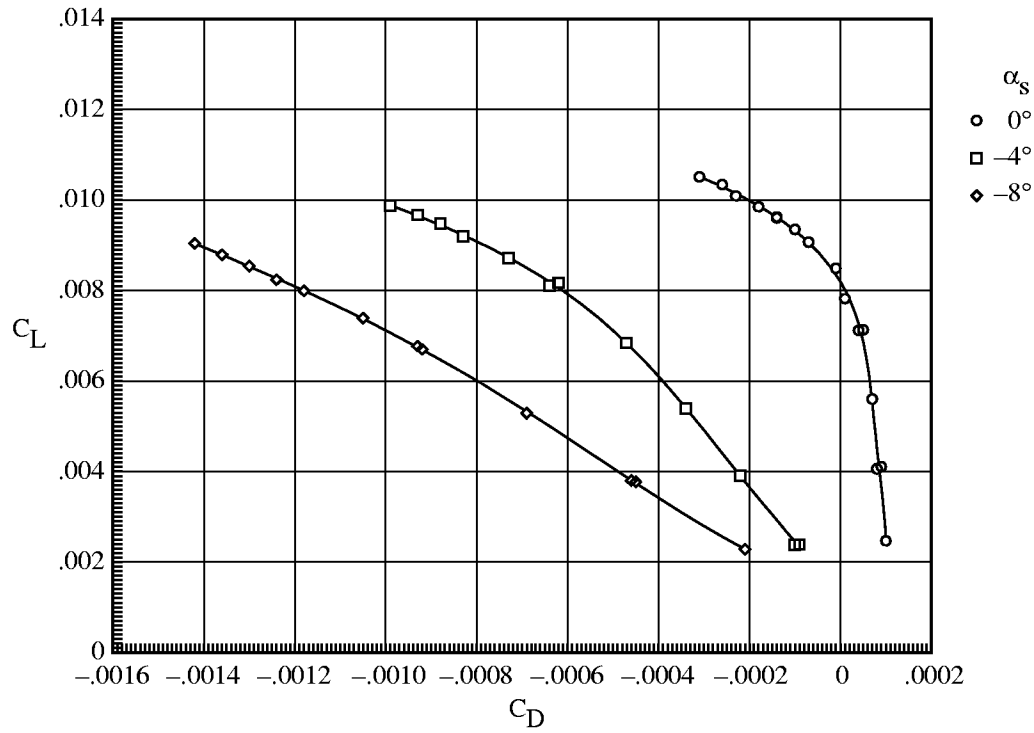


(a) C_L versus C_D .

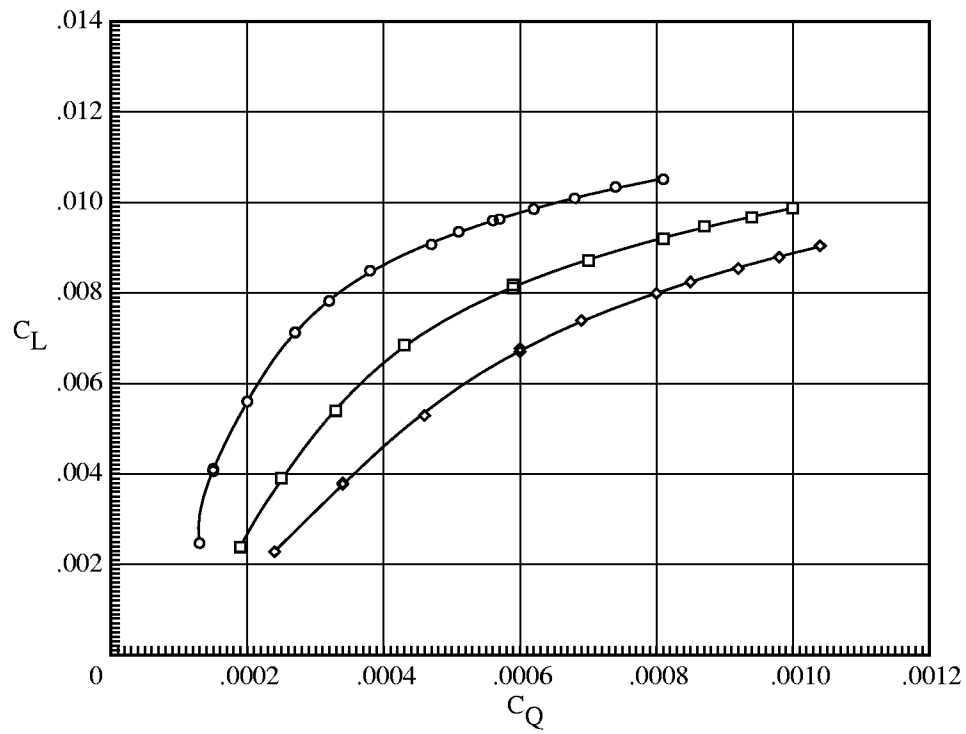


(b) C_L versus C_Q .

Figure A3. Basic forward-flight characteristics of baseline rotor for $\mu = 0.25$.

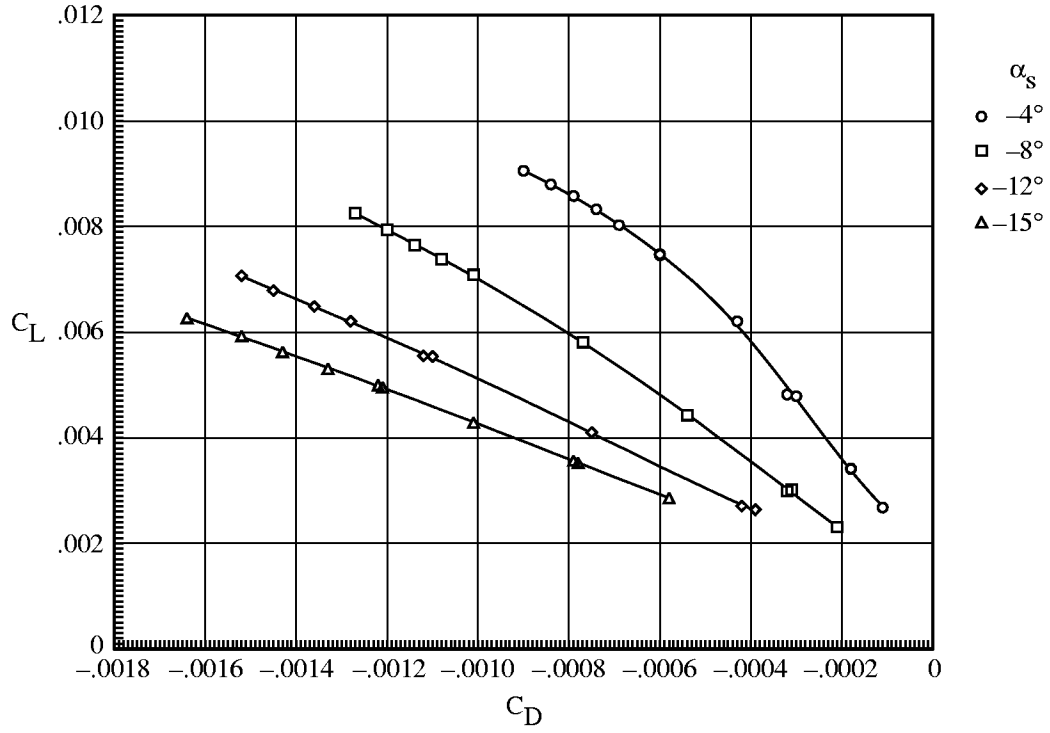


(a) C_L versus C_D .

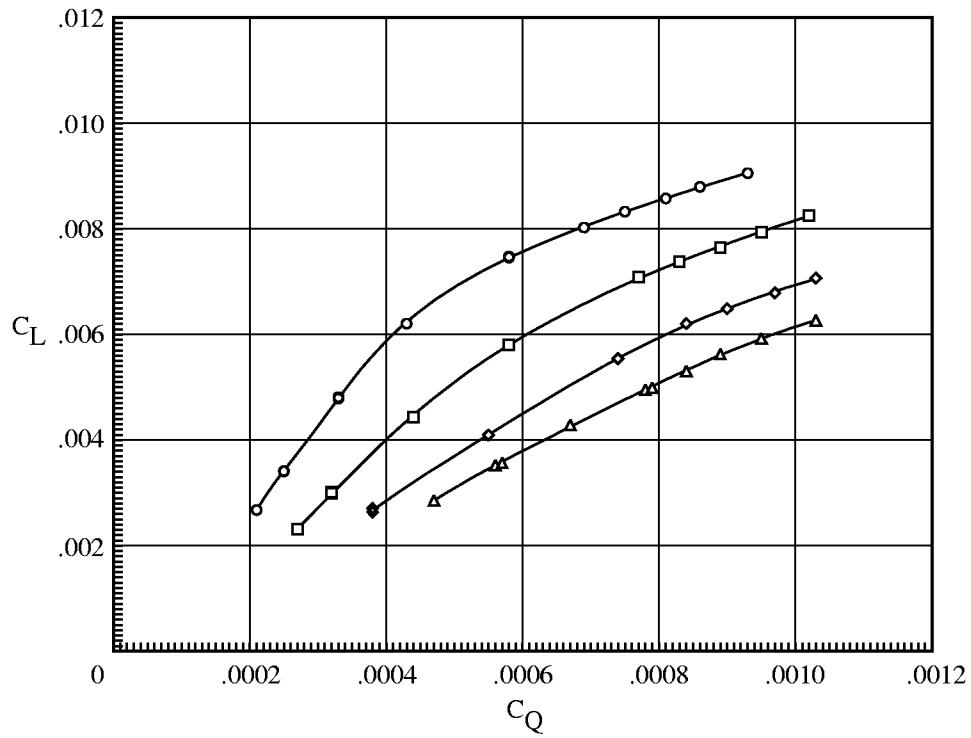


(b) C_L versus C_Q .

Figure A4. Basic forward-flight characteristics of baseline rotor for $\mu = 0.30$.

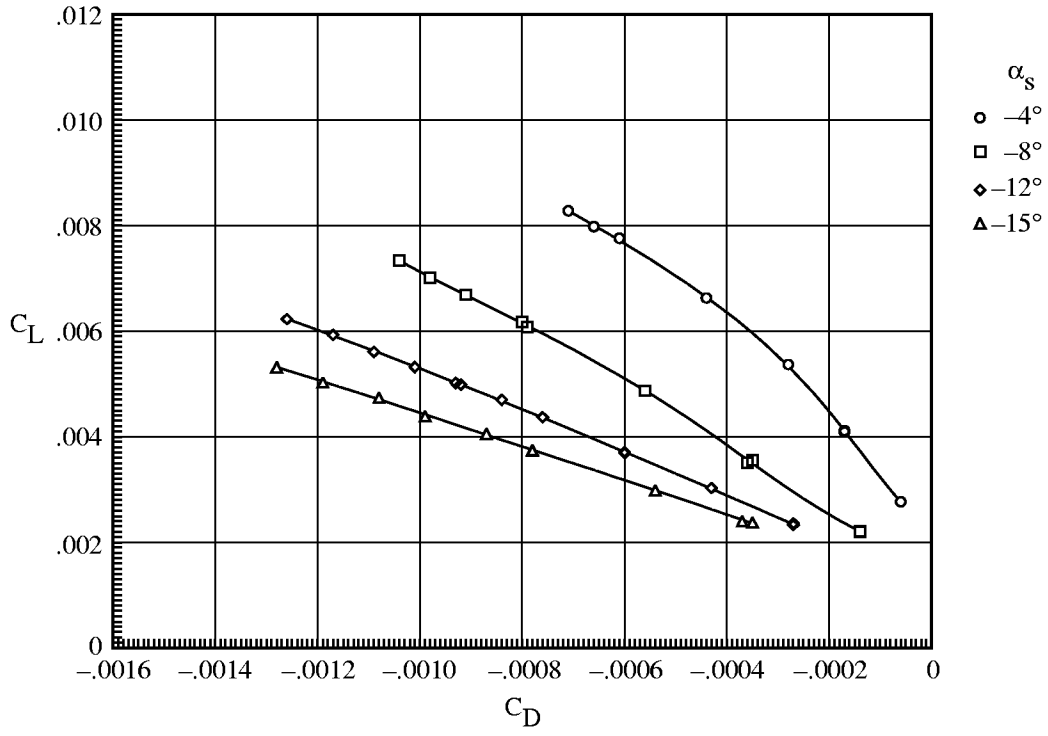


(a) C_L versus C_D .

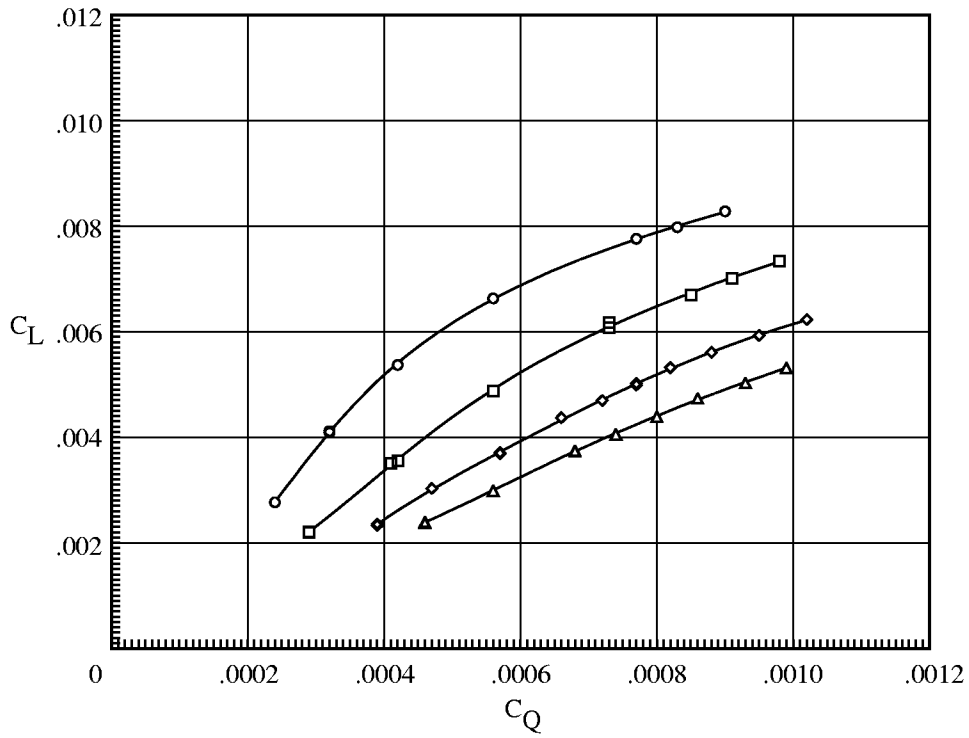


(b) C_L versus C_Q .

Figure A5. Basic forward-flight characteristics of baseline rotor for $\mu = 0.35$.

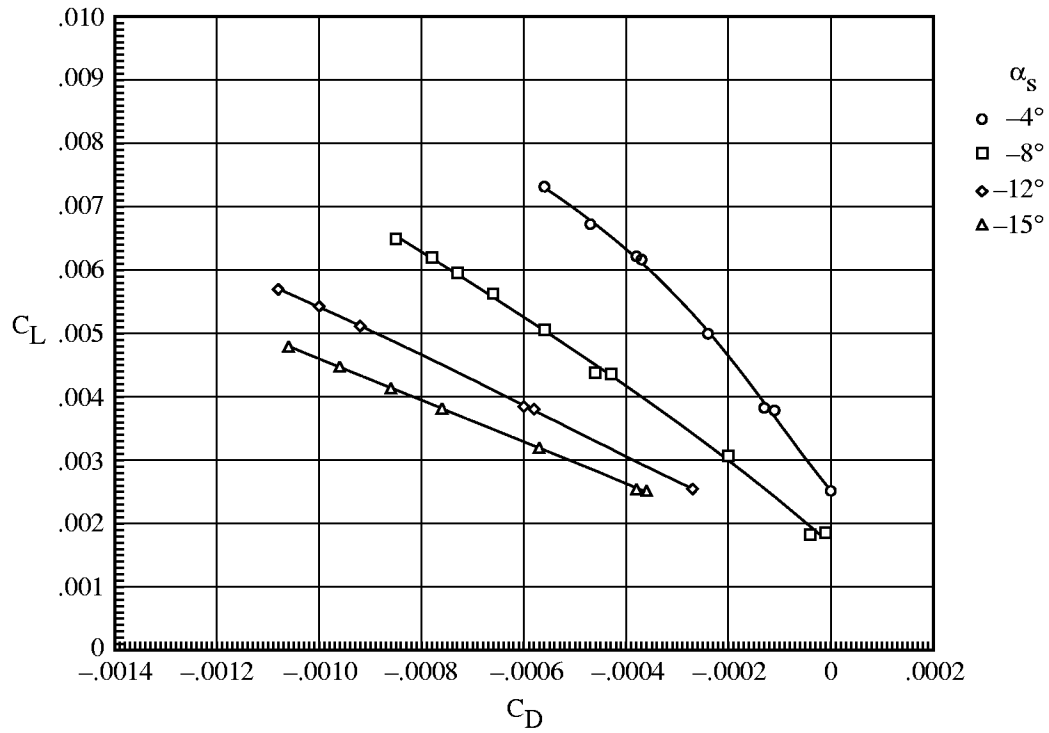


(a) C_L versus C_D .

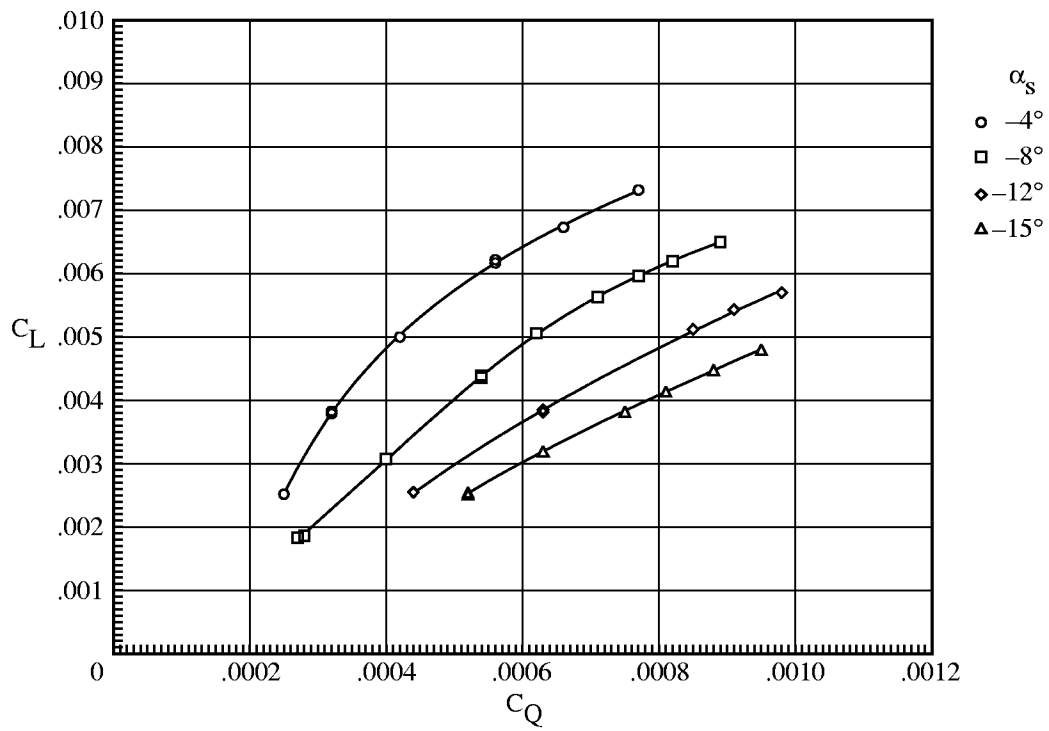


(b) C_L versus C_Q .

Figure A6. Basic forward-flight characteristics of baseline rotor for $\mu = 0.40$.

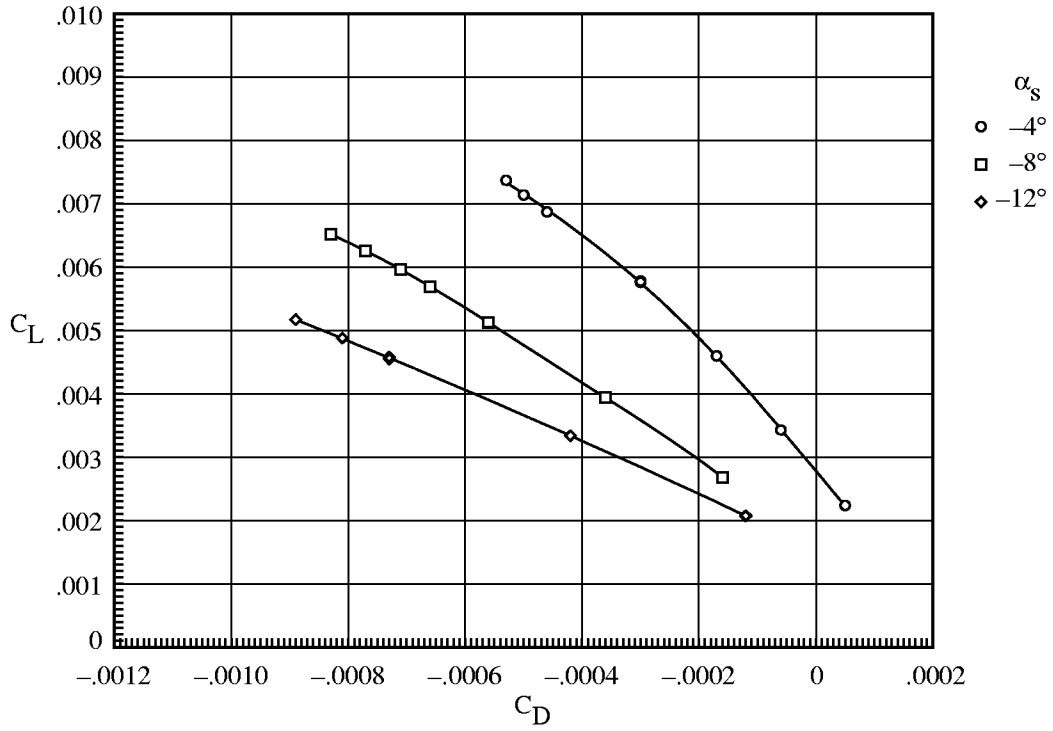


(a) C_L versus C_D .

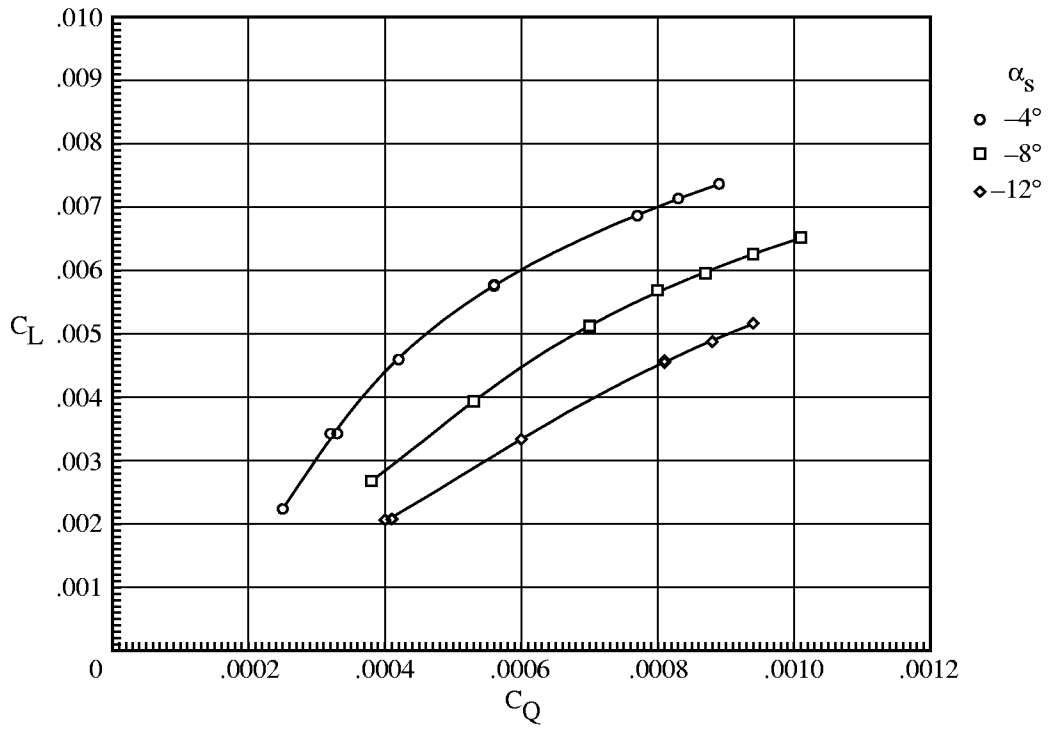


(b) C_L versus C_Q .

Figure A7. Basic forward-flight characteristics of baseline rotor for $\mu = 0.43$.

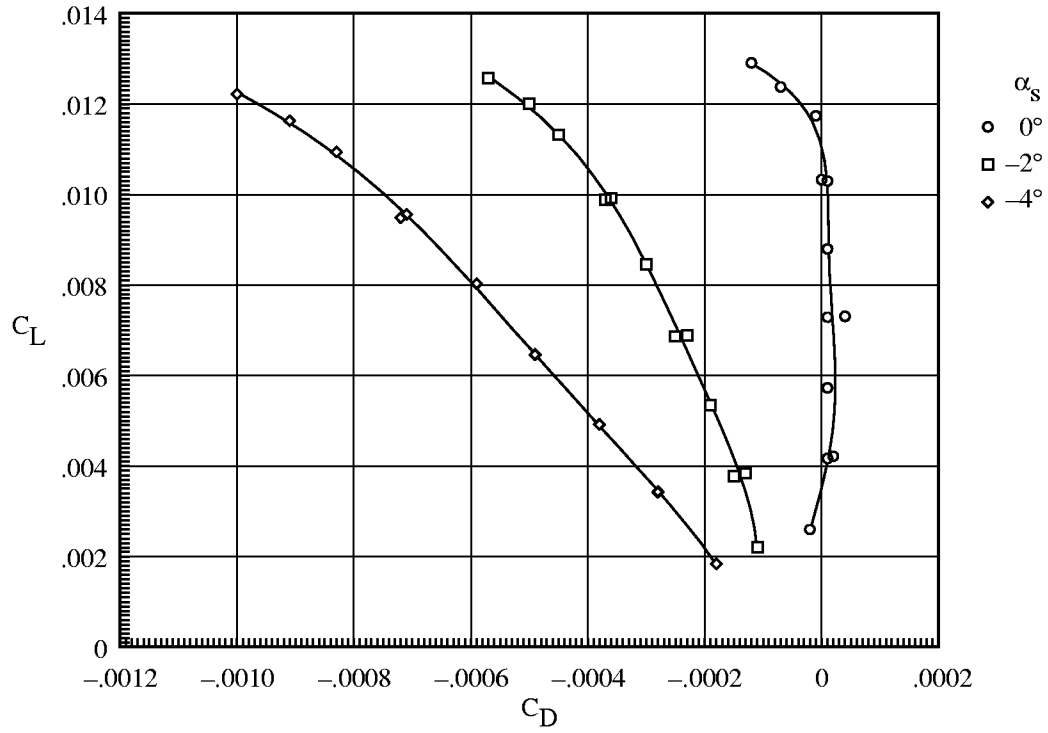


(a) C_L versus C_D .

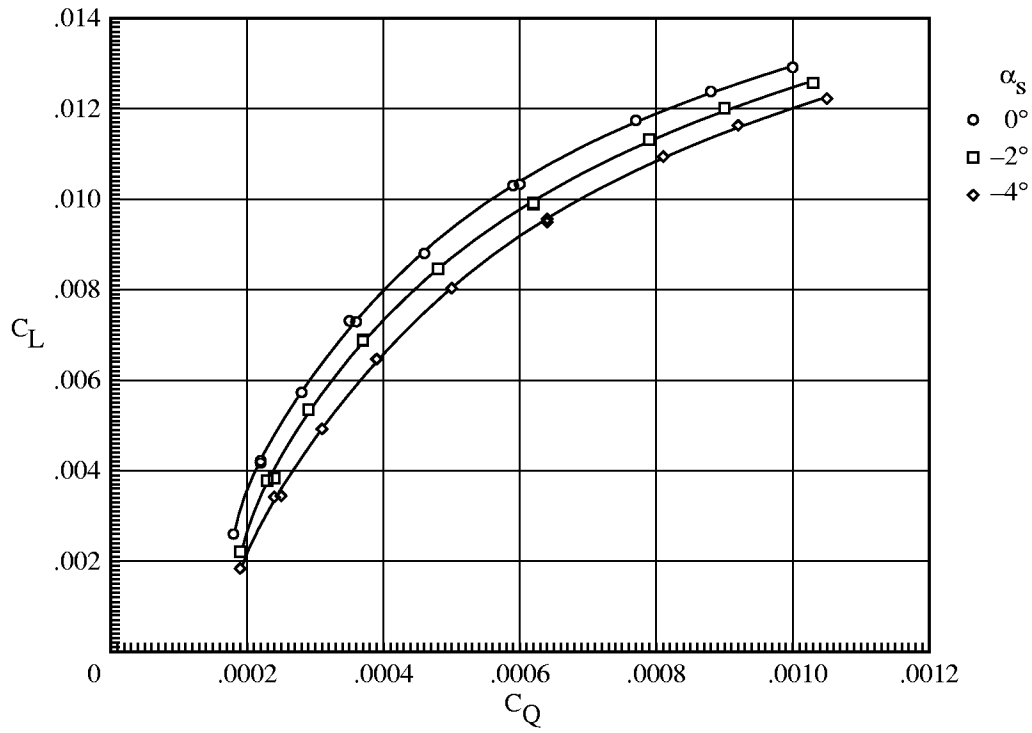


(b) C_L versus C_Q .

Figure A8. Basic forward-flight characteristics of baseline rotor for $\mu = 0.45$.

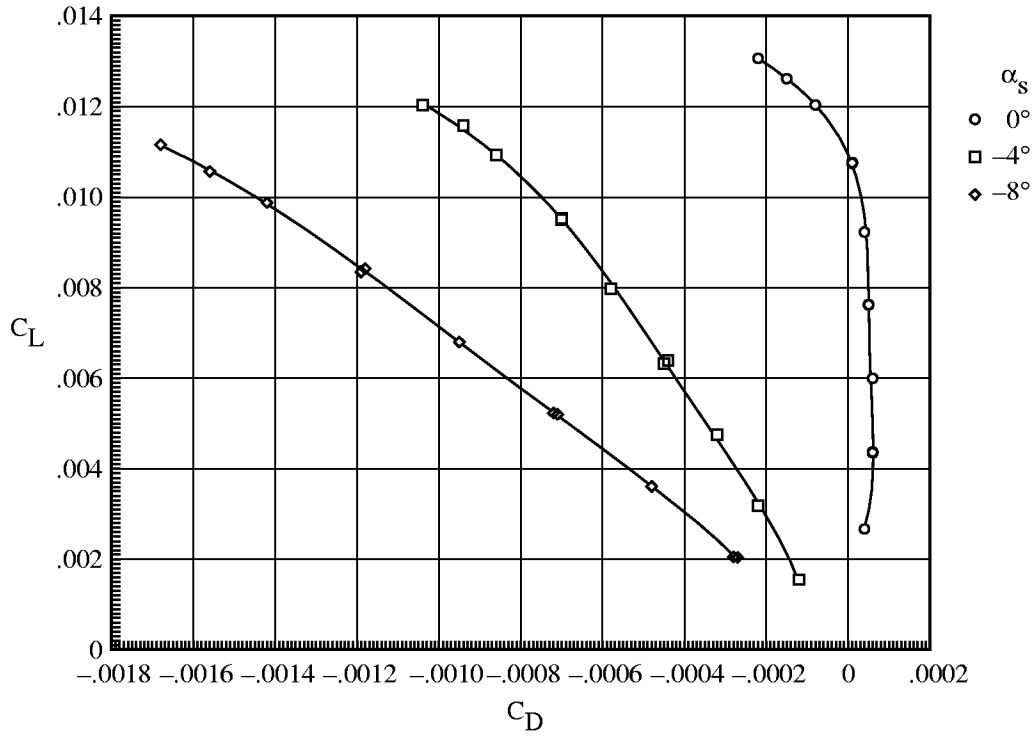


(a) C_L versus C_D .

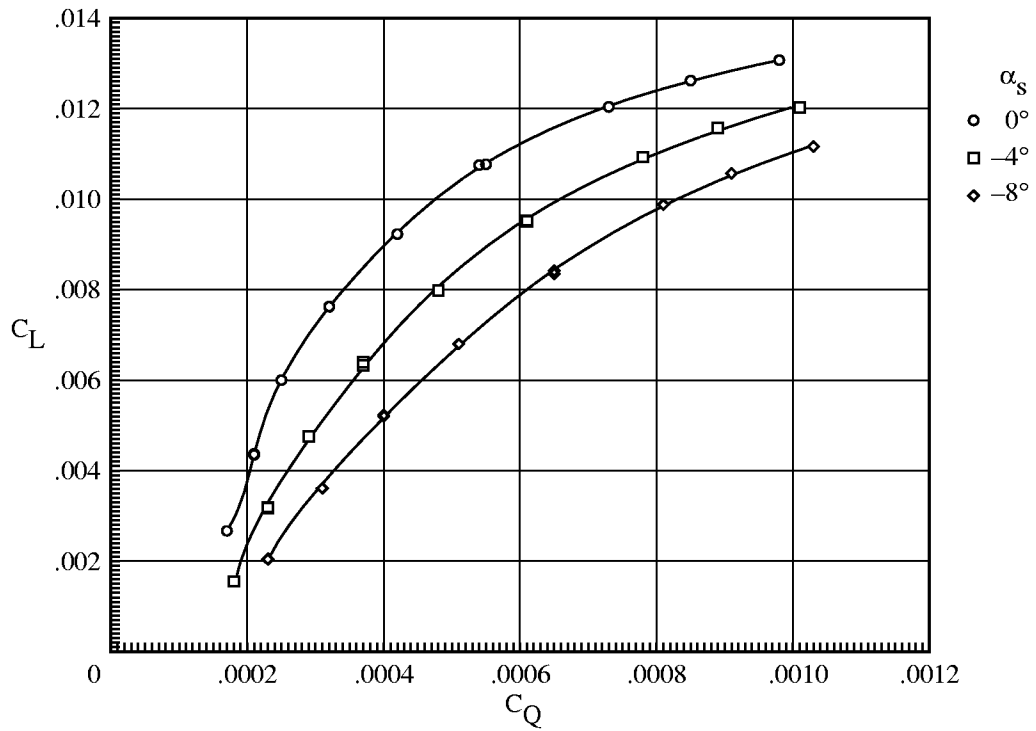


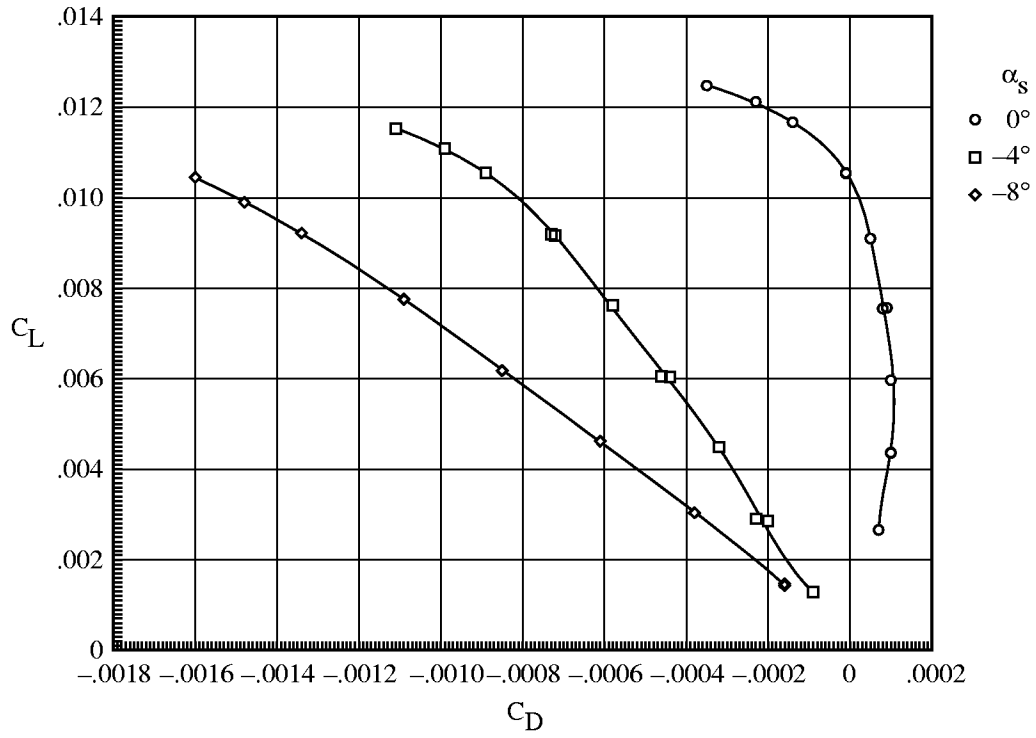
(b) C_L versus C_Q .

Figure A9. Basic forward-flight characteristics of -6° LE slat rotor for $\mu = 0.15$.

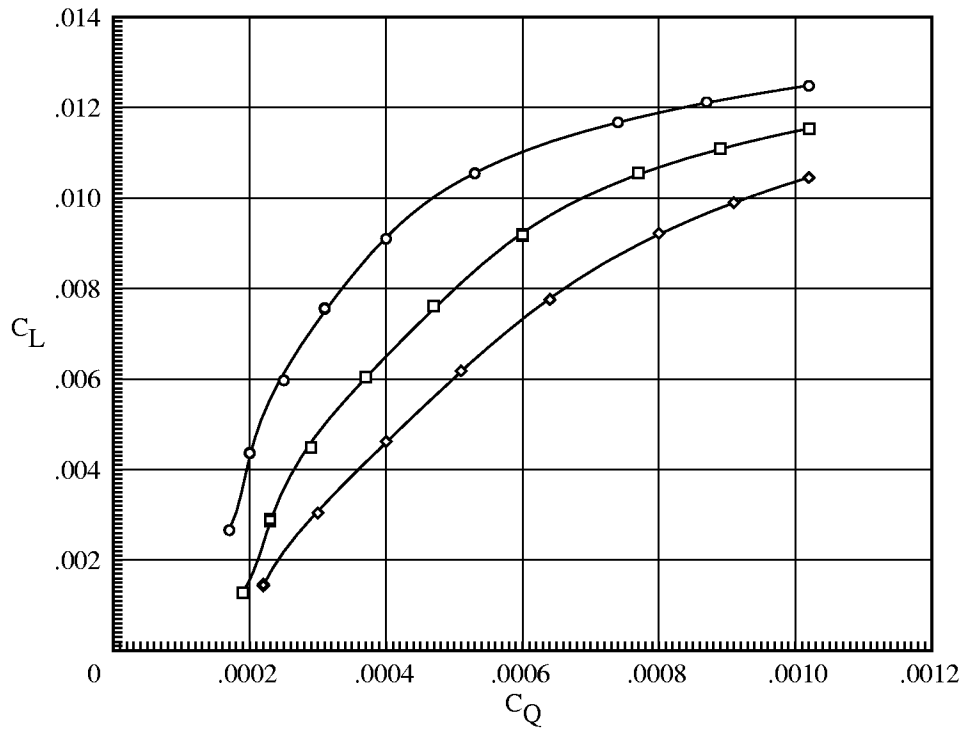


(a) C_L versus C_D .



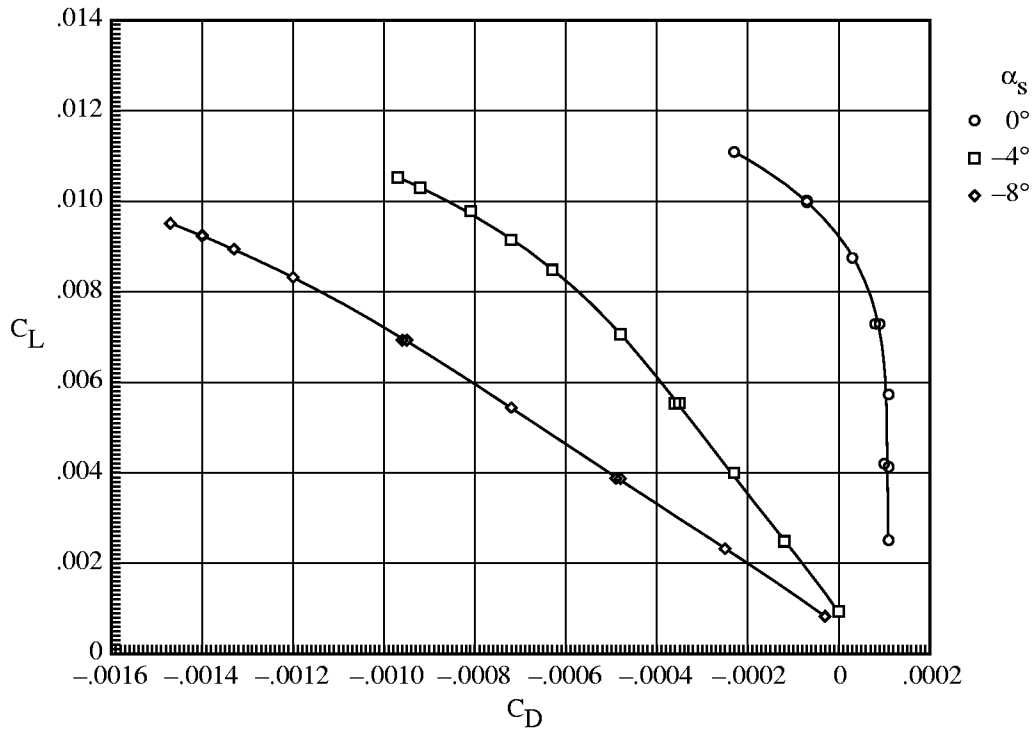


(a) C_L versus C_D .

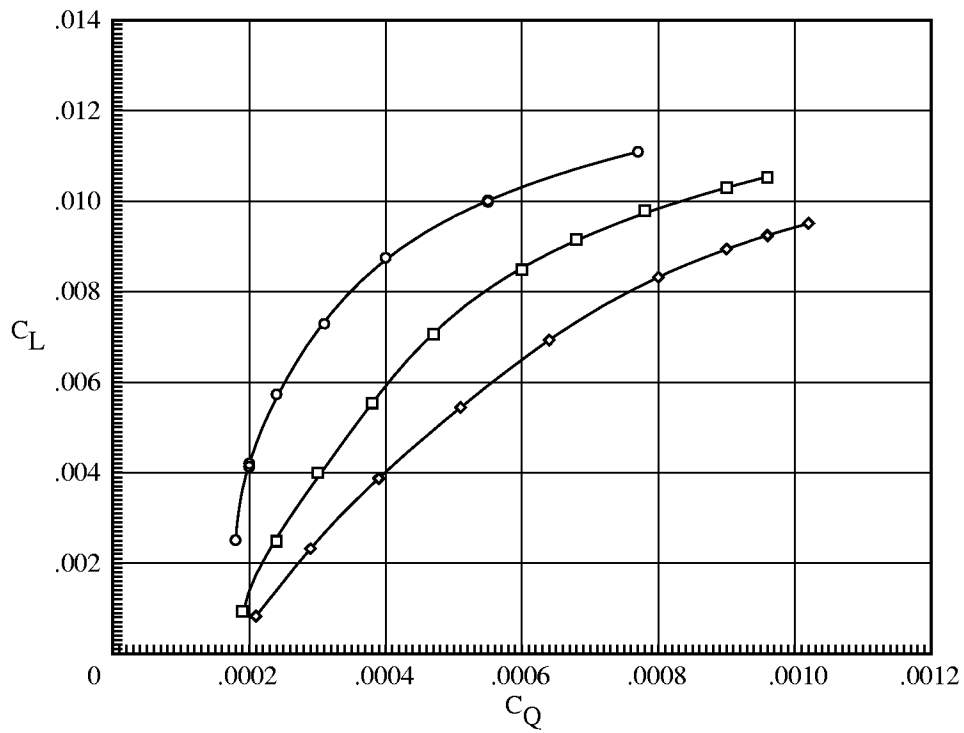


(b) C_L versus C_Q .

Figure A11. Basic forward-flight characteristics of -6° LE slat rotor for $\mu = 0.25$.

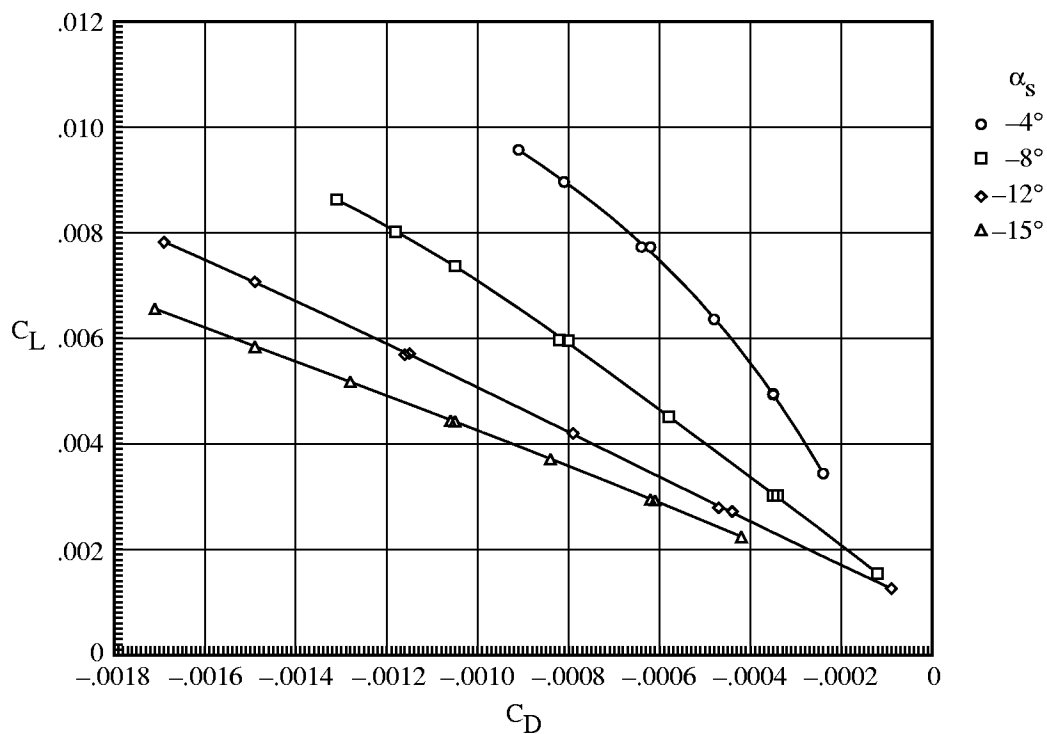


(a) C_L versus C_D .

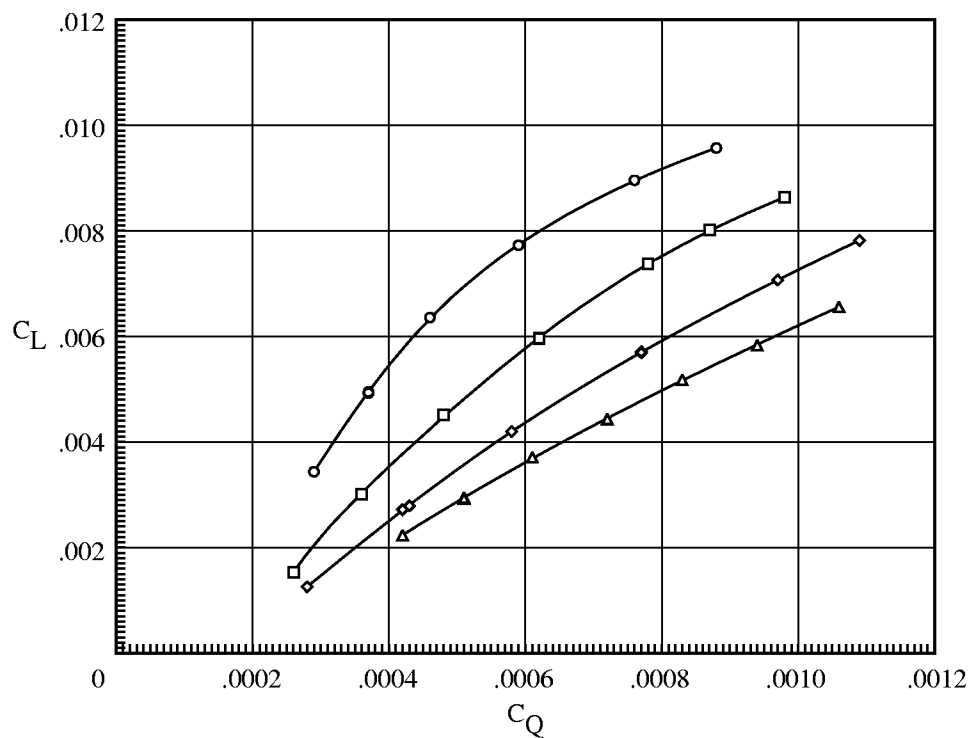


(b) C_L versus C_Q .

Figure A12. Basic forward-flight characteristics of -6° LE slat rotor for $\mu = 0.30$.

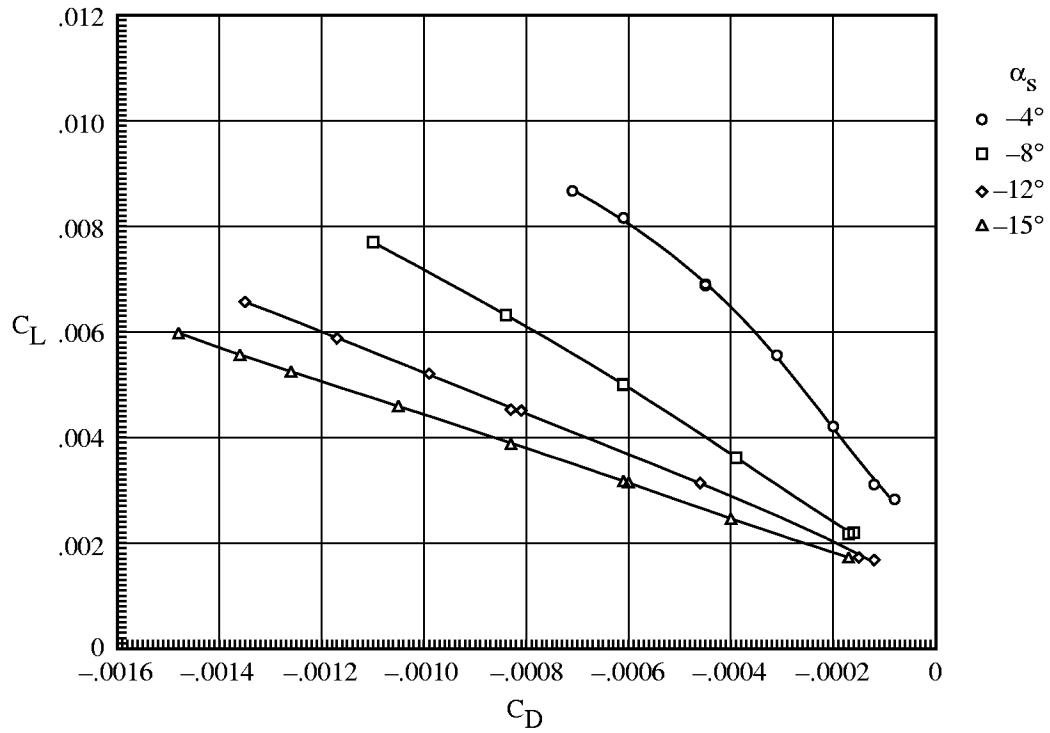


(a) C_L versus C_D .

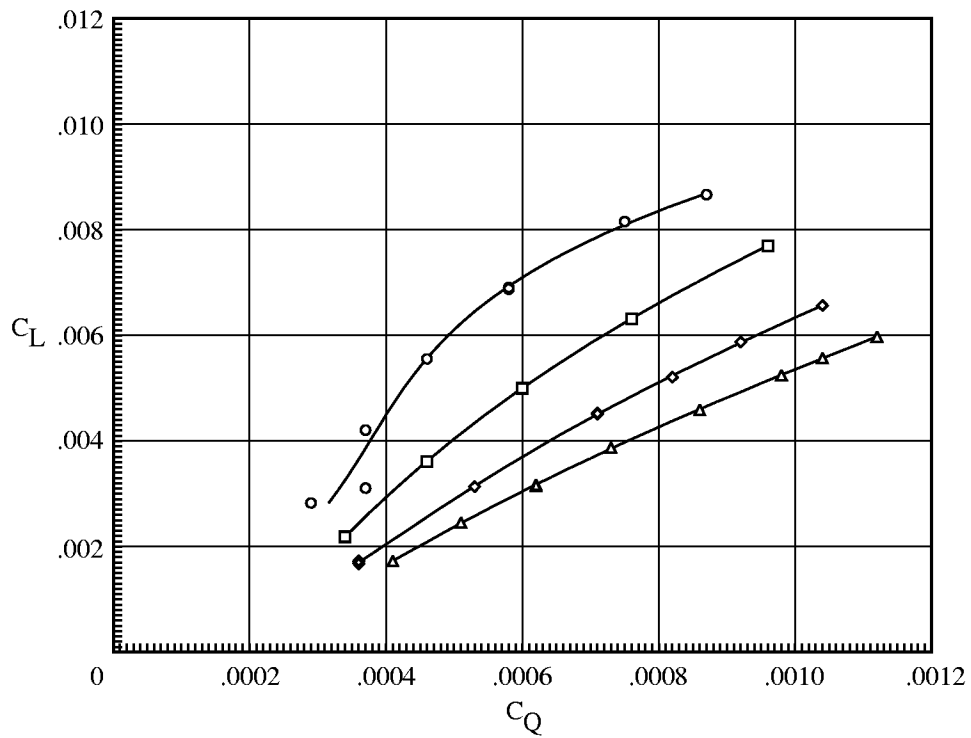


(b) C_L versus C_Q .

Figure A13. Basic forward-flight characteristics of -6° LE slat rotor for $\mu = 0.35$.

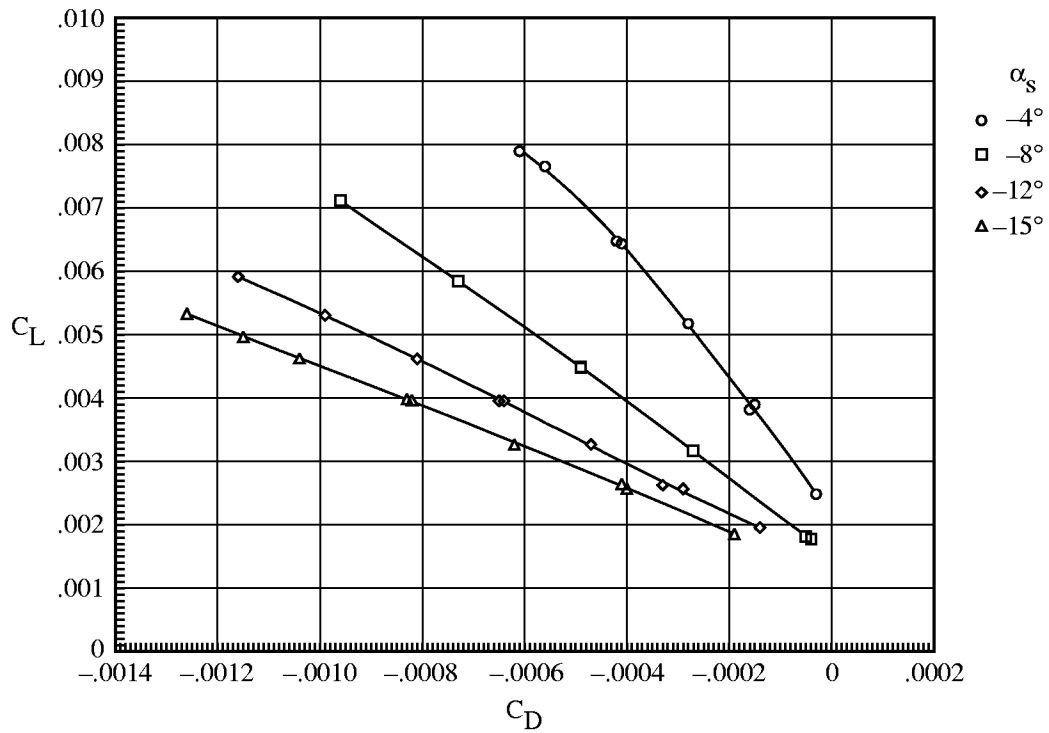


(a) C_L versus C_D .

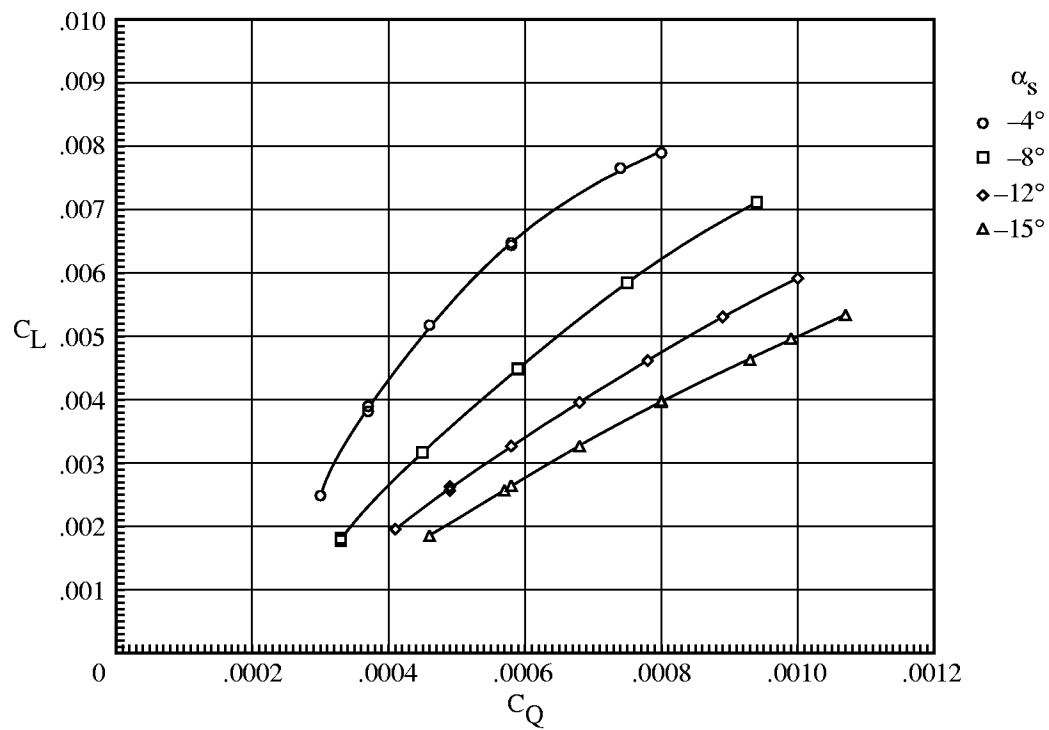


(b) C_L versus C_Q .

Figure A14. Basic forward-flight characteristics of -6° LE slat rotor for $\mu = 0.40$.

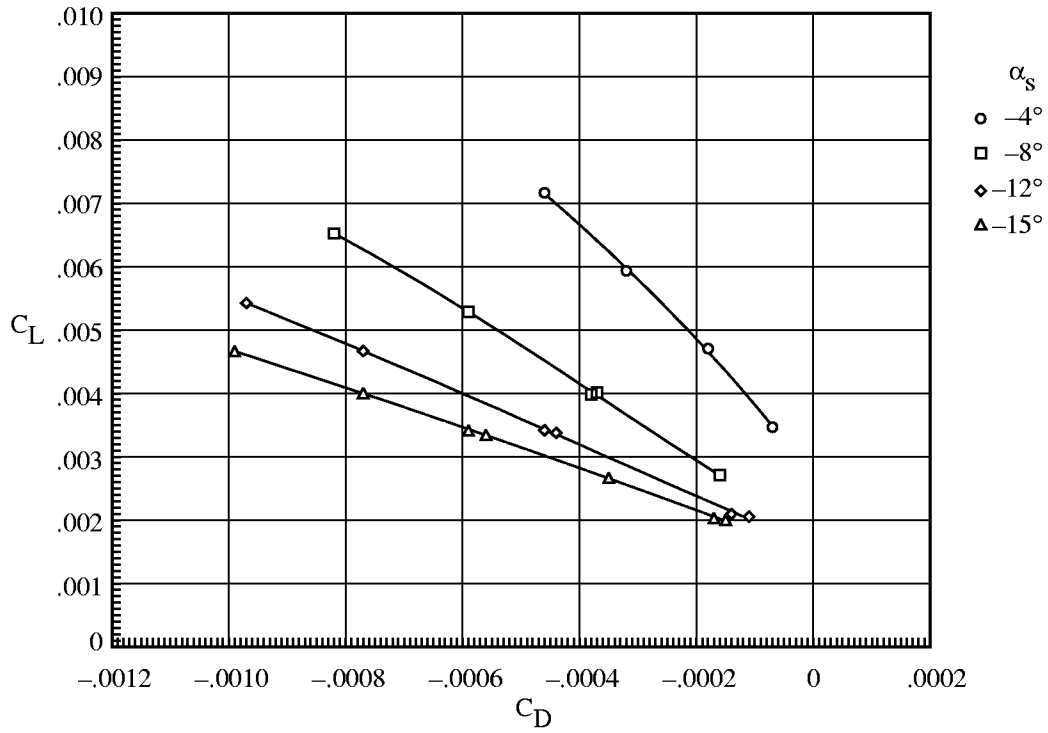


(a) C_L versus C_D .

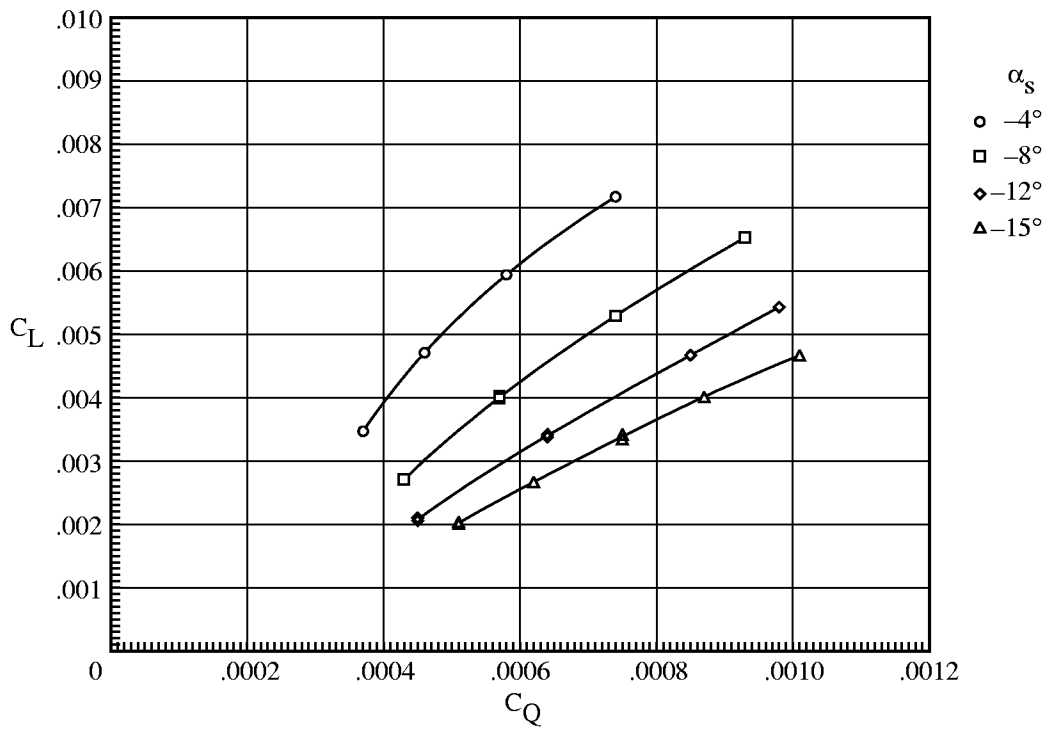


(b) C_L versus C_Q .

Figure A15. Basic forward-flight characteristics of -6° LE slat rotor for $\mu = 0.43$.

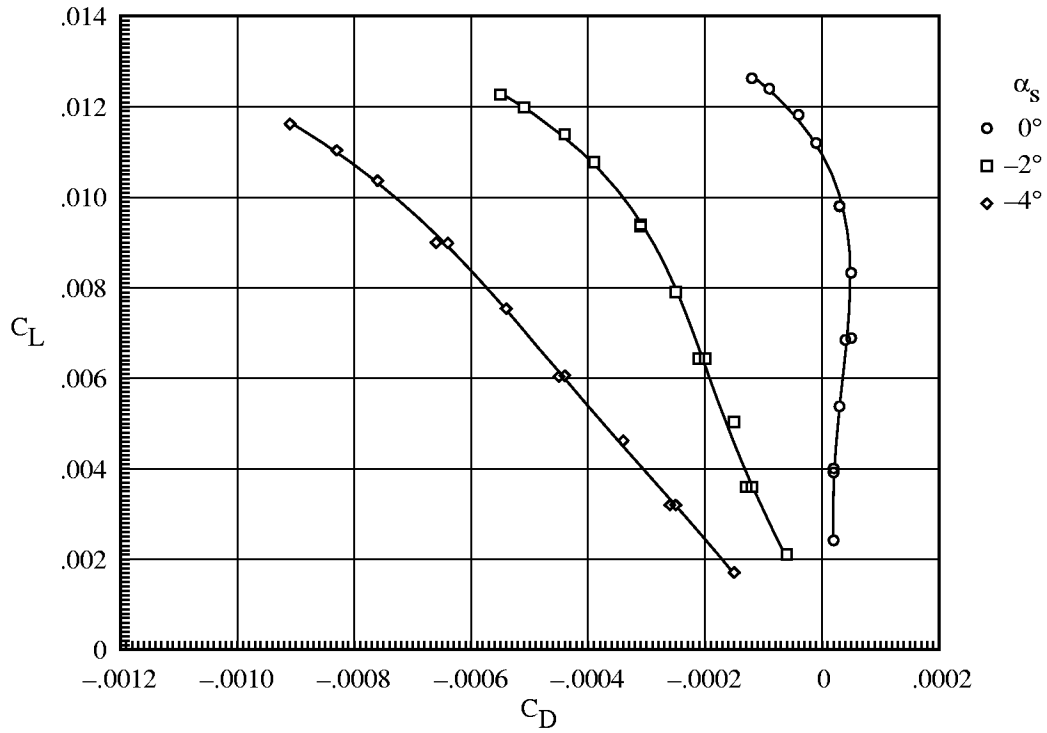


(a) C_L versus C_D .

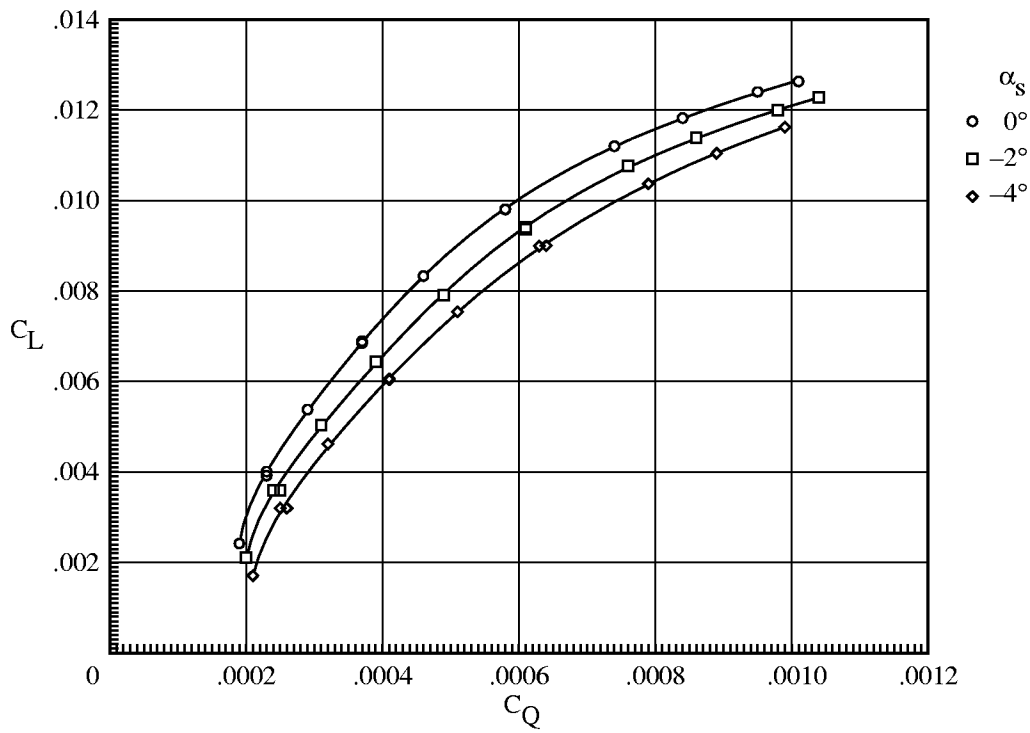


(b) C_L versus C_Q .

Figure A16. Basic forward-flight characteristics of -6° LE slat rotor for $\mu = 0.45$.

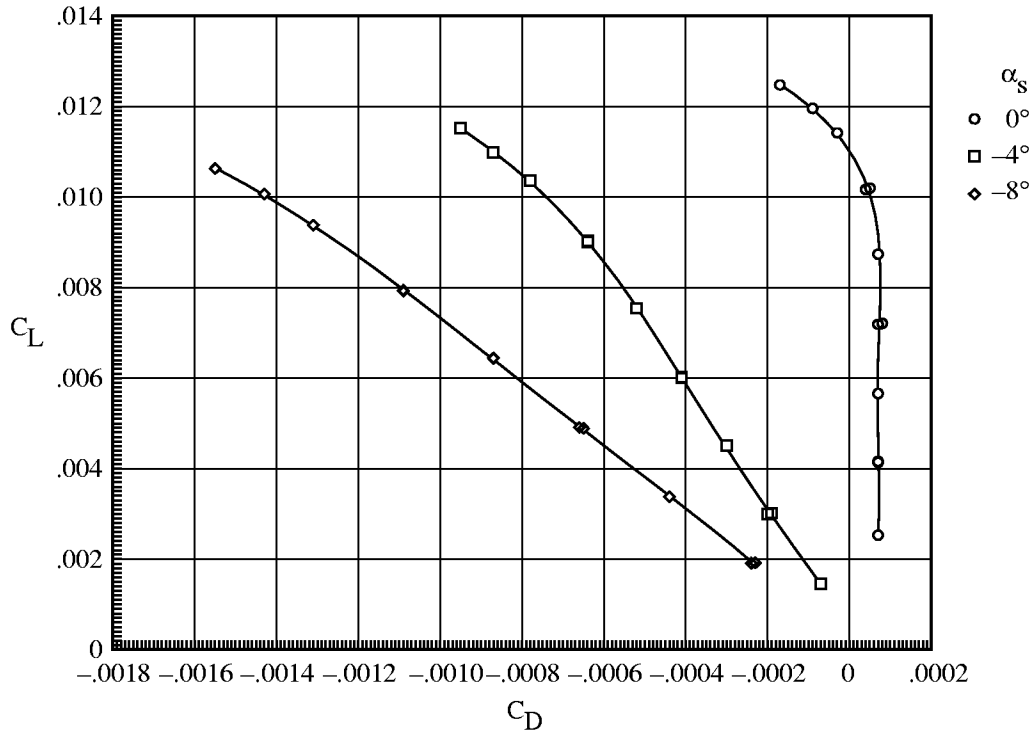


(a) C_L versus C_D .

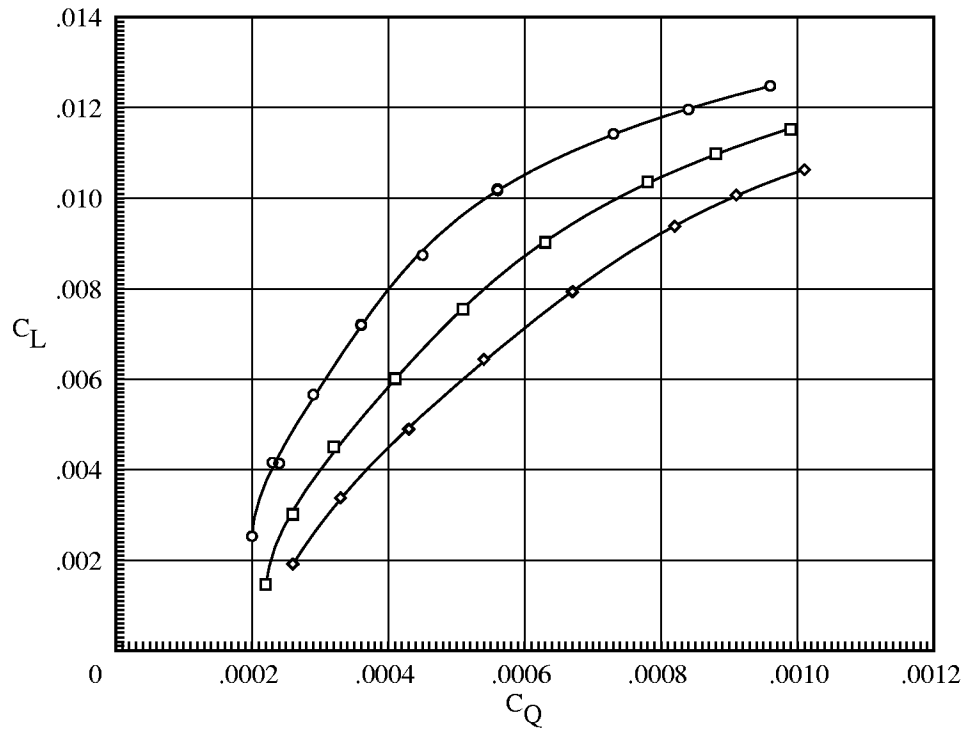


(b) C_L versus C_Q .

Figure A17. Basic forward-flight characteristics of -10° LE slat rotor for $\mu = 0.15$.

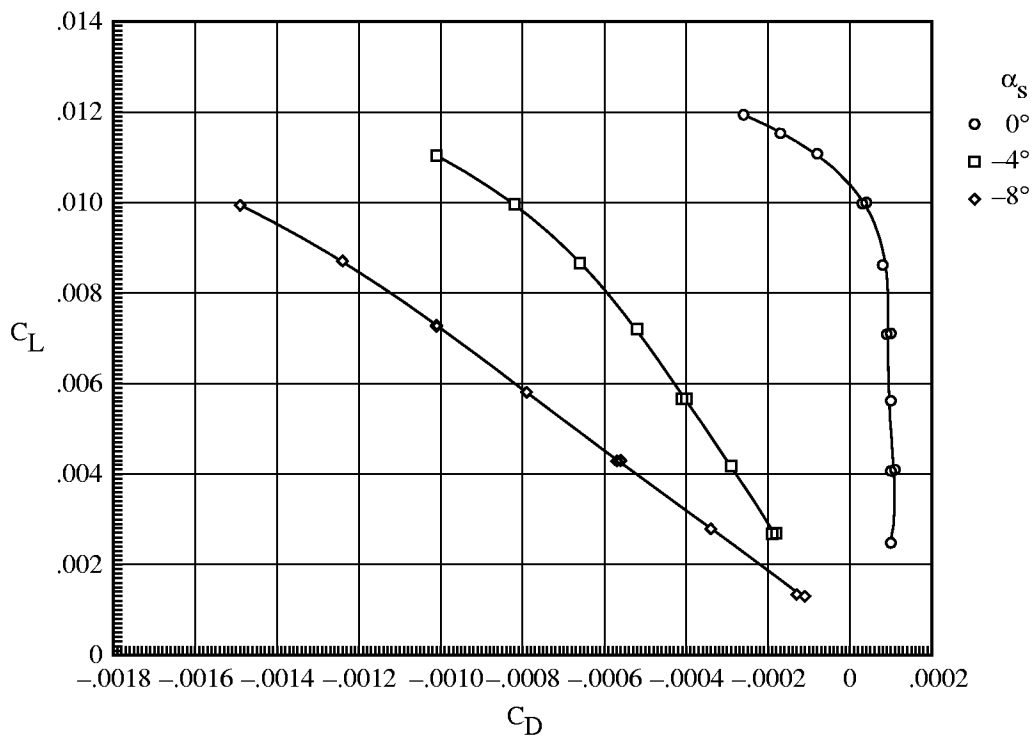


(a) C_L versus C_D .

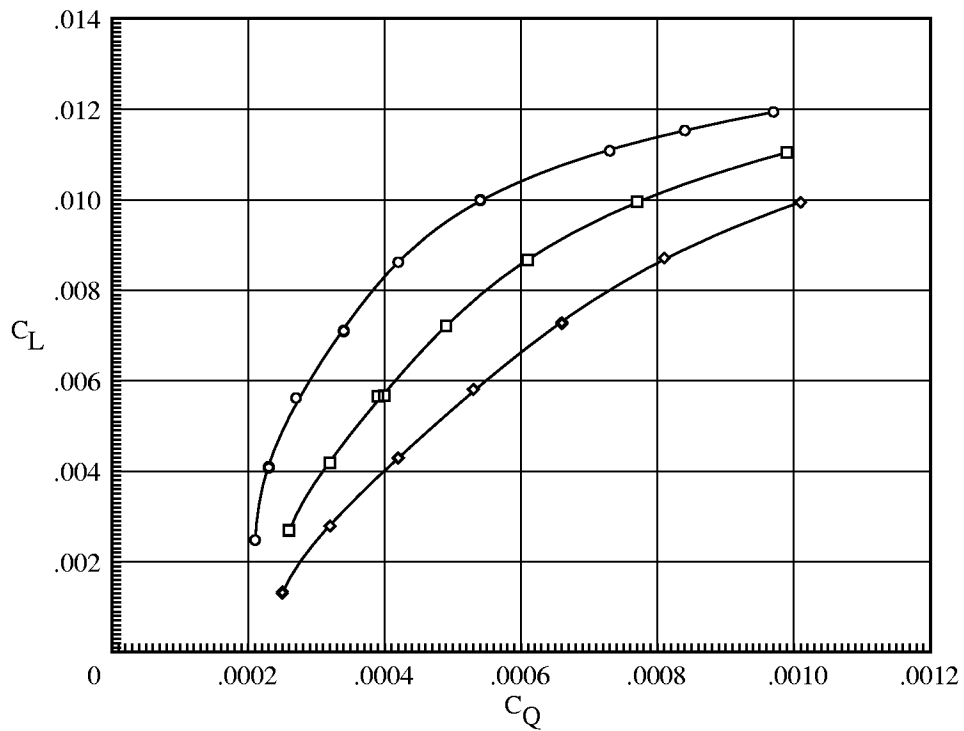


(b) C_L versus C_Q .

Figure A18. Basic forward-flight characteristics of -10° LE slat rotor for $\mu = 0.20$.

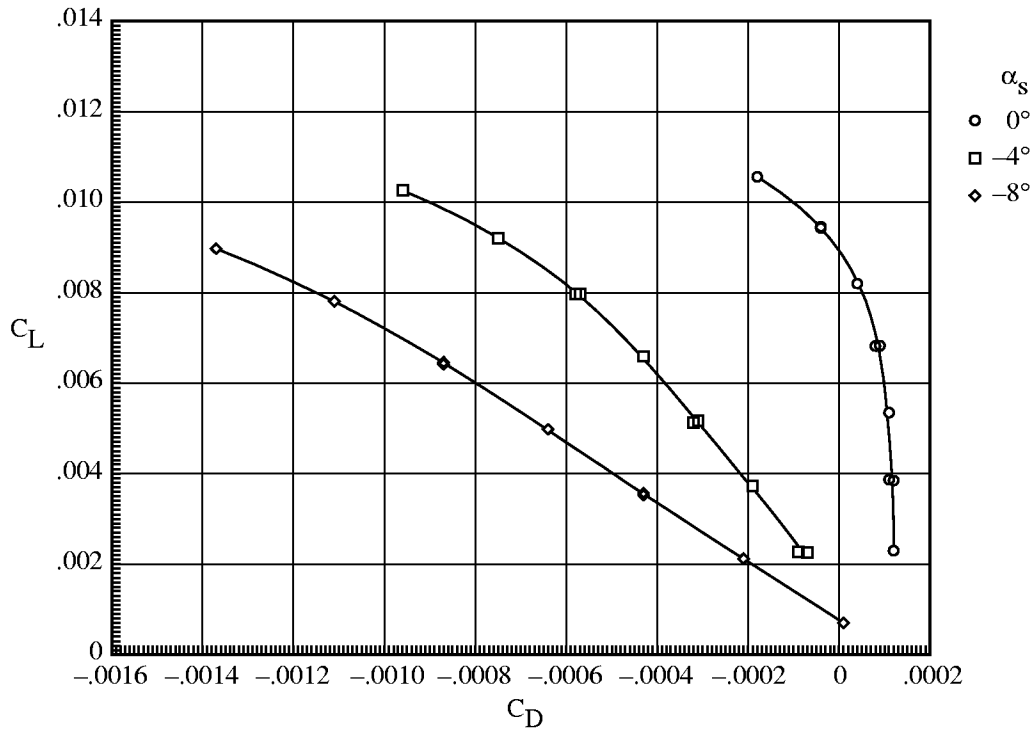


(a) C_L versus C_D .

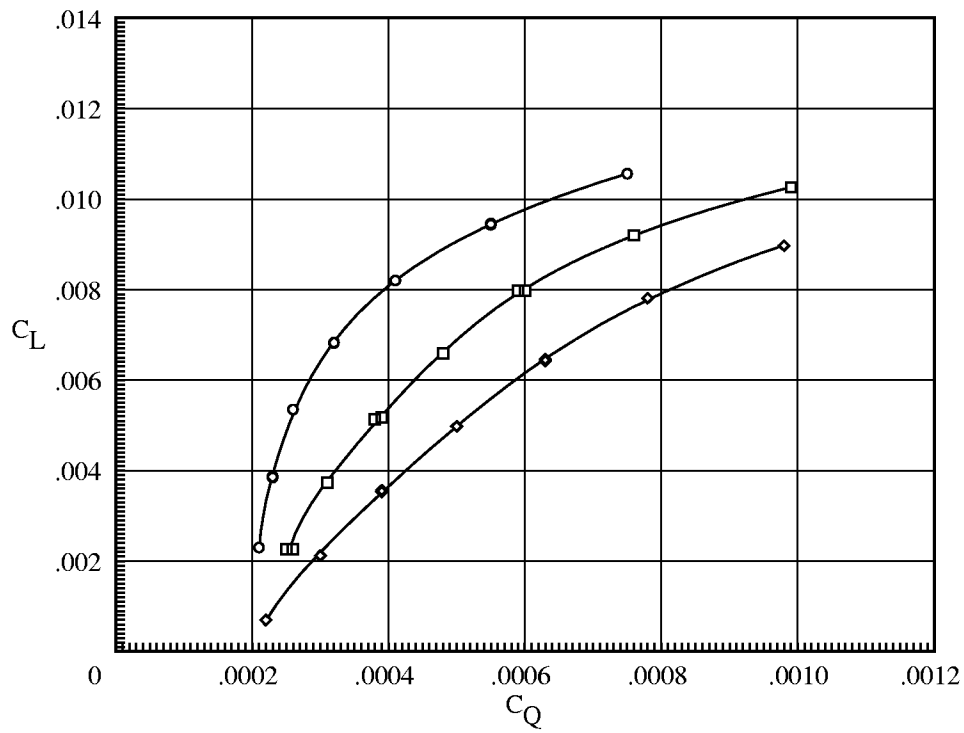


(b) C_L versus C_Q .

Figure A19. Basic forward-flight characteristics of -10° LE slat rotor for $\mu = 0.25$.

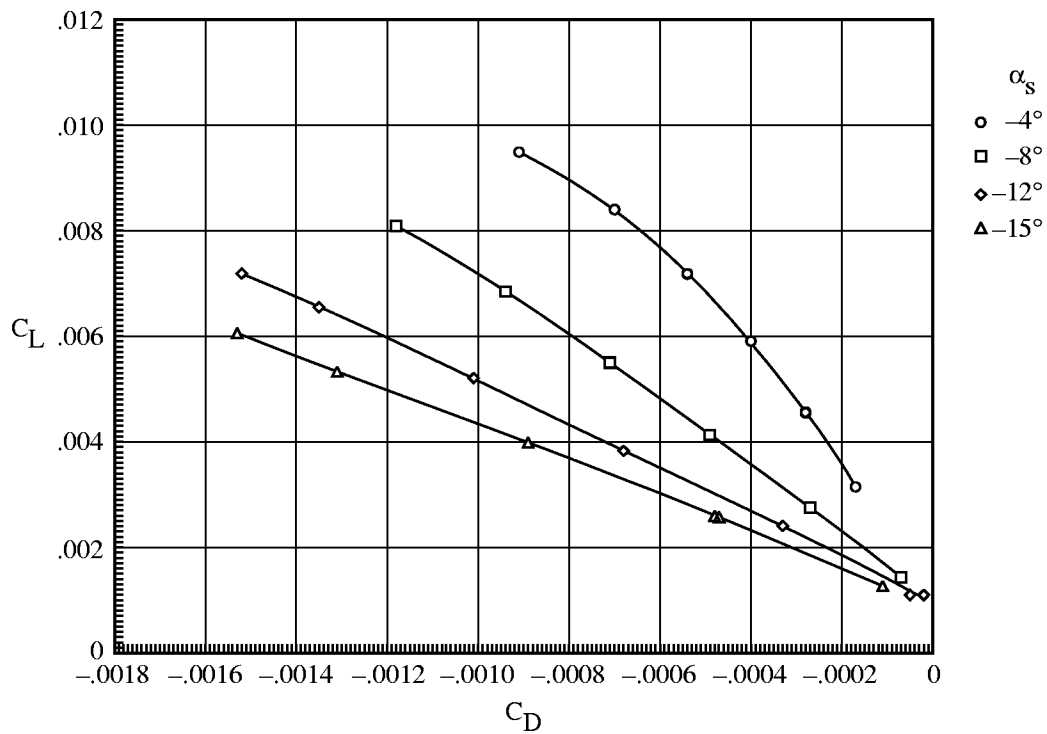


(a) C_L versus C_D .

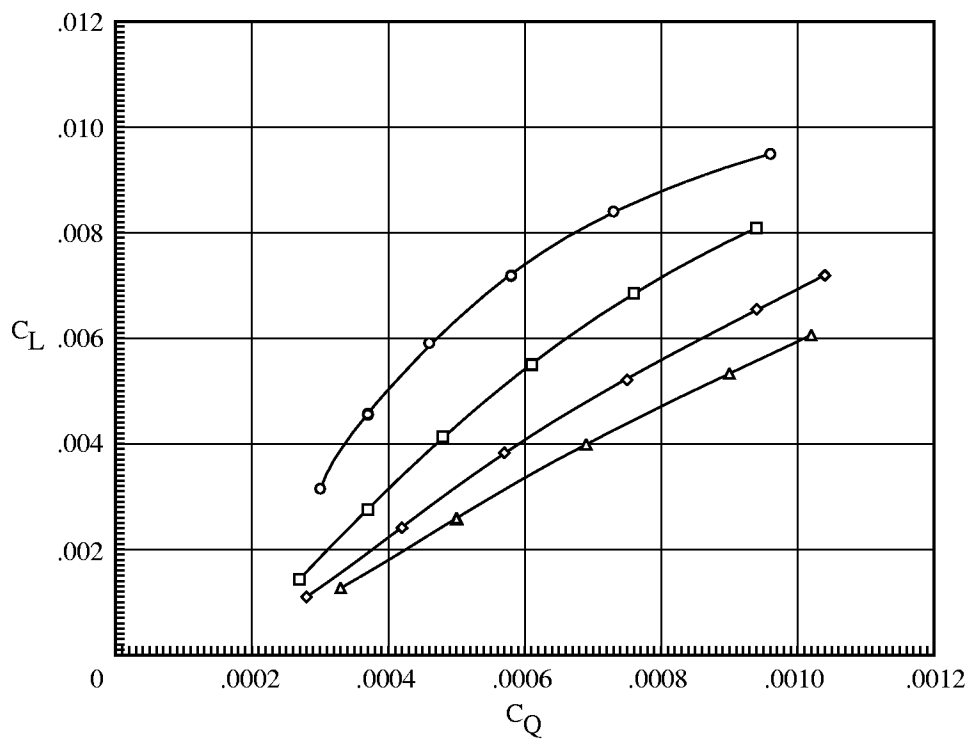


(b) C_L versus C_Q .

Figure A20. Basic forward-flight characteristics of -10° LE slat rotor for $\mu = 0.30$.

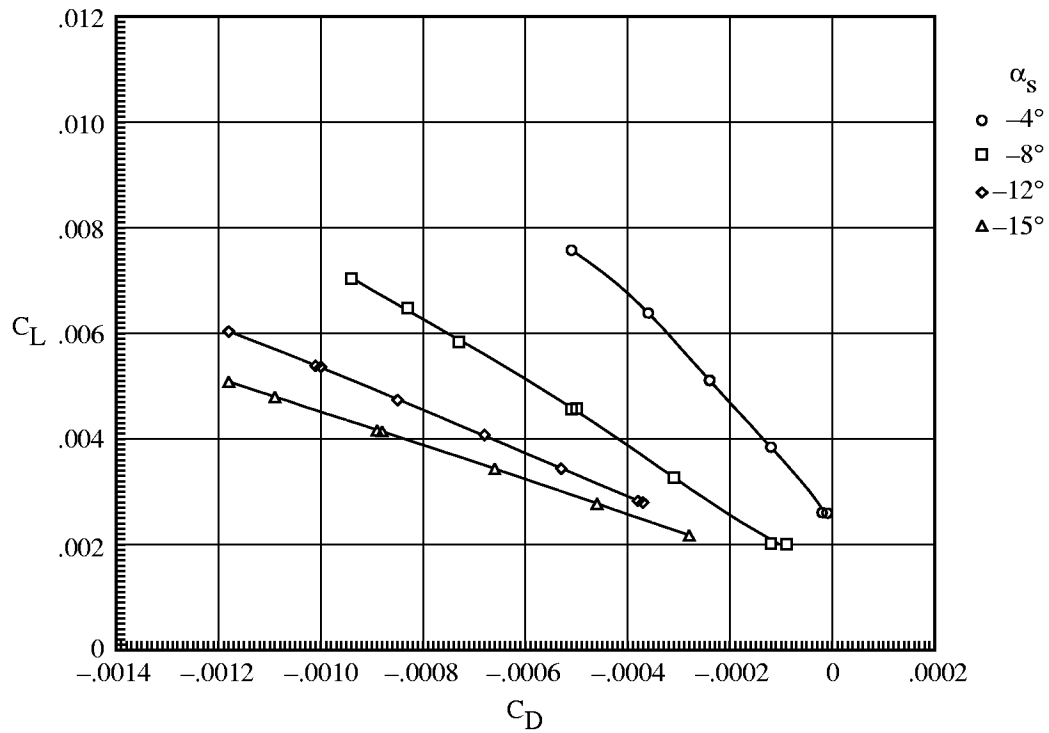


(a) C_L versus C_D .

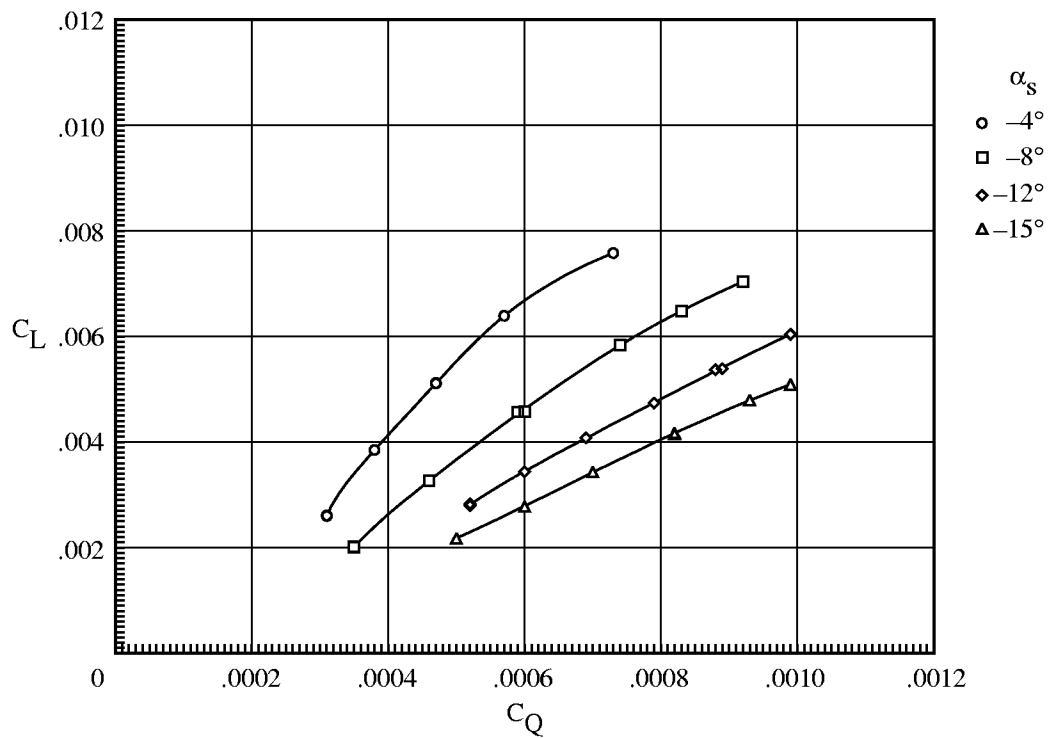


(b) C_L versus C_Q .

Figure A21. Basic forward-flight characteristics of -10° LE slat rotor for $\mu = 0.35$.

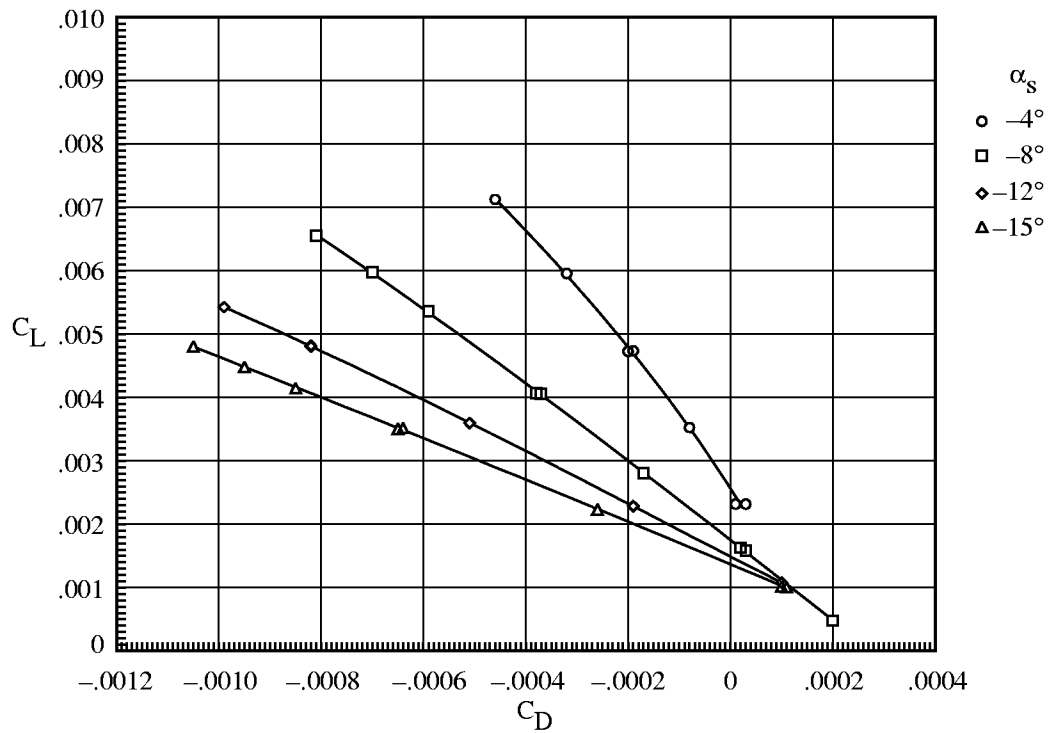


(a) C_L versus C_D .

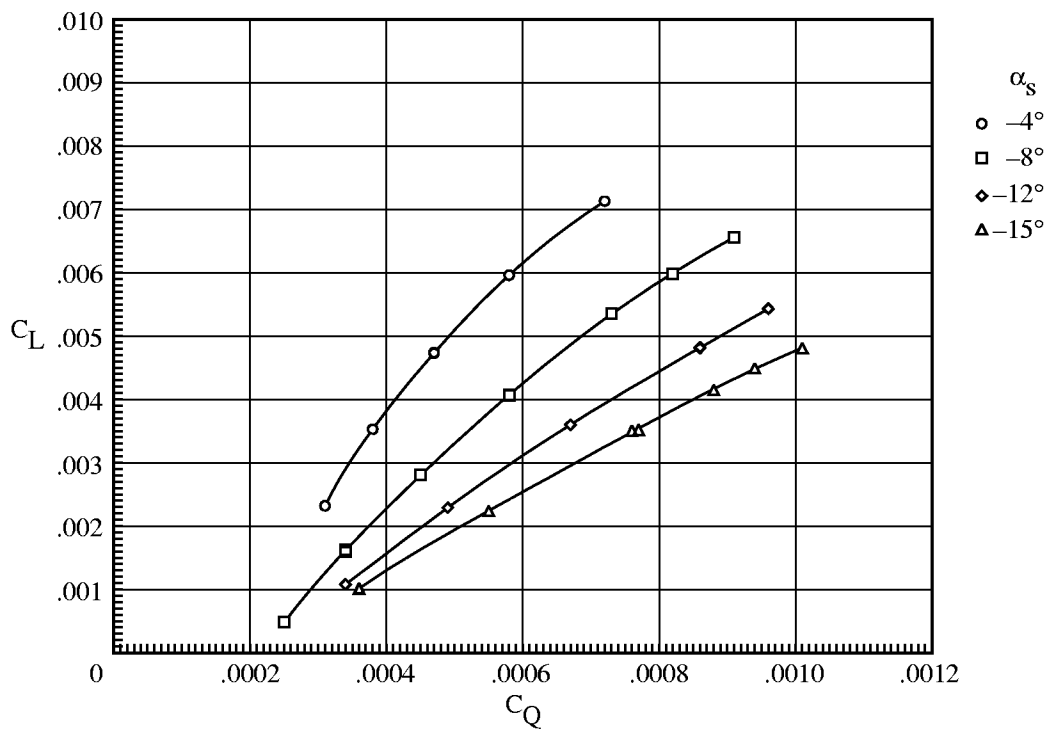


(b) C_L versus C_Q .

Figure A22. Basic forward-flight characteristics of -10° LE slat rotor for $\mu = 0.40$.

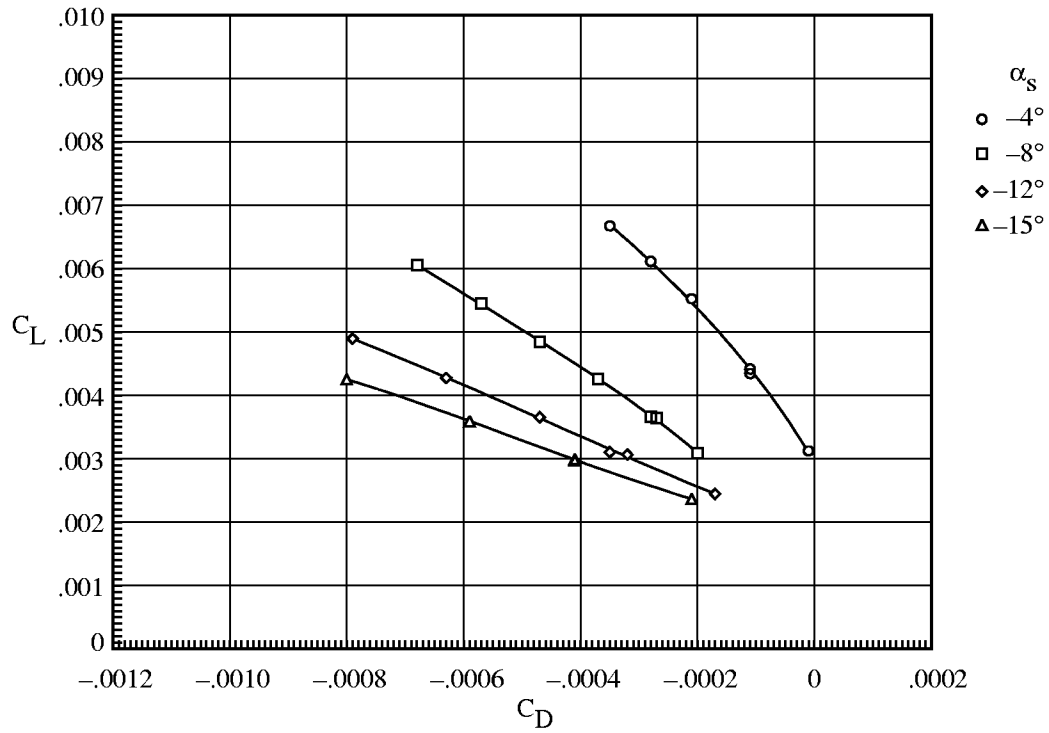


(a) C_L versus C_D .

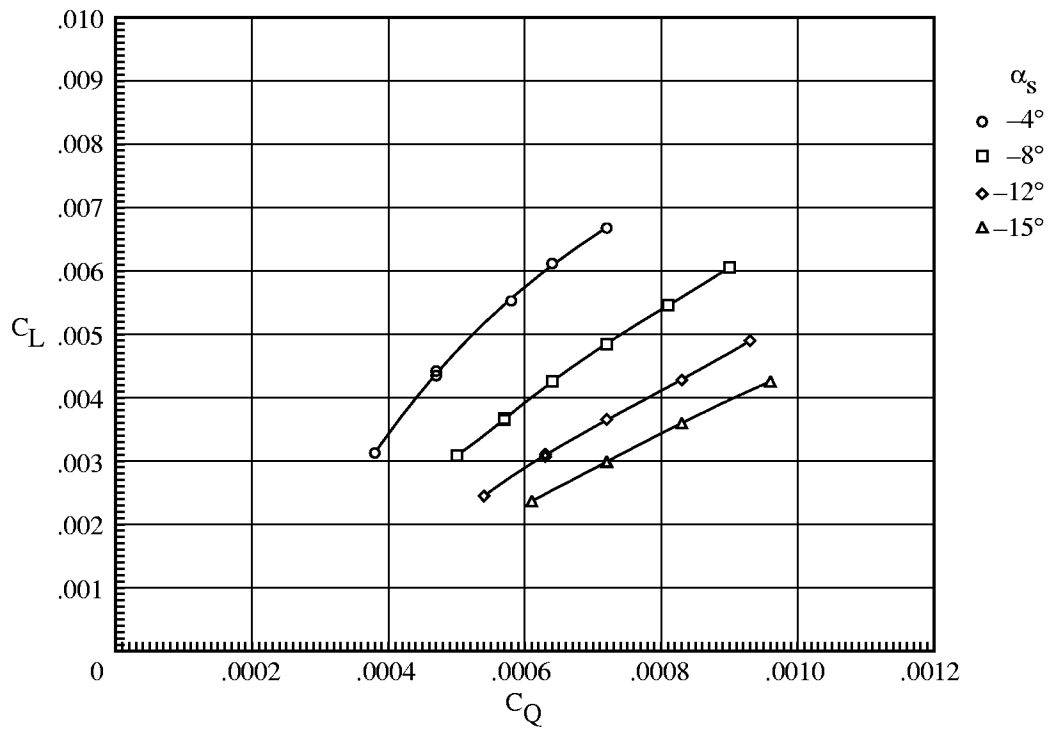


(b) C_L versus C_Q .

Figure A23. Basic forward-flight characteristics of -10° LE slat rotor for $\mu = 0.42$.

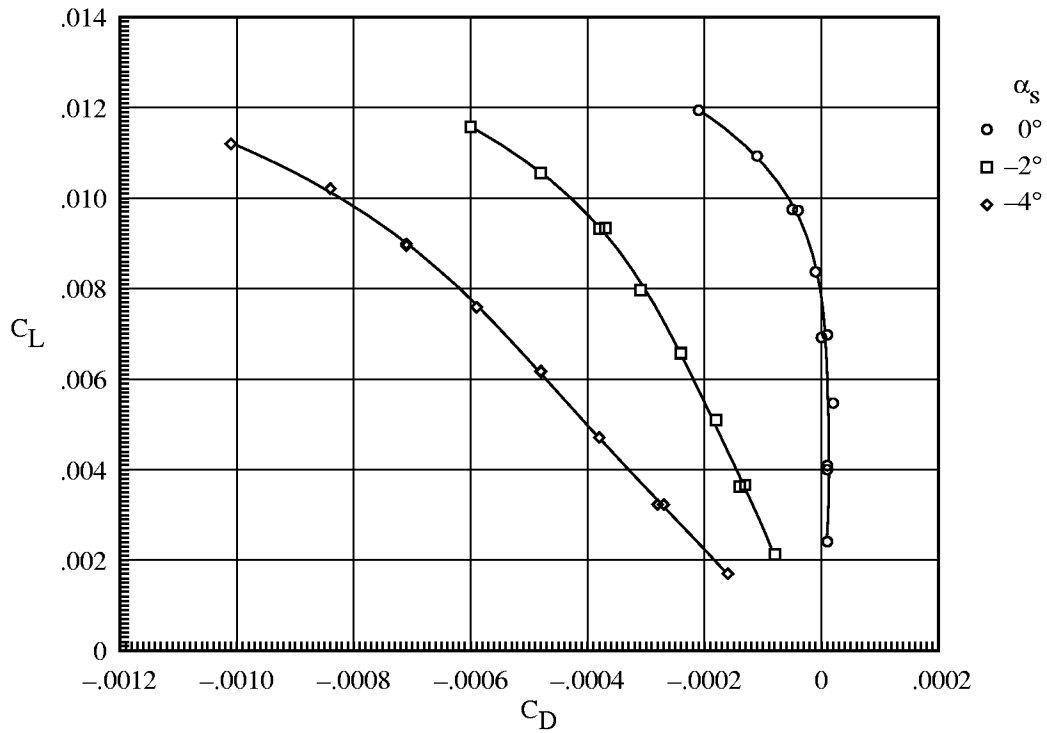


(a) C_L versus C_D .

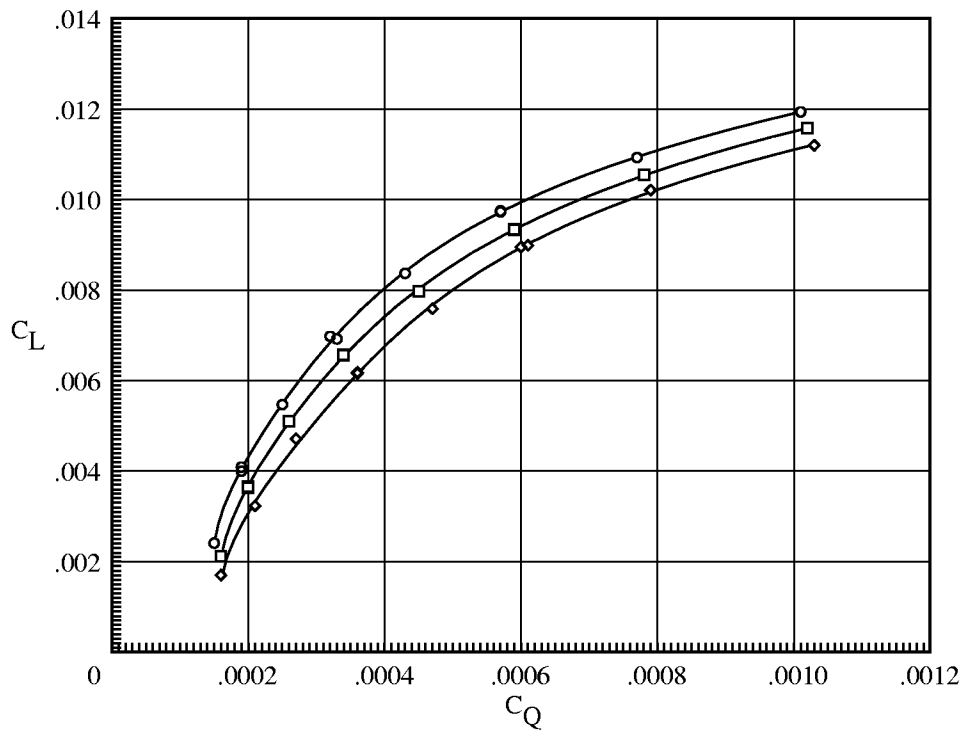


(b) C_L versus C_Q .

Figure A24. Basic forward-flight characteristics of -10° LE slat rotor for $\mu = 0.45$.

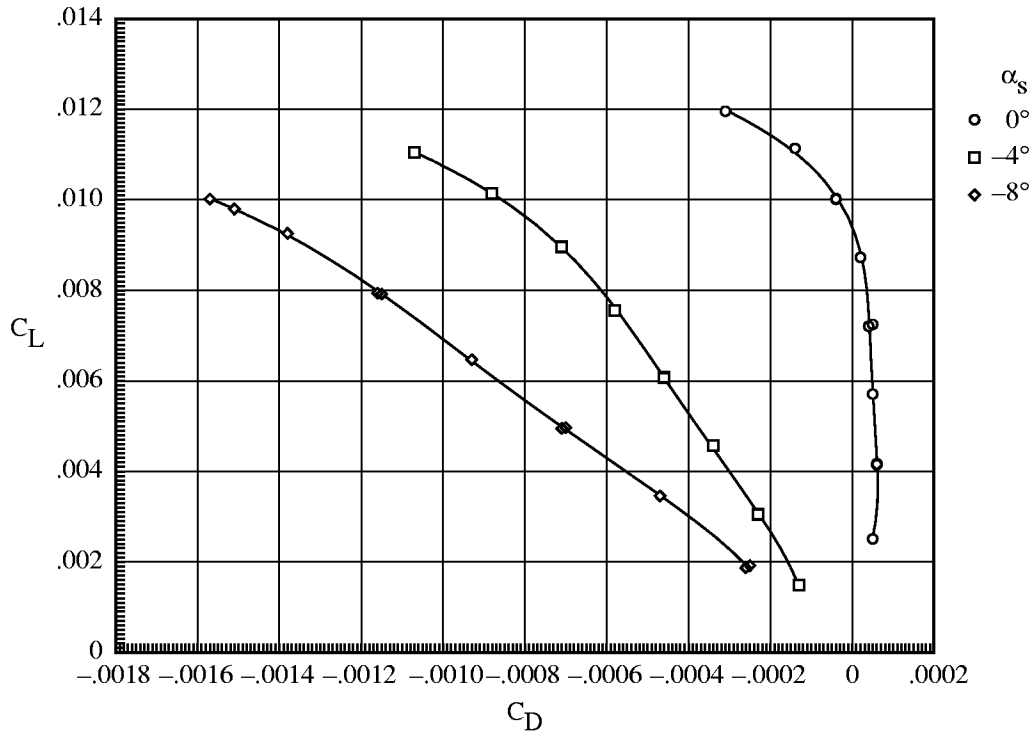


(a) C_L versus C_D .

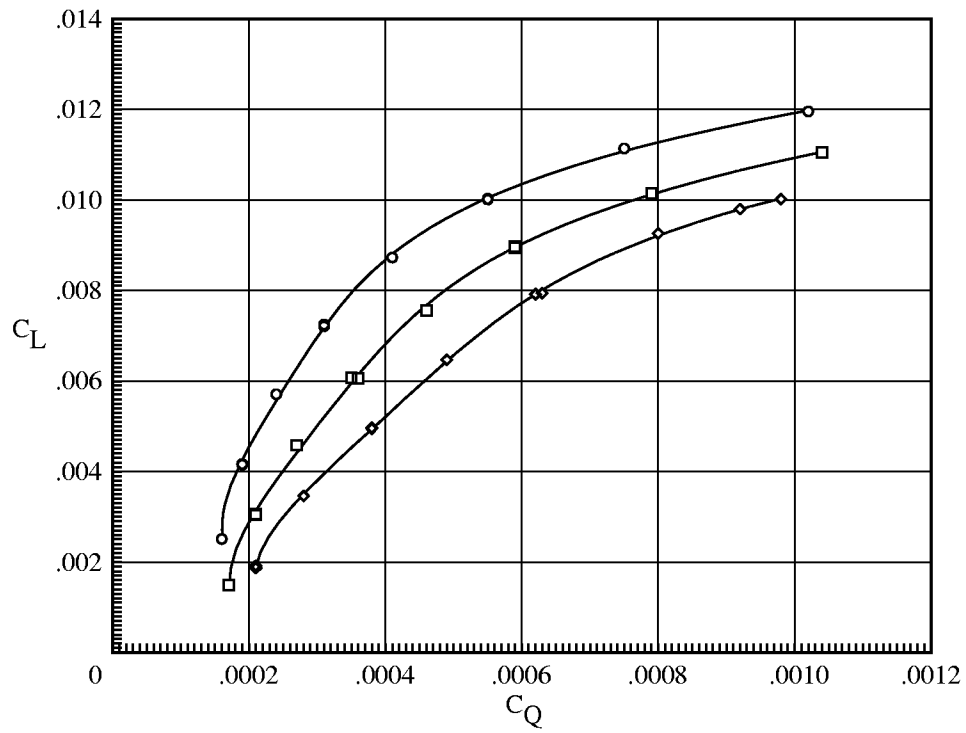


(b) C_L versus C_Q .

Figure A25. Basic forward-flight characteristics of 3° TE flap rotor for $\mu = 0.15$.

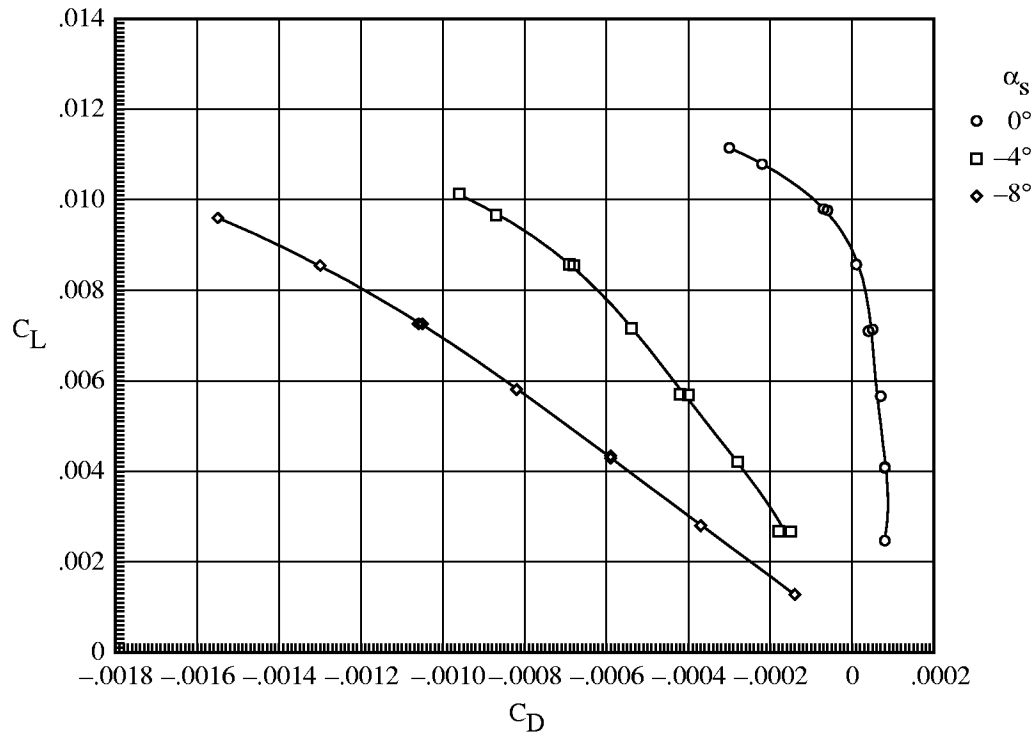


(a) C_L versus C_D .

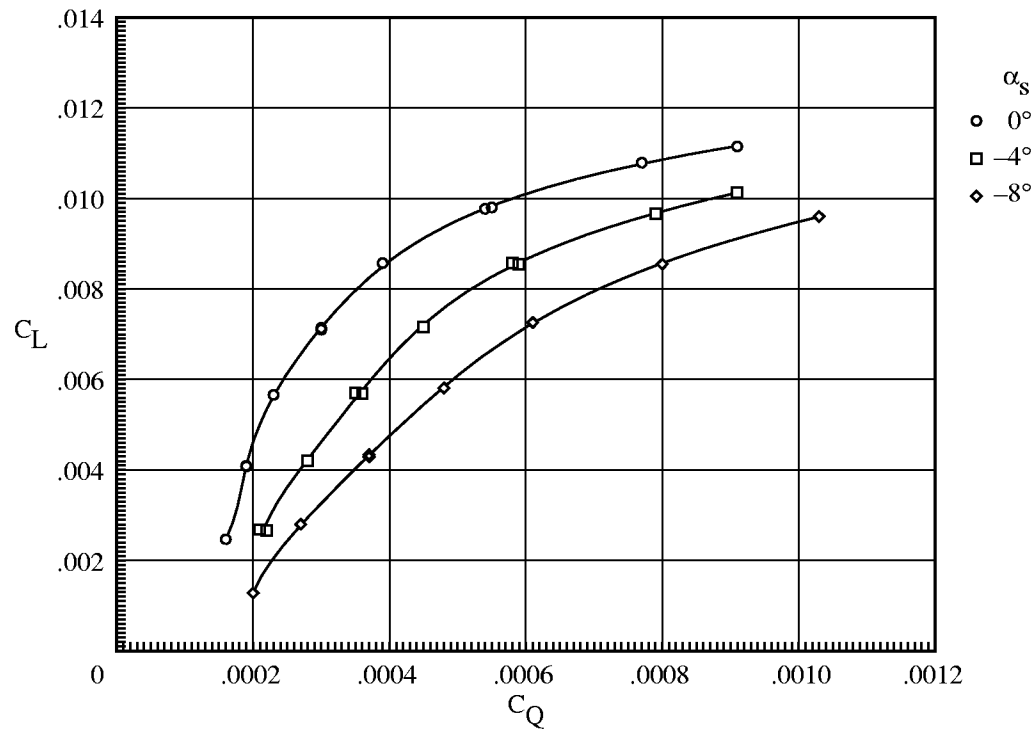


(b) C_L versus C_Q .

Figure A26. Basic forward-flight characteristics of 3° TE flap rotor for $\mu = 0.20$.

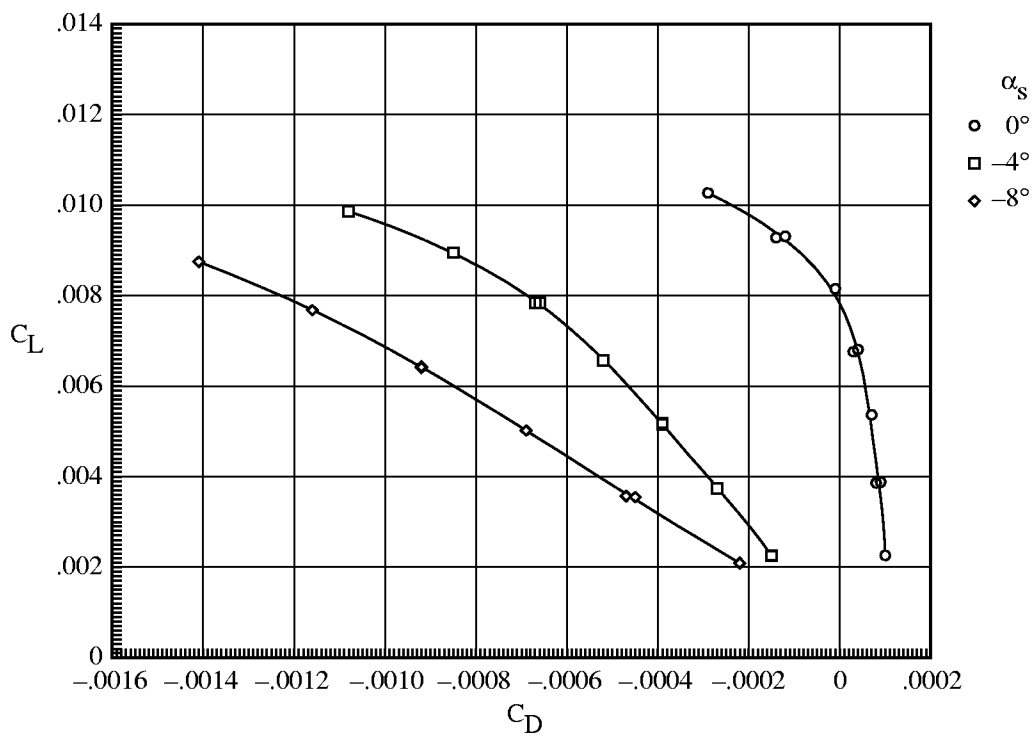


(a) C_L versus C_D .

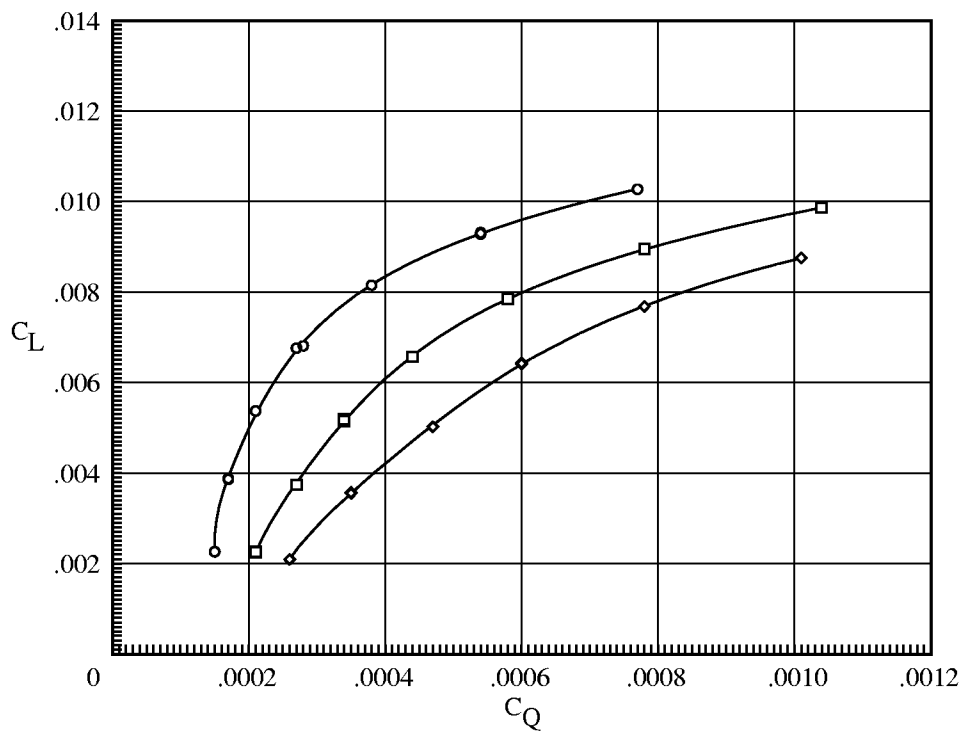


(b) C_L versus C_Q .

Figure A27. Basic forward-flight characteristics of 3° TE flap rotor for $\mu = 0.25$.

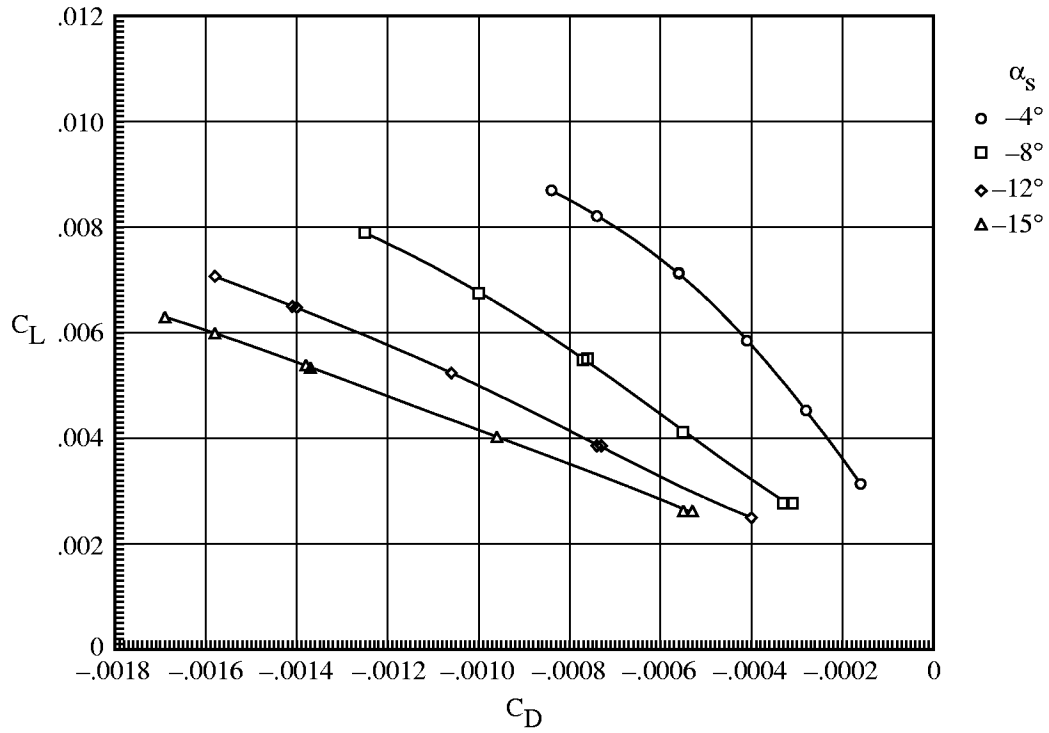


(a) C_L versus C_D .

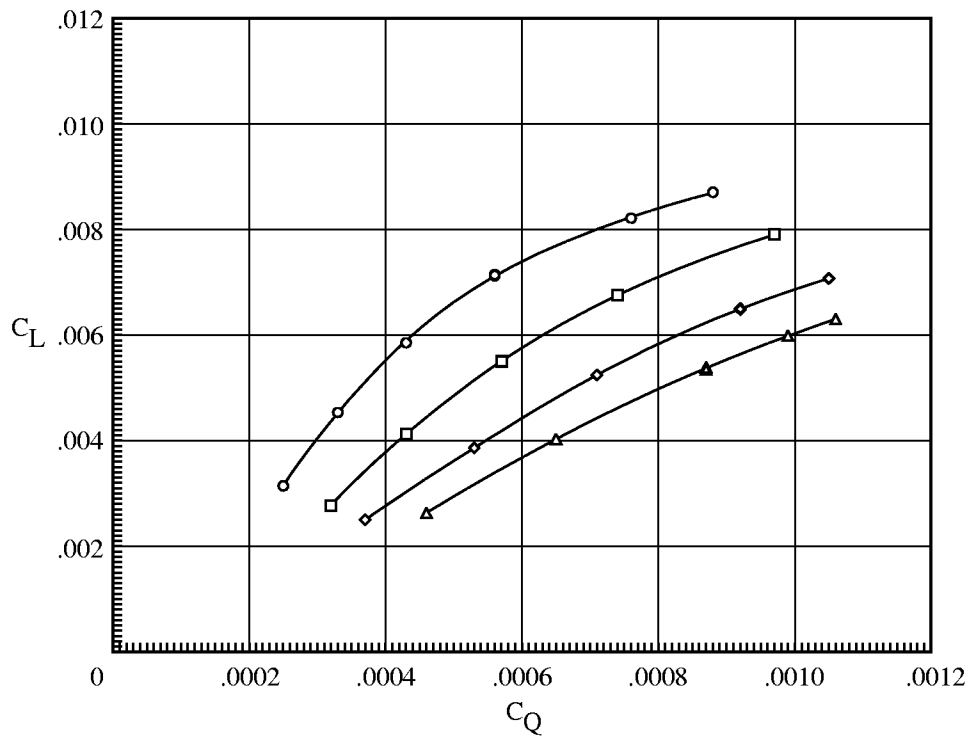


(b) C_L versus C_Q .

Figure A28. Basic forward-flight characteristics of 3° TE flap rotor for $\mu = 0.30$.

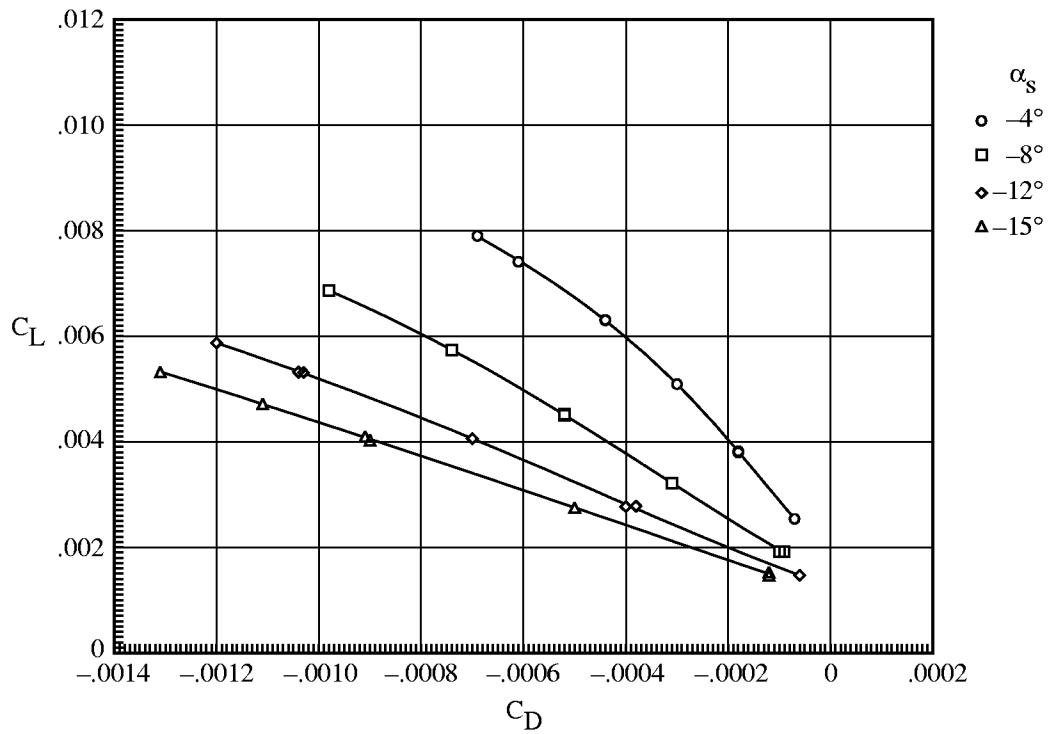


(a) C_L versus C_D .

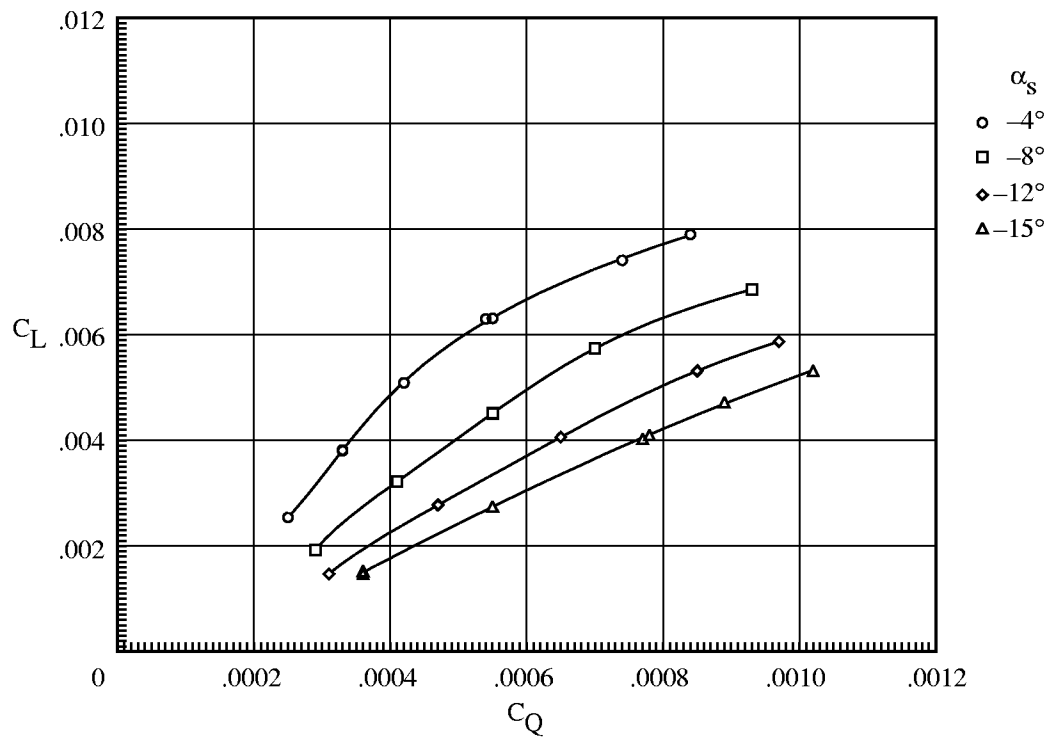


(b) C_L versus C_Q .

Figure A29. Basic forward-flight characteristics of 3° TE flap rotor for $\mu = 0.35$.

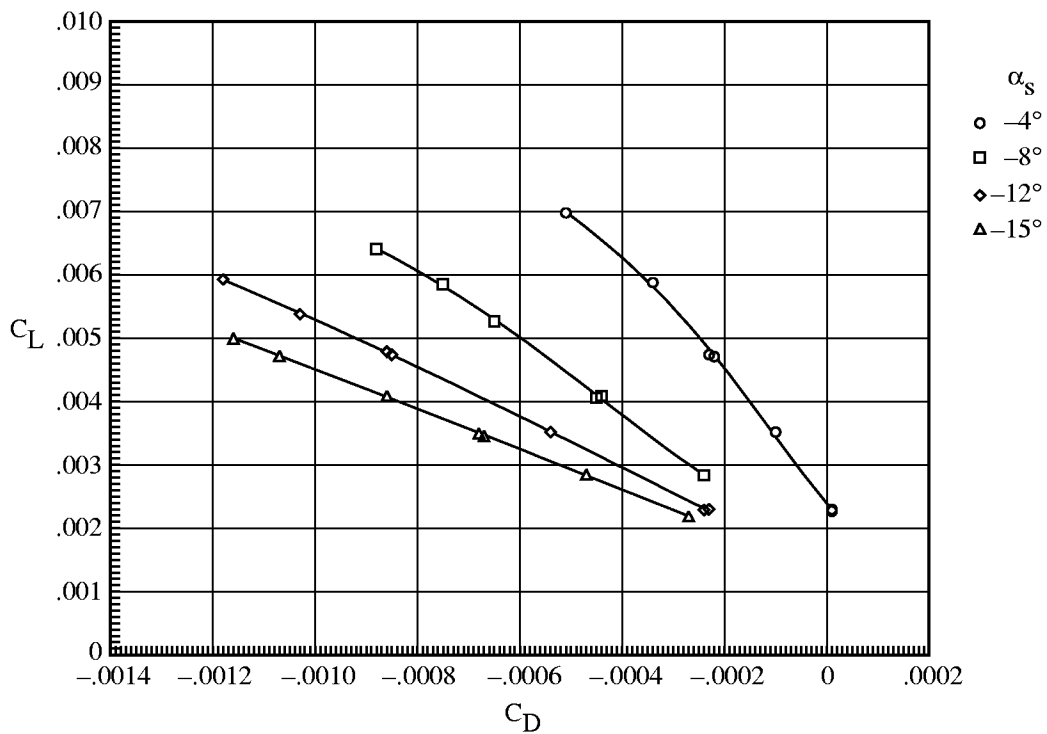


(a) C_L versus C_D .

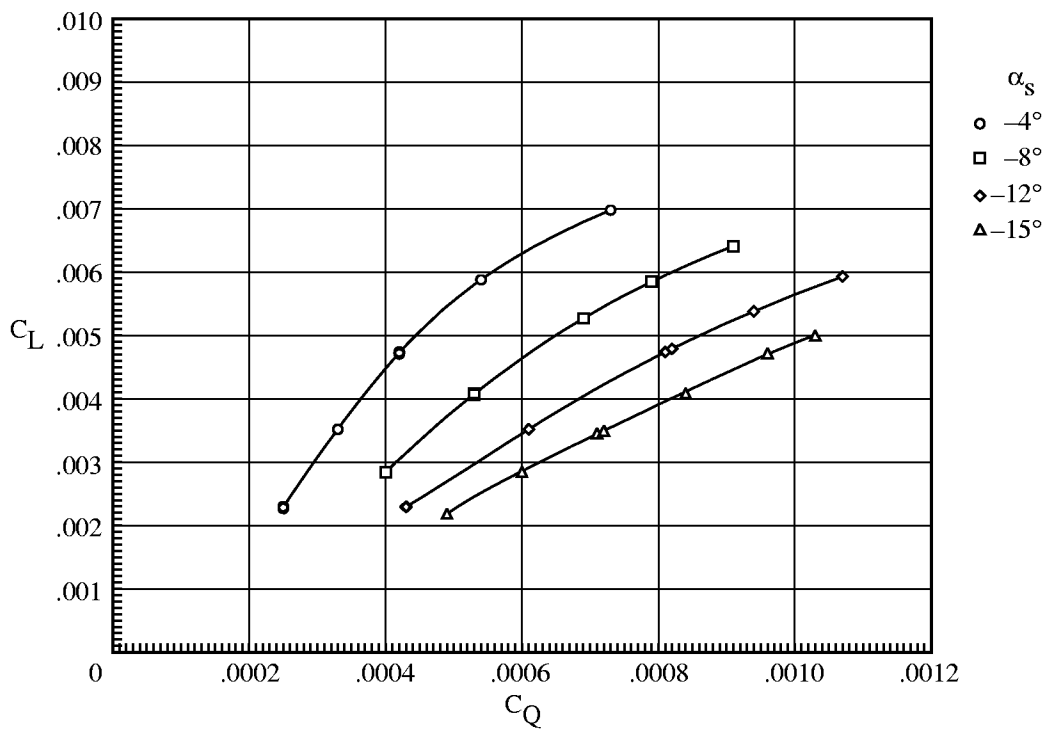


(b) C_L versus C_Q .

Figure A30. Basic forward-flight characteristics of 3° TE flap rotor for $\mu = 0.40$.

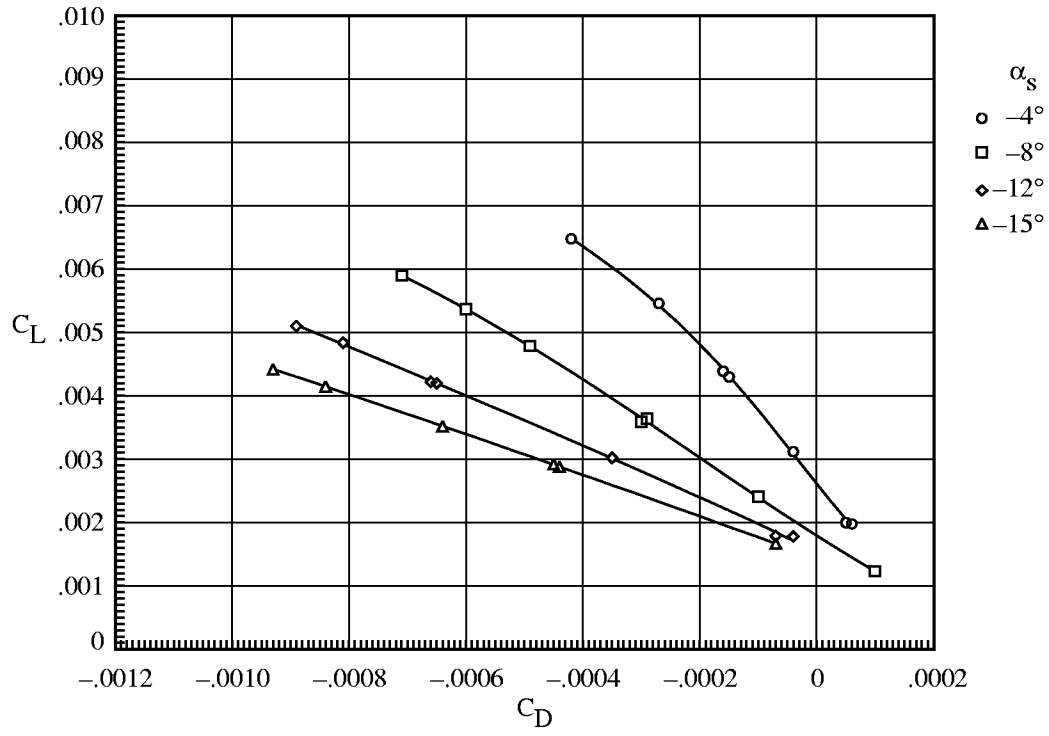


(a) C_L versus C_D .

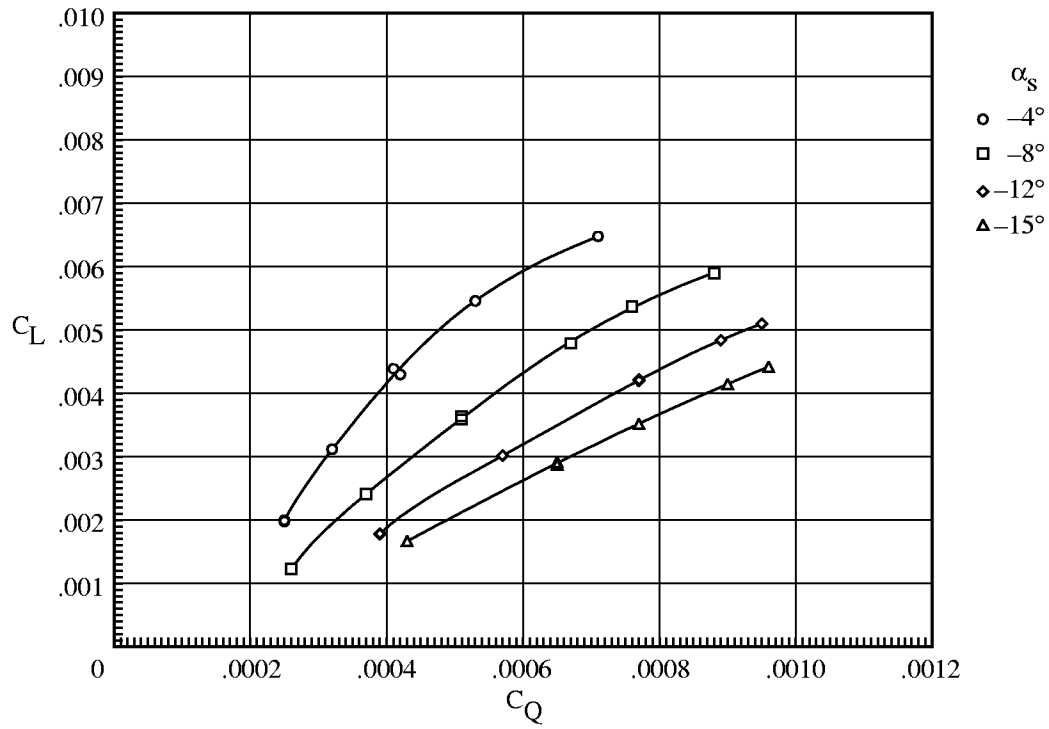


(b) C_L versus C_Q .

Figure A31. Basic forward-flight characteristics of 3° TE flap rotor for $\mu = 0.42$.

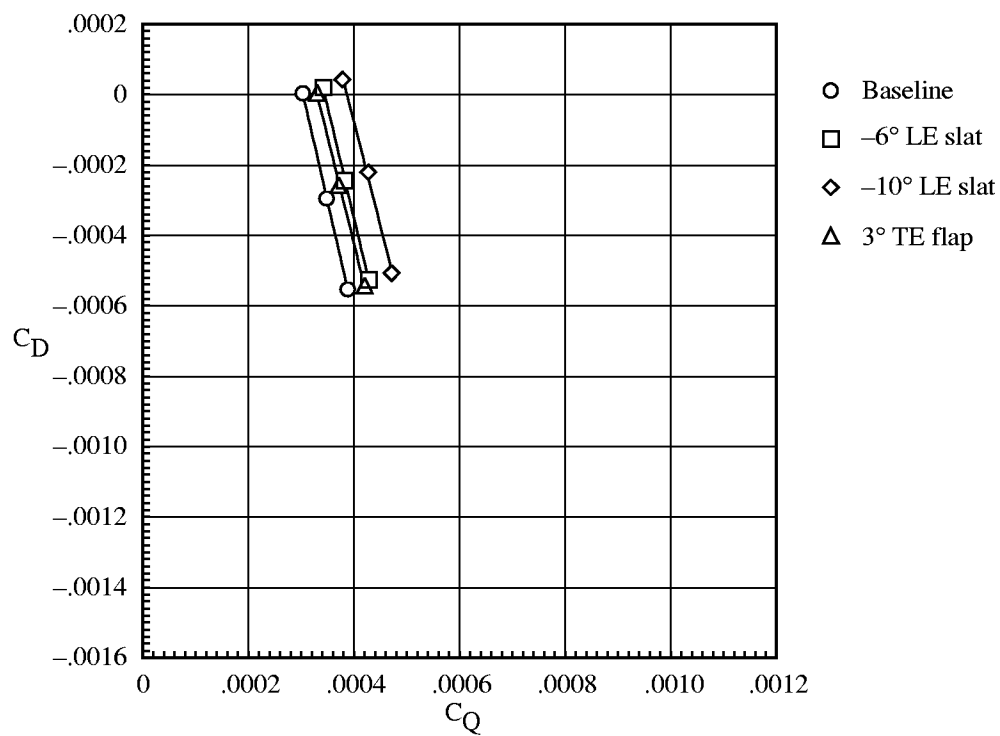


(a) C_L versus C_D .

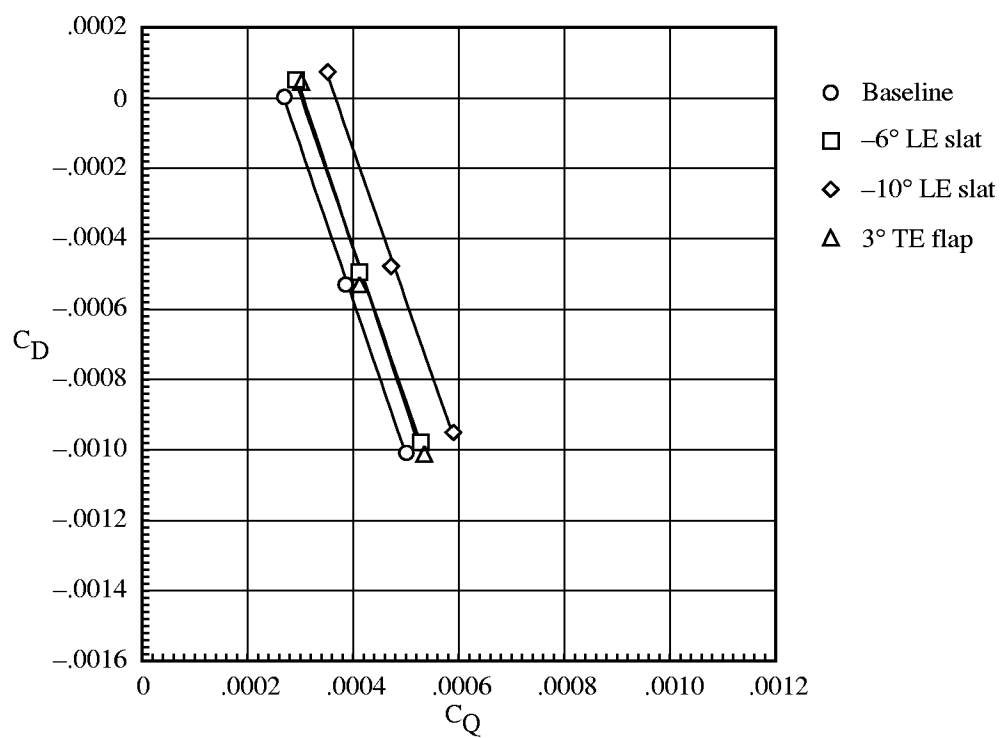


(b) C_L versus C_Q .

Figure A32. Basic forward-flight characteristics of 3° TE flap rotor for $\mu = 0.45$.

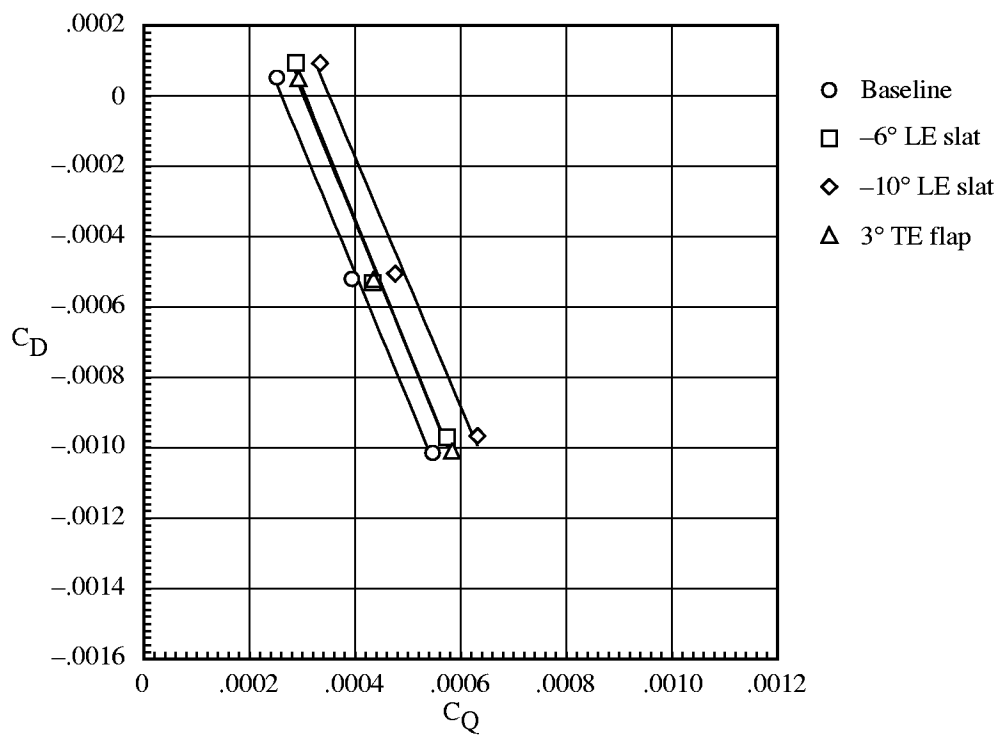


(a) $\mu = 0.15$.

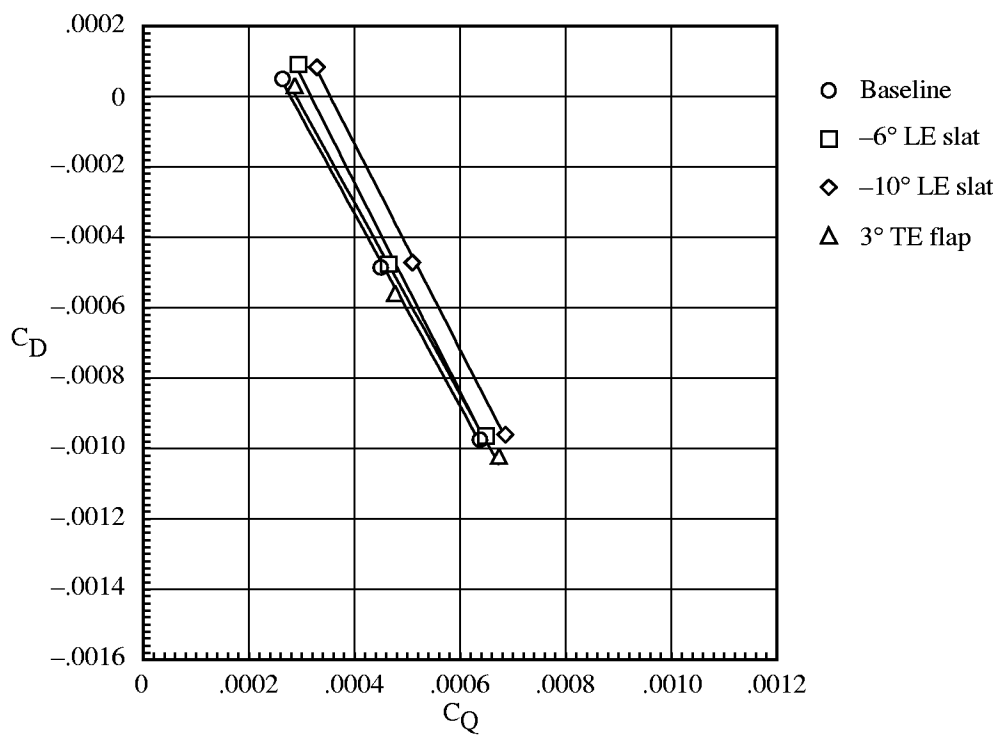


(b) $\mu = 0.20$.

Figure A33. Variation of rotor drag coefficient with rotor torque coefficient for $C_L = 0.007$.

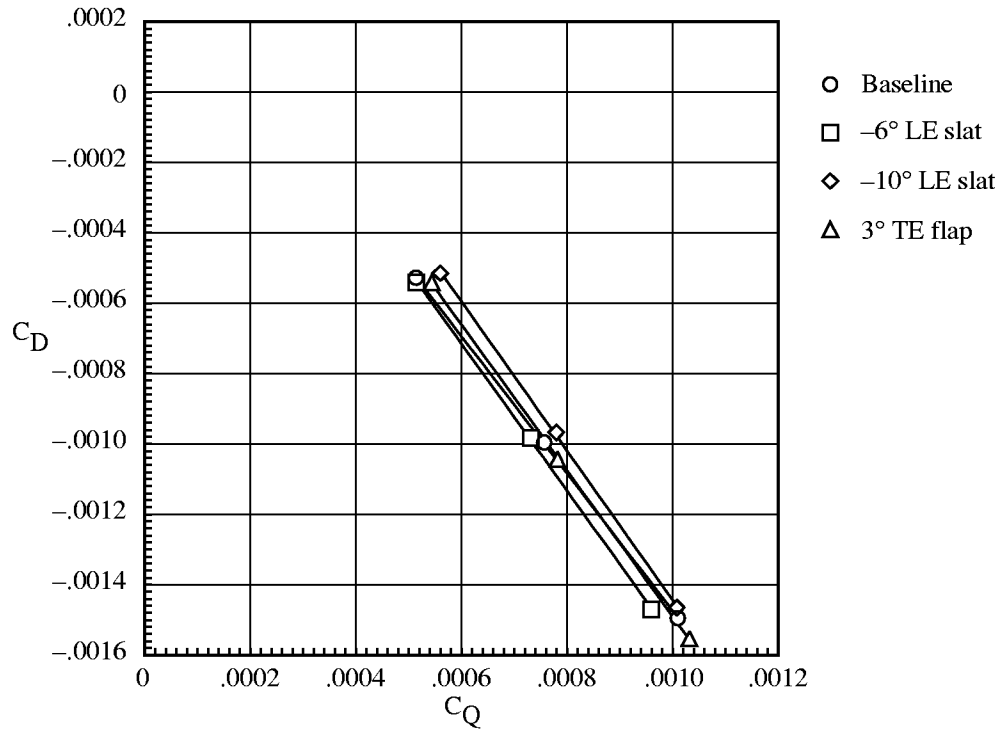


(c) $\mu = 0.25$.

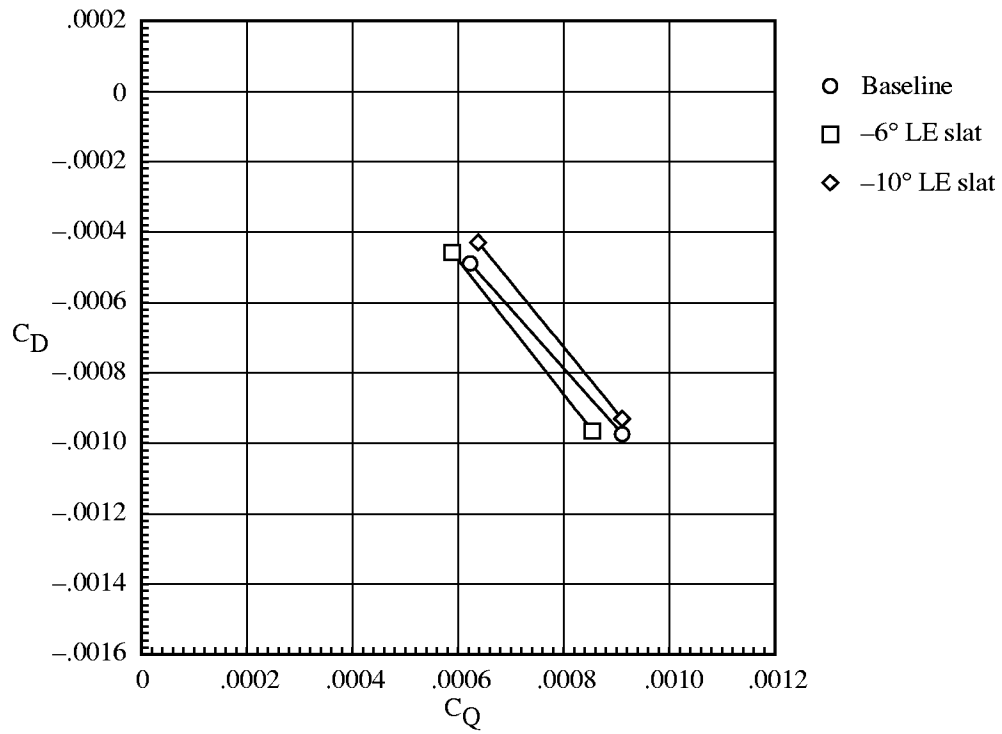


(d) $\mu = 0.30$.

Figure A33. Continued.

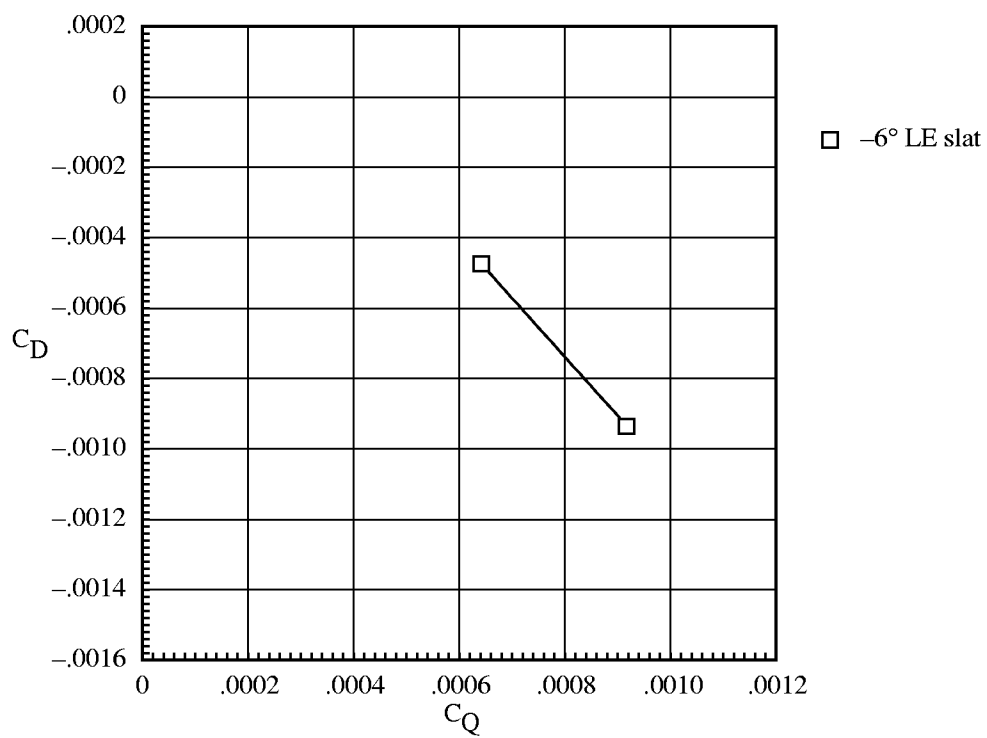


(e) $\mu = 0.35$.



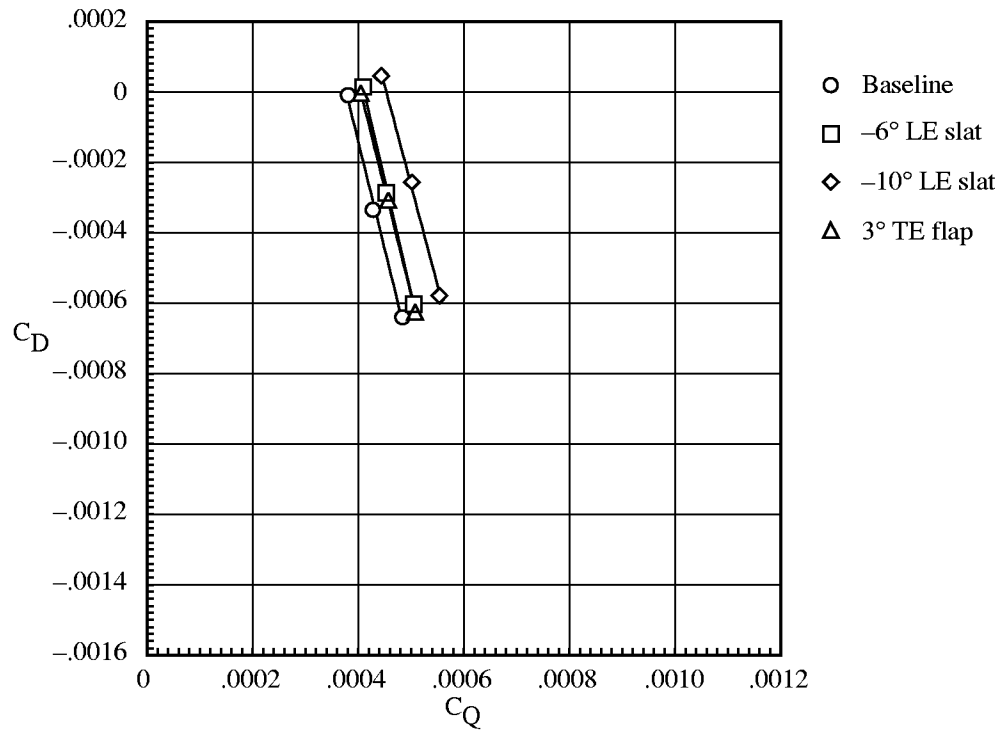
(f) $\mu = 0.40$.

Figure A33. Continued.

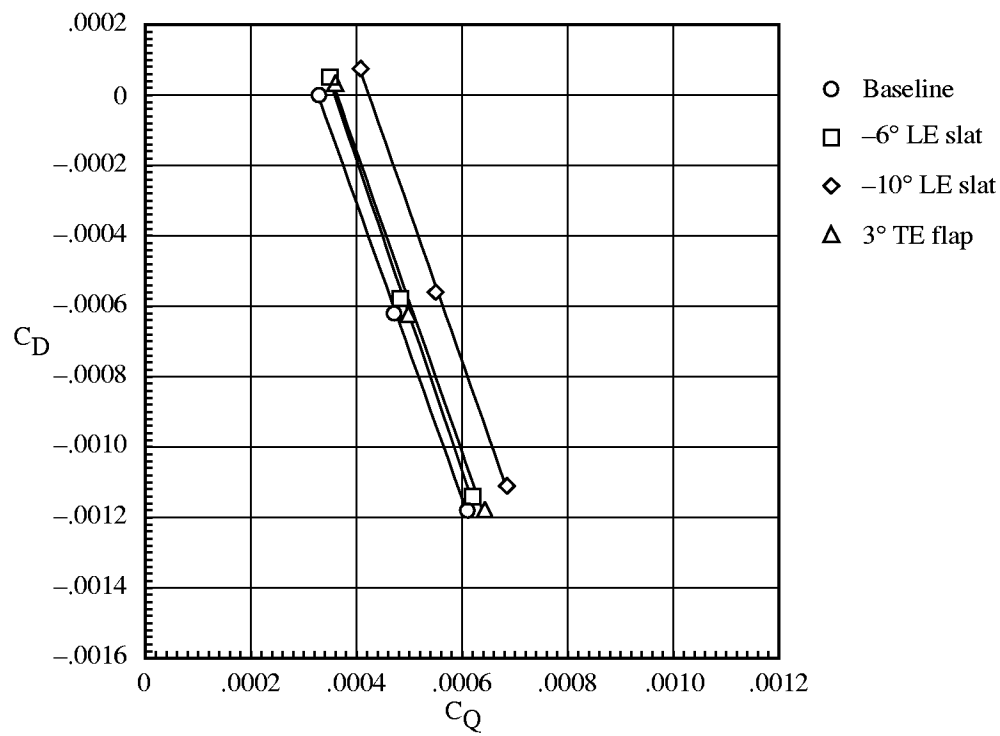


(g) $\mu = 0.43$.

Figure A33. Concluded.

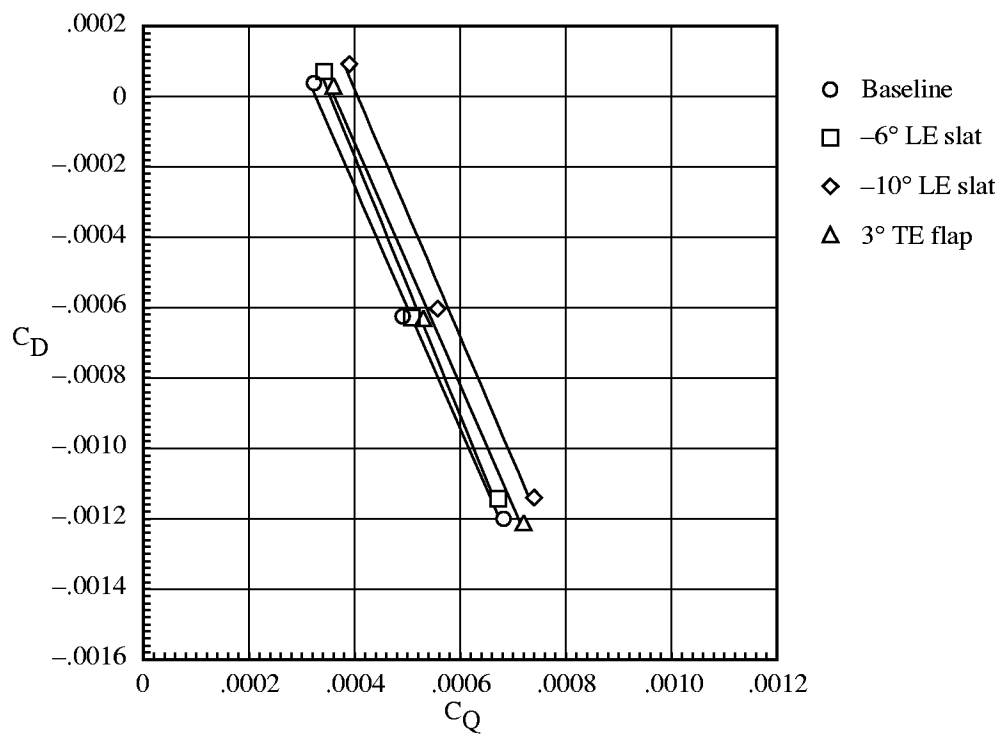


(a) $\mu = 0.15$.

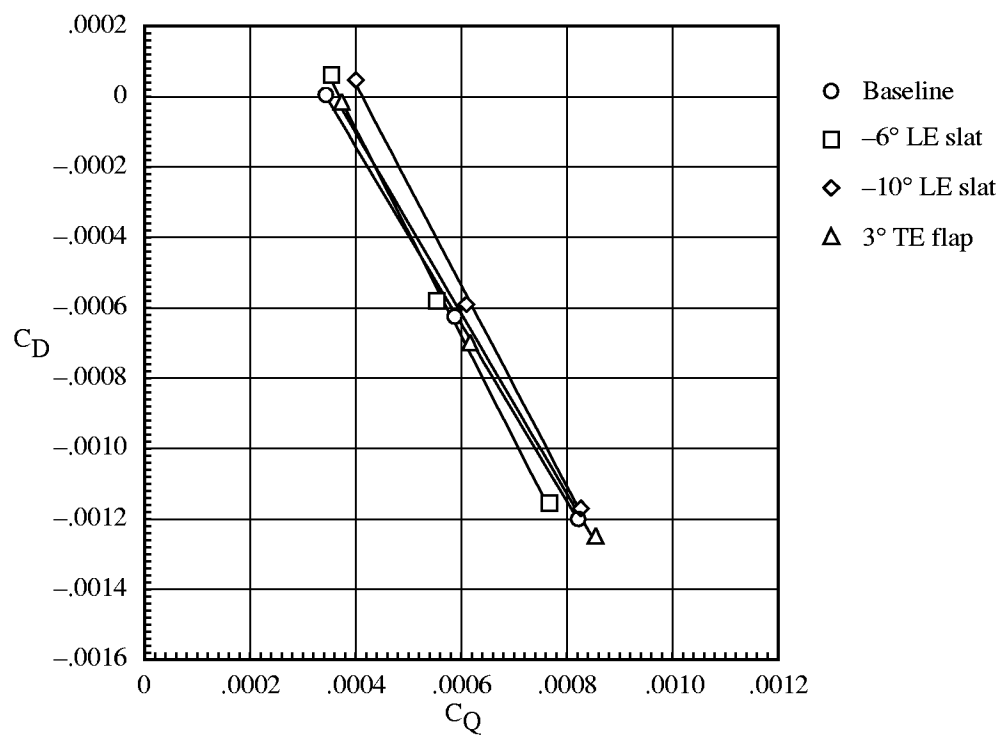


(b) $\mu = 0.20$.

Figure A34. Variation of rotor drag coefficient with rotor torque coefficient for $C_L = 0.0081$.

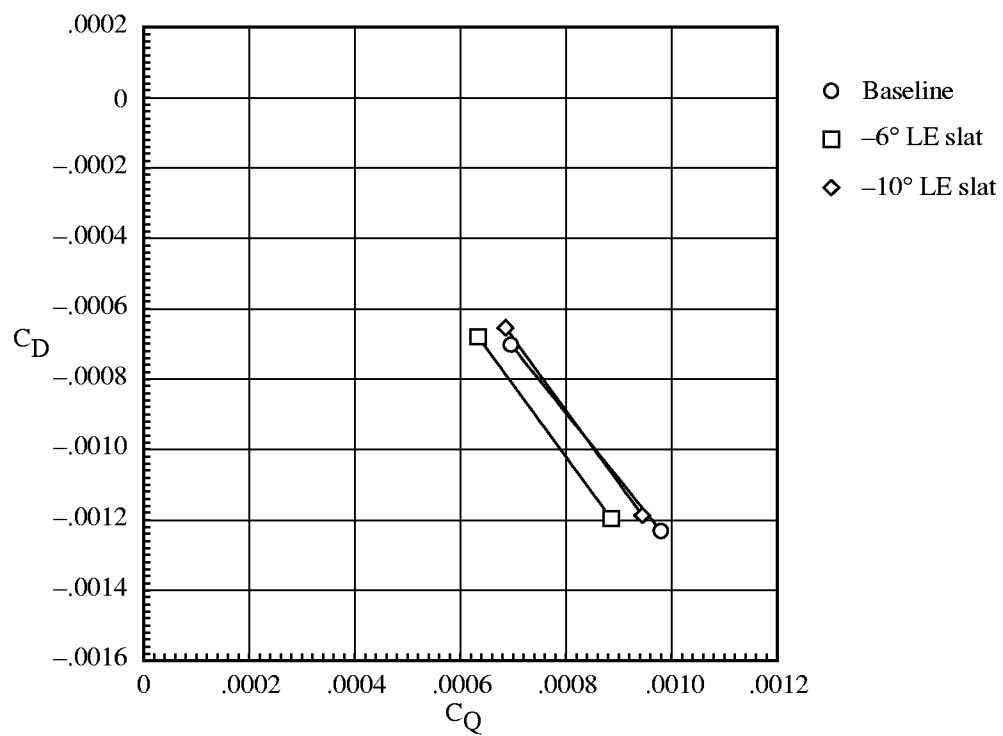


(c) $\mu = 0.25$.



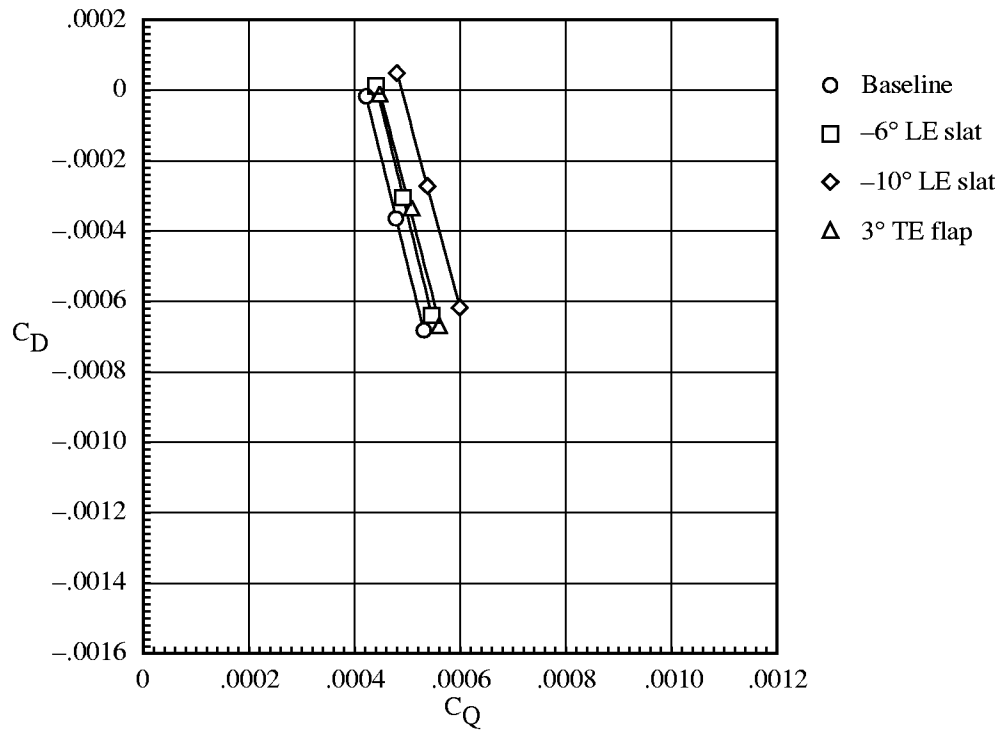
(d) $\mu = 0.30$.

Figure A34. Continued.

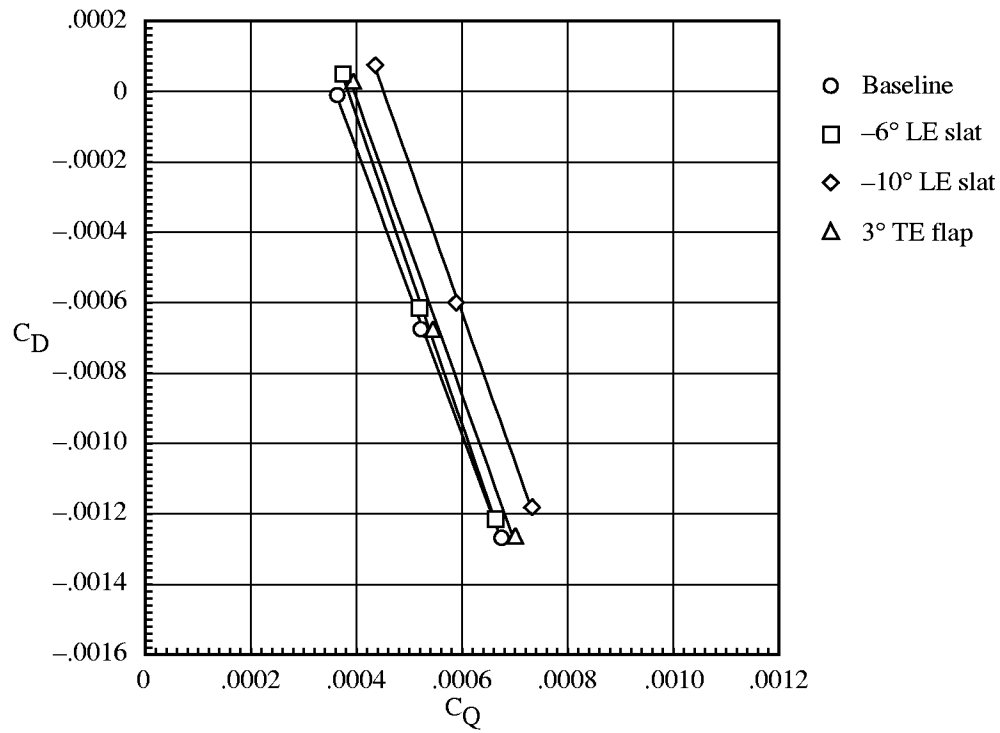


(e) $\mu = 0.35$.

Figure A34. Concluded.

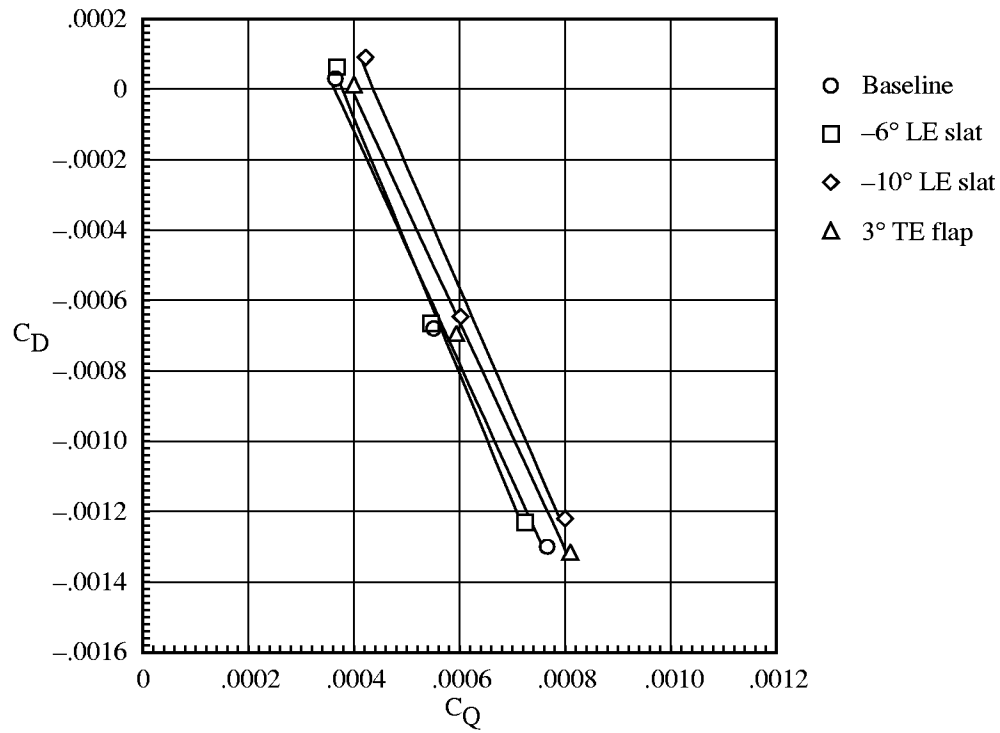


(a) $\mu = 0.15$.

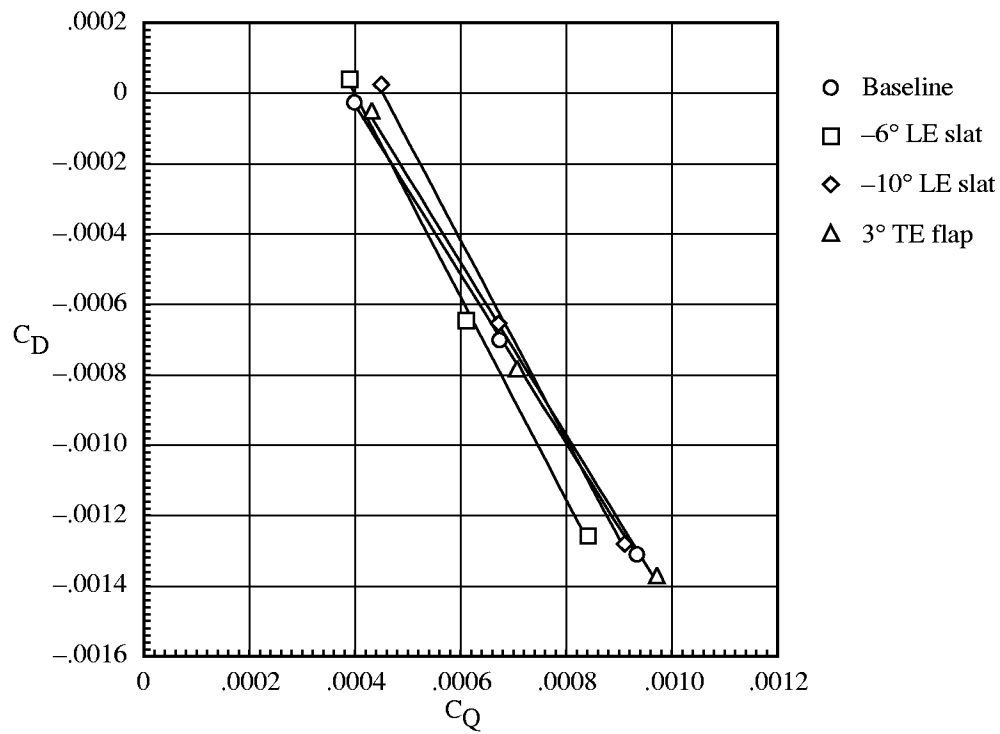


(b) $\mu = 0.20$.

Figure A35. Variation of rotor drag coefficient with rotor torque coefficient for $C_L = 0.0086$.

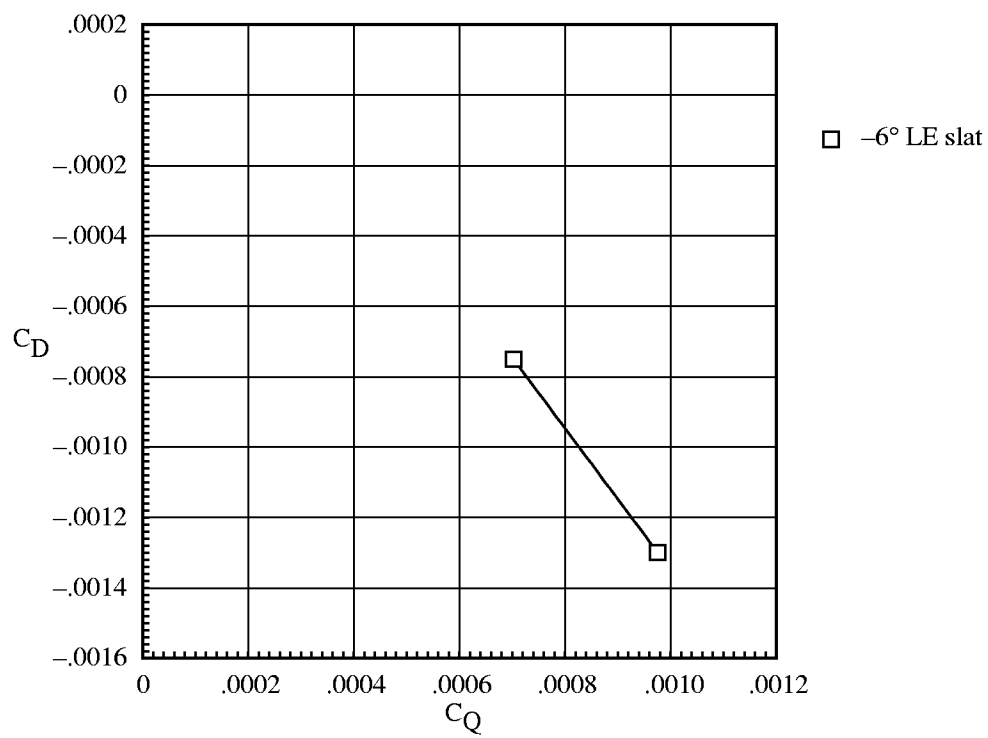


(c) $\mu = 0.25$.



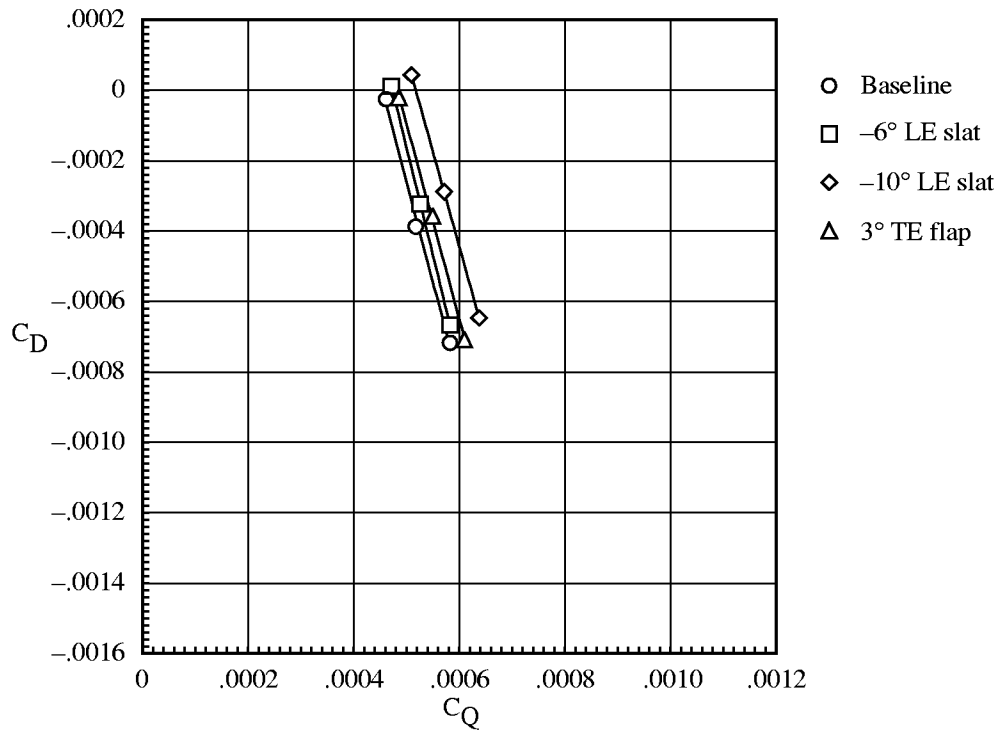
(d) $\mu = 0.30$.

Figure A35. Continued.

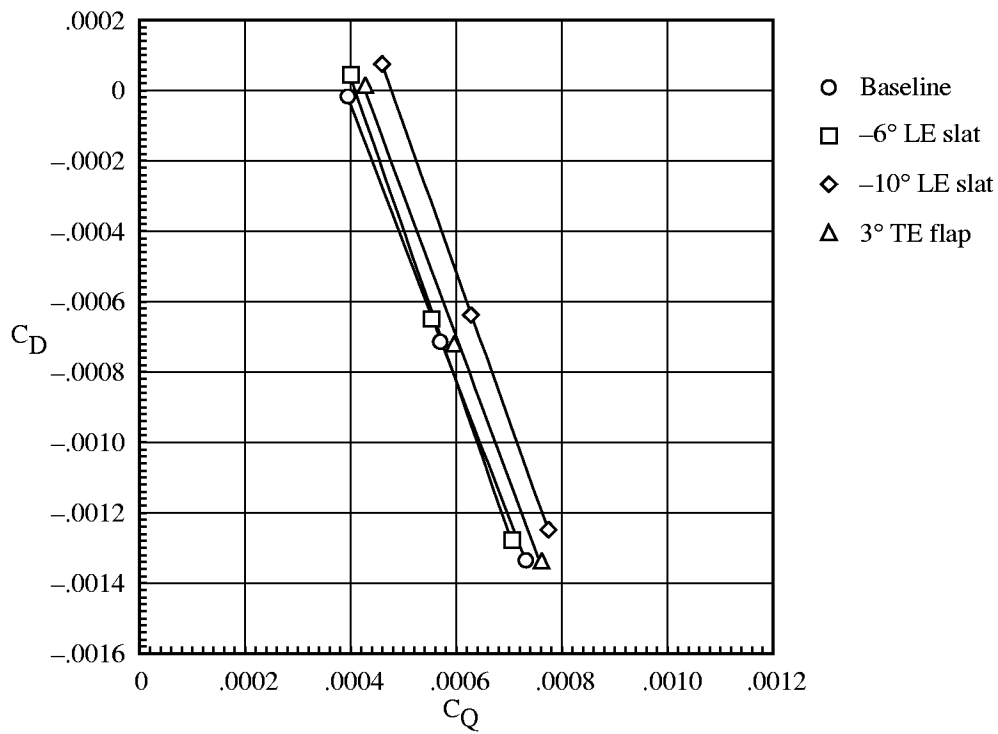


(e) $\mu = 0.35$.

Figure A35. Concluded.

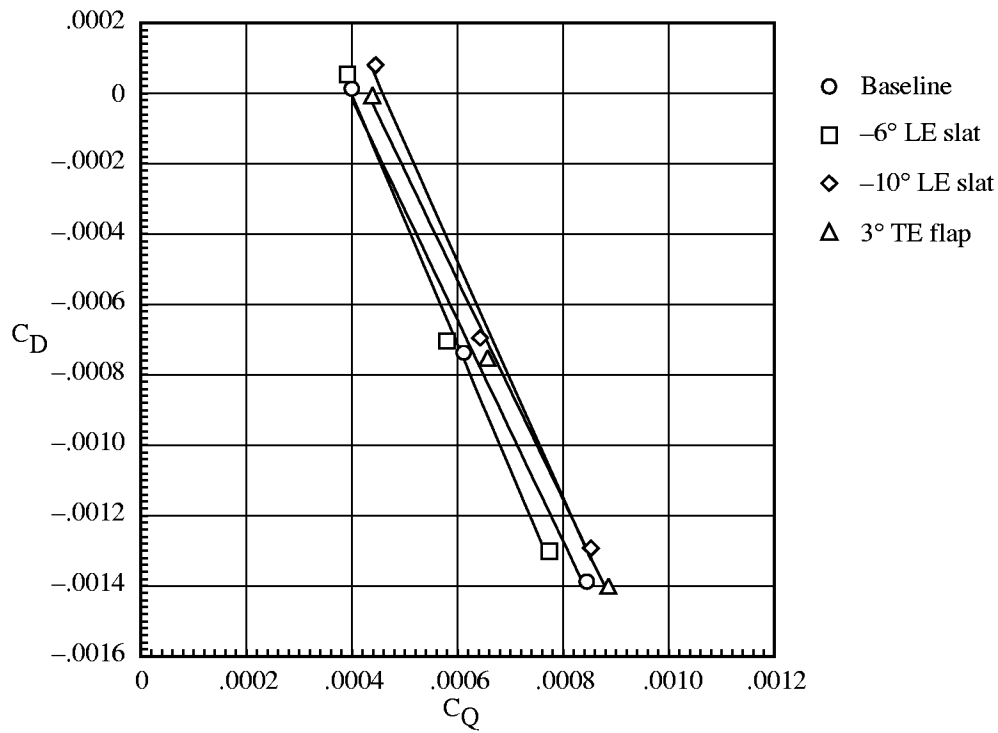


(a) $\mu = 0.15$.

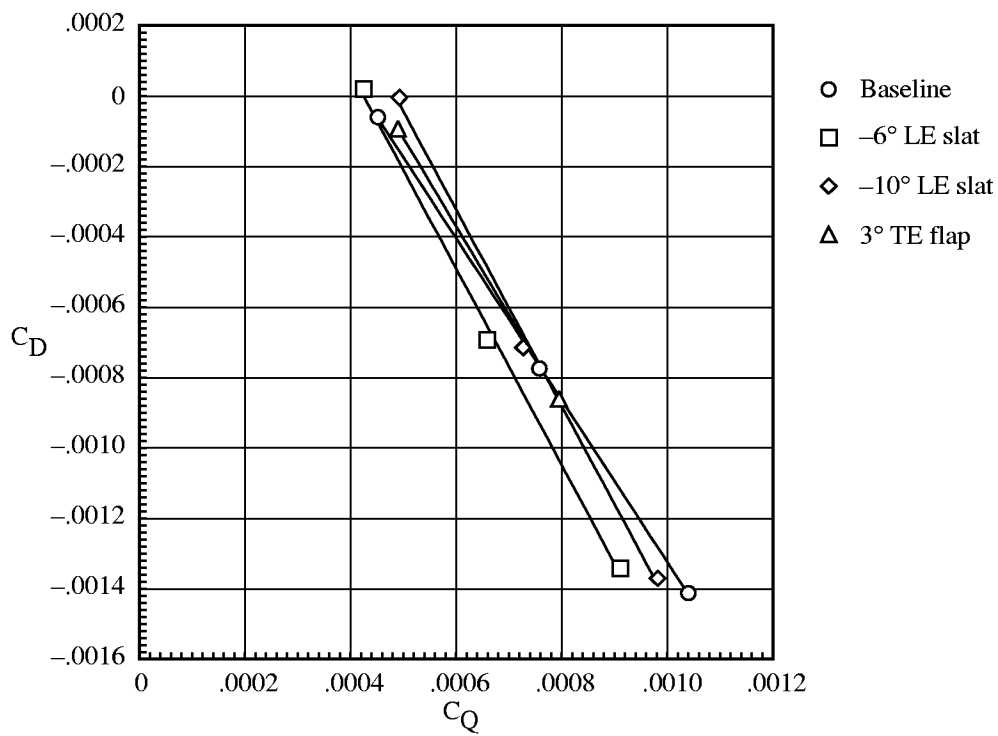


(b) $\mu = 0.20$.

Figure A36. Variation of rotor drag coefficient with rotor torque coefficient for $C_L = 0.009$.

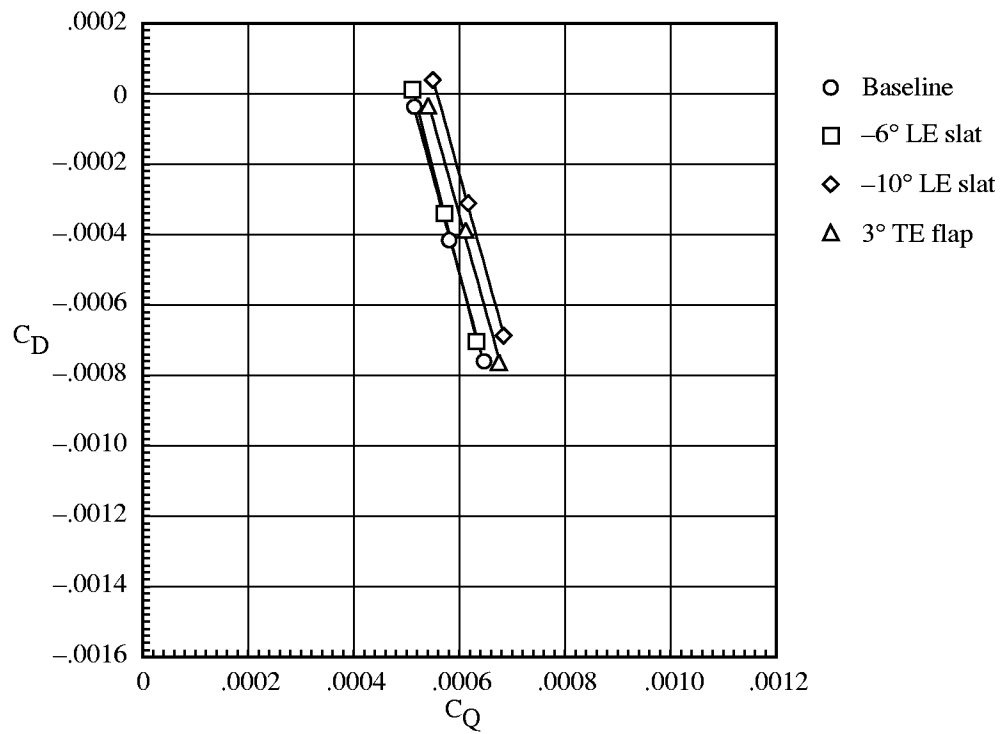


(c) $\mu = 0.25$.

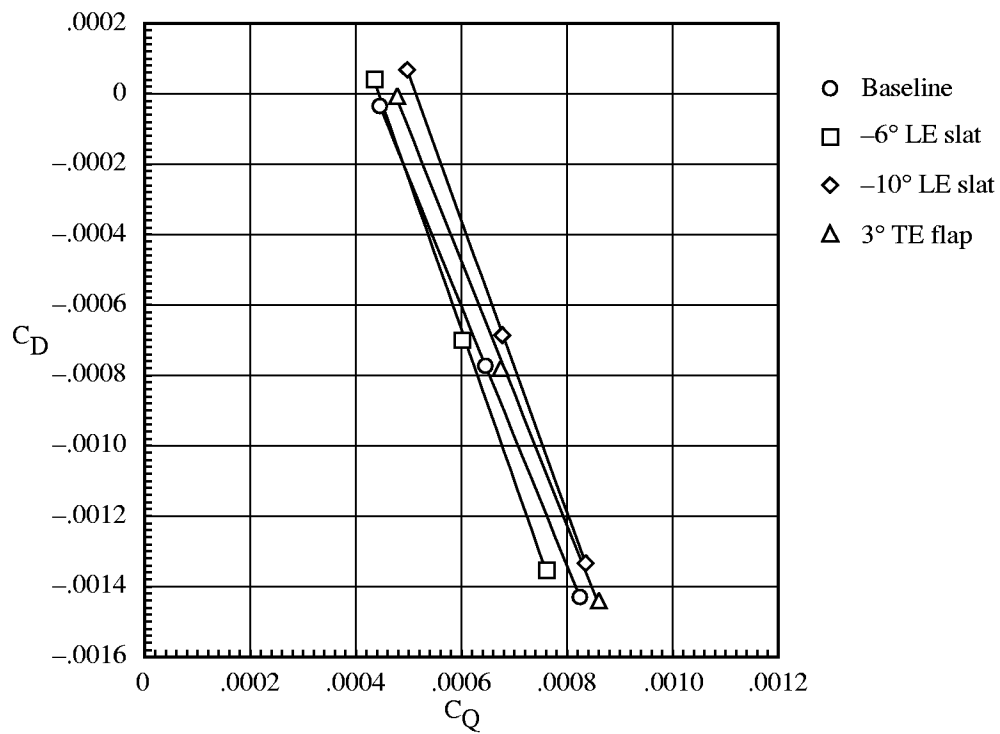


(d) $\mu = 0.30$.

Figure A36. Concluded.

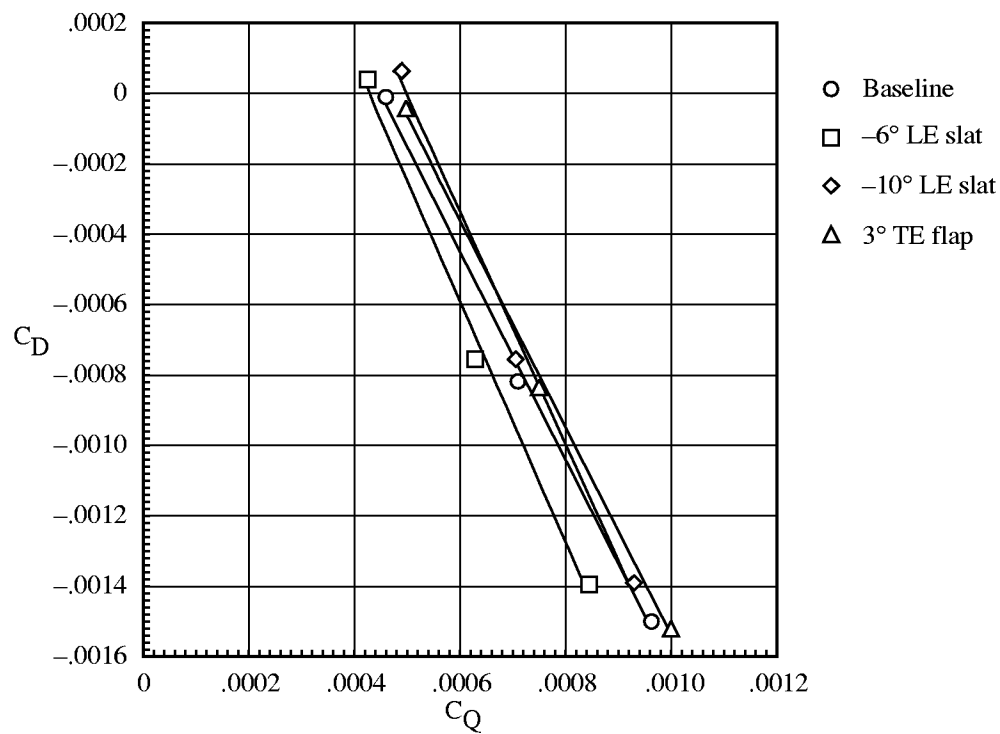


(a) $\mu = 0.15$.

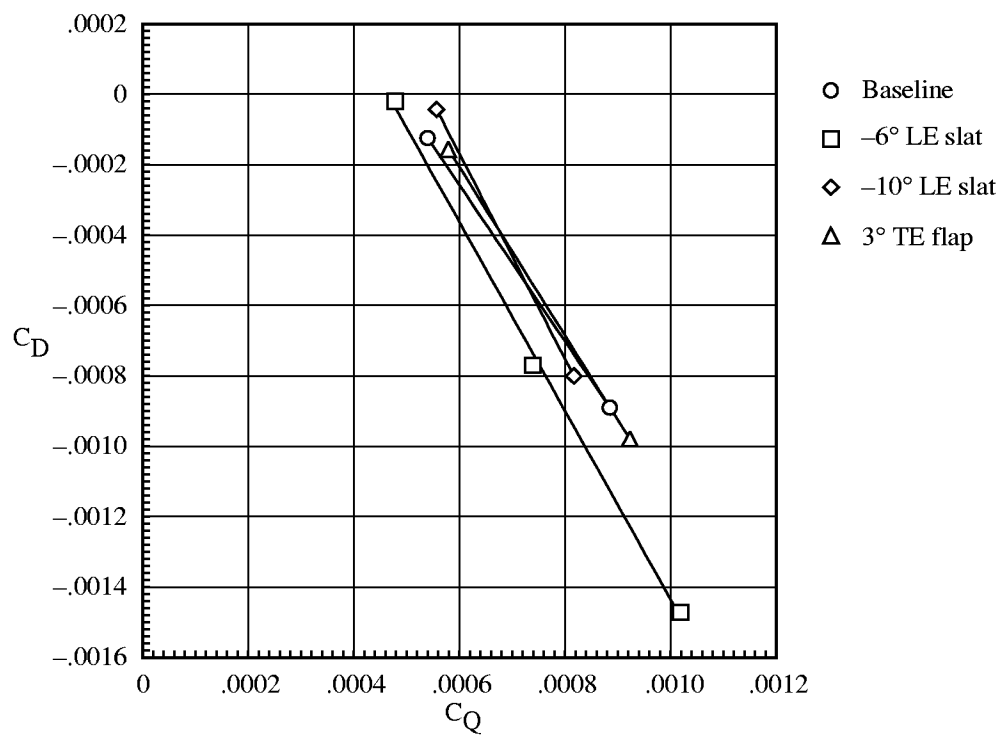


(b) $\mu = 0.20$.

Figure A37. Variation of rotor drag coefficient with rotor torque coefficient for $C_L = 0.0095$.

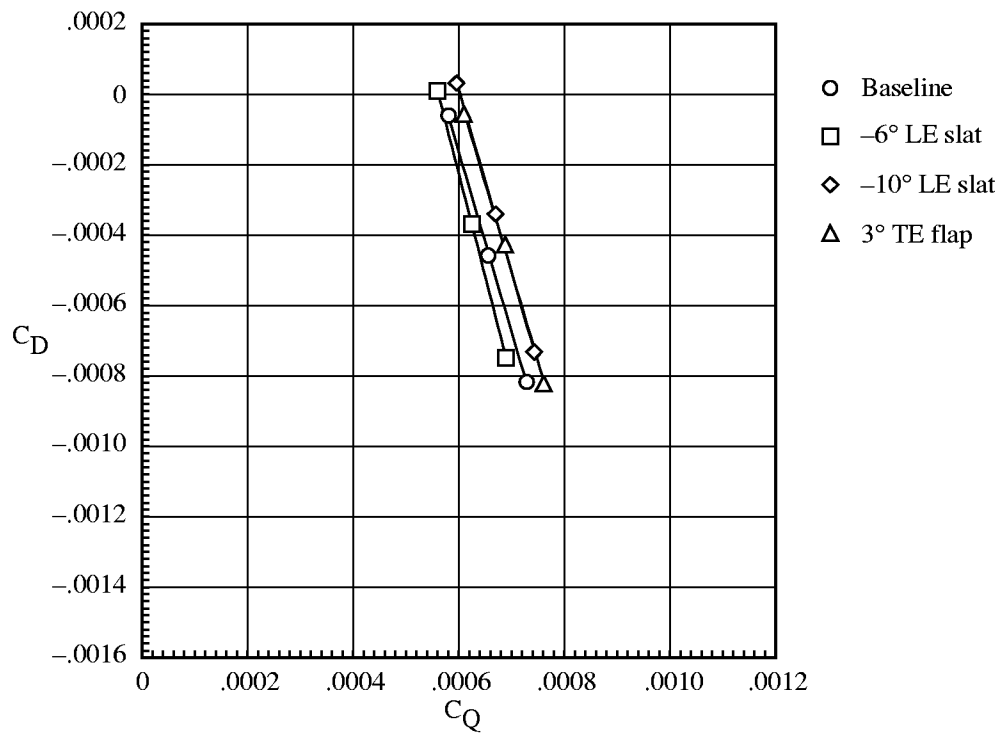


(c) $\mu = 0.25$.

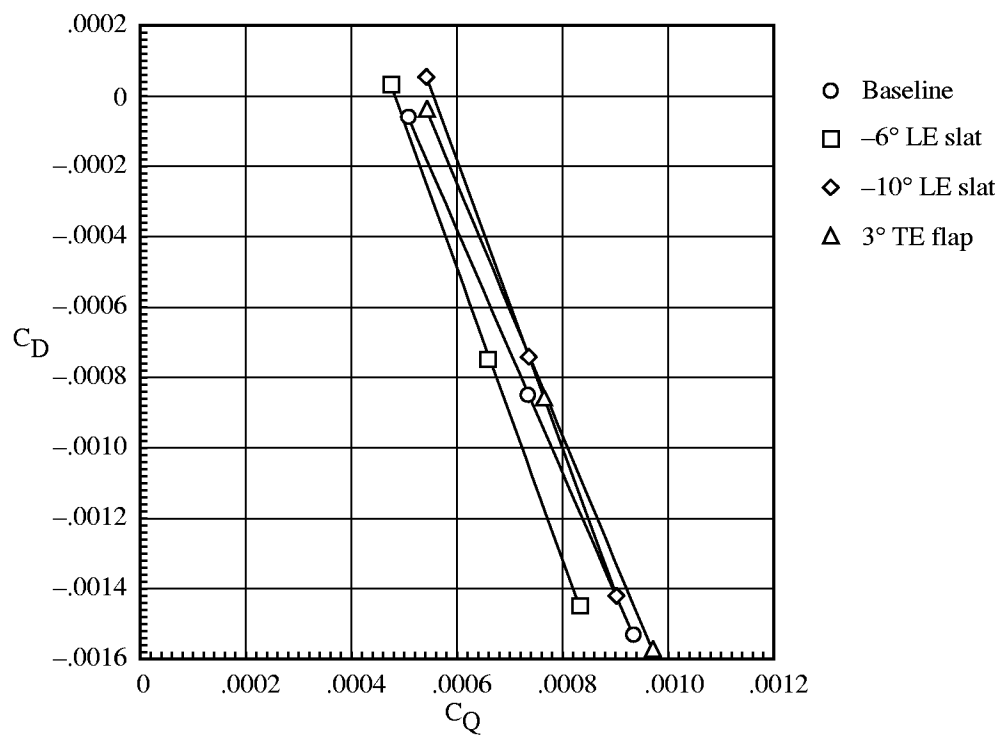


(d) $\mu = 0.30$.

Figure A37. Concluded.

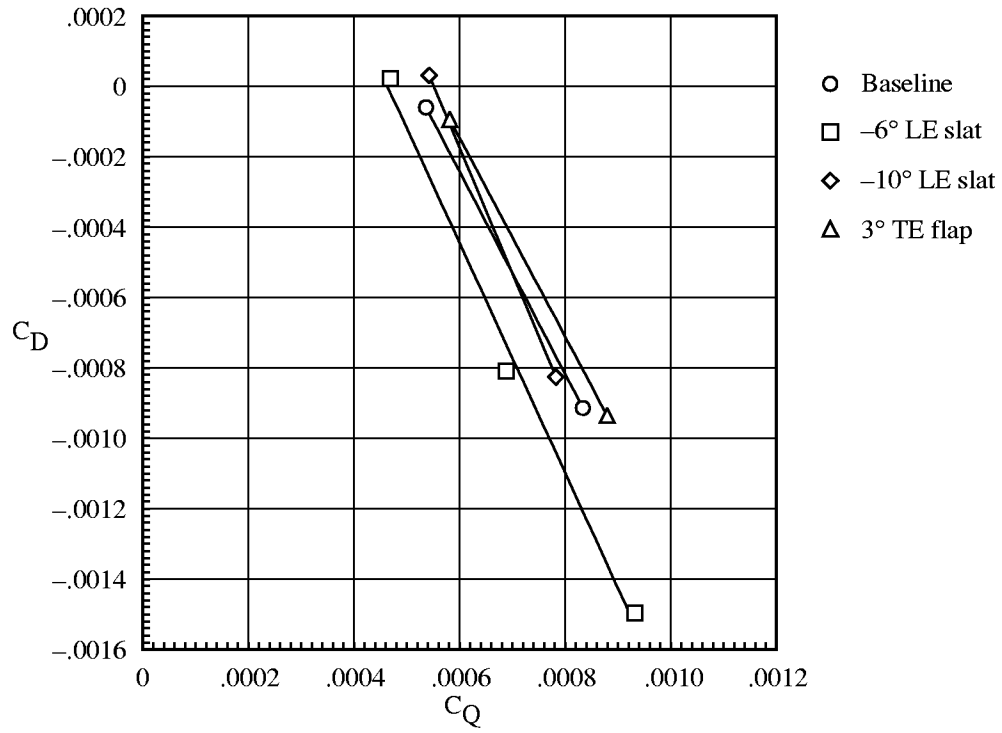


(a) $\mu = 0.15$.

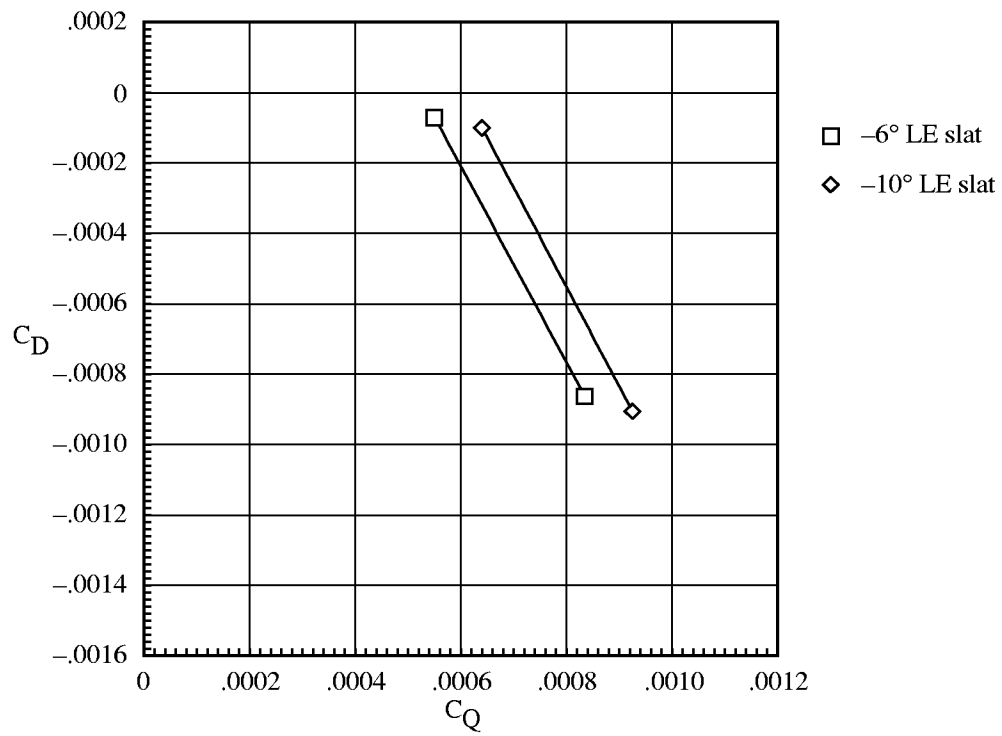


(b) $\mu = 0.20$.

Figure A38. Variation of rotor drag coefficient with rotor torque coefficient for $C_L = 0.010$.

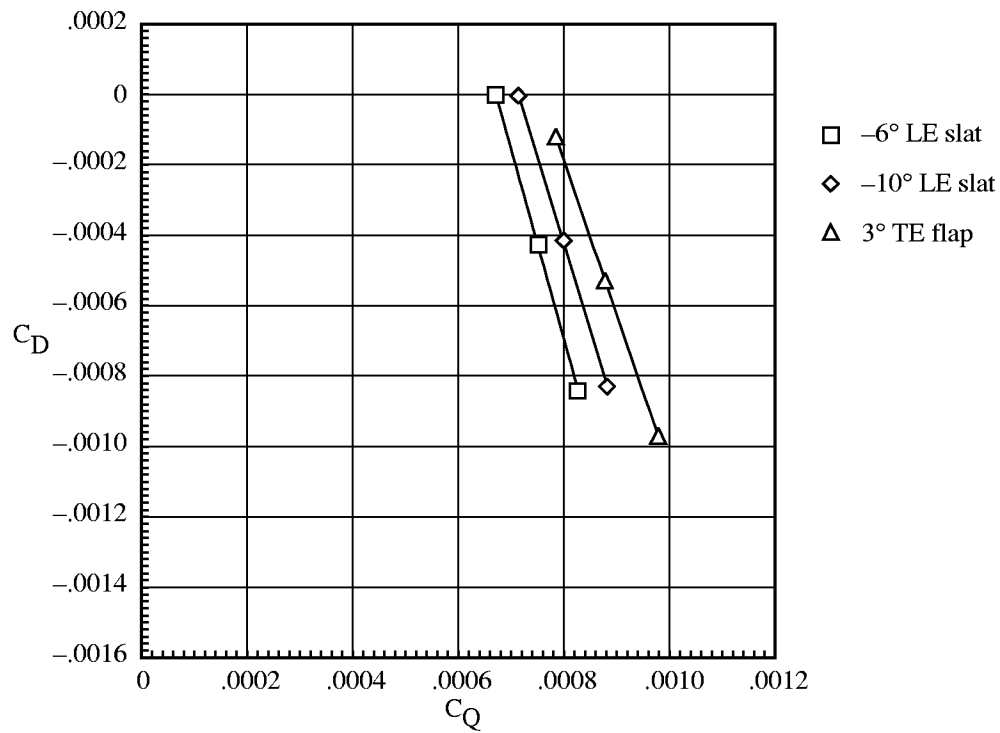


(c) $\mu = 0.25$.

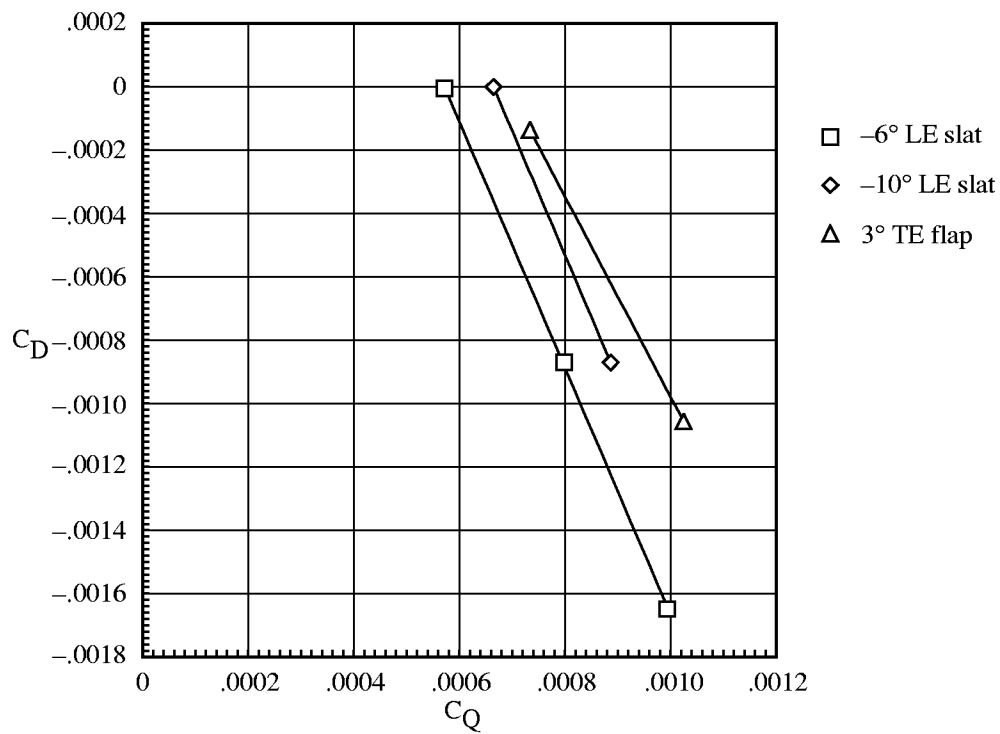


(d) $\mu = 0.30$.

Figure A38. Concluded.

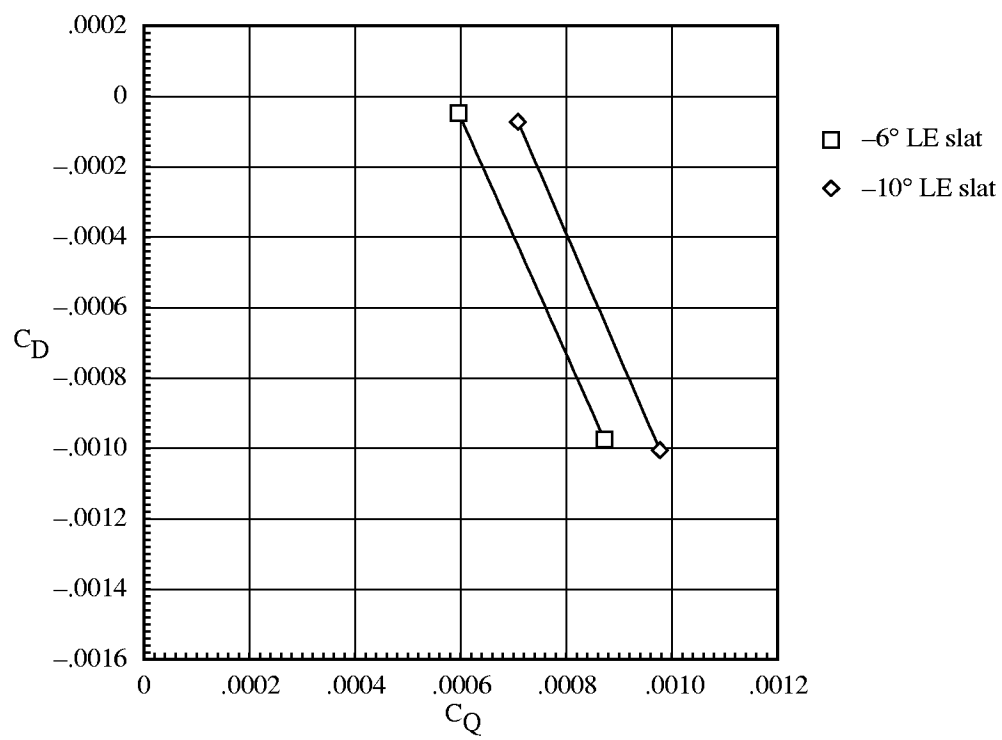


(a) $\mu = 0.15$.



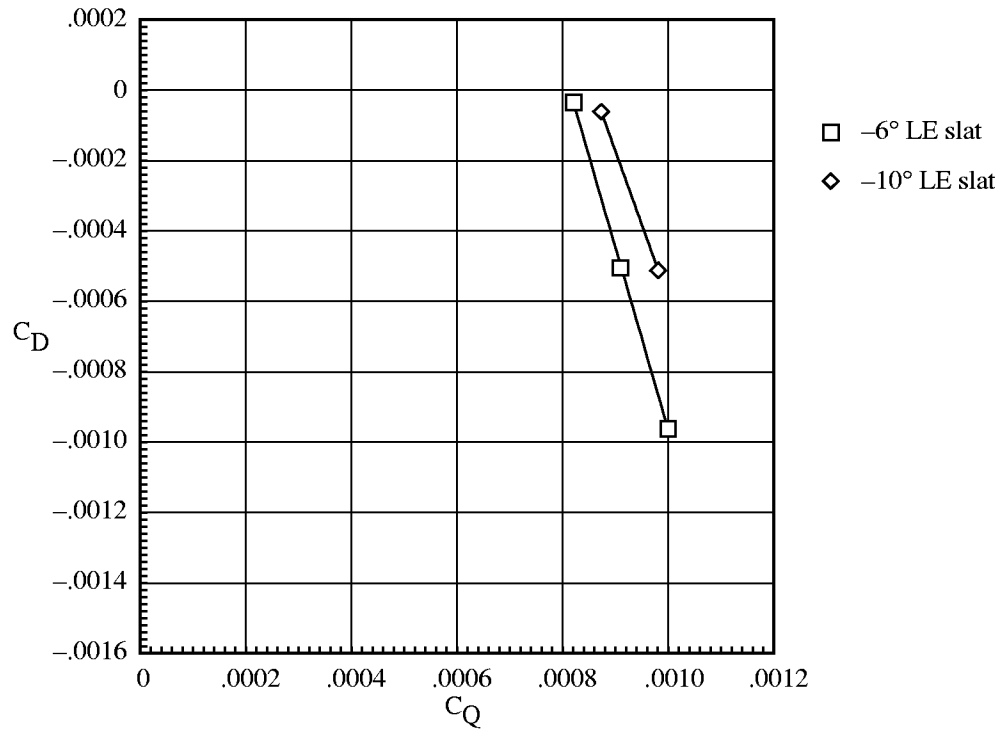
(b) $\mu = 0.20$.

Figure A39. Variation of rotor drag coefficient with rotor torque coefficient for $C_L = 0.011$.

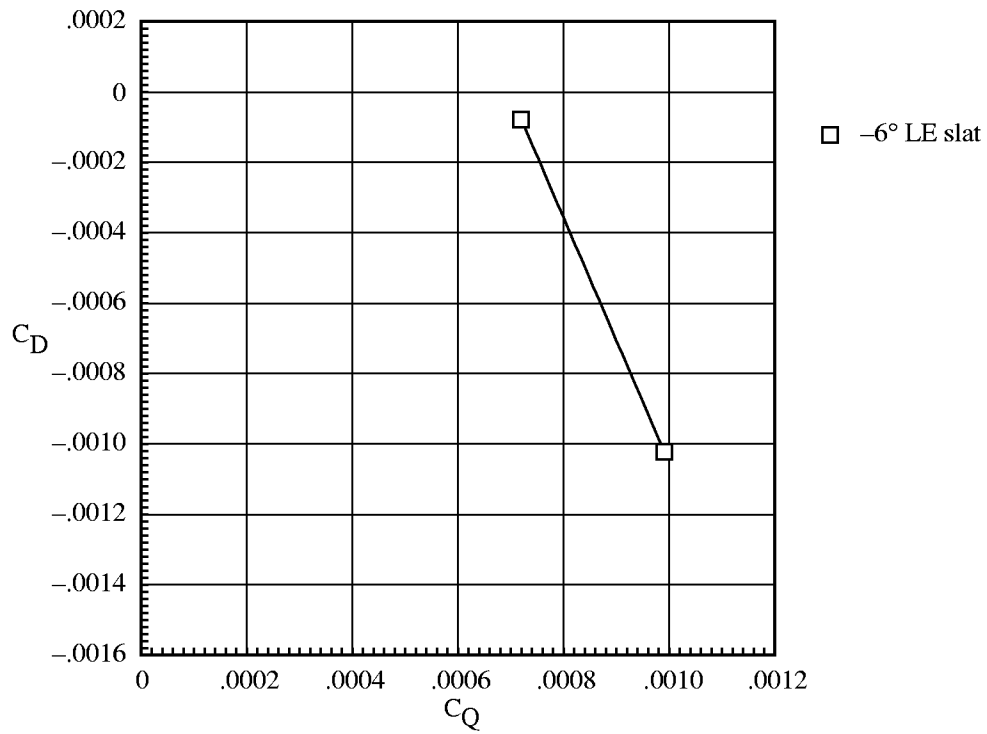


(c) $\mu = 0.25$.

Figure A39. Concluded.



(a) $\mu = 0.15$.



(b) $\mu = 0.20$.

Figure A40. Variation of rotor drag coefficient with rotor torque coefficient for $C_L = 0.012$.

REPORT DOCUMENTATION PAGE			Form Approved OMB No. 0704-0188	
Public reporting burden for this collection of information is estimated to average 1 hour per response, including the time for reviewing instructions, searching existing data sources, gathering and maintaining the data needed, and completing and reviewing the collection of information. Send comments regarding this burden estimate or any other aspect of this collection of information, including suggestions for reducing this burden, to Washington Headquarters Services, Directorate for Information Operations and Reports, 1215 Jefferson Davis Highway, Suite 1204, Arlington, VA 22202-4302, and to the Office of Management and Budget, Paperwork Reduction Project (0704-0188), Washington, DC 20503.				
1. AGENCY USE ONLY (Leave blank)		2. REPORT DATE December 2001		3. REPORT TYPE AND DATES COVERED Technical Publication
4. TITLE AND SUBTITLE Wind Tunnel Evaluation of a Model Helicopter Main-Rotor Blade With Slotted Airfoils at the Tip			5. FUNDING NUMBERS WU 581-10-11-01	
6. AUTHOR(S) Kevin W. Noonan, William T. Yeager, Jr., Jeffrey D. Singleton, Matthew L. Wilbur, and Paul H. Mirick				
7. PERFORMING ORGANIZATION NAME(S) AND ADDRESS(ES) Joint Research Program Office Aeroflightdynamics Directorate U.S. Army Aviation and Missile Command NASA Langley Research Center Hampton, VA 23681-2199 Vehicle Technology Center U.S. Army Research Laboratory NASA Langley Research Center Hampton, VA 23681-2199			8. PERFORMING ORGANIZATION REPORT NUMBER L-17776	
9. SPONSORING/MONITORING AGENCY NAME(S) AND ADDRESS(ES) National Aeronautics and Space Administration Washington, DC 20546-0001 U.S. Army Aviation and Missile Command Moffett Field, CA 94035-1000			10. SPONSORING/MONITORING AGENCY REPORT NUMBER NASA/TP-2001-211260 AMCOM/AFDD/TR-00-A-003 ARL-TR-2154	
11. SUPPLEMENTARY NOTES Noonan: JRPO, Aeroflightdynamics Directorate, AMCOM, Langley Research Center, Hampton, VA; Yeager, Singleton, Wilbur, and Mirick: Vehicle Technology Center, ARL, Langley Research Center, Hampton, VA.				
12a. DISTRIBUTION/AVAILABILITY STATEMENT Unclassified-Unlimited Subject Category 02 Availability: NASA CASI (301) 621-0390 Distribution: Standard			12b. DISTRIBUTION CODE	
13. ABSTRACT (Maximum 200 words) Data for rotors using unconventional airfoils are of interest to permit an evaluation of this technology's capability to meet the U.S. Army's need for increased helicopter mission effectiveness and improved safety and survivability. Thus, an experimental investigation was conducted in the Langley Transonic Dynamics Tunnel (TDT) to evaluate the effect of using slotted airfoils in the rotor blade tip region (85 to 100 percent radius) on rotor aerodynamic performance and loads. Four rotor configurations were tested in forward flight at advance ratios from 0.15 to 0.45 and in hover in-ground effect. The hover tip Mach number was 0.627, which is representative of a design point of 4000-ft geometric altitude and a temperature of 95°F. The baseline rotor configuration had a conventional single-element airfoil in the tip region. A second rotor configuration had a forward-slotted airfoil with a -6° slat, a third configuration had a forward-slotted airfoil with a -10° slat, and a fourth configuration had an aft-slotted airfoil with a 3° flap (trailing edge down). The results of this investigation indicate that the -6° slat configuration offers some performance and loads benefits over the other three configurations.				
14. SUBJECT TERMS Helicopters; Helicopter rotor performance; Model rotor testing; Slotted airfoils; Blade loads			15. NUMBER OF PAGES 132	
			16. PRICE CODE	
17. SECURITY CLASSIFICATION OF REPORT Unclassified	18. SECURITY CLASSIFICATION OF THIS PAGE Unclassified	19. SECURITY CLASSIFICATION OF ABSTRACT Unclassified	20. LIMITATION OF ABSTRACT UL	